UNIVERSITÀ DEGLI STUDI DI MILANO
DIPARTIMENTO DI CHIMICA

Scuola di Dottorato in Scienze e Tecnologie Chimiche
Corso di Dottorato in Chimica – XXVII Ciclo

PHOTOCATALYTIC REACTIONS FOR ENERGY CONVERSION

Tutor: Prof. Elena Selli
Coordinatore: Prof. Emanuela Licandro

Tesi di Dottorato di:
Francesca RIBONI
Matr. N° R09687

A.A. 2013-2014

Table of Contents

Chapter 1

Introduction

Since ever, sunlight (*i.e.* the radiation produced and sustained through nuclear reactions occurring inside the Sun) enables the evolution of Earth's living organisms, promotes photosynthesis for food and biomass production and, indirectly, represents the source of hydroelectric and wind energies.

The conversion of this clean and naturally abundant carbon-free resource into useful energy forms, to continuously feed society's prosperity without damage for the environment, is the most important issue of the 21st century which, not by any chance, has been defined the *energy-challenge* century [1,2].

Back in the geological eras, sunlight has also provided Earth with fossil fuels (*e.g.*, oil, natural gas, carbon and biomass), the non-renewable energy source most eagerly consumed [3].

According to Balzani *et al.*, energy is not easy to be defined but can be envisaged as "*an ubiquitous entity looking like heat, electricity and motion that […] shapes and drives every singular instant of our lives*" [2].

Nowadays, the majority of energy is provided by fossil fuels, which, besides being irregularly distributed on the Earth's surface, are progressively diminishing due to population growth and extensive industrialization and civilization [1,3]. In addition, their continue use produces harmful effects such as pollution, jeopardizing human health, and greenhouse gases (GHGs) emission, heavily impacting on global warming.

Oil is the most valuable good in world trade, with a daily consumption of ~ 85 million of barrels (according to estimates dating back to 2003), doomed to grow mainly as a result of increasing car ownership in Asian countries. Being in liquid form, oil is the ideal fuel since it is easy to extract and transport and is practically impossible to replace for some applications [2].

Coal represents the most abundant and, simultaneously, the dirtiest of fossil fuels such that the near future energy-problem related to its use is not represented by its availability but is most likely related to the environmental sustainability.

Indeed, coal burning accounts for 10–15% of CO_2 emitted [4] and the increasing trend in its utilization is in conflict with global efforts for a sustainable climate policy [2].

Finally, biomass in the form of wood is currently sold worldwide at prices not far from fuel price (*i.e.*, 16.5 \$ GJ^{-1} and 16.3 \$ GJ^{-1}, respectively) but, although the competitive market along with comparable heat energy released when they are combusted (*i.e.*, ~ 20 MJ per kg of dry wood and ~ 25–55 MJ per kg of burnt oil), 16 billion metric tons of fossil fuel hydrocarbons are annually burnt instead of biomass because of the unsustainability in producing the approximately 32 billion of metric tons of biomass cheaply enough to produce the same amount of energy, using available land and adopting environmentally-friendly agricultural methods [1].

The ultimate challenge is the production of a fuel that could be stored and easily transported, thus overwhelming both the energy crisis and the environmental emergency. Since the 1970s, molecular hydrogen has been viewed as the ideal synthetic fuel mainly because *i*) it is one of the most abundant element both on the Earth and in the Cosmos, *ii*) it has already been demonstrated that hydrogen-fed vehicles can be successfully designed, *iii*) when it is combusted with oxygen, it generates heat, along with electricity in a fuel cell, *iv*) the only by-product obtained, upon combustion, is water instead of CO_2 and a variety of pollutants as typically occurs from burning fossil fuels. However, H_2 production from hydrogen-containing compounds requires the use of energy; therefore, rather than being an alternative fuel, it should be envisaged as an efficient energy carrier [5,6].

Conversely, solar energy is clean, abundant and represents a virtually cheap energy source. Nevertheless, its greatest limitation is due to the impossibility of being utilized as it is and directly converted into alternative energy sources [3]. To be more precise, though solar power impinging on the Earth's surface amounts to ~ 170 W m^{-2}, it is diffuse and intermittent, so that it first needs to be concentrated and then stored. Estimates of the total energy annually used by mankind assess at ~ 5×10^{20} J, which corresponds to the energy evenly distributed and delivered on the Earth surface by the sun in one hour [3]. Thus, the great potentiality enclosed in this unlimited source is readily unveiled.

The main goal to accomplish is to take inspiration from Nature which, by means of photochemical processes, is able to efficiently capture sunlight and convert it into valuable chemical energy. The maximum light-energy conversion is 6.7% but only a fraction of it can be practically achieved [2].

In photosynthetic organisms, light is harvested by antennae systems. The most widely investigated are the complexes of purple bacteria, composed of two groups of molecules (*i.e.*, bacteriochlorophyll BChl) able to trap the energy of radiation and pass it from one molecule to another until reaching the reaction center (RC) proteins where it can be converted through an excited-state electron-transfer process, into electrochemical energy [2,3].

Though simplistic in its description, the mechanism, so far, has been barely reproduced with artificial devices, as predictable by the findings that evolution took ~ 2 billion years to develop natural photosynthesis [7].

Within this general framework, scientific research is required to urgently provide efficient remedies to harmful pollutants and CO_2 emissions and/or alternatives to the currently misused energy sources.

More than one century ago, the Italian chemist Giacomo Ciamician in his article “The photochemistry of the future” suggested that “*industries should wait any longer before taking advantage of the chemical effects produced by light*” and foresaw that “*forests of glass tubes will extend over the plains and glass buildings will rise everywhere; inside of these will take place the photochemical processes […] that will have been mastered by human industry which will know how to make them bear even more abundant fruit than nature, for nature is not in a hurry and mankind is*” [8].

REFERENCES

[1] E.W. McFarland, *Energy Environ. Sci.* **2014**, *7*, 846.
[2] N. Armaroli, V. Balzani, *Angew. Chem. Int. Ed.* **2007**, *46*, 52.
[3] V. Balzani, A. Credi, M. Venturi, *Chemsuschem* **2008**, *1*, 26.
[4] K.S. Lackner, *Eur. Phys. J. Special Topics* **2009**, *176*, 93.
[5] N. Armaroli, V. Balzani, *Chemsuschem* **2011**, *4*, 21.
[6] B.A. Pinaud, J.D. Benck, L.C. Seitz, A.J. Forman, Z. Chen, T.G. Deutsch, B.D. James, K.N. Baum, G.N. Baum, S. Ardo, H. Wang, E. Millere, T.F. Jaramillo, *Energy Environ. Sci.* **2013**, *6*, 1983.
[7] J.M. Olson, *Science* **1970**, *168*, 438.
[8] G. Ciamician, *Science* **1912**, *36*, 387.

Chapter 2

Theoretical background

2.1 Photocatalysis

Meaningfully, the word *photocatalysis* comprises both the prefix *photo* (from ancient Greek, *phos*: light) and the word *catalysis* (from ancient Greek, *katalyo*: decompose), so that the generally accepted definition is that of a process in which light can be used to activate a substance (*i.e.*, the photocatalyst, most often a semiconductor), which is then able to modify the rate of the chemical reaction, without being involved in the chemical transformation [1].

Despite being a simple and useful definition, it conceals the fact that both an oxidation and a reduction reaction occur simultaneously on the surface of the photocatalyst, on sites often separated by a distance of few angstroms. Both processes have to be carefully balanced in order for the photocatalyst to remain unchanged at the end of the reaction, which is, by definition, one of the essential requirements for a catalyst [2,3].

Contrary to the widespread acceptance that the milestone of photocatalysis is represented by the literature report on Nature by Honda and Fujishima, dating back to 1972 [4], which overcomes 400 citations per year in the first decade of the current century, the earliest work concerning photocatalysis appeared in 1921. Renz reported that TiO_2 (the most adopted photocatalyst) is partially reduced when illuminated with sunlight and in the presence of an organic compound, such as glycerol, with the oxide turning from white to dark colour (*i.e.*, grey, blue or black). The same phenomenon was also observed, under the same experimental conditions, with metal oxide semiconductors such as CeO_2, Nb_2O_5 and Ta_2O_5 [5].

It was only in 1924 that Baur *et al.*, observing the reduction of a silver salt to metallic Ag on irradiated ZnO, introduced the idea of oxidation and reduction reactions concurrently occurring and driven by holes and electrons, respectively, photogenerated upon the illumination of the semiconductor metal oxide [6].

From that moment onward, research on photocatalysis greatly expanded spanning from environmental remediation for water and air pollutants removal, biological applications, hydrogen production and, in more general terms, energy conversion, carbon dioxide reduction and finally, when coupled with electrochemistry, opened up the field of photoelectrochemistry (PEC), with the result of being often envisioned as one of the most promising techniques to be adopted to face the energy-challenge of the current century [7].

2.1.1 Band structure of photocatalysts

The majority of the photocatalysts adopted in heterogeneous systems are metal oxide semiconductors, so that their electronic structure can be described according to the *band theory*.

Semiconductors bands are typically formed by closely spaced atomic orbitals, one for each individual atom. Due to the large number of overlapped orbitals, the difference in energy between those adjacent, within a given energy band, is relatively small so that each band can be envisaged as a continuum of energy levels [8].

Each band has a different energy and the electrons fill these energy levels in a way that resembles the occupation of orbitals in a single atom. The highest occupied energy level (analogous to HOMO in a molecular orbital) is called *valence band*, VB, and the next higher band, correspondingly analogous to LUMO, is called *conduction band*, CB, with the highest and lowest energy levels of each band being referred to as *band edges*. The difference in energy between the upper edge of the valence band and the lower edge of the conduction band is called *band gap*, E_g, which determines the properties of the material and can be considered as the third, though forbidden, band such that electrons move vertically from the VB to the CB with no spatial change occurring [9]. Usually, for semiconductors, the band gap width lies within 1 and 5 eV [1,8].

Upon absorption of photons with suitable wavelength (*i.e.*, energy), electrons can be promoted from the valence band into the conduction band, with the consequent formation of a hole-electron couple (h^+/e^-), the lifetime of which is in the order of nanoseconds.

Photogenerated electrons and holes, also called charge carriers, are responsible for the conductivity of the material and promote all subsequent steps of a photocatalytic reaction: both can move freely in their respective bands, they may be trapped in suitable sites on the semiconductor surface, transfer to the adsorbed substrate and finally reduce it (e^-) or oxidize it (h^+) (Figure 2.1a).

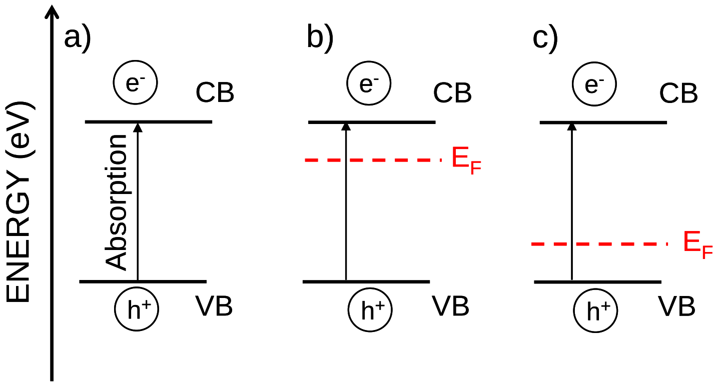

Figure 2.1 – a) Simplified scheme of a semiconductor activation. b) *n*-type semiconductor. c) *p*-type semiconductor. VB, Valence Band; CB, Conduction Band; E_F, Fermi level [8,9].

It has been pointed out that, immediately after the band-to-band transition, e^- and h^+ are trapped by the semiconductor crystal lattice sites which enhances their spatial separation and decreases the probability of their recombination (which would be detrimental for the overall photocatalytic process); however, the exact location, density and spatial distributions of these sites, along with the charge carriers migration mechanism, greatly influencing the initial stage of photocatalysis, have still to be clearly outlined [9].

Another important parameter to be considered when discussing the band structure of photocatalysts is their Fermi level, E_F. By definition, E_F is the energy level at which the probability of occupation by an electron is ½ [8]. For an intrinsic semiconductor (*i.e.*, with no impurities) the Fermi level lies exactly at the mid-point of the band gap. A change in the distribution of the electrons within the solid, usually attained by doping (*i.e.*, introducing atoms of a different element in the semiconductor hosting lattice), affects the position of E_F. In particular, in *n*-type semiconductors, where the dominant charge carriers are electrons, the Fermi level lies just below the conduction band (Figure 2.1b), whereas in *p*-type semiconductors, where the majority of charge carriers are the positively-charged holes, it lies above the valence band (Figure 2.1c) [2,8,10].

When a semiconductor comes into contact with another phase (*e.g.*, liquid or gas phase, as typically occurs in heterogeneous photocatalysis), charge redistribution usually occurs, in order for the two phases to be in equilibrium and the so-called Schottky barrier is formed. From the point of view of energy levels, this implies that the electrochemical potentials of the two species must be the same, with the electrochemical potential of a solution being the redox potential of the electrolyte, while that of a semiconductor being its Fermi level [8,11].

In most of the *n*-type semiconductors, Fermi levels are more cathodic (higher in energy) than the redox potential of the electrolyte, hence the electrons lying in donor levels slightly below the CB are injected into the electrolyte. Thus, since the majority charge carriers (e^-) are removed, a depletion layer is formed and this generates an upward bending of the band edges (Figure 2.2a).

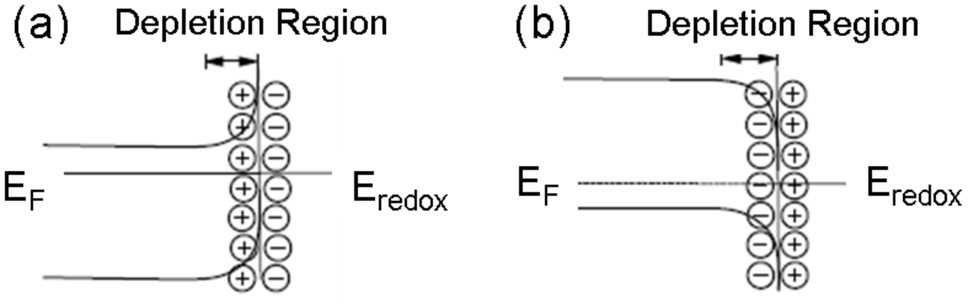

Figure 2.2 – Band bending for (a) an *n*-type semiconductor and (b) a *p*-type semiconductor, both in equilibrium with a solution [8].

Conversely, for a *p*-type semiconductor, where the Fermi level is more anodic than the electrolyte redox potential, the system equilibration is achieved when electrons are transferred from the solution to the semiconductor, with the consistent downward bending of the band edges. Also in this case, the dominant charge carriers (h^+) are removed from the semiconductor/liquid junction and a depletion layer is consequently formed (Figure 2.2b) [8,9,11].

2.1.2 TiO_2 as photocatalyst

Titanium dioxide is by far the most adopted semiconductor, either in photocatalysis or in photoelectrochemical devices. It is non toxic and relatively cheap, it has a high chemical stability, hence it can be used in a wide pH range; it is capable of absorbing light in the near UV region and undergoing electronic transitions and finally, due to the suitable position of its valence band edge (E^0_{VB} ~ 2.6 V *vs* SHE at pH 0 [2]) has a high oxidation ability toward most of the organic pollutants.

TiO_2 crystallizes in three main different structures: anatase (A), rutile (R) and brookite (B) and evidence that these phases stability is largely dependent on the TiO_2 nanoparticles (NPs) size has been recently reported. In particular, anatase phase was found to be the most stable phase for nanoparticles smaller than 11 nm, the rutile form is the most stable for NPs with diameters above 35 nm and brookite for the intermediate size range (*i.e.*, 11 – 35 nm) [12].

Despite being a natural phase, brookite is the less abundant and the most difficult to prepare. It has an orthorhombic symmetry and typically reported cell parameters are a = 5.436 Å, b = 9.166 Å, c = 5.135 Å [13]. It is constituted by an elementary cell containing 8 formula units. The Ti surrounding coordination polyhedron is an octahedron, with a high oxygen atom packing. It usually forms very flat small tubular crystals with variable color, from yellow to brown reddish. Finally, being metastable, out of a restricted pressure and temperature interval, it is converted into the other two phases.

Both the anatase and the rutile polymorphs are more largely adopted for photocatalytic applications. Their basic building blocks consist of a titanium atom surrounded by six oxygen atoms in a more or less distorted octahedral configuration [13].

Rutile (tetragonal cell with typical cell parameters a = b = 4.584 Å and c = 2.953 Å [13]) has three main crystal faces: (110), (100) and (001). The latter is thermally the less stable, the (110) being the most stable. Highly distorted TiO_6 formula unit, in octahedral configurations, constitute the structure. Each Ti ion is surrounded by six O ions, whereas every O ion is surrounded by 3 Ti ions at the edges of an equilateral triangle; thus the whole structure can be envisaged as a central body cubic lattice of Ti ions (Figure 2.3a). The crystallites is naturally black or reddish, but also transparent when the oxide has nearly no impurities [2,10].

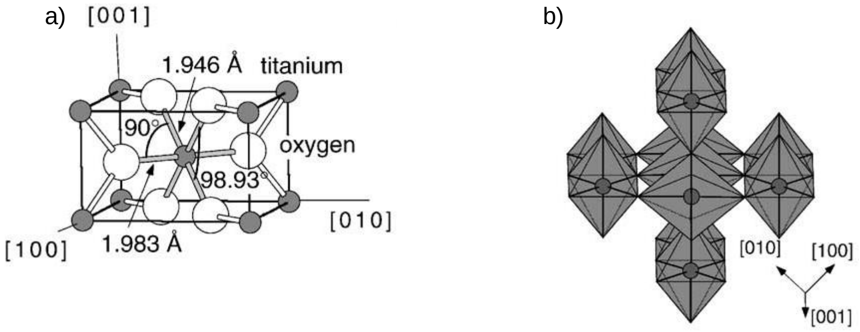

Figure 2.3 – a) Tetragonal unit cell of the rutile phase. Also the bond lengths and the bond angles of the octahedrally distorted TiO_6 unit cell are reported. b) Stacking of the octahedral units in the rutile structure [13].

Anatase (tetragonal cell with typical cell parameters a = b = 3.782 Å and c = 9.502 Å [13]) has two low energy surfaces, (101) and (001), which are the most abundant in nature. The first face, usually corrugated due to the spatial distribution of O and Ti atom rows, is the most prevalent phase for anatase, while

the (001) is usually flat. The less common (100) surface is usually formed in rod-like anatase, grown by hydrothermal synthesis [2].
It has a tetragonal bipyramidal symmetry, which resembles an elongated octahedron (Figure 2.4a) and the main difference with rutile is represented by its more distorted structure [14]. Crystals are small, with color ranging from blue to yellow-brown.

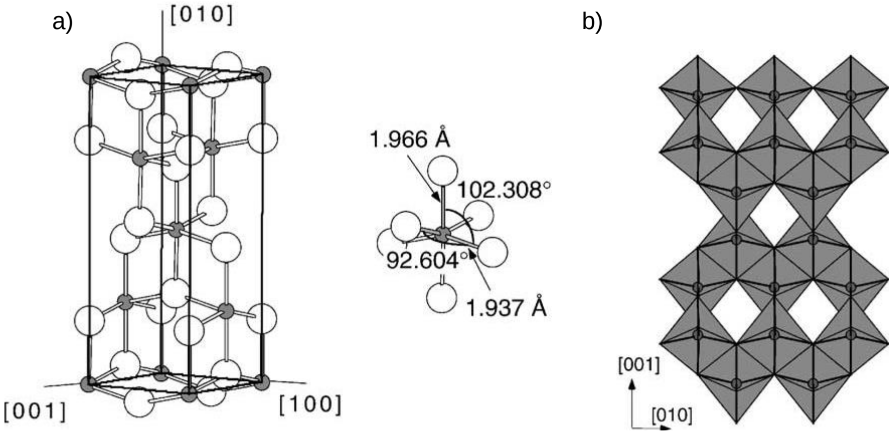

Figure 2.4 – a) Tetragonal unit cell of the anatase phase. Also the bond lengths and the bond angles of the octahedral distorted TiO_6 unit cell are reported. b) Stacking of the octahedral units in the anatase structure [13].

All the listed faces of each polymorph display different photocatalytic activity but the deep reasons for these observations have not yet been elucidated [2].
Anatase and rutile polymorphs are also characterized by different bulk optical properties. Indeed, difference in lattice structures yields significant differences in the electronic band structures between the two forms of TiO_2 [14].
A semiconductor absorption threshold is the lowest photon energy at which the probability to generate charge carriers is maximized and can be defined as the efficient coupling between the highest density of states (DOS) close to the VB maximum and the highest density of states near the CB minimum. Both energy states are characterized by a given crystal momentum; when the crystal momentums are the same, the charge carriers generation occurs through a *direct* mechanism; conversely, when they are different the mechanism is *indirect*. TiO_2 absorption thresholds are well known and always largely cited; anatase is an indirect band gap semiconductor, with absorption threshold at ~ 3.2 eV, whereas rutile is a direct band gap material with absorption threshold at ~ 3.0 eV [15].

2.1.3 Surface modification of TiO_2 with noble metal nanoparticles

Once electrons and holes are generated upon semiconductor band gap excitation, other than being trapped at semiconductor trapping sites, they may also undergo recombination, with a detrimental effect for the photocatalytic process to proceed. The process of this back-reaction occurs in time-scale of the order of microsecond and is one of the drawbacks most likely limiting TiO_2 photoactivity [2,16]. Kinetics, governing the recombination, may vary depending on the process: if a single electron is firstly excited and then recombines with a h^+, the recombination rate obeys the first-order rate law; when the process involves multiple h^+/e^- pairs the rate obeys a second-order rate law [2].

One of the most adopted techniques to limit this drawback is represented by the deposition, on the semiconductor surface, of noble metal nanoparticles (*e.g.*, Pt, Ag, Au, Pd, Ir) which by virtue of their high work function (*i.e.*, the energy required to remove an electron from a solid, calculated with respect to the vacuum level) efficiently trap excited e^- enhancing the spatial separation with h^+, trapped on the photocatalyst surface, and decreasing the charge carriers recombination rate.

Electron trapping

Resembling band bending phenomenon occurring at the junction between a solid semiconductor and a liquid/gas phase (see Section 2.1.1), when a semiconductor comes into contact with a metal electrons spontaneously transfer, due to the work function difference. In particular, if the work function of the metal (Φ_m) is higher than that of the semiconductor (Φ_s), the electrons flow from the latter to the former (Figure 2.5) [10]. Electrons transfer will proceed until the Fermi levels of the two materials equilibrate (Figure 2.5c).

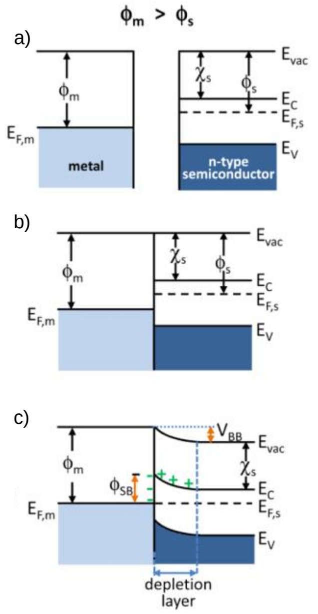

Figure 2.5 - Energy band diagrams of metal and *n*-type semiconductor contacts. In detail, a) not in contact; b) in contact; c) in contact after equilibrium. E_{vac}, vacuum energy level; E_C, energy of CB minimum; E_V, energy of VB maximum; Φ_m, metal work function; Φ_s, semiconductor work function; χ_s, electron affinity of the semiconductor; $E_{F,m}$ and $E_{F,s}$, Fermi levels of metal and semiconductor, respectively [10].

Accordingly to the semiconductor/liquid interface, under equilibrium, the metal is negatively charged, due to electrons accumulation, while semiconductor is positively charged and a depletion layer is readily formed, also yielding band upward bending (Figure 2.5c). The degree of band bending in the semiconductor (V_{BB}) equals the difference between the work functions of the two materials (2.1)

$$V_{BB} = |\Phi_m - \Phi_s| \tag{2.1}$$

Furthermore, when $\Phi_m > \Phi_s$, a Schottky barrier (Φ_{SB}) forms at the metal/semiconductor junction, which is defined as the difference between the metal work function and the semiconductor electron affinity, χ_s, (2.2)

$$\Phi_{SB} = (\Phi_m - \chi_s) \tag{2.2}$$

In ionic semiconductors, such as TiO_2, both V_{BB} and Φ_{SB} depend on the work function difference at a higher extent than in covalent semiconductors (*e.g.*, Si, GaAs) [10].

Since the initial report of water splitting yielding hydrogen and oxygen evolution [4], the most extensively studied noble metal for promoting TiO_2 photocatalysis is Pt [15,17]. Indeed, the work function of Pt (Φ_{Pt} ~ 5.3 – 5.6 eV [18]) is much higher than that of TiO_2 (Φ_{TiO2} ~ 4.6 – 4.7 eV [18]), so the electrons transfer to the Pt NPs deposited on the surface of TiO_2, while the holes remain trapped in the semiconductor VB. Furthermore, the enhanced photoactivity of the Pt/TiO_2 systems has also been attributed to *i*) the greater electron scavenging capability for molecular O_2 [19], *ii*) the promotion of $OH^{\bullet}$ formation [20], *iii*) de-aggregation of TiO_2 particles in suspension [21]. Recently, investigation of the Pt/TiO_2 performance has been mainly focused on photocatalytic hydrogen production, rather than an oxygen evolution, due to the suitable match between the reduction potential of Pt-trapped electrons and the H^+ reduction potential [17]. Most promising results have been obtained when alcohols, such as methanol, have been used as hole scavengers [22,23]. Indeed, since the reduction potential of methanol (0.13 V) is lower than that of oxygen to water (1.23 V), alcohols are more efficient in scavenging TiO_2-trapped holes, further preventing recombination back-reactions.

Plasmonic noble metal nanoparticles

Along with the high probability of charge carriers recombination, the relatively high band gap of TiO_2 allows only the use of the UV portion of the solar spectrum to promote photocatalytic reactions. Aside the extensively investigated non-metal (*e.g.,* N, S, C, B etc.) doping able to induce intra-band gap states within the semiconductor electronic structure, thus reducing its band gap and, in some cases, opening up photoactivity by visible light irradiation [24], also noble metals (*e.g.,* Au, Ag, Cu) strongly absorb visible light, due to Localized Surface Plasmon Resonance (LSPR), which may initiate photocatalytic processes on semiconductor nanoparticles [25].

Plasmonic induced photoactivity on a optically inert semiconductor was first reported in 2008. It was shown that Au NPs, deposited on SiO_2, efficiently photodegraded formic acid under visible light illumination [26].

LSPR is the collective oscillation of the metal valence electrons, promoted upon suitable irradiation and occurring when the incident photons frequency matches with the oscillation frequency of the metal surface free electrons, against the restoring force of the positively charged nuclei. This positive interaction results in the photon energy confinement, on the surface of metal nanostructures, for much longer times than they would normally spend [27-29].

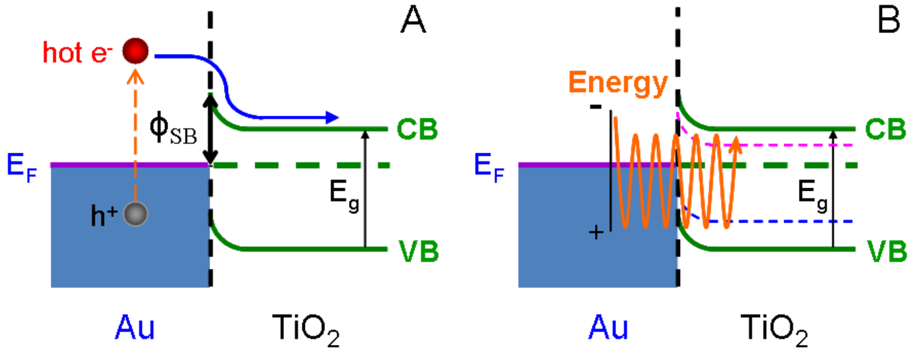

Figure 2.6 – (A) Mechanism of hot electron generation due to LSPR and consequent injection into the CB of TiO_2. (B) Mechanism of Plasmon Resonance Energy Transfer (PRET) from resonating Au plasmon to the band gap of TiO_2. Φ_{SB}, Schottky barrier junction; E_g, band gap energy.

Hence, LSPR excitation produces a large accumulation of photon intensity (*i.e.*, strong electric field), as well as a high concentration of energetic electrons at nanostructured surfaces. Both the incident excitation wavelength and the intensity of LSPR depend on the type of metal, its dimension and shape. LSPR decay takes place on a femtosecond time-scale either through radiative processes, such as re-emission of photons characteristic of larger nanoparticles (> 50 nm), or non-radiatively by conveying excess energy in the generation of charge carriers, which may be transferred or, ultimately, relax through electron-electron or electron-phonon collisions and are converted into heat. This second process is usually more favourable for nanoparticles < 30 nm [27,28,30].

After the non-radiative decay, metal electrons are excited from occupied energy levels above the Fermi energy. In particular, *d* band energy levels lie 2.4 eV and 4 eV below the E_F for Au and Ag, respectively. Surface plasmons, in these metal nanostructures, can transfer energies to hot electrons, up to approximately 1 eV and 4 eV [30,31]). An efficient mechanism for trapping hot electrons is to form a Schottky barrier with an appropriate semiconductor, such that formed at Au/TiO_2 junction. Hot electrons with energies higher than the Φ_{SB} can be injected into the semiconductor conduction band and initiate the photocatalytic process. Indeed, electrons with ~1 eV energy have extremely long mean-free path (~ 17 – 50 nm) in noble metals, so that a large fraction of them can successfully move through the metal nanostructure and reach the metal/semiconductor junction (Figure 2.6(A)) [30,32]. Conversely, tunnelling across the barrier usually takes place with much lower probability. Useful characteristic of SPR is that the energy needed for hot electrons to overcome the Schottky barrier is considerably smaller than the semiconductor band gap [30]. Plasmonic nanoparticles can thus be thought as dye-sensitizer, injecting negative charge, with excellent mobility of charge carriers and higher absorption cross section than semiconductors [28].

It is often reported that the plasmonic radiative energy transfer can also occur through the near-field electromagnetic mechanism, based on the interaction of the semiconductor with the strong SPR-induced electric field generated close to the metallic nanostructures [27]. Photoexcited plasmonic E is much more intense than the electromagnetic field born by the photons used to excite the metal nanostructures, it is spatially non-homogeneous and the highest intensity is localized on the metal surface and decreases exponentially with the distance. Hence, when a semiconductor is in the proximity of a photo-excited SPR, it experiences this intense field. Since the rate of charge carriers in a photocatalyst is directly proportional to the incident electromagnetic field (more properly, to $|E|^2$), h^+/e^- may either be promoted or their generation rate may be enhanced (when h^+/e^- pairs are generated through different pathways). In this case, plasmonic metal act as antenna o nanosized concentrators, which amplify the local light intensity (Figure 2.6(B)). The mechanism most likely occurs in the region of the semiconductor closest to the plasmonic nanostructures, that is near the surface or, in other words, at the semiconductor/liquid junction where they can be readily separated, driven by the different electrochemical potentials of the two species (see Section 2.1.1), and initiate photocatalytic reactions [27].

Several authors reported that plasmonic nanostructures can also efficiently dissipate incident light energy leading to an increase in local temperature of the system [31]. Also this temperature increase may be a reason for plasmonic photocurrent generation and promotion of plasmonic photocalysis and will be discussed in deeper details in Section 4.2.2.

Gold is often proposed to be more efficient than silver, mainly due to its higher work function (Φ_{Au} ~ 5.1 – 5.3 eV, Φ_{Ag} ~ 4.5 – 4.7 eV [18]), though the reasons for one of the above mentioned mechanisms to prevail over the other in promoting plasmonic photocatalysis on TiO_2 are still under debate (see Section 4.1 for further details).

2.1.4 Composite TiO_2-based nanomaterials

Lengthening of photogenerated h^+/e^- pairs lifetimes, along with increased interface electron transfer rate, both favorable for the enhancement of the quantum efficiency of a photocatalytic process, may be attained also with TiO_2-based composite nanomaterials. By definition, a composite is the combination of one or more materials with TiO_2. These combinations may have the form of layered or core-shell structures, as well as that of coupled mixed oxides [17].

For instance, by coupling TiO_2 with another metal oxide having the conduction band lower in energy than the CB of TiO_2 and the valence band almost at the same value or even lower in energy than the VB of TiO_2, photopromoted electrons are transferred from the CB of TiO_2 to the CB of the coupled metal oxide, while photogenerated holes might be trapped within the TiO_2 particles [33]. Redox reactions can now occur on separate surface sites since the probability of charge recombination is diminished. Thus, a heterojunction composite structure can be rationally designed to produce a favourable band offset and band positions [17]. Figure 2.7 graphically summarizes the mechanism occurring in TiO_2-WO_3 mixed oxides.

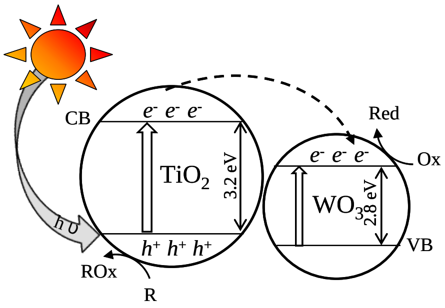

Figure 2.7 – TiO_2-WO_3 mixed oxide photocatalyst. Electrons (e^-) photopromoted in TiO_2 CB are efficiently transferred to the WO_3 CB, due to the lower energy of the latter, where they can reduce adsorbed oxidants. Conversely, photogenerated holes preferentially remain trapped in TiO_2 VB where they can be scavenged by organic species [33].

Recent examples of effective mixed oxides photocatalysts with increased photocatalytic activity in either liquid or gas phase reactions include sol‑gel synthesized WO_3-TiO_2 [33], Fe_2O_3-TiO_2 and Y_2O_3-Fe_2O_3-TiO_2 [34], ball-milling and sol‑gel synthesized ZnO-TiO_2 photocatalysts, whose activity has been measured in both reduction and oxidation processes [16,35], and the mesoporous PdO-TiO_2 nanocomposites synthesized by a simple sol‑gel process in the presence of a copolymer as templating agent and employed in CH_3OH photo-oxidation [36].

However, the most common and simple TiO_2-based composite is commercial Degussa P25, or simply P25 for short, constituted by the intimate mixing between anatase and rutile polymorphs in concentration ~ 20 : 80 (R : A) [17]. In 1996 electrochemical impedance spectroscopy highlighted that the conduction band of anatase lies ca. 0.2 eV above that of rutile [37]. This band alignment favours the transfer of photogenerated electrons from anatase to rutile and that of holes in the opposite direction, though the yield for the latter process is heavily suppressed since the valence band position of the two polymorphs are very similar [38], ensuring enhanced charge carriers separation and, in combination with other suitable physico-chemical characteristics, accounts for P25 high photocatalytic activity.

In addition to the improvement of photocatalytic efficiency, composite structures bear also other benefits. For example, by selecting oxides with different surface properties (*e.g.*, roughness, acidity, etc.), that of the resulting material can be easily adjusted in order to favour the adsorption of substrate molecules, always identified as one of the critical factors of any catalytic process. Furthermore, core-shell materials are known to stabilize nanoparticles, preventing their sintering and aggregation, whereas composites can be exploited to create highly porous materials, hollow shells or hierarchical structures by templating methods [17].

Specifically concerning TiO_2-WO_3 mixed oxides, WO_3 coupling has been widely used to improve the photoelectrochemical and photocatalytic performance of TiO_2 since it is more acidic and can serve as an electron accepting species [39]. Band gaps of WO_3 and TiO_2 are 2.8 and 3.2 eV, respectively; while TiO_2 can be excited only by photons with wavelengths shorter than 387 nm, WO_3, in theory, may be excited by photons with wavelengths up to 443 nm, but it actually shows only low photocatalytic activity under UV light. When WO_3 and TiO_2 form a mixed photocatalyst, they can be excited simultaneously under UV illumination. As the conduction band of WO_3 is lower than that of TiO_2 ($E_{CB}(TiO_2) = -0.52$ V and $E_{CB}(WO_3) = 0$ V, both referred to NHE at pH 0 [16,33,40]), the former can act as a sink for the photogenerated electrons with the formation of reduced W^{5+} species which not only efficiently assist charge separation but act also as reduction sites [41] (Figure 2.7).

Interestingly, WO_3 has been also reported to retard titania anatase to rutile phase transition typically occurring in TiO_2 calcined at temperature above 600 °C, thus yielding, under specific conditions, higher photoactivities attained with the composite sample than with pristine TiO_2. Notwithstanding the enhanced photocatalytic efficiency of TiO_2-WO_3 mixed oxides, high concentration of W domains may also introduce defect states where the charge carriers recombination can be promoted so that WO_3/TiO_2 molar ratios higher than 3 mol.% are often reported to be detrimental for the composite materials photoactivity [33,42,43].

2.2 Strategies for the reduction of CO_2

Despite the growth of non-fossil energy (such as nuclear and hydropower) considered as non-emitting source, the global share of fossil fuels has remained relatively unchanged over the past 40 years and, in 2010, fossil sources accounted for 81% of the global Total Primary Energy Supply [44].

Fossil-fuel burning, upon combustion or other oxidative processes, results in the transformation of the fuel carbon content into carbon dioxide, one of the major greenhouse gases (GHGs) contributing to global warming [45].

According to the "*CO_2 Emission from Fuel Combustion – 2012 Edition*" released by the International Energy Agency (IEA), global CO_2 emission rose by 4.6% in 2010, after having declined in 2009 due to the impact of the financial crisis, in particular in Western economies.

Traditionally, industrialized countries have emitted the majority of anthropogenic GHGs but recent investigations revealed that, in 2011, the CO_2 emissions of developing countries continued to increase at a faster rate than those of the developed ones, mainly as a result of growing fossil fuel consumption in some of the largest countries, such as China and India.

IEA also reported an overview of the global carbon dioxide emission detected in 2010, on the basis of different indicator sources and methods (Table 2.1).

Indicator	CO_2 amount
Total CO_2 emission from fossil fuel combustion	30276.1 $MtCO_2$
CO_2 emission/GDP	0.59 $kgCO_2$/2005 USD
CO_2 emission/population	4.44 tCO_2/capita
CO_2 emission/kWh from electricity generation	565 gCO_2/kWh

Table 2.1 – Global CO_2 emission from different indicator sources [44].

Thus, general upward trends in CO_2 emissions from fuel combustion illustrate the need for all countries to shape a more sustainable energy future and, as suggested by Lackner *et al.*, "*if the world cannot afford to dump more carbon dioxide into the atmosphere, then the ability to remove it should be viewed as an essential goal to be achieved*" [46]. Special emphasis should be first addressed to the industrialized nations that have the highest per-capita incomes and that are responsible for the bulk of cumulative emissions [44].

Despite the efforts carried out by numerous research teams in the last 20 years, mainly through *i*) Carbon Capture and Storage (CCS) technologies in aqueous solutions or through wet absorbent resins, *ii*) (photo)electrochemistry and/or *iii*) (photo)catalysis, affordable and industry-scalable remedies are still out of reach, the thermodynamic stability and kinetic inertness of the CO_2 molecule being the main barriers to overcome.

Each of the above mentioned remediation technologies implies the presence of water and, depending on the pH of the solution, the occurrence of different equilibria [47-49]:

- pH < 8, direct CO_2 hydration

$$CO_2 + H_2O \rightleftarrows H_2CO_3,\ E_{a,\rightarrow} \sim 80\ \text{kJ mol}^{-1} \qquad \text{(R2.1)}$$
$$E_{a,\leftarrow} \sim 72\ \text{kJ mol}^{-1}$$

$$H_2CO_3 + OH^- \rightarrow HCO_3^- + H_2O,\ \text{instantaneous reaction} \qquad \text{(R2.2)}$$

- pH > 10, direct reaction with OH^-

$CO_2 + OH^- \rightleftarrows HCO_3^-$, $E_{a,\rightarrow} \sim 64$ kJ mol^{-1} (R2.3)
$E_{a,\leftarrow} \sim 114$ kJ mol^{-1}

$HCO_3^- + OH^- \rightarrow CO_3^{2-} + H_2O$, instantaneous reaction (R2.4)

- 8 < pH < 10, both mechanisms are important and consequently, near neutral conditions, the three species HCO_3^-, CO_2 and H_2CO_3 are all present.

Furthermore, also the equilibrium between gaseous and aqueous CO_2, should be taken into account:

$CO_{2(g)} \rightleftarrows CO_{2(aq)}$ $K_{eq} = 3 \times 10^{-2}$ M atm^{-1} (R2.5)

Thus, depending on the experimental procedures, the above reactions (R2.1–4) may lead to substantial changes in the CO_2 partial pressure above a solution and in the concentration of dissolved species [47].
Maeder *et al.* recently investigated the kinetics of the water (R2.1) and of the hydroxide (R2.3) paths, determining both activation enthalpies ($\Delta H^{\neq}$) and entropies ($\Delta S^{\neq}$) by means of stopped-flow technique [49]. From their findings, it is possible to calculate the Gibbs free energies of activation ($\Delta G^{\neq}$) for both reactions at 298 K, reported in Table 2.2.

$CO_2 + H_2O \rightarrow H_2CO_3$ (R2.1)	$\Delta H^{\neq} = 79$ kJ/mol	$\Delta G^{\neq} = 91$ kJ/mol
	$\Delta S^{\neq} = -41 \times 10^{-3}$ kJ/(mol K)	
$CO_2 + OH^- \rightarrow HCO_3^-$ (R2.3)	$\Delta H^{\neq} = 62$ kJ/mol	$\Delta G^{\neq} = 50$ kJ/mol
	$\Delta S^{\neq} = 40 \times 10^{-3}$ kJ/(mol K)	

Table 2.2 – Thermodynamic parameters for CO_2 hydration reaction.

Furthermore, strictly concerning (photo)electrochemical processes, it should not be neglected that, in neutral aqueous solution (pH 7, T = 298 K), the overall thermodynamic requirements for the reduction of water to hydrogen and of carbon dioxide to CO or formate are similar [47]:

$2H_2O_{(l)} + 2e^- \rightarrow H_{2(g)} + 2OH^-_{(aq)}$ $E^0 = -0.65$ V *vs.* SCE (R2.6)

$CO_{2(g)} + H_2O_{(l)} + 2e^- \rightarrow CO_{(g)} + 2OH^-_{(aq)}$ $E^0 = -0.77$ V *vs.* SCE (R2.7)

$CO_{2(g)} + H_2O_{(l)} + 2e^- \rightarrow HCO_2^-{}_{(aq)} + OH^-_{(aq)}$ $E^0 = -0.55$ V *vs.* SCE (R2.8)

and, hence, the two processes often compete.

In addition, both H_2O and CO_2 one-electron reductions are highly energy-demanding processes [47,50,51], since the 1-e$^-$ reduction products ($H^\bullet$ and $CO_2^{-\bullet}$ formate radical anion) are extremely energetic species

$$H^+ + e^- \rightarrow H^\bullet \qquad E^0 = -2.7 \text{ V } vs \text{ NHE} \qquad \text{(R2.9)}$$

$$CO_2 + e^- \rightarrow CO_2^{-\bullet} \qquad E^0 = -1.9 \text{ V } vs \text{ NHE} \qquad \text{(R2.10)}$$

so that either H_2O or CO_2 reduction, directly involving the (free) one-electron products, are expected to be very slow and thermodynamically hindered.

Therefore, alternative ways to prevent H_2O reduction at the expense of that of CO_2 or to stabilize 1-e$^-$ reduction species shall be explored.

In particular, the one-electron reduction of CO_2 is prohibitively high in energy, thus requiring high reduction potential to be applied, because of its adiabatic electron affinity in aqueous solutions (47.4 kcal/mol) and its linear geometry [52]. Indeed, a change in geometry from the linear CO_2 to a bent $CO_2^{-\bullet}$ is required (bond angle of 134°), giving rise to a very slow self-exchange rate for the $CO_2/CO_2^{-\bullet}$ couple and to a significant overpotential to drive the reduction [50].

All the calculations and equations so far reported prove that, either the (photo)electrochemistry reduction of CO_2 (R2.7, R2.8, R2.10) or its hydration for the uptake in the capture/absorption mechanism (R2.1–4) are energy-demanding processes, with a threshold that needs to overwhelm to initiate the reaction and that necessarily calls for external energy to be provided.

2.2.1 Carbon Capture and Storage (CCS) technology

In the last decades, carbon dioxide capture and sequestration from ambient air has been proposed as an attracting technology to compensate for all CO_2 emissions into the atmosphere [53].

Air capture is an industrial process able to uptake CO_2 from ambient air, producing a pure gas stream either for use or disposal [54].

Capturing CO_2 directly from air is often regarded as a premature process, being its concentration in air ~ 0.04% and, most importantly, since there is still no power plant able to capture it from industrial exhaust emissions [55].

Nevertheless, an increasing number of studies suggests it may represent a near-term successful approach, long before industrial emissions can be lowered down to zero [54,55].

The developed approaches could be based on the use of either aqueous alkanolamines and alkali solutions [56], as patented in 1930 by Bottoms and involving gas-liquid interface reactions, or of a solid sorbent mainly in the form of amine-based anion exchange resin [53,57].

From a chemical point of view, a good sorbent for these applications has to bind CO_2 strongly enough to absorb the gas, without holding it so strongly that subsequently releasing it for storage purposes becomes expensive [46].

Absorbents in liquid form can be attractive because they can be transferred between the collector (where the gas is absorbed) and regenerator (where it is released) relatively easily. In detail, CO_2 is absorbed from a flue or combustion gas near ambient temperature into an aqueous solution of amine with low volatility. The amine is then regenerated by stripping with water vapor and, as the water is condensed, CO_2 is released and compressed for geologic sequestration [56]. The majority of power plants adopting this technique mainly uses mono- and di-ethanolamine with an estimated total cost of $52/ton of CO_2 removed. However, the greatest drawback of this approach is the high heat capacity of these aqueous solutions, making the endothermic regeneration step (*i.e.*, stripping) very energy intensive and costly. These amines are also more suitable for the capture of CO_2 from oxygen free gas mixtures since they tend to degrade over time [58].

Alkali solutions may represent a good alternative, being strong absorbents, contamination-insensitive and with minimal water loss, all factors that lower the cost and technical risk related to the absorption step [55]. However, the formation of stable carbonates, with bond strength > 50 kcal mol^{-1}, requires intense thermal energy to desorb CO_2 from the sequestration solution [53,57].

To lower the energy cost, amines and polyamines deposited on solid supports have also been investigated [58]. Solid sorbents are desirable because their surface can be roughened, creating more binding sites for CO_2 molecules, thus raising uptake rates. Lackner *et al.*, who first proposed in 1999 the direct capture of CO_2 from ambient air as a method to restrain global warming [59], recently reported a study on the use of amine-based anion exchange resin dispersed on a fleet shell of polypropylene. The resin was found to absorb carbon dioxide in dry ambient and release it under humid conditions.

Realistic cost for collecting and releasing CO_2 is around $15/ton of CO_2 collected, much lower than the cost predicted for stripping the gas from a flue stack. However, so far, most of the expenditure is due to production, maintenance and regeneration of these solid sorbents [46].

2.2.2 Pyridine-catalyzed electrochemical reduction of CO_2

Concerning electrocatalytic remediation performed with the traditional three electrode cell configuration, in aqueous solutions CO_2 reduction competes with the reduction of protons or water to H_2 (R2.6–8), often leading to low product and electrochemical yields.

In the past, different strategies had been proposed to accelerate CO_2 reduction at the expense of protons reduction, such as the use of *i*) redox active enzymes (*e.g.*, formate dehydrogenase enzyme, [60]), *ii*) molecular redox mediators (*e.g.*, N,N'-dialkyi-4,4'-bipyridinium redox polymer, [61]) and *iii*) polypyridyl metal complexes (*e.g.*, 2,2'-bipyridine or 2,2',2"-terpyridine Ru and Rh metal complexes, [62]); however, in all these systems the problem of high overpotential still remained, resulting in extremely low electrochemical efficiency even though product yields for CO_2 reduction were high.

Furthermore, most electrochemical and photoelectrochemical systems produce only the $2e^-$ reduction products, *i.e.* CO and formate (R2.7, R2.8); although some authors reported on the further reduction of CO_2 to products such as methane, methanol and ethanol, typically this kind of systems requires extensive energy input to overcome the kinetic barriers or posseses poor chemical stability [63,64].

As recently reviewed, the use of catalysts and co-catalysts such as tetra-alkylammonium salts [65], aromatic esters and nitriles [66,67], ionic liquids [68] and pyridinium derivatives [51,63,64,69] represents an attracting alternative to bare metal electrodes, especially because of the high product selectivity to CO, oxalate or methanol and because of the surprisingly low overpotential required [70].

By the end of the 90s, Bocarsly *et al.* found out that the electroreduction of pyridinium in mildly acidic solutions (E^0 = -0.58 V *vs* SCE, on Pd electrodes at pH 5.3), yielding pyridinyl radical, may represent an efficient alternative to the highly energy-demanding CO_2 direct reduction [63].

Indeed, in the presence of CO_2, pyridinyl radicals act as electron shuttles, binding the CO_2 molecule to the protonated N site, through a proton exchange mechanism driven by acid-base interaction. As a consequence of the proton-electron transfer, pyridine is able to regain its original aromaticity and, at the same time, CO_2 is reduced to formate. As generally accepted, the formation of the carbamate proceeds through a nucleophilic attack where pyridinyl radical approaches CO_2 with its N lone pair directed toward the electrophilic C of CO_2. As N-C distance decreases, CO_2 bends and a proton transfers from pyridinyl radical to CO_2, revealing the occurrence of a Proton-Coupled Electron Transfer (PCET) mechanism (Scheme 2.1) [52].

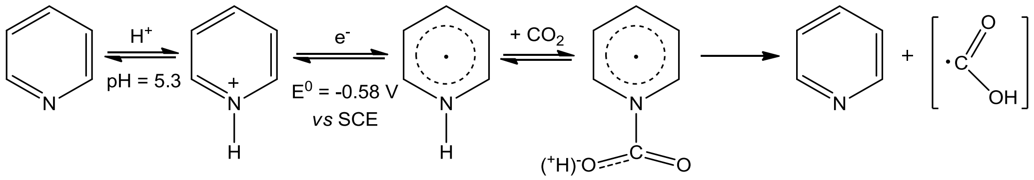

Scheme 2.1 – Scheme of the pyridine-catalyzed electrochemical reduction of CO_2 yielding formate, reported by Bocarsly [51,63,64,69].

More recently, many authors performed quantum mechanical calculations on the pyridinyl system and asserted the unfeasibility of the mechanism proposed by Bocarsly [51,63,64,69,71]. In particular, their criticisms concern *i*) the reduction potential required in the *homogeneous* reduction of the pyridinium cation [72], *ii*) the pyridinyl radical's pK_a value reported by Bocarsly *et al.*, which was proved to be too high for the acid-base interaction with CO_2 [52,72,73] and finally *iii*) due to the diffusion-controlled mechanism operating in the electrochemical reduction of pyridinium, it was suggested that the electro-reduction step is electrode-surface dependent, while all the chemical processes possibly occur either on the surface or in the bulk solution [73].

To clarify the actual mechanism also with the aim of introducing alternative ways for CO_2 reduction, overwhelming the great limitation induced by H_2O reduction competition, photolysis experiments of aqueous solutions of pyridine (Py) containing *iso*-propanol (H-atom donor) were carried out either in the presence or in the absence of carbon dioxide. Prior to photolysis, the solutions were always acidified in order to ensure that Py was largely present in its protonated form (pyridinium, PyH^+).

The formation of a carbamate species occurred, triggered by acid-base interaction between protonated nitrogen and CO_2, as shown by Bocarsly [64], followed by electron-transfer yielding formate and pyridine. The formation of the latter is favored, due to the re-gain in aromaticity of the heterocyclic molecule and proved the catalytic role played by pyridine in the *homogeneous* CO_2 reduction.

For experimental details, see Section 3.3.4 and 3.3.6. All the obtained results are discussed in Chapter 5.

Pyridines photolysis and Electron Spin Resonance (ESR) spectroscopy

Pyridine (Py) is the simplest of all nitrogen heterocycles and its photochemical and photophysical characteristics, both in the gas phase and in solution, have been extensively investigated by means of time-resolved spectroscopies and steady-state studies.

As determined by transient absorption spectroscopy, pyridine (and pyridinyl radicals) has intense absorption with maxima around 300 and 400 nm, as also confirmed by parallel studies where substituted and non-substituted pyridinyl radicals were found to be weakly colored in dilute solution, with a weak absorption band in the visible or near IR (640 – 1250 nm) and two stronger bands (365 – 410 nm and 240 – 280 nm) in the near UV [74,75].

The photolysis of pyridine under intermittent UV irradiation has been widely performed in the past, mainly by Leuschner *et al.* [76-78]. They observed the formation of N-hydropyridinyl radicals in various solvent mixtures containing water, *iso*-propanol and acetone in different amounts, as well as in neat *iso*-propanol and investigated the self-termination reaction rate of the so-formed radicals through Time-Resolved Electron Spin Resonance.

During the light period of intermittent photolysis, a pyridinyl radical steady-state concentration of ~ 9 µM was reached. In the dark period, a decay of the signal corresponding to a second-order self-termination reaction of the radicals was measured as the slope of the linearized plot of the decay data and was determined to be ~ $10^8 – 10^9$ $M^{-1}s^{-1}$.

Prerequisite for the second order self-termination reaction was the initial exclusion of O_2, a well-known triplet state quencher [76].

With the aim of elucidating structure and properties of the short-lived excited triplet state of pyridine, Electron Spin Echo (ESE) spectroscopy, coupled with pulsed laser radiation, has also been applied [79].

The structure of the triplet state (T_1) of Py has been found heavily distorted with respect to that of its ground state. Indeed, in the ground state, the six-atom membered ring mostly resembles the regular hexagonal structure of benzene [79,80] while, upon excitation into T_1, the structure deviates toward a boat-like configuration with the N atom tilted with respect to the plane of both ortho- and meta-carbon atoms (tilting angle ~ 40°) [81]. In addition, also the para-C atom has been found tilted out of the molecular plane, though to a much lesser extent [80].

These observations suggested that in T_1 the hybridization of the atomic orbitals on the N atom could still be described by sp^2, that of the para-C atom slightly deviated from the original sp^2 while that of the ortho-C atoms dramatically changed, being more accurately described by sp^3 orbitals.

Furthermore, the deviation of T_1 from the planar geometry of the ground state has been attributed to its $n\pi^*$ and $\pi\pi^*$ mixed character [81], which also implies a deviation of the spin-density distribution. About 50% of the spin-density was indeed found to be localized on the nitrogen atom, characteristic that could not be expected neither for a pure $n\pi^*$, nor for a $\pi\pi^*$ state [80].

By means of femtosecond transient absorption spectroscopy, Zewail *et al.* deeply investigated the dynamics of excited pyridine decay. They were able to identify two distinct behaviors for the decay processes from the excited singlet states $S_2(\pi\pi^*)$ and $S_1(n\pi^*)$ [75].

The higher energy benzene-like S_2 state (with planar configuration) is readily deactivated (τ ~ 100 fs) along a Potential Energy Surface (PES) which forms a conical intersection with the PES of pyridine ground state, S_0. Crossing of this intersection results in the isomerization to the prefulvene form, by means of a two-step mechanism which takes place within ~ 2.2 ps.

Conversely, the nonradiative (*i.e.*, horizontal) deactivation of $S_1(n\pi^*)$ excited state (with non-planar configuration) takes longer time (~ 9 – 23 ps) and could either lead to pyridine triplet state (through Intersystem Crossing, ISC) or to other isomers (*i.e.*, Kekulé or Dewar) through interconversion (IC).

However, since S_1 non-planar geometry would require large-amplitude motions in order to form isomers, the IC process results less likely with respect to the Intersystem Crossing yielding the excited triplet state, T_1 [75].

Pyridinium as an efficient (photo)electrochemical catalyst for CO_2 reduction

In 1994, Bocarsly and co-workers proposed pyridinium cation as a novel *homogeneous* catalyst for the reduction of CO_2 to methanol, on Pd electrodes [63]. Mass spectrometry proved the formation of methanol as the main product and of formaldehyde as a side product, while gas chromatography analysis revealed methanol concentration of about 0.5 mM after about 12 h of electrolysis.

Further and more recent Bocarsly's publications mainly aimed at optimizing the experimental conditions, also by changing the material used as electrode, and by studying the reaction into details [51,63,64,69,71,82,83].

In 2010, Bocarsly *et al.* proved that the complete reduction of CO_2 to the $6e^-$-reduced species, *i.e.* methanol, went sequentially through the $2e^-$- and the $4e^-$-reduced intermediates, *i.e.* formic acid and formaldehyde, respectively [64].

In aqueous mildly acidic conditions (pH ~ 5.3), pyridine is protonated to pyridinium (PyH^+), whose electrochemical reduction to the pyridinyl radical ($1\text{-}PyH^•$) proceeds through a $1e^-$-reduction step (R2.11):

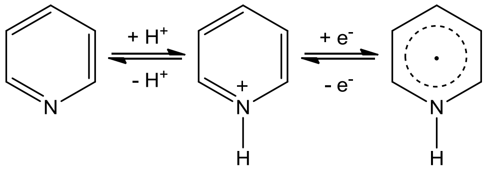

(R2.11)

Cyclic voltammetries, in the presence of Ar or CO_2, were recorded on Pd [63], *p*-GaP [69], glassy-carbon and Pt [64] and on FeS_2 [71] electrodes.

In the absence of CO_2, the cathodic peak, associated to the nonreversible reduction of PyH^+ to $1\text{-}PyH^•$, appeared at ~ -0.5/-0.6 V *vs* SCE.

Conversely, after purging with CO_2, all electrodes, except for glassy-carbon, showed an enhancement of the cathodic peak current associated with pyridinium reduction, with the phenomenon being assigned to the reduction of CO_2 (or a species in equilibrium with it), running in parallel with the pyridinium-catalyzed process, yielding the regeneration of pyridine [63,64].

A deeper insight revealed that the one electron reduction product, either the radical anion $CO_2^{-•}$ or the solvated hydroxyformyl radical $^•COOH$, is obtained (R2.12) through an inner-sphere mechanism, rather than a simple outer-sphere reaction, as determined by applying the Marcus cross-relation [64].

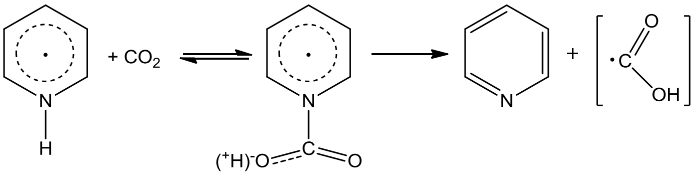

(R2.12)

The second electron transfer was proposed to yield formic acid, following three different possible routes:

- starting from hydroxyformyl radical (R2.13)

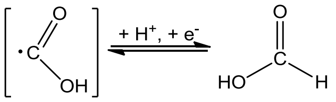

(R2.13)

- direct reduction of pyridinyl radical-CO_2 adduct (R2.14)

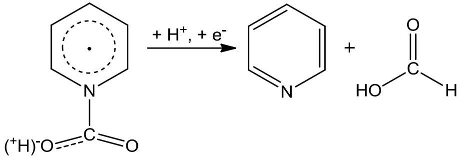

(R2.14)

- reaction between the pyridinyl radical-CO_2 adduct and another pyridinyl radical (R2.15)

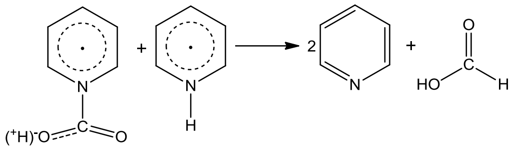

(R2.15)

none of which display sufficiently reliable features to be addressed as the occurring one [64].

Despite that, pyridinyl radical was shown to play a crucial role undergoing addition-elimination reactions and providing a pyridine-stabilized hydroxyformyl radical, also promoted by the electrophilic attack of the carbon of CO_2.

Indeed, pyridinium has the majority of its electron density at the N site and, upon reduction, the electron density further increases, making the nitrogen a stronger Lewis base capable of binding the proton more tightly and to promote CO_2 binding as well [51].

Under the applied conditions (*i.e.*, pH 5.3), formic acid is mainly present as formate anion, which is electrochemically inert. Thus, only upon lowering the pH of the pyridinium solution, a voltammetric response was recorded which was assigned to formic acid reduction. Hence, since the reducible species is more likely formic acid rather than formate anion, a localized acidic pH gradient is required near the electrode surface. Indeed, simulated CV analysis proved that surface adsorbed formic acid dissociates into hydroxyformyl radical which can be reduced to formyl radical (R2.16):

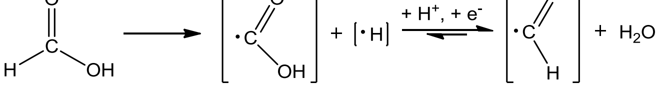

(R2.16)

further reacting with $1\text{-PyH}^{\bullet}$ and yielding formaldehyde (R2.17):

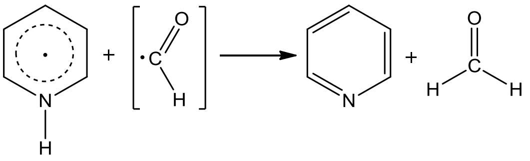

(R2.17)

Gaussian calculations showed a bonding interaction between the nitrogen of 1-PyH• and the carbon of the formyl group [64].

However, since the reduction of formic acid to formaldehyde by pyridinyl radicals was shown to be the least energetically favorable process (ΔG = -38 kcal/mol), if compared to CO_2 reduction to formic acid (ΔG = -43 kcal/mol) and to formaldehyde reduction to methanol (ΔG = -61 kcal/mol), formic acid appeared to be more likely a reaction product, rather than being completely converted to formaldehyde [64].

Even though formaldehyde is known to be electrochemically active and can be directly reduced to methanol with some selected electrode materials, its very low steady-state concentration (indeed, $k(\bullet COH \rightarrow HCOH) = 8.9\ M^{-1}s^{-1}$ and $k(HCOH \rightarrow CH_3OH) = 23\ M^{-1}s^{-1}$), together with huge quantities of pyridinyl radicals available at the electrode surface, can promote the following reactions:

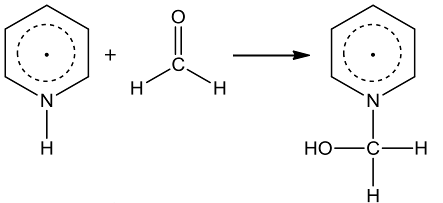

(R2.18)

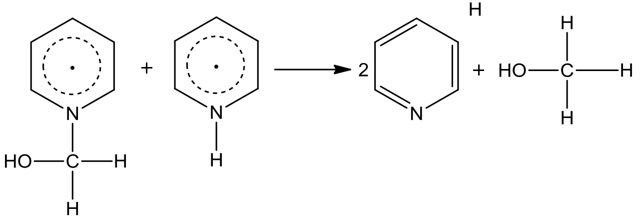

(R2.19)

By Gaussian calculations, the new pyridine-hydroxymethyl radical adduct was shown to be characterized by N-C bond length and N-C-O bond angle indicating that the carbon hybridization switched from sp^2 to sp^3 [64].

Thus, from the detailed investigation of the whole process, Bocarsly and co-workers were able to prove that pyridinium/pyridinyl radical catalysts are effective and stable catalysts for the reduction of CO_2 to various products, operating at low overpotential [64].

An overall second order rate law was determined, with the formation of the one-electron reduced carbamate-like species being the rate determining mechanistic step. The temperature dependence, in the range 0 – 45 °C, and an Arrhenius-like fitting of the obtained data allowed for the determination of a $\Delta H^0_{act} = (69 \pm 10)\ kJ\ mol^{-1}$ activation barrier for the pyridinium catalyzed CO_2 reduction [51]. Pyridinium was also shown to effectively transfer all the 6 electrons necessary for transforming CO_2 to methanol, reacting with all the intermediate species, even though it is not common that a single catalyst has the ability to reduce multiple species.

Finally, Bocarsly's group investigated also systems other than pyridine (4-*tert*-butylpyridinium, 2-methylpyridinium and 4-methylpyridinium [64]) finding out that electron-donating groups on the pyridine ring would increase the Lewis basicity of pyridinyl nitrogen, potentially increasing also the rate for the formation of the carbamate species.

Nevertheless, a delicate balance between kinetics and thermodynamics should be taken into account. Since the pyridinyl-CO_2 adduct must dissociate for the mechanism to proceed, a strongly bonded and thermodynamically stabilized intermediate would be detrimental for the following reduction steps [51].

When *N*-methyl pyridinium was employed, no methanol formation was detected upon 50 h of electrolysis, suggesting that the hydrogen bonded to the nitrogen site in the reduced pyridinium species is the transferable reducing agent [63].

Modelling of the pyridine-CO_2 system with Density Functional Theory calculations

To validate the roles of pyridinium and pyridinyl radical in the reduction of carbon dioxide, Quantum Chemical calculations using first-principles Density Functional Theory were performed.

In particular, the investigations aimed at *i*) determining the species possibly involved in the (photo)electrocatalytic reaction [72], *ii*) predicting the acidity constants for substituted pyridinium ions and pyridinyl radicals, to describe the acid/base interaction [84], *iii*) assessing the role of water [85] and, finally, the feasibility of the overall CO_2 reduction mechanism [73].

By calculating gas phase and aqueous phase deprotonation energies, Carter *et al.* determined pyridinyl radical $pK_a \sim 27$ [72], much higher than that predicted by Bocarsly [64].

This finding would imply serious consequences on the mechanism since, if the formation of the carbamate-like species was the rate determining step [64], the deprotonation of the pyridinyl radical leaving the pyridinyl N site able to bind with CO_2 is a reasonable indicator of the overall reduction reaction. On the basis of the calculations, it was proved to be not facile at all [72].

Thus, due to the very low acidity of 1-$PyH^{\bullet}$, acid-base chemistry was excluded to promote the formation of carbamate [73], opening up to the possibility of a water-assisted mechanism [52,72,73].

Furthermore, a large difference between the observed redox potential for the CO_2 reduction catalyst (-0.58 V *vs.* SCE [51,63,64,69,71]) and the calculated *homogeneous* redox potentials for pyridinium (-1.44 V *vs.* SCE [72,86]) was predicted, in line with the observation that the reduction of PyH^+ to 1-$PyH^{\bullet}$ implies that the added electron resides on the π^* antibonding orbital of pyridinium, so that substantial energy would be required, not entirely provided by the experimentally determined overpotential.

Since the results ruled out the possibility of *homogeneous* pyridinium reduction to pyridinyl radical, other feasible processes were examined, suggesting the formation of bipyridine-like species as a possible secondary route since the calculated redox potential of the 4,4'-bipyridinium cation corresponds to that measured by Bocarsly (-0.58 V at pH 5.3), resulting in the formation of 4,4'-bipyridinyl radical, with a pK_a low enough to allow the proton-CO_2 exchange to form the carbamate species [72].

Other possible intermediates included singlet carbenes, as well as anions and cations obtained from the 2-electron reduction of pyridine to *ortho*- or *para*-dihydropyridine [73], with the calculated two-electron reduction potential of the latter being ~ -0.72 V (at pH ~ 5.3), comparable with the experimental value.

The final issue was the determination of the chemical reaction barrier in solution to investigate the proton/CO_2 exchange on pyridinyl or dihydropyridinyl radicals, yielding formic acid [52,73].

Carter *et al.* calculated the free energy barriers for this process using n = 1, 2, 3 or 4 water clusters, either in the gas phase or in the liquid phase at 298 K [73]. The progressive increase in the number of water molecules resulted in the monotonic decrease of the gas-phase free energy barriers, suggesting that the reaction pathway is not stabilized with respect to the maximum number of assisting water molecules.

On the other hand, aqueous energy barriers appeared to converge with n = 4 water clusters, with activation free energies consistently greater than ~ 30 kcal/mol [73]. Thus, according to their predictions, H/CO_2 exchange in water appears energetically prohibitive, regardless of the species in solution, and additional catalysis, most likely occurring on the electrode surface, is necessary to drive the processes [73].

On a parallel work, Musgrave *et al.* employed quantum chemical calculations to investigate the mechanism of *homogeneous* CO_2 reduction, catalyzed by pyridine, in the Py/*p*-GaP system, predicting a ~ 46 kcal/mol enthalpic barrier, which was significantly higher than the experimental barrier of ~ 17 kcal/mol determined by Bocarsly *et al.* [51]. The considerable difference suggests that either the *heterogeneous* processes involving the *p*-GaP electrode, which may catalyze the carbamate formation, or alternative lower barrier pathways are possibly involved in the *homogeneous* phase [52].

The most likely hypothesis implies H_2O molecules acting as proton relays, thus significantly lowering the activation barrier for the 1-PyH$^\bullet$ + CO_2 reaction. Indeed, H_2O molecules were supposed to play a central role in facilitating the PyCOOH carbamate formation through a solvent-assisted Proton-Coupled Electron Transfer (PCET) mechanism [52].

The reaction proceeds through a nucleophilic attack where pyridinyl radicals move toward CO_2 with the electron-rich N directed toward the electrophilic C. As the two centers approach (*i.e.*, as $R_{N\text{-}C}$ decreases), CO_2 bends as a result of the nucleophilic attack and a proton transfer from 1-PyH$^\bullet$ to CO_2. Accordingly, the charge on CO_2 becomes more negative and, simultaneously, that on pyridinyl radical more positive, while proceeding from reactant toward the transition state, suggesting that the reaction proceeds *via* a stepwise-like mechanism, with electron transfer (ET) preceding proton transfer (PT) rather than being concurrent [52].

Calculations were also performed by varying the number of H_2O molecules (n = 1, 2, 3, 4) which assisted the proton shuttling from 1-PyH$^•$ to CO_2. In each case, the water molecules were arranged to facilitate the PT step, *i.e.*, with the H atoms forming hydrogen bonds with both nitrogen and oxygen of 1-PyH$^•$ and CO_2, respectively (Scheme 2.2).

When n =1, the activation barrier (ΔH^0_{act}) was found to be ~ 30 kcal/mol while increasing n results in progressively lower ΔH^0_{act}, with the minimum value (16.5 kcal/mol, in accordance with the experimentally determined value [51]) obtained when n = 4. Hence, multiple water molecules were suggested to form a chain of proton shuttles where H^+ are relayed from one H_2O to the next one, until reaching CO_2, providing lower barriers pathway for the proton transfer reaction and catalyzing PyCOOH formation [52].

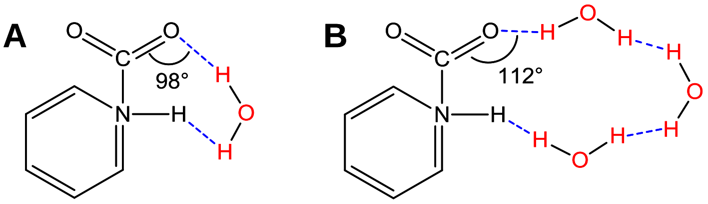

Scheme 2.2 – H_2O molecules acting as proton shuttles. A) n = 1; B) n = 3.

If ΔH^0_{act} is calculated with explicit H_2O molecules solvating the reaction complex, the value further lowers down to ~ 13 kcal/mol (which will be found in accordance with that proposed in Chapter 5 [87]), suggesting that solvation may stabilize $PyCOO^-$ rather than PyCOOH formation.

The exceedingly high ΔH^0_{act} calculated in the absence of water was mainly attributed to the C-O-H angular strain (α) with α being ~ 79° in the transition state when n = 0, while that predicted for the product configuration being 112°. As expected, the presence of water was found to considerably reduce the strain, being α ~ 109° when n = 1 [52].

Finally, the reduced acidity of pyridinyl radicals (pK_a ~ 31) was proved to be not indicative of the reactivity of 1-PyH$^•$ to CO_2 reduction, since the electron transfer, preceding proton transfer, effectively lowers the pK_a of the partially oxidized pyridinyl radicals, favoring the acid-base interaction between the two reactants [52].

2.3 Fenton oxidation and gas-liquid interface reactions

2.3.1 Fenton reaction at aqueous interfaces

Fenton reaction is identified as the process involving a mixture of hydrogen peroxide and ferrous salts (*i.e.*, Fenton's reagents), which are effective oxidants of a large variety of organic substrates [88-90]; the first report dates back to 1894 when Fenton demonstrated the oxidation of tartaric acid in the presence of H_2O_2 and iron(II) [91].

Indeed, Fe^{2+} is able to release the oxidative ability of hydrogen peroxide by transforming it into more reactive intermediates. The extensive availability of these reagents and their ubiquitous importance becoming increasingly evident promoted a huge quantity of experimental and theoretical works, highlighting their key-roles in both chemical and biological reactions [92-97].

High-valent iron species ($Fe^{IV}O^{2+}$), formed as reaction intermediates, have been shown fundamental catalysts for oxidative transformations mediated by iron-containing oxygenases, the class of enzymes capable of oxidizing a substrate by transferring oxygen from molecular O_2 to the substrate itself. For example, the complex cyto-chrome P450 and, more generally speaking ferryl species ($Fe^{IV}O^{2+}$), was proved to catalyze C-H hydroxylation of highly saturated C centres of organic compounds [90].

Iron- and oxygen-binding proteins (*e.g.*, ferritin (an iron sequestration protein) and transferrin receptor (an iron uptake protein)) catalyzes i*n vivo* reactions which control iron metabolism in human cells [98].

Moreover, the majority of the reactions occurring in the atmosphere and participating, among the others, in the oxidation of SO_2 and NO_x has been shown to be Fenton-like reactions involving mineral dust and atmospheric H_2O_2 [99,100].

Finally, under incident irradiation, Fe(II)/Fe(III) couples in the presence of H_2O_2 produce radicals such as $^{\bullet}OH$, $HO_2^{\bullet-}$ and $HO_2^{\bullet}$ which enhance the photo-oxidation of organic pollutants, by means of the so-called Advanced Oxidation Processes (AOPs) [96,101,102].

Despite its unquestionable importance, the mechanism of Fenton reaction is not yet fully understood, with $^{\bullet}OH$ radicals species thought to be most likely involved in photocatalysis and atmospheric chemistry and ferryl intermediates in biochemical and *in vivo* reactions.

Indeed, the coordination sphere of Fe^{2+}, under specific conditions, may either promote the outer-sphere one-electron transfer producing $^{\bullet}OH$ radicals through the Haber-Weiss mechanism (R2.20) [103]

$$Fe^{2+} + H_2O_2 \rightarrow Fe^{3+} + OH^- + {}^{\bullet}OH \qquad \text{(R2.20)}$$

Hydroxyl radicals may then be scavenged by reaction with another Fe^{2+}:

$$^{\bullet}OH + Fe^{2+} \rightarrow OH^{-} + Fe^{3+} \qquad (R2.21)$$

Also Fe^{3+} catalytically decomposes H_2O_2 following a radical mechanism:

$$Fe^{3+} + H_2O_2 \leftrightarrows Fe_2OOH^{2+} + H^{+} \qquad (R2.22)$$

$$Fe_2OOH^{2+} \rightarrow HO_2\bullet + Fe^{2+} \qquad (R2.23)$$

$$Fe^{2+} + HO_2\bullet \rightarrow Fe^{3+} + HO_2^{-} \qquad (R2.24)$$

$$Fe^{3+} + HO_2^{-} \rightarrow Fe^{2+} + H^{+} + O_2 \qquad (R2.25)$$

$$OH^{\bullet} + H_2O_2 \rightarrow H_2O + HO_2^{\bullet} \qquad (R2.26)$$

It has also been reported that the Fenton reaction may proceed also through inner-sphere two-electron oxidation, via O-atom transfer, yielding $Fe^{IV}O^{2+}$, following the Bray-Gorin mechanism (R2.27)

$$Fe^{2+} + H_2O_2 \rightarrow Fe^{IV}O^{2+} + H_2O \qquad (R2.27)$$

Experimental evidence for these reactions (R2.20–7) has been usually provided indirectly, through the identification and detection of the reaction products present in bulk water.

Nevertheless it should be considered that, throughout in Nature, Fenton reactions in clouds, living tissues, bio-membranes and nanoparticles and accounting for all the phenomena previously described, are mostly *interfacial* reactions governed by mechanisms extremely different from those occurring in bulk gas or liquid phases [104].

Indeed, it has been revealed that the dynamics and thermodynamics regulating ions hydration at aqueous interfaces cannot be predicted from the properties correspondingly observed in bulk-water ions [105]. These considerations are of great interest, particularly due to the well-established analogy between the phenomenon of ion adsorption at the air/water interface and that regulating the adsorption at hydrophobe/water interfaces of, for example, proteins and atmospheric aerosol nanoparticles [106].

Given this framework, only recent investigations performed by means of online ElectroSpray Ionization Mass Spectrometry (ESI-MS) provided evidences which opened up to the possibility of finally unravelling the Fenton reaction mechanism [104].

Starting from $FeCl_2$ aqueous microjets exposed to H_2O_2 or O_3 gaseous streams, a series of products were detected which accounted for the prompt formation of mono- and poly-iron ferryl ($Fe^{IV}O^{2+}$) species as primary products, suggesting that, at aqueous interfaces, R2.27 is more likely to occur [104]. This result also implies that interfacial Fe^{2+} are readily reactive as O-atom acceptor from O_3 or H_2O_2, opposite to the electron-transfer reaction (R2.20).

It was suggested that Fe^{2+} concentration is progressively higher as approaching the outermost interfacial layers, with the remarkably fast reaction ascribed to the incomplete hydration of the metal cation shell that can favour the inner-sphere O-atom transfer over the outer-sphere one-electron transfer [104].

Hence, Fe^{IV} ferryl species gain a predominant role, more significant than that hitherto predicted, in Fenton and Fenton-like reactions occurring at the air/water or hydrophobe/water interfaces and most likely accounting for reactions governing atmospheric chemistry, in aerosol and clouds, as well as *in vivo* reactions in proteins and living tissues and, finally, biochemical processes in bio-membranes and bio-microenvironments.

2.3.2 Gas-liquid interfacial reactions and implication for atmospheric chemistry

Atmospheric aerosols are colloidal systems constituted of a solid or liquid phase dispersed in a gas phase. Solid aerosol may either be organic or inorganic particles (wet or dry) with dimensions ranging from sub-micron to a few microns, while liquid aerosol includes rain, fog, snow, ice and cloud droplets. These core nuclei provide available sites for the condensation of water as well as organic or inorganic molecules [107].

Since aerosols *i*) take part into a huge variety of heterogeneous processes (HPs) with gases and atmospheric oxidants and *ii*) absorb and reflect sunlight, hence greatly affecting climate changes, they are the main actors to take into consideration when discussing tropospheric chemistry also in view of the early recognition of their large specific surface areas (*i.e.*, $S/V \sim 10^{-4} – 10^{-5}$ cm^{-1}) [108].

Figure 2.8 schematically represents an atmospheric aqueous aerosol particle, along with all the possible interactions with a gas-phase molecule [107,109].

As previously outlined, recent investigations evidenced that the surface of water droplets is unique in its characteristics, which cannot be deduced from those of the bulk [105,110,111]. The surface tension of water is one of the highest, so that the air-water interface can be envisaged as the most hydrophobic, non-polar environment, able to allow hydrophobic moieties adsorption [107], among which Volatile Organic Compounds (VOCs), emitted from both anthropogenic and biogenic sources (such as isoprene, extensively discussed in Chapter 6), represent a considerable portion.

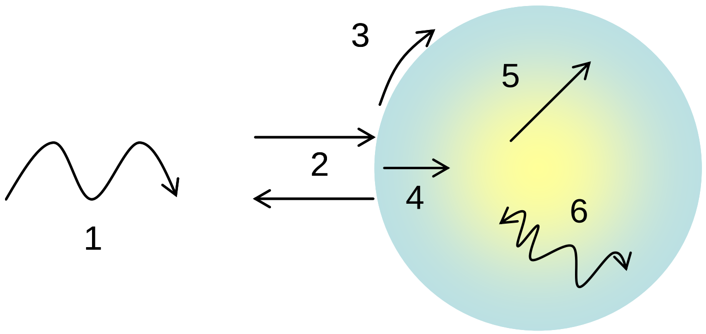

Figure 2.8 – Schematic representation of transport and reaction processes involving atmospheric aqueous aerosol and gas-phase reactants. In particular, 1) gas-phase diffusion, 2) adsorption (→) and desorption (←) at the surface, 3) reaction at the surface, 4) solvation and incorporation in the bulk liquid, 5) reaction in the bulk liquid and 6) diffusion of trace gas species in the bulk liquid [107,109].

The model which best describes the interaction of a trace gas species with a liquid surface, thus resembling atmospheric reactions, is the so-called *resistor model* where all processes, schematically represented in Figure 2.9, are formulated in terms of a resistance opposed to an uptake coefficient [109]. The uptake coefficient (γ), which properly describes the interaction of gases with liquids, is given by

$$\gamma = 4J/(n_g\, c_{AV}) \qquad (2.4)$$

where J is the flux of the gas into the condensed phase, n_g is the concentration of gas-phase molecules and c_{AV} is the average speed of gaseous molecules. Hence, γ represents the probability that the gas-phase molecule will be taken up by the liquid [109].

Two different gas uptake processes may naturally occur: *i*) non-reactive and *ii*) reactive gas uptake. Being more pertinent with the data presented in Chapter 6, only the second process will be discussed in details.

In addition to the gas-phase molecule diffusion through the gas itself (1 in Figure 2.8), its relative rate of adsorption and desorption on the surface of the liquid phase (2 in Figure 2.8) and the rate of transfer into the bulk (4 in Figure 2.8) characterizing also the non-reactive uptake process, it should be considered that gaseous molecules may undergo chemical reactions either on the surface (3 in Figure 2.8) or in the bulk (5 in Figure 2.8) of the condensed phase. The resistance to uptake due to the reactions possibly occurring in the condensed phase ($1/\Gamma_{rxn}$) is given by:

$$1/\Gamma_{rxn} = (c_{AV}/4HRT)\,(1/D_l\, k_{rxn})^{-1/2} \qquad (2.5)$$

with R being the gas constant, T the gas-phase temperature, H the Henry's law coefficient (which describes the solubility of the gas into the liquid), D_l the diffusion coefficient for trace gas species into the liquid-phase and k_{rxn} the reaction rate [109]. In terms of the resistor model, the reactive uptake process can be represented by Figure 2.9, where the factor describing the gas solubility into the condensed phase (4 in Figure 2.8 and $1/\Gamma_{sat}$ in Figure 2.9) and that taking into account the liquid-phase reaction (5 in Figure 2.8 and $1/\Gamma_{rxn}$ in Figure 2.9) are represented as parallel resistances [109].

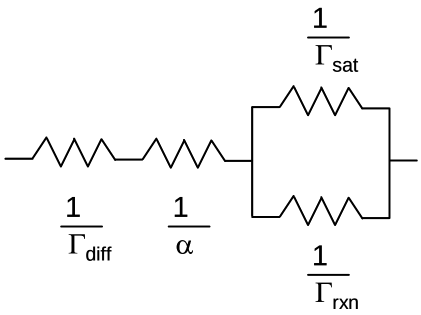

(a) $1/\Gamma_{sat} = c_{AV}/4HRT\ (t\pi/D_l)^{-1/2}$

(b) $1/\Gamma_{diff} = (0.75 + 0.238\ Kn)/(1+ Kn)$

Figure 2.9 – Schematic representation of the resistor model for the reactive gas uptake. Γ_{diff}, gas-phase diffusion term; α, accommodation coefficient; Γ_{sat}, gas solubility in the condensed phase; Γ_{rxn}, liquid-phase reaction terms. (a) Equation describing the resistance to gas solubility in the liquid-phase. The time-dependence (*t*) is highlighted. (b) Equation formulation of the resistence to the gas-phase diffusion into the condensed phase. *Kn* is the Knudsen number which linearly depends on the gas-phase mean free path [109].

If surface reactions (3 in Figure 2.8) are negligible, the uptake coefficient describing the resistor model represented in Figure 2.9, is expressed as:

$$1/\gamma = 1/\Gamma_{diff} + 1/\alpha + 1/(\Gamma_{sat} + \Gamma_{rxn}) \tag{2.6}$$

where α is the mass accommodation (*i.e.*, the probability that a molecule that hints on the liquid surface enters the bulk liquid). When the solubility dominates over the reaction process ($\Gamma_{sat} > \Gamma_{rxn}$), equation 2.6 reduces to

$$1/\gamma = 1/\Gamma_{diff} + 1/\alpha + 1/(\Gamma_{sat}) \tag{2.7}$$

Conversely, when the reaction is fast with respect to the solubility ($\Gamma_{rxn} > \Gamma_{sat}$) equation 2.6 becomes

$$1/\gamma = 1/\Gamma_{diff} + 1/\alpha + 1/(\Gamma_{rxn}) \tag{2.8}$$

In the case of fast reaction and high solubility, $1/(\Gamma_{sat} + \Gamma_{rxn})$ becomes negligible and the net uptake is governed by mass accommodation (α) and gas-phase diffusion (Γ_{diff}). Finally, the surface-reaction term (Γ_{surf} and 3 in Figure 2.8) can be defined as

$$1/\Gamma_{\text{surf}} = c_{\text{AV}}/(4k_{\text{surf}}\, b') \qquad (2.9)$$

with b' being the surface adsorption equilibrium constant and k_{surf} the rate for the reaction occurring on the surface. Since Γ_{rxn} is proportional to the square root of the bulk reaction rate (2.5), while Γ_{surf} is linearly proportional to k_{surf}, it is experimentally possible to distinguish between bulk and surface reactions, respectively, since liquid phase reactions vary with the square root of the reactant concentration with the surface reactions exhibiting a linear dependence [109].

REFERENCES

[1] D.I. Kondarides, *Encyclopedia of Life Support Systems* (EOLSS), **2009**, chapter 16th.

[2] A. Fujishima, X. Zhang, D.A. Tryk, *Surf. Sci. Rep.* **2008**, *63*, 515.

[3] D.W. Bahnemann, M. Hilgendorff, R. Memming, *J. Phys. Chem. B* **1997**, *101*, 4265.

[4] A. Fujishima, K. Honda, *Nature* **1972**, *238*, 37.

[5] C. Renz, *Helv. Chim. Acta* **1921**, *4*, 961.

[6] E. Baur, A. Perret, *Helv. Chim. Acta* **1924**, *7*, 910.

[7] N. Armaroli, V. Balzani, *Angew. Chem. Int. Ed.* **2007**, *46*, 52.

[8] A.W. Bott, *Current Separ.* **1998**, *17*, 87.

[9] B. Ohtani, *J. Photochem. Photobiol. C* **2010**, *11*, 157.

[10] Z. Zhang, J.T. Yates, Jr., *Chem. Rev.* **2012**, *112*, 5520.

[11] M.A. Fox, M.T. Dulay, *Chem. Rev.* **1993**, *93*, 341.

[12] H. Zhang, J.F. Banfield, *J. Phys. Chem. B* **2000**, *104*, 3481.

[13] U. Diebold, *Surf. Sci. Rep.* **2003**, *48*, 53.

[14] A.L. Linsebigler, G. Lu, J.T. Yates, Jr., *Chem. Rev.* **1995**, *95*, 735.

[15] M.A. Henderson, *Surf. Sci. Rep.* **2011**, *66*, 185.

[16] C. Shifu, C. Lei, G. Shen, C. Gengyu, *Powder Techn.* **2005**, *160*, 198.

[17] M. Dahl, Y. Liu, Y. Yin, *Chem. Rev.* **2014**, *114*, 9853.

[18] *CRC Handbook of Chemistry and Physics, 87th ed.*, Taylor & Francis, **2006**, 12.

[19] B. Sun, P.G. Smirniotis, P. Boolchand, *Langmuir* **2005**, *21*, 11397.

[20] Y.L. Chen, D.Z. Li, X.C. Wang, X.X. Wang, X.Z. Fu, *Chem. Comm.* **2004**, *20*, 2304.

[21] C.Y. Wang, R. Pagel, J.K. Dohrmann, D.W. Bahnemann, *Compt. Rend. Chimie* **2006**, *9*, 761.

[22] G.L. Chiarello, M.V. Dozzi, M. Scavini, J.D. Grunwaldt, E. Selli, *Appl. Catal. B* **2014**, *160–161*, 144.

[23] G.L. Chiarello, A. Di Paola, L. Palmisano, E. Selli, *Photochem. Photobiol. Sci.* **2011**, *10*, 355.

[24] M.V. Dozzi, E. Selli, *J. Photochem. Photobiol. C* **2013**, *14*, 13.

[25] A. Bumajdad, M. Madkour, *Phys. Chem. Chem. Phys.* **2014**, *16*, 7146.

[26] X. Chen, H.Y. Zhu, J.C. Zhao, Z.F. Zheng, X.P. Gao, *Angew. Chem. Int. Ed.* **2008**, *47*, 5353.

[27] P. Christopher, H. Xin, A. Marimuthu, S. Linic, *Nat. Mater.* **2012**, *11*, 1044.

[28] M.J. Kale, T. Avanesian, P. Cristopher, *ACS Catal.* **2014**, *4*, 116.

[29] W. Hou, S.B. Cronin, *Adv. Funct. Mater.* **2013**, *23*, 1612.

[30] C. Clavero, *Nat. Photon.* **2014**, *8*, 95.

[31] A.O. Govorov, H. Zhang, H.V. Demir, Y.K.Gun’ko, *Nano Today* **2014**, *9*, 85.

[32] E.W. McFarland, J. Tang, *Nature* **2003**, *421*, 616.

[33] F. Riboni, L.G. Bettini, D.W. Bahnemann, E. Selli, *Catal. Today* **2013**, *209*, 28.

[34] A.A. Ismail, *Appl. Catal. B* **2005**, *58*, 115.

[35] T. Ivanova, A. Harizanova, T. Koutzarova, B. Vertruyen, *J. Non-Cryst. Sol.* **2011**, *357*, 2840.

[36] A.A. Ismail, *Appl. Catal. B* **2012**, *117–118*, 67.

[37] L. Kavan, M. Graetzel, S.E. Gilbert, C. Klemenz, H.J. Scheel, *J. Am. Chem. Soc.* **1996**, *118*, 6716.

[38] D.O. Scanlon, C.W. Dunnill, J. Buckeridge, S.A. Shevlin, A.J. Logsdail, S.M. Woodley, C.R.A. Catlow, M.J. Powell, R.G. Palgrave, I.P. Parkin, G.W. Watson, T.W. Keal, P. Sherwood, A. Walsh, A.A. Sokol, *Nat. Mater.* **2013**, *112*, 798.

[39] B. Gao, Y. Ma, Y. Cao, W. Yang, J. Yao, *J. Phys. Chem. B* 2006, **110,** 14391.

[40] J.A. Renfigo-Herrera, M.N. Blanco, L.R. Pizzio, *Appl. Catal. B* **2011**, *110*, 126.

[41] D. Zhao, C. Chen, C. Yu, W. Ma, J. Zhao, *J. Phys. Chem. C* **2009**, *113*, 13160.

[42] X.Z. Li, F.B. Li, C.L. Yang, W.K. Ge, *J. Photochem. Photobiol. A* **2001**, *141*, 209.

[43] K.K. Akurati, A. Vital, J.P. Dellemann, K. Michalowa, T. Graule, D. Ferri, A. Baiker, *Appl. Catal. B* **2008**, *79*, 53.

[44] Annual Energy Report, U.S. Energy Information Administration (www.eia.gov/forecasts/aeo).

[45] G.A. Olah, G.K.S. Prakash, A. Goeppert, *J. Am. Chem. Soc.* **2011**, *133*, 12881.

[46] Lackner, K. S. *Scient. Amer.* **2010**, 66.

[47] F.R. Keene, C. Creutz, N. Sutin, *Coord. Chem. Rev.* **1985**, *64*, 247.

[48] D.M. Kern, *J. Chem. Educ.* **1960**, *37*, 14.

[49] X. Wang, W. Conway, R. Burns, N. McCann, M. Maeder, *J. Phys. Chem. A* **2010**, *114*, 1734.

[50] H.A. Schwarz, R.W. Dodson, *J. Phys. Chemistry* **1989**, *93*, 409.

[51] A.J. Morris, R.T. McGibbon, A.B. Bocarsly, *Chemsuschem* **2011**, *4*, 191.

[52] C.H. Lim, A.M. Holder, C.B. Musgrave, *J. Am. Chem. Soc.* **2013**, *135*, 142.

[53] K.S. Lackner, *Eur. Phys. J.* **2009**, *176*, 93.

[54] K.S. Lackner, *Science* **2003**, *300*, 1677.

[55] D.W. Keith, *Science* **2009**, *325*, 1654.

[56] G.T. Rochelle, *Science* **2009**, *325*, 1652.

[57] T. Wang, K.S: Lackner, A. Wright, *Environm. Sci. Techn.* **2011**, *45*, 6670.

[58] A. Goeppert, M. Czaun, R.B. May, G.K.S. Prakash, G.A. Olah, S.R. Narayanan, *J. Am. Chem. Soc.* **2011**, *133*, 20164.

[59] K.S. Lackner, P. G. Hans-Joachim Ziock *Proceed. 24th Ann. Techn. Conf. Coal Util. Fuel Systems. Clearwater, FL* **1999**, 885.

[60] B.A. Parkinson, P.F. Weaver, *Nature* **1984**, *309*, 148.

[61] C.J. Stalder, S. Chao, M.S: Wrighton, *J. Am. Chem. Soc.* **1984**, *106*, 3673.

[62] C.M. Bolinger, B.P. Sullivan, D. Conrad, J.A. Gilbert, N. Story, T.J. Meyer, *J. Chem. Soc. – Chem. Comm.* **1985**, *12*, 796.

[63] G. Seshadri, C. Lin, A.B. Bocarsly, *J. Electroanal. Chem.* **1994**, *372*, 145.

[64] E. Barton Cole, P.S. Lakkaraju, D.M. Rampulla, A.M. Morris, E. Abelev, A.B. Bocarsly, *J. Am. Chem. Soc.* **2010**, *132*, 11539.

[65] J.O. Bockris, J.C. Wass, *J. Electrochem. Soc.* **1989**, *136*, 2521.

[66] A. Gennaro, A.A. Isse, M.G. Severin, E. Vianello, I. Bhugun, J.M. Saveant, *J. Chem. Soc. – Faraday Trans.* **1996**, *92*, 3963.

[67] S. Matsuoka, T. Kohzuki, C.J. Pac, S. Yanagida, *Chem. Lett.* **1990**, *11*, 2047.

[68] M. Feroci, M. Orsini, L. Rossi, G. Sotgiu, A. Inesi, *J. Org. Chem.* **2007**, *72*, 200.

[69] E. Barton Cole, D.M. Rampulla, A.B. Bocarsly, *J. Am. Chem. Soc.* **2008**, *130*, 6342.

[70] Y. Oh, X.L. Hu, *Chem. Soc. Rev.* **2013**, *42*, 2253.

[71] A.B. Bocarsly, Q.D. Gibson, A.J. Morris, R.P. L'Esperance, Z.M. Detweiler, P.S. Lakkaraju, E.L. Zeitler, T.W. Shaw, *ACS Catalysis* **2012**, *2*, 1684.

[72] J.A. Keith, E.A. Carter, *J. Am. Chem. Soc.* **2012**, *134*, 7580.

[73] J.A. Keith, E.A. Carter, *Chem. Sci.* **2013**, *4*, 1490.

[74] E.M. Kosower, *Top. Curr. Chem.* **1983**, *112*, 117.

[75] M. Chachisvilis, A,H. Zewail, *J. Phys. Chem. A* **1999**, *103*, 7408.

[76] R. Leuschner, H. Krohn, J.K. Dohrmann, *Ber. Buns. Gesellsch. – Phys. Chem. Chem. Phys.* **1984**, *88*, 462.

[77] R. Leuschner, J.K. Dohrmann *Ber. Buns. Gesellsch. – Phys. Chem. Chem. Phys.* **1984**, *88*, 50.

[78] H. Krohn, R. Leuschner, J.K. Dohrmann, *Ber. Buns. Gesellsch. – Phys. Chem. Chem. Phys.* **1981**, *85*, 139.

[79] F.C. Bos, W.J. Buma, J. Schmidt, *Chem. Phys. Lett.* **1985**, *117*, 203.

[80] W.J. Buma, E.J.J. Groenen, J. Schmidt, R. de Beer, *J. Phys. Chem.* **1989**, *91*, 6549.

[81] W.J. Buma, E.J.J. Groenen, J. Schmidt, *Chem. Phys. Lett.* **1986**, *127*, 189.

[82] K.A. Keets, E. Barton Cole, A.J. Morris, N. Sivasankar, K. Teamey, P.S. Lakkaraju, A.B. Bocarsly, *Ind. J. Chem.A* **2012**, *51*, 1284.

[83] A.J. Morris, A.B. Bocarsly, *Abstr. Papers Am. Chem. Soc.* **2011**, *241*.

[84] J.A. Keith, E.A. Carter, *J. Chem. Theory Comput.* **2012**, *8*, 3187.

[85] A.B. Munoz-Garcia, E.A. Carter, *J. Am. Chem. Soc.* **2012**, *134*, 13600.

[86] J.A. Tossell, *Comput. Theor. Chem.* **2011**, *977*, 123.

[87] F. Riboni, E. Selli, M.R. Hoffmann, A.J. Colussi, *J. Phys. Chem. A* **2014**, just accepted.

[88] S. Goldstein, D. Meyerstein, G. Czapski, *Free Rad. Biol. Med.* **1993**, *15*, 435.

[89] C. Walling, *Acc. Chem. Res.* **1975**, *8*, 125.

[90] J.T. Groves, *J. Inorg. Biochem.* **2006**, *100*, 434.

[91] H.J.H. Fenton, *J. Chem. Soc.* **1894**, *65*, 899.

[92] L. Deguillaume, M. Leriche, N. Chaumerliac, *Chemosph.* **2005**, *60*, 718.

[93] F. Gozzo, *J. Mol. Catal. A* **2001**, *171*, 1.

[94] R.J. Campion, TJ. Conocchioli, N. Sutin, *J. Am. Chem. Soc.* **1964**, *86*, 4591.

[95] L. Deguillaume, M. Leriche, K. Desboeufs, G. Mailhot, C. George, N. Chaumerliac, *Chem. Rev.* **2005**, *105*, 3388.

[96] S.H. Bossmann, E. Oliveros, S. Go1b, S. Siegwart, E.P. Dahlen, L. Payawan, Jr., M. Straub, M. Wo1rner, A.M. Braun, *J. Phys. Chem. A* **1998**, *102*, 5542.

[97] K.B. Cho, X. Wu, Y.M. Lee, Y.H. Kwon, S. Shaik, W. Nam, *J. Am. Chem. Soc.* **2012**, *134*, 20222.

[98] T.A. Rouault, *Science* **2009**, *326*, 676.

[99] E. Harris, B. Sinha, D. van Pinxteren, A. Tilgner, K. W. Fomba, J. Schneider, A. Roth, T. Gnauk, B. Fahlbusch, S. Mertes, T. Lee, J. Collett, S. Foley, S. Borrmann, P. Hoppe, H. Herrmann, *Science* **2013**, *340*, 727.

[100] J.H. Seinfeld, S.N. Pandis, *Atmospheric Chemistry and Physics: From Air Pollution to Climate Change, 2nd ed.*, Wiley Hoboken, **2006**.

[101] M. Mroewetz, E. Selli, *J. Photchem. Photobiol. A* **2004**, *162*, 89.

[102] C. Weller, S. Horn, H. Herrmann, *J. Photochem. Photobiol. A* **2013**, *268*, 24.

[103] F. Haber, J. Weiss, *Proc. Royal Soc. London A* **1934**, *147*, 332.

[104] S. Enami, Y. Sakamoto, A.J. Colussi, *Proc. Natl. Acad. Sci. U.S.A.* **2014**, *111*, 623.

[105] H. Mishra, S. Enami, R.J. Nielsen, L.A. Stewart, M.R. Hoffmann, W.A. Goddard III, A.J. Colussi, *Proc. Natl. Acad. Sci. U.S.A.* **2012**, *109*, 18679.

[106] D.E. Otten, P.R. Shaffer, P.L. Geissler, R.J. Saykally, *Proc. Natl. Acad. Sci. U.S.A.* **2012**, *109*, 701.

[107] K.T. Valsaraj, *Open J. Phys. Chem.* **2012**, *2*, 58.

[108] F.R. Kameel, F. Riboni, M.R. Hoffmann, S. Enami, A.J. Colussi, *J. Phys. Chem. C* **2014**, DOI: dx.doi.org/10.1021/jp505010e.

[109] P. Davidovits, C.E. Kolb, L.R. Williams, J.T. Jayne, D.R. Worsnop, *Chem. Rev.* **2006**, *106*, 1323.

[110] S. Enami, H. Mishra, M.R. Hoffmann, A.J. Colussi, *J. Phys. Chem. A* **2012**, *116*, 6027.

[111] S. Enami, L.A. Stewart, M.R. Hoffmann, A.J. Colussi, *J. Phys. Chem. Lett.* **2010**, *1*, 3488.

Chapter 3

Experimental and characterization techniques

3.1 Nanoparticles preparation

Among the parameters which strongly influence the photoactivity of metal oxides, surface area, surface hydration and hydroxylation extent, crystal phase, surface-charge due to the accumulation of either positive or negative ions, degree of crystallinity and the presence of defects in the lattice are the most relevant [1].
Thus, controlling the synthesis procedure of metal oxide nanoparticles represents the key-point for successful applications in photocatalysis [2].
Limiting the discussion to TiO_2, different synthesis methods have been reported and extensively reviewed: sol-gel [3-5] and, more generally, wet methods [6-8], Chemical Vapour Decomposition (CVD) [9,10], Flame Spray Pyrolysis (FSP) [11], hydrothermal processes [12,13], Evaporation-Induced Self-Assembly (EISA) [14]. Recent literature revealed that sol-gel method is one of the most commonly adopted, since it enables the preparation of titania (and titania-modified) nanopowders at relatively low temperature and under safe conditions [15].

However, the commonly encountered problem with the sol-gel method is that amorphous to low-crystalline materials are produced. Thus, post-synthesis annealing treatments at high temperature are required which, if not properly controlled, may cause particles aggregation and sintering with a detrimental effect on the (photo)catalytic applications [16].

As anticipated in Chapter 2, titania photoactivity can be improved adopting different strategies, among which coupling with another metal oxide and/or the surface modification through noble metal (NM) nanoparticles (NPs) are those of relevance in this thesis.

Several methodologies can be applied to pursue both modifications. In particular, tailoring the previously mentioned methods for pristine titania preparation with the addition of the coupled metal oxide precursor and the consequent tuning of synthetic specific conditions (*e.g.*, solvent, temperature, pressure, annealing treatment) leads to successful syntheses of TiO_2-MO_y coupled semiconductors, with M being *e.g.* Fe, W, V, Bi, Co, Cu [17].

Conversely, the surface modification by NM nanoparticles deposition is usually attained *via* post-synthesis methods. The most commonly adopted are photoreduction [18], deposition-precipitation [19] and chemical reduction [20].

3.1.1 Sol-gel process

Theoretical background

As the name reveals, the sol-gel procedure involves the presence of a *sol* (*i.e.*, a colloidal suspension), which, at a controlled rate and under specific conditions, evolves toward the formation of a *gel* (*i.e.*, a solid network) generating a biphasic system, which contains both a liquid and a solid phase.

Typical precursors for this synthetic route are either inorganic metal salts or metal organic compounds, such as metal alkoxides ($M(OR)_n$) or oxoalkoxide ($MO(RN)_n$) [21,22].

The synthesis can be described as a sequence of inorganic polymerization reactions, namely *i*) formation, *ii*) nucleation, *iii*) growth and *iv*) aging.

The precursor concentration, plotted as a function of the whole reaction time course, is shown in Figure 3.1.

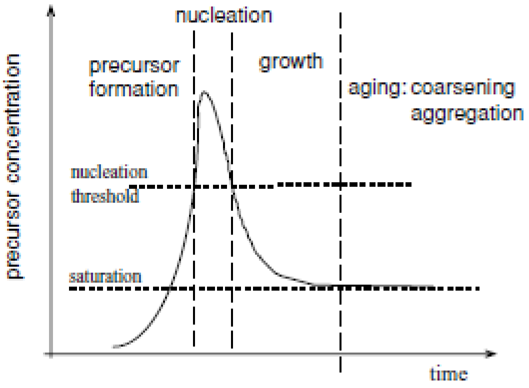

Figure 3.1 – Precursor concentration *vs* time plot representing the nucleation, growth, and aging of nanoparticles prepared by sol-gel synthesis [2].

The *formation* step consists of the hydroxylation, *via* hydrolysis reaction, of the metal precursor, resulting in a stable solution (the *sol*) of either the organic or inorganic metal oxide precursor

$$\text{M-OR} + H_2O \rightarrow \text{M-OH} + \text{R-OH} \qquad \text{(R1)}$$

and leading to the formation of zero-charge molecules (M-OH), with a specific water/hydroxyl content, essential prerequisite for polymerization [2].

Once the precursor concentration reaches a supersaturation level and overcomes the nucleation threshold, *nucleation* starts [23] and proceeds both through *olation* reactions (*i.e.*, formation of hydroxo bridges through condensation of M-OH_2 and/or HO-M groups)

$$\text{M-OH} + \text{HO-M} \rightarrow \text{M-(OH)}_2\text{-M} \qquad \text{(R2a)}$$

and *oxolation* reactions (*i.e.*, formation of oxygen bridges through condensation of two M-OH groups)

$$\text{M-OH} + \text{HO-M} \rightarrow \text{M-O-M} + H_2O \qquad \text{(R2b)}$$

During *nucleation*, a solid phase is formed and the creation of a surface occurs. Hence, thermodynamically, the system Gibbs free energy (ΔG) changes:

$$\Delta G = n\,(\mu_S - \mu_L) + A\gamma \qquad (3.1)$$

with n being the number of moles in the newly-formed nucleus, μ_S and μ_L the chemical potentials of the solid and the liquid phases, respectively, A the surface area and γ the surface energy at the solid-liquid interface.

Since the chemical potentials are related to the solution supersaturation (S) through the following equation:

$$(\mu_S - \mu_L) = -RT\ ln\ (c_L/c_S) = -RT\ ln\ S \qquad (3.2)$$

with c_L being the precursor concentration in the solution, c_S the solubility of the solid, R and T the gas constant and the temperature, respectively, equation 3.1 can be rearranged as follows:

$$\Delta G = -nRT\ ln\ S + (36\pi n^2 V_m^2 \gamma^3)^{1/3} \qquad (3.3)$$

where V_m is the molar volume of the solid material.

When the first derivative of ΔG in *n* equals zero ($\delta(\Delta G)/\delta n = 0$), the energy required to start the *nucleation* process (*i.e.*, the minimum energy to form a critical nucleus) is obtained:

$$\Delta G^* = 16\pi V_m^2 \gamma^3 / 3(RT\ ln\ S)^2 \qquad (3.4)$$

which is strictly related with both the surface energy (γ) and the supersaturation (S).

Finally, the nucleation rate (J_N) can be defined as a function of ΔG*:

$$J_N = J_0 \exp(-\Delta G^*/RT) = J_0 \exp(-16\pi V_m^2 \gamma^3 / 3(RT)^3 (ln\ S)^2) \qquad (3.5)$$

Equation 3.5 clearly highlights that the nucleation rate (J_N) strongly increases with decreasing the surface energy (γ) and with increasing the supersaturation (S) which, in turn, is directly proportional to the precursor concentration in the solution (c_L) and inversely related to the solubility of the solid (c_S), see equation (3.2).

As the *nucleation* phase progresses, the precursor concentration lowers and, when it is again below the nucleation threshold, additional *growth* becomes possible (Figure 3.1).

Two main regimes govern the growing step: *i*) a kinetically-limited mechanism, where the rate is linearly dependent on the particle size; hence, faster growth is expected for larger particles and *ii*) a diffusion-limited mechanism, occurring when the incorporation of atoms is fast and the rate is determined by diffusion to a very small spherical object, implying that smaller particles grow at faster rate. This latter regime is favourably occurring during the metal oxide nanoparticles synthetic process [2].

After nucleation and growth, the *aging* step, during which the total amount of solid material remains constant, transforms the gel into a solid mass by polycondensation reactions, along with contraction of the gel network and expulsion of the solvent from gel pores.

Coarsening, or Ostwald ripening, and aggregation are the two processes occurring at this stage of the reaction.

The first mechanism predicts that the solubility of smaller particles is higher than that of the larger ones, mainly due to capillary effects [24]:

$$c_r = c_{r=\infty} \exp(2\gamma V_m/RTr) \qquad (3.6)$$

where c_r is the solubility of a r-radius particle and $c_{r=\infty}$ is the solubility of an infinite-radius particle (*i.e.*, a flat surface).

The rate is influenced by the solubility of the metal oxide, the solid-solution surface energy and the solution viscosity.

Differently, aggregation may occur either randomly or with a preference for epitaxial assembly [2] and is strictly dependent on the pH of the solution, which in turn influences both the surface charge of the nanoparticles and the surface adsorption of molecules and/or ions. Indeed, when the solution is more basic than the pH at which the nanoparticles surface is nearly neutral (pH_{pzc}, pH of point of zero-charge), *i.e.* $pH_{sol} > pH_{pzc}$, their surface is negatively charged and, if present, cations are preferentially adsorbed. Unlike, if $pH_{sol} < pH_{pzc}$, the nanoparticles surface positively charges and electron-rich and/or anions are favourably adsorbed.

The progressive sequence of these events leads to the formation of a white slurry, still dispersed in the aqueous solvent.

Drying of the gel is attained through different procedures (*e.g.*, heating under controlled atmosphere, heating in oven, solvent evaporation under reduced pressure), which strongly affect the nanoparticles surface features and their bulk and morphological characteristics [26-27].

Finally, in order to obtain crystalline solid metal oxide nanoparticles, thermal annealing (also known as calcination) is required.

The degree of crystallinity and the metal oxide oxidation extent depend on the temperature adopted.

In detail, at different temperature ranges, various phenomena occur:

- desorption of physically adsorbed solvent and water molecules (100 – 200°C)
- decomposition of residual organic groups into CO_2 (300 – 500°C)
- collapse of small pores (400 – 500°C)
- collapse of larger pores (700 – 900°C)
- continued polycondensation (100 – 700°C)

which also influence the evolution of different crystalline phases.

Synthesis of TiO_2 and TiO_2-WO_3 modified nanopowders

This section describes the preparation of TiO_2 and TiO_2-WO_3 samples that have been employed in the study described in Chapter 4.

A pure TiO_2 photocatalyst was synthesized by a sol-gel method, starting from titanium(IV) isopropoxide (TTIP Aldrich, purity 97%) as titanium precursor, following a procedure similar to that described in [3,4].

An anhydrous ethanol solution (100 mL, purity > 99.8%) containing 10 mL of dissolved TTIP was heated at 30 ◦C under vigorous stirring. Then 34 mL of water were added dropwise in order to attain a Ti/H_2O = 1/58 molar ratio.

The low titanium-to-water molar ratio was adopted since it favors the development of Ti-O-Ti chains, representing the proper network for the formation of metal oxides nanoparticles (1 – 100 nm) during the following synthetic steps [22,28].

After stirring and refluxing for 1 hour, the suspension was concentrated under reduced pressure at 35 °C. The so-obtained white slurry was kept in oven at 70 °C overnight to eliminate organic compounds and then calcined at both at 500 and 700 °C under a 100 mL min^{-1} air flow, for 4 h.

To prepare the tungsten oxide-modified titania photocatalysts, tungsten(VI) hexa-ethoxide ($W(OC_2H_5)_6$, Alfa-Aesar 99.8% (metal basis), 5 wt.% in ethanol), was adopted as WO_3 organic precursor.

Indeed, a previous study already proved that unsuccessful mixing between TiO_2 and WO_3 is obtained when an alkoxide, $Ti(OCH(CH_3)_2)_4$, and an inorganic metal salt (Na_2WO_4) are selected as Ti and W precursors [3].

All TiO_2-WO_3 samples were prepared according to the procedure yielding pristine TiO_2, with the only difference that the required amount of tungsten(VI) hexa-hethoxide was added to the TTIP ethanol solution in order to produce samples with nominal W/Ti molar ratio equal to 1, 3, and 5%. The so-obtained solutions were then treated following step by step the procedure adopted for the preparation and calcination of pure titania.

The samples were labelled TW*x*_*y*, with *x* referring to the W/Ti molar ratio (*i.e.*, 0 – 5%) and *y* to the calcination temperature (*i.e.*, 500 or 700 °C).

Most of the employed chemicals were purchased from Sigma-Aldrich and used as received. All solutions were prepared employing ultra-pure water (18.2 MΩ cm at 25 °C), supplied by a Millipore Direct-Q 3 water purification system.

Synthesis of N-doped TiO_2 nanopowders

This section describes the preparation of the nitrogen-doped TiO_2 sample that has been employed in the study described in Chapter 4.

A N-doped TiO_2 photocatalyst was synthesized by a sol-gel method, starting from titanium(IV) isopropoxide (TTIP Aldrich, purity 97%) as titanium precursor, following a procedure similar to that described in the previous section.

An anhydrous ethanol solution (100 mL, purity > 99.8%) containing 10 mL of dissolved TTIP was heated at 30 ◦C under vigorous stirring.

Afterwards, 34 mL of a NH_3 aqueous solution were added dropwise in order to attain a Ti/H_2O = 1/58 molar ratio. The concentration of the ammonium/water solution was fixed to have N/Ti = 25 mol.%.

After stirring and refluxing for 1 hour, the suspension was concentrated under reduced pressure at 35 °C. The so-obtained yellowish slurry was kept in oven at 70 °C overnight to eliminate organic compounds and then calcined at 500 °C under a 100 mL min^{-1} air flow, for 4 h. The sample was labelled as N-TiO_2.

Most of the employed chemicals were purchased from Sigma-Aldrich and used as received. All solutions were prepared employing ultra-pure water (18.2 MΩ cm at 25 °C), supplied by a Millipore Direct-Q 3 water purification system.

3.1.2 Noble metal nanoparticles deposition

Photodeposition of Pt nanoparticles on TiO_2 *and* TiO_2-WO_3 *powders*

This section describes the preparation of Pt/TiO_2 and Pt/TiO_2-WO_3 powders that have been employed in the study described in Chapter 4.

Pt nanoparticle-modified TiO_2 and TiO_2-WO_3 samples were prepared by photodeposition, starting from 6 vol.% methanol–water suspensions containing 3 g L^{-1} of TW*x_y* and the required amount of the metal precursor (*i.e.*, H_2PtCl_6) to obtain a fixed nominal metal loading of 0.5 wt.%.

Such a loading had already been reported to be optimal for improving the rate of formic acid photocatalytic oxidation, since it represents the best balance between *i*) possible shielding effects of NM nanoparticles deposed on the semiconductor surface which decrease the fraction of light actually absorbed by TiO_2, and *ii*) the beneficial role in trapping conduction band electrons, thus reducing the recombination of the photogenerated charge carriers (*i.e.*, e^- and h^+) [29].

By irradiating the suspensions for 2 h under nitrogen atmosphere with an immersion fluorescent, low pressure mercury arc lamp (Jelosil) emitting in the 300 – 400 nm range and with a maximum emission peak at 360 nm, the photoreduction of precursor Pt(VI) to metallic Pt^0 occurs, yielding metal nanoparticles uniformly distributed on the oxide surface.

The so-obtained Pt-modified samples were then recovered from the suspension by means of a rotavapor. The samples were afterwards washed, through washing-centrifugation cycles in water, up to the complete removal of organics and residual ions, *i.e.*, until the concentration of chloride anions in the solution was assessed below 1 ppm, as checked after every cycle through Ion Chromatography. They were finally dried at 70 °C for 1 day and stored in the absence of light and humidity.

These samples were identified as Pt/TW*x_y*, in line with the labels already mentioned in Section 3.1.1.

The actual Pt loading was determined through ICP analysis, performed using a Thermo Electron ICAP 6300 after microwave digestion of the photocatalysts in a 3:1 HCl/HNO_3 mixture, which confirmed quantitative deposition of the noble metal.

Most of the employed chemicals were purchased from Sigma-Aldrich and used as received. All solutions were prepared employing ultra-pure water (18.2 MΩ cm at 25 °C), supplied by a Millipore Direct-Q 3 water purification system.

Preparation of Au-loaded TiO_2-based powders

This section describes the preparation of Au/TiO_2-based powders, modified with different amounts of gold, which have been employed in the study described in Chapter 4.

Aside the photoreduction process described in the previous section, also chemical reduction in H_2 stream or with $NaBH_4$ has been reported as a successful method to achieve the deposition of metal nanoparticles on metal oxides surfaces [20,29]. The procedure here adopted mainly consists of the initial adsorption of NM ions on the titania surface and their subsequent reduction with $NaBH_4$, producing homogeneously dispersed nanoparticles in intimate contact with TiO_2.

As titania supports for the deposition of different gold loading amount, three different samples were selected: *i*) a fully stoichiometric TiO_2, *ii*) a N-doped TiO_2 characterized by the presence of intra band-gap states lying close to the semiconductor valence band (VB) and *iii*) a reduced TiO_2 with oxygen-vacancies (V_Os) states located close to the CB.

While a detailed description of the sol-gel synthesis of N-TiO_2 has been already provided in Secton 3.1.1, both the stoichiometric and the reduced TiO_2 samples, labelled as w- and b-TiO_2, respectively, were prepared according to the procedure already described in [30]. A high surface area (BET surface area ≥ 500 m^2/g) commercial titanium dioxide powder was calcined at 500°C for 1 h under continuous O_2 flow, resulting in the formation of the stoichiometric TiO_2 sample; conversely, the highly defective b-TiO_2 was obtained by annealing the same commercial precursor under H_2 stream, followed by fast cooling in inert environment down to room temperature, avoiding the instantaneous exposure to air which would result in a grey coloration of the powder as a consequence of the TiO_2 lattice rearrangement into a more stoichiometric form [30].

All the selected titania samples were modified by the surface deposition of Au nanoparticles: 500 mg of each TiO_2 sample were suspended in 40 mL of water and sonicated for 20 min. Afterwards, a $HAuCl_4$ water solution, containing the required amount of the metal precursor to attain a nominal Au loading ranging from 1 to 10 wt.%, was added and the obtained suspension was stirred for 30 min. Finally, the addition of a $NaBH_4$ solution (10 mg in 10 mL of H_2O), allowed to react with the powder suspension for 10 min, resulted the reduction and consequent deposition of the metal NPs precursor. The so-obtained products were centrifuged, washed 3 times with H_2O and dried under vacuum (10^{-5} mbar).

The metal-modified powders were labelled as *x*%Au/w-, b- or N-TiO_2, with *x* referring to the Au nominal loading amount.

3.2 Characterization techniques

This section describes the main physico-chemical characterization techniques adopted throughout the experimental work, *i*) to characterize all the TiO_2-based samples employed with the aim of drawing a features-photoactivity correlation.

3.2.1 X-ray diffraction

X-ray diffraction (XRD, also known as XRPD when referred to powdered samples) is a non-destructive analytical technique that characterizes the crystallographic structure, crystallite size and preferred orientation in solid samples.

Due to the distinctive diffraction pattern produced by each crystalline plane, this technique is commonly adopted to identify unknown substances, by comparing the diffraction data with those from the international database (JCPDS, provided by the International Center for Diffraction Data, is the most widely cited in literature). Moreover, when coupled with one of the available refinement methods (*e.g.*, Rietveld refinement), it can also provide useful quantitative information on the crystalline phases constituting heterogeneous solid mixtures.

The principle that governs the process of diffraction is described in terms of incident and reflected (*i.e.*, diffracted) x-rays, each forming an angle θ with a fixed crystal plane where the sample atoms are arranged. If the atom inter-distances are of the same order of magnitude as the wavelength of the incident radiation, either constructive or destructive interferences between the diffracted rays occur and the Bragg law can be applied

$$n\lambda = 2d\ \mathrm{sen}2\theta \qquad (3.7)$$

where *n* is integer positive number (1,2,3…), λ the X-ray incident wavelength, *d* the distance between crystal planes and θ represents both the incident and the reflection angles.

Diffracted X-rays are collected by the detector and, given the incident λ and the measured θ angle, the distance parameter *d* can be calculated.

Since the inter-plane distance is characteristic of each species, crystalline phases are readily determined.

A typical diffractometer consists of a plot of reflected intensities as a function of the 2θ angle (comprising both the incident and the diffraction angles.

Given the peak width measured at half height ($\beta_{½}$), the particles average size (d_P) for each crystalline phase can be determined through the Scherrer equation

$$d_P = 0.94\lambda/\beta_{½}\cos\theta \qquad (3.8)$$

X-ray diffraction patterns of the TiO_2-WO_3 materials discussed in Sections 3.1.1, 3.1.2 and 4.1 were collected using a Phillips PW3020 powder diffractometer, operating at 40 kV and 40 mA, employing filtered Cu Kα radiation (λ = 1.54056 Å) as X-ray emitting source.

X-ray diffraction patterns of the TiO_2-based powders discussed in Sections 3.1.1, 3.1.2 and 4.2 were collected using a Siemens D500 diffractometer operating at 40 kV and 30 mA and at Cu Kα radiation (λ = 1.54056 Å) source. Data were collected by continuous scanning at 1.25 deg/min and a step size of 0.02 deg.

3.2.2 BET analysis

Introduced for the first time by Brunauer *et al.* in 1938 [31] and named after the paper's three co-authors, the B.E.T. theory is mainly adopted to obtain, through the evaluation of the samples adsorption isotherms, essential information on the specific surface area, SSA ($m^2\ g^{-1}$), and pore distribution, among the most important parameters characterizing any type of surface.

The technique involves the principles of physical adsorption of an inert gas, typically N_2, by an initially clean solid surface, at constant temperature, T, and as a function of the gas pressure, p.

To maximize the quantity of physisorbed molecules, the measurements are conducted at low temperature, usually that of liquid nitrogen at its boiling point (*i.e.*, 77 K at 1 atm), while the amount of gas adsorbed is expressed in terms of its volume at standard conditions of temperature and pressure (*i.e.*, 0 °C and 760 torr).

Briefly, the model is based on the multilayer condensation theory described by the equation

$$V/V_m = c\ p/[p_0-p]\ [1+ (c-1)\ p/p_0] \qquad (3.9)$$

with V being the volume of adsorbed gas at pressure p, V_m the monolayer volume, p and p_0 the gas pressure and the saturation gas pressure, respectively, and where the parameter c, which includes the heat of adsorption and liquefaction, is fairly constant for a given class of materials (*e.g.*, oxides and metals).

Rearrangement of 3.9, for p/p_0 values in the 0.05 – 0.30 range, gives

$$p/V(p-p_0) = 1/V_m c + [(c-1)/V_m c]\ (p/p_0) \qquad (3.10)$$

which can be plotted as $p/V(p-p_0)$ *vs.* (p/p_0), with slope (s) and intercept (i)

$$s = (c-1)/V_m c \quad (3.11a) \qquad i = 1/V_m c \quad (3.11b)$$

Solving 3.11a and b both the monolayer volume V_m and the parameter c are readily determined.

Given that the surface occupied by a N_2 molecule (S_{N2}) is 16.2 x 10^{-20} m^2, SSA is finally derived

$$SSA = V_m N_A S_{N2}/V_{SC} m_S \tag{3.12}$$

with N_A being the Avogadro number (6.023 x 10^{23} mol^{-1}), V_{SC} the volume occupied by 1 mole of gas in Standard Conditions (22.414 dm^3 mol^{-1}) and m_S the mass of the analyzed sample.

Nitrogen physisorption measurements of the TiO_2-WO_3 materials discussed in Sections 3.1.1, 3.1.2 and 4.1 were performed on a Micrometrics Tristar 3000 apparatus at 77 K. Prior to each measurement, the samples were outgassed for 4 h at 300 °C.

3.2.3 UV-vis Diffuse Reflectance Spectroscopy

Essential prerequisite for a photochemical reaction to take place is that a *chemical substance* must absorb light. Concerning photocatalysis, the *chemical substance* is identified with the semiconductor photocatalyst; hence, the estimation of its optical properties (which comprise both absorption and reflection) is one of the essential step [32].

A photoabsorption spectrum is a plot of the extent of absorption, expressed as a function of the incident wavelength, which can be reported using either unit of absorbance or the Kubelka-Munk function.

Absorbance *A* is defined as log (I/I_0), with I_0 and I being the intensities of incident and transmitted light, respectively [32].

Conversely, the Kubelka-Munk function (K-M) has the form

$$(1 - R_d^2)/2R_d = \alpha/s \tag{3.13}$$

where R_d, α and s are the diffuse reflectance (*i.e.*, I/I_0), the absorption and the scattering coefficients, respectively.

Absorption spectra of the TiO_2-WO_3 materials discussed in Sections 3.1.1, 3.1.2 and 4.1 were recorded with a Jasco V-650 UV-vis spectrophotometer, equipped with an integrating sphere in order to collect all the diffuse reflections, enhancing the signal-to-noise ratio. A Ba_2SO_4 plate, supplied by the equipment factory, was used as internal reference and its spectrum was collected prior to each samples campaign.

Absorption spectra of the TiO_2-based powders discussed in Sections 3.1.1, 3.1.2 and 4.2 were recorded with a UV-vis reflectance spectrophotometer (Thermo Scientific Evolution 600), equipped with a diffuse reflectance accessory Praying-Mantis sampling kit (Harrick Scientific Products, USA). The powders were carefully ground before collecting the spectra and a Spectralon® disk was used as reference material.

3.2.4 XPS

X-ray Photoelectron Spectroscopy is one of the analytical techniques that allow the determination of a surface elemental composition, with a typical "sampling depth" of few nanometers. This requires extremely cleaned and non-contaminated surfaces to be analyzed.

In XPS, the sample is irradiated with low-energy X-rays (~ 1.5 keV) initiating the photoelectric effect. A high-resolution electron spectrometer measures the energy spectrum of the photoemitted electron.

For this reason, the analysis is conducted under vacuum (~ 10^{-10} torr) so that the transmission of the emitted photoelectron to the analyzer is facilitated and the rate of the re-contamination of a freshly cleaned sample is drastically suppressed.

X-rays sources usually adopted are either Al Kα ($h\upsilon$ = 1486.6 eV) or Mg Kα ($h\upsilon$ = 1253.4 eV).

A typical XPS spectrum shows the recorded intensity as a function of Binding Energy (BE), characteristic of specific elements; hence, the technique can be directly used to identify materials of unknown composition.

BE is defined considering the photoemission process.

Before the photoemission occurs, the total energy of the irradiated system is composed of the energy of the incident X-ray photon ($h\upsilon$) and the energy of the target atom in its background state (E_i).

Once the photoemission has occurred, the total energy of the system is expressed as the kinetic energy of the emitted photoelectron (E_k) plus the energy of the ionized atom (E_f).

Thus, the total energy of the system, before and after photoemission, is expressed as follows

$$h\upsilon + E_i = E_k + E_f \tag{3.14}$$

and the BE, being the difference between the final and the initial states of the target atom ($E_f – E_i$) is readily proved to be elemental-sensitive by

$$BE = E_f - E_i = h\upsilon - E_k \tag{3.15}$$

due to the strict dependence on the energy of photoemitted electron and characteristics of specific electrons in specific atoms.

Interestingly, the Binding Energy scale is usually drawn from right to left, so that, conversely, the photoelectron kinetic energies measured by the spectrometer increase from left to right.

XPS spectra of the TiO_2-WO_3 materials discussed in Sections 3.1.1, 3.1.2 and 4.1 were recorded by means of a Leybold LHS 10/12 spectrometer equipped with a hemispherical electron energy analyzer using Al Kα radiation (hυ = 1486.6 eV). Photoelectron spectra were recorded in constant analyzer energy mode and the binding energies were referred to the C 1s peak at 284.6 eV [3].

3.2.5 ICP-OES

ICP-OES technique is based upon the emission of photons from atoms or ions (OES, Optical Emission Spectrometry) excited in a radiofrequency-induced argon plasma (ICP, Inductively Coupled Plasma, is a specific plasma source where the energy is supplied by electric currents produced *via* electromagnetic induction) [33].

If samples are in the liquid or in the gas form, they can be directly injected into the instrument. If in solid form, they first need to undergo extraction or acid digestion, in order to reduce the analytes to the liquid state.

The sample solution is then converted to an aerosol, injected into the plasma where is quickly vaporized, reaching a temperature of thousands of K.

Hence, analyte elements are in the form of free atoms in the gaseous state and, due to collisional excitation experienced within the plasma, they gain additional energy and are promoted to the excited states.

The relaxation to the ground state of both atomic and ionic excited species results in the emission of a photon. The wavelength of these photons can be used to identify the elements from which they originated.

Being the number of photons with a specific energy directly proportional to the concentration of the emitting element, the technique can be used also for the quantitative estimation of the analyte composition.

To that purpose, ICP-OES analysis of the Pt-modified TiO_2-WO_3 materials discussed in Sections 3.1.1, 3.1.2 and 4.1 and of the Au-modified TiO_2-based powders discussed in Sections 3.1.1, 3.1.2 and 4.2 was performed with a ICAP 6300, Thermo Electron after microwave digestion of samples in a 3:1 HCl/HNO_3 mixture.

3.2.6 Electron Microscopy

Electron microscopy is extensively adopted in the characterization of solids to study structure, morphology and crystallite size, to examine defects, and to determine the distribution of elements.

The basic principles underlying an electron microscope are similar to that of an optical microscope, except that a beam of accelerated electrons is used as incident source, rather than visible light.

The description of the technique provided throughout this paragraph, is taken from ref. [34].

The wavelength associated with electrons is defined as

$$\lambda[\text{Å}] = (150/V)^{1/2} \tag{3.16}$$

where V represents the accelerating potential.

Since electrons have much shorter λ than X-rays, they can interact more strongly with atoms, yielding numerous kinds of signals that can be used for analytical purposes.

Whenever an electron beam interacts with a thin specimen, it generates a signal due to three types of transmitted electrons: *i*) unscattered electrons, *ii*) elastically scattered electrons and *iii*) inelastically scattered electrons.

Three types of electronic signals can also be emitted from the surface of the sample exposed to the incident beam: *i*) backscattered electrons, with energy close to that of the incident electron, *ii*) secondary low-energy electrons, generated through random energy loss processes and *iii*) Auger electrons produced by the de-excitation of atoms. All these signals can be exploited for imaging purposes and, in particular, *i*) and *ii*) are used in the Scanning Electron Microscopy (SEM), whereas *iii*) generates signals for the scanning Auger microscope.

Transmission Electron Microscopy

Transmission Electron Microscopy (TEM) provides high resolution direct images of a solid at high magnification, directly from the electrons transmitted through a ultrathin sample. Due to that, TEM provides images of the bulk structure and can detect crystal defects.

The electron beam is generated by an electron gun (usually, a tungsten filament or lanthanum hexaboride crystal subjected to potentials of hundreds volts) along with an assembly of electromagnetic lenses (*i.e.*, two condenser lenses where the electrons are generated and an objective lens focusing them onto the sample), under high vacuum.

Once the electrons strike the sample, some are deflected whereas those passing through it are detected and form a two-dimensional projection; the instrument can either detect the direct primary beam, providing an image as a dark feature on a bright background (the so-called *bright-field mode*), or the diffracted beam and the formed image consists of a dark background with bright areas from the selected reflections (*i.e.*, *dark-field mode*).

Also High-Resolution TEM (HR-TEM) is very useful, being able to provide images with a resolution as low as 0.1 nm, allowing the individual atoms and defects to be detected.

However, TEM resolution is dictated by aberrations (*e.g.*, astigmatism, chromatic and spherical aberrations) in the lens system which affect the focusing of the beam.

Modern advances have recently been developed to finely correct the system aberrations, so that a resolution as low as 0.05 nm can be achieved.

HR-TEM images of the TiO_2-based powders discussed in Sections 3.1.1, 3.1.2 and 4.2 were recorded using a Zeiss Libra 200FE instrument. The samples were finely ground using an agate mortar and dispersed in isopropanol, by means of a ultrasonic bath. A drop of the suspension was gently deposited on a holey-carbon film supported on a copper 300 mesh grid. After solvent evaporation, TEM micrographs were taken spanning wide regions of all examined samples, to provide a truly representative statistical map of the powders. The size distribution of the Au NPs deposited on TiO_2 was calculated by sampling, on average, 400 metallic NPs.

Scanning Transmission Electron Microscopy

The Scanning Transmission Electron microscope (STEM) combines scanning ability of SEM together with the high resolution achieved in TEM.

To that purpose, the electron incident beam has to be finely focused down to a very small spot (*e.g.*, < 1–10 nm where the point-to-point resolution is limited by the size of the electron beam) and then scanned across the sample.

The transmitted electrons are collected, yielding a high-resolution image of both the inner structure and the sample surface.

Very small clusters and even isolated heavy atoms can be imaged on very thin supporting materials.

Aside coherently scattered electrons, in STEM also high-angle scattered electrons are produced, due to the close interaction with the nuclei, and give rise to useful imaging, also known as High-Angle Annular Dark-Field imaging (HAADF-STEM) or Z-contrast imaging.

In this case, each atom acts as an independent scatterer and no interference between those electrons occurs (that is, they are incoherent), so that the intensity of each incoherent scattering is sensitive to the atomic number of the target atom.

HAADF-STEM images of the TiO_2-WO_3 materials discussed in Sections 3.1.1, 3.1.2 and 4.1 were recorded on an aberration-corrected HD-2700CS Hitachi STEM microscope, operated at acceleration potential of 200 kV (electron gun: cold-field emitter), using an annular dark field detector (HAADF), at the Institute for Chemical and Bioengineering at ETH in Zurich, within a cooperation with Prof. J.A. van Bokhoven. Analytical investigations of selected spots and areas were performed in the normal mode, by means of an Energy Dispersive X-ray spectrometer (EDXS, Genesis Spectrum version 6.2 (EDAX)) attached to this microscope. A few drops of the material suspended in ethanol were deposited onto a perforated carbon foil supported on a copper grid. After drying, the grid was mounted on the single tilt holder of the microscope.

3.2.7 Electron Paramagnetic Resonance (EPR)

Electron Paramagnetic Resonance (EPR) techniques have been widely adopted to investigate paramagnetic species, *i.e.*, those species that contain one or more unpaired electrons.

By virtue of its extremely higher sensitivity compared to that of other spectroscopic techniques, EPR has been often used to investigate and characterize also low-abundance active sites on the catalyst surface [35].

Furthermore, it represents a useful technique also for the detection of hypothetical paramagnetic intermediates in catalytic reactions, such as O^- and O_2^- species in oxidation reactions.

Briefly, a free electron is characterized by a spin angular momentum (**S**) which can assume only two values ($M_S = \pm \frac{1}{2}$). The electron magnetic moment, $\boldsymbol{\mu}_S$, collinear and antiparallel to the spin, is a function of the free electron *g* value (g_e) and the Bohr magnetron ($\mu_B = eh/4\pi mc = 9.27 \times 10^{-21}$ erg G^{-1}):

$$\boldsymbol{\mu}_S = - g_e \, \mu_B \, \mathbf{S} \qquad (3.17)$$

The interaction energy between the electron magnetic moment ($\boldsymbol{\mu}_S$) and an externally applied magnetic field is given by

$$E = - \boldsymbol{\mu}_S \cdot \mathbf{B} \qquad (3.18)$$

where **B** is the magnetic flux density which corresponds to the effect induced by a magnetic field strength on the matter.

Assuming that **B** lies only in the *z* direction (*i.e.*, $B_x = B_y = 0$ and $B = B_z$), the energies corresponding to the allowed orientations of the spin are

$$E = g_e \, \mu_B \, \mathbf{B} \cdot \mathbf{S} = g_e \, \mu_B \, B_z \, S_z = (\pm \tfrac{1}{2}) \, g_e \, \mu_B \, B \qquad (3.19)$$

These two energy levels are often referred to as Zeeman levels, with the lower ($M_S = - \frac{1}{2}$) corresponding to the situation in which B and μ_S are parallel and the higher ($M_S = + \frac{1}{2}$) to that in which B and μ_S are antiparallel. Therefore, the energy difference between these two levels is

$$\Delta E = g_e \, \mu_B \, B \qquad (3.20)$$

By irradiating the paramagnetic sample by means of a suitable electromagnetic radiation (for the magnetic field usually adopted in laboratory experiments, the required radiation belongs to the microwave region) and by taking into account that the radiation frequency υ has to fulfil the resonance condition, the transition between the two Zeeman levels can be induced:

$$h\upsilon = g_e \mu_B B \tag{3.21}$$

In EPR spectra, the resonance signal corresponds to the energy absorption necessary to promote electrons from the lower to the upper level. When the odd electrons from the upper level give up the energy ($E = h\upsilon$) to return to the lower level, E can be dissipated within the lattice as phonons (*i.e.*, vibrational, rotational and translational energy) and the so-called spin-lattice relaxation occurs, which is characterized by an exponential decay of energy with time (T_{1e}); additionally, E can also be dissipated due to energy exchange between spins without transferring energy to the lattice, *i.e.*, the spin-spin relaxation occurs, characterized by the time constant T_{2e}.

In general $T_{2e} > T_{1e}$ and the EPR signal mainly depends on spin-spin interaction.

The typical paramagnetic resonance lines can either be described by Gaussian ($y = ae^{-bx2}$) or Lorentzian ($y = a/(1-bx^2)$) functions.

In modern EPR spectrometry, the detector is designed in order to measure, with high sensitivity, the microwave absorption in a sample as a function of the external applied magnetic field.

Solid samples to be analysed are usually placed in quartz tubes and connected to vacuum lines or gas-handling, in order to activate the samples surface or adsorb the desired reactant at the desired temperature and pressure. Spectra are often acquired at 77 K using a special Dewar fitting into the cavity measurement.

EPR spectra of the TiO_2-WO_3 materials discussed in Sections 3.1.1, 3.1.2 and 4.1 were recorded by means of a Bruker EMX spectrometer equipped with cylindrical cavity and operating at a 100 kHz field modulation, at the Department of Chemistry at the University of Turin, within a cooperation with Prof. E. Giamello. The measurements were carried out at the liquid nitrogen temperature (77 K) in quartz cells that can be connected to a conventional high-vacuum apparatus (residual pressure $<10^{-4}$ mbar). EPR spectra were simulated using the Easyspin program.

3.3 (Photo)catalytic tests and set ups

3.3.1 Photocatalytic degradation of formic acid

Formic acid (FA) photocatalytic degradation tests were performed to determine the photocatalytic activity of TiO_2-WO_3 and Pt-modified TiO_2-WO_3 samples. The results are discussed in detail in Section 4.1.

Slightly different conditions (see below) were applied in the FA photocatalytic degradation performed with Au-modified stoichiometric and defective TiO_2 samples (*i.e.*, w-, N- and b-TiO_2); the obtained results are presented in Section 4.2.

Formic acid photo-oxidation leads to its mineralization, according to the following reaction

$$HCOOH + \frac{1}{2} O_2 \rightarrow CO_2 + H_2O \qquad \text{(R3.3)}$$

which was monitored in terms of FA consumed throughout the irradiation time.

FA represents a suitable organic substrate for photocatalytic oxidation reaction tests because it undergoes complete conversion to CO_2 without forming any intermediate stable species possibly competing for adsorption on the photocatalyst surface; thus, kinetic studies of this reaction are greatly simplified.

Moreover, HCOOH does not absorb light in the 320 – 400 nm range, which is often selected for UV-vis photocatalytic reactions, and does not evaporate form aqueous solution at ambient temperature [36]. Finally, aside being actually dissolved in industrial effluents, FA also represents one of the stable intermediates in the complete mineralization of many organic pollutants toward CO_2, often recalcitrant to further oxidation [37]

The photo-oxidation of FA was performed under atmospheric conditions in a 60 mL cylindrical quartz reactor, magnetically stirred and housed in a homemade equipment consisting of a black box mounted on an optical bench [3].

The reaction water suspension contained a fixed amount of photocatalyst powder, *i.e. i*) 0.1 g L^{-1}, for the TiO_2-WO_3 and Pt-modified TiO_2-WO_3 samples [3], *ii*) 0.2 g L^{-1} for the Au-modified w-, N- and b-TiO_2 samples.

The initial concentration of formic acid was always fixed at 1.0×10^{-3} mol L^{-1}.

All photocatalysts were preliminarily suspended in water, by treating them in a ultrasound bath for 30 min. Then, the required amount of formic acid was added and, before starting irradiation, the suspension was left under dark conditions and magnetic stirring for 15 min, until the adsorption-desorption equilibrium of the substrate on the photocatalyst surface was achieved.

Two different irradiation sources were selected:

i) an Osram Powerstar HCI-T 150 W/NDL lamp was adopted in kinetic tests with the TiO_2-WO_3 and Pt-modified TiO_2-WO_3 samples. This lamp mainly emits visible light above 400 nm, but has also a small emission in the 350–400 nm range, as evidenced by the emission spectrum reported in Figure 3.2. The lamp full emission intensity on the photoreactor was 2.53×10^{-7} Einstein s^{-1} cm^{-2}, as periodically checked by ferrioxalate actinometry.

ii) a home-built *Light Emitting Diode* (LED) was adopted in studies on Au-modified w-, N- and b-TiO_2 samples. The LED emits mainly monochromatic visible light centred at $\lambda = 532$ nm with an incident light intensity, measured within the reactor, of *ca*. 6 mW/cm^2, as checked prior to any photocatalytic run by means of an optical powermeter (ThorLabs, PM 200).

The residual amount of formate anions contained in the samples withdrawn from the photoreactor at different times was determined by Ion Chromatography with conductivity detection, after centrifugation.

Also the pH of the suspensions was checked before and after each kinetic run, by means of an Amel model 2335 pHmeter.

A pH increase from *ca.* 3.5 – 3.6 initial value provided a thorough estimation of the formic acid mineralization extent to CO_2 and H_2O (the highest the final pH, the highest the amount of FA degraded).

All photocatalytic runs were repeated at least twice, to check their reproducibility.

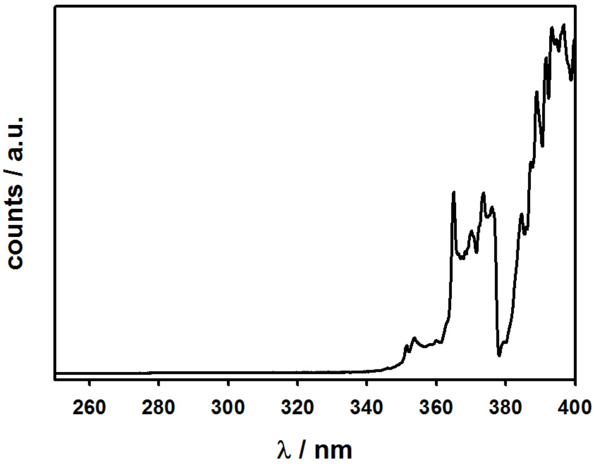

Figure 3.2 – Emission spectrum of the Osram Powerstar HCI-T 150 W/NDL lamp adopted as irradiation source in formic acid photodegradation runs performed with TiO_2-WO_3 and Pt-modified TiO_2-WO_3 photocatalysts.

3.3.2 H_2 production by methanol photo-steam reforming

H_2 production by methanol photo-steam reforming was performed to determine the photocatalytic activity of TiO_2-WO_3 and Pt-modified TiO_2-WO_3 samples. The results are discussed in detail in Section 4.1.

The assembly of the set up used in the kinetic runs and the optimization of the working conditions have been the core of previous studies of the research group [11,38-40].

Overall, methanol (photo-)steam reforming occurs according to the following reaction

$$CH_3OH + H_2O \rightarrow CO_2 + 3H_2 \qquad \text{(R3.4)}$$

The photocatalyst bed consisted of the semiconductor powder deposited on quartz beads by mechanically mixing 14 mg of sample with 3 g of quartz, along with 1.2 mL of distilled water.

After drying at 70 °C overnight, the photocatalyst bed was inserted in a flat cylindrical photoreactor, frontally equipped with a Pyrex glass optical window, providing an actual surface of ~ 20 cm^2 available for irradiation.

The photoreactor was then connected to a closed stainless steel system and, prior to any run, the whole set up was purged for 30 min with nitrogen (used also as carrier gas) to remove oxygen traces.

During irradiation, the photoreactor was continuously flushed with N_2 gas, at constant rate (40 mL min^{-1}) by means of a metal bellow pump.

The carrier gas was also bubbled through a 20 vol.% CH_3OH aqueous solution maintained at 30 °C (methanol molar fraction, $x_{CH3OH} = 0.10$) and saturated with that vapor, continuously feeding the photoreactor as well.

A thermocouple placed inside the cell monitored the reactor temperature (30 ± 2 °C), while the absolute pressure at the beginning of the runs was 1.2 bar, slightly increasing during irradiation due to the accumulation of the products in the gas phase.

Typically, runs lasted 6 hours when testing TiO_2-WO_3 samples; three consecutive 2 hour-long runs were instead performed with the Pt-modified TiO_2-WO_3 samples, due to the high products accumulation, with 30 min N_2 purging, in the dark, between each irradiation cycle.

During the runs, the recirculating gas phase was withdrawn at specific interval time by means of a pneumatic valve and injected in a Agilent 6890 N gas-chromatograph, equipped with two columns (HP-PlotU and Molesive 5A), two detectors (thermoconductivity and flame ionisation) and a Ni-catalyst kit for CO and CO_2 methanation.

An iron halogenide mercury arc lamp (Jelosil, 250 W) was adopted as irradiation source, anchored at 20 cm from the photoreactor and always switched on 30 min before the beginning of the run.

The lamp emits in the 330 – 450 nm wavelength range, with a full irradiation intensity of 6.0×10^{-8} Einstein s^{-1} cm^{-2}, as periodically checked by ferrioxalate actinometry.

The reproducibility of kinetic results was always tested by repeating the runs twice.

As discussed in detail in previous works [11,38-40], the concentration of H_2, CO_2, CO and CH_4, accumulated in the gas-phase, increased linearly with time, according to a pseudo-zero order rate law, due to the high excess of reactants (indeed, water and methanol concentration did not significantly vary under steady-state conditions).

Conversely, the concentration of formaldehyde and other minor by-products rapidly increased at the beginning of irradiation and then stabilized due to their accumulation in the methanol-water liquid solution when the carrier gas bubbled into it. Formic acid concentration was never detected by GC analysis but its formation and accumulation in the liquid solution was confirmed by Ion Chromatography analysis performed at the end of each run.

3.3.3 Catalytic selective hydrogenation of 1-nitro-4-vinylbenzene to 4-vinylaniline

The heterogeneous hydrogenation of 1-nitro-4-vinylbenzene to 4-vinylaniline (in the followings, 4-nitrostyrene and 4-aminostyrene, respectively) was performed with the Pt-modified TiO_2-WO_3 samples calcined at 500 °C.

The kinetic tests were run at the Institute for Chemical and Bioengineering at ETH in Zurich, within a cooperation with Prof. J.A. van Bokhoven, and the results are discussed in details in Section 4.1.

Since the development of the industrial chemistry related to polymer production, agrochemicals, pharmaceuticals and dyes, chemoselective hydrogenation of substituted nitrobenzene to aniline and its derivatives has been considered a reaction of valuable interest [41-43].

Conventional active metals such as Pt, Pd, Ni, Cu and Au have been proposed as catalysts for the reaction, also supported on various materials: *i*) “inert” activated C, $CaCO_3$ and SiO_2 or *ii*) better performing, in terms of preferential hydrogenation, TiO_2 and Fe_2O_3 metal oxides, by virtue of their strong metal-support interaction [44].

More recently, Makosch *et al.* have shown that the thiol-surface modification of Pt/TiO_2 catalysts, employed for the liquid phase selective hydrogenation of 4-nitrostyrene, led to 4-aminostyrene as the exclusive product. By contrast, the primary product obtained with bare Pt/TiO_2 was 4-ethylnitrobenzene, along with considerable amounts of the fully hydrogenated 4-ethylaniline.

The distinct behaviours displayed by the two systems was mainly ascribed to the flat adsorption of the benzene ring on unmodified Pt, thus simultaneously exposing both the reducible groups (*i.e.*, vinyl- and nitro-groups) to the catalyst active sites [42].

Relevant conclusion to these observations was the direct impact that the support has on the reaction mechanism, actively influencing it.

Thus, the effect induced on the hydrogenation of 4-nitrostyrene by the presence of increasing amounts of WO_3 in the Pt/TW*x*_500 series was investigated.

All catalytic tests were performed in a 50 cm^3-Premex stainless steel autoclaves with polyetheretherketone (PEEK) inlets. The reaction composition consisted of *i*) 20 g of toluene, used as solvent; *ii*) 1 mmol of mestylene, as internal standard; *iii*) 50 mg of catalyst powder and *iv*) 0.67 mmol of 4-nitrostyrene. This mixture was filled into the autoclave and purged three times, under vigorous stirring, after sealing by using H_2 (5 bar).

The autoclave was then pressurized to 10 bars by using H_2 and the inner temperature was increased up to 80 °C under constant stirring, allowing the reaction to start. Samples were withdrawn from the autoclave at fixed time intervals by means of a sample tube; they were then filtered and finally analyzed by means of an Agilent 7820 A gas-chromatograph, equipped with an apolar 30 m HP 5 MS column. The adopted temperature program consisted of 20 °C min^{-1} heating steps from 80 to 300 °C at a split ratio of 60/1.

3.3.4 Homogeneous CO_2 reduction by photogenerated pyridinyl radicals in 2-propanol/water mixtures

Homogeneous CO_2 photoreduction in pyridine/alcohol aqueous mixtures was performed at the Linde Center for Global Environmental Science at the California Institute of Technology, under the supervision of Dr. A.J. Colussi and Prof. M.R. Hoffmann. The results are extensively discussed in Chapter 5, where a detailed mechanism is provided, comprising also the main side-reactions occurring.

Recent literature revealed that CO_2 can be reduced up to the six-electron reduction products (methanol, CH_3OH), using pyridine (Py) either as a co-catalyst in photo-electrochemical assisted processes or as catalyst in photochemical homogeneous reactions [45,46].

With the aim of elucidating the reaction mechanism which is still only partially understood, photolysis experiments were performed starting from aqueous pyridine solutions, containing also a fixed amount of isopropyl alcohol (2-PrOH), a H-atom donor, which promotes the formation of pyridinyl radicals strictly required for the overall reaction to start. The mixtures pH were always adjusted to pH ~ 3 with HCl, ensuring that Py (pK_a = 5.3 [45]) was largely present as pyridinium, PyH^+ [47].

The photochemical reactions were carried out in a sealed custom-made glass reactor, equipped with silica sleeve to house a Pen-Ray (P/N 90-0012) monochromatic Hg lamp emitting ~ 3×10^{15} 254 nm photons s^{-1}, whose output was filtered with a short-pass filter that blocked weak spurious 365 nm emissions. As reported by many authors, the triplet excited state of pyridine ($^3Py^*$) and pyridine-like species is considered to be of mixed character between $n\pi^*$ and $\pi\pi^*$ states [48-50], with the ground-to-excited state transition occurring at ~ 4 eV (92 kcal/mol) [51].

Since the Hg lamp provided photons with an associated energy of 112 kcal/mol, the photon energy threshold matched with the energy required to promote pyridine excitation.

Prior to any photolysis experiments, the Py/2-PrOH/H_2O solutions were degassed *in situ* by freezing-and-thawing cycles under vacuum, in order to evacuate oxygen and prevent all the possible quenching side-reactions.

CO_2 was then bubbled for 1 hour into the reactor, at overpressure ~ 12 psi (0.8 atm), guaranteeing the saturation of both the solution and the reactor dead volume.

Finally, the lamp was introduced into the internal quartz tube and the photolysis was run by irradiating for 1 h, collecting the sample at the end of the irradiation period, from a silicone rubber septum.

The temperature was maintained at (25 ± 2) °C throughout, by means of a ice/water bath.

The obtained solutions were then analyzed by means of an Electrospray Ionization Mass Spectrometer (ESI-MS) both in the positive and in the negative modes, after collecting a UV-vis absorption spectrum.

Different irradiation times, as well as different pyridine concentrations (1 – 100 mM), were also tested while the amount of 2-PrOH was kept constant (10 v/v% 2-PrOH/H_2O), always being in large excess with respect to pyridine.

All reagents were of chemical grade. Pyridine and *iso*-propanol were purchased from Sigma-Aldrich, CO_2 from Air Products. They were all used as received. Milli-Q water was supplied by a Millipore purification system.

3.3.5 Fenton oxidation of gaseous isoprene on aqueous surface

Heterogeneous oxidation of gas-phase isoprene *via* Fenton reaction was performed at the Linde Center for Global Environmental Science at the California Institute of Technology, under the supervision of Dr. A.J. Colussi and Prof. M.R. Hoffmann.

Experiments were carried out by intersecting, in the spraying chamber of an electrospray (ES) ionization mass spectrometer (Agilent 1100 Series, LC/MSD high performance ion trap mass spectrometer), acidic 1 µM $FeCl_2(aq)$ microjets with ISO(g)/N_2(g), H_2O_2(g)/N_2(g) or ISO(g)/H_2O_2(g)/N_2(g) gas streams. The spectrometer was run at ambient temperature and pressure [52].

1 µM aqueous $FeCl_2$ solutions were prepared by dissolving the required amount of $FeCl_2 \times 4H_2O$ (> 98 % Sigma-Aldrich) in deionized water, then acidified to pH ~ 2.0 with HCl(aq).

Fe^{2+}(aq) was continuously pumped at 25 µL min^{-1} into the spraying chamber of the ESI spectrometer through a grounded stainless steel needle injector.

Concurrently, liquid isoprene (Sigma-Aldrich, 98.0%) which, prior to use, was purified by fractional distillation collecting the fraction boiling between 40 and 45 °C, was maintained at 273 K and sparged with 15 cm^3 min^{-1} N_2 gas flow. Similarly, 50 wt. % H_2O_2 (Sigma-Aldrich), kept at 303 K, was sparged with 150 cm^3 min^{-1} N_2(g).

A T-connector conveyed ISO(g)/N_2(g) and H_2O_2(g)/N_2(g) streams, independently flowing, by merging them into the spraying chamber and, finally, a Teflon catheter positioned near the liquid microjets, directed ISO(g)/N_2(g), H_2O_2(g)/N_2(g) or ISO(g)/H_2O_2(g)/N_2(g) gas streams toward Fe^{2+}(aq) drops.

The reaction products were obtained during encounters of gaseous ISO and/or H_2O_2 with the surface of the aqueous microjets as they emerged from the nozzle, *i.e.*, before they were broken up by the nebulizer gas into submicrometer-sized droplets which, carrying excess charge of either positive or negative sign, held the actual information registered by the mass spectrometer [53,54].

The experimental design of the adopted apparatus is shown in Chapter 6.

The gaseous reagents concentration at the surface of the microjets were: *i*) [ISO(g)] $\sim 5 \times 10^{15}$ molecules cm^{-3}, as estimated by assuming that the 15 cm^3 min^{-1} of N_2 carrier flow was completely saturated with ISO vapour at 288 K (*i.e.*, value averaged between ISO(g) 273 K and H_2O_2(g) 303 K temperatures), prior to entering the spraying chamber, where it was diluted by a factor of 1.9×10^{-3} due to the 8 L min^{-1} nebulizer N_2 gas flow; *ii*) [H_2O_2(g)] $\sim 4 \times 10^{14}$ molecules cm^{-3}, as determined according to the reported composition of the vapor in equilibrium with 50 wt.% H_2O_2 solutions at 303 K.

The reaction pathway leading to the oxidation products was established by replacing H_2O_2 solution with deionized H_2O, or by sparging deionized H_2O instead of ISO, always keeping the combined gas flow rate at 165 cm^3 min^{-1}.

In some experiments *tert*-butanol (an efficient $^{\bullet}OH$ scavenger, with $k(^{\bullet}OH + tert\text{-}BuOH) = 5 \times 10^8$ M^{-1} s^{-1} in bulk water, [55]) was added to the 1 µM $FeCl_2$ solutions, in order to determine the role of $^{\bullet}OH$ radicals in the formation of the observed products.

The structures of the major products were also elucidated via MS^2 spectrometry, performed both in the positive and in the negative ion modes throughout the entire investigated mass range (50 to 600 Da).

3.3.6 Electrospray Mass Spectrometry (ES-MS)

ES-MS was adopted for products determination in both the homogeneous photochemical reduction of CO_2, introduced in Section 3.3.4 and thoroughly discussed in Chapter 5, and the Fenton-oxidation of gaseous isoprene on aqueous surfaces, introduced in Section 3.3.5 and reported in Chapter 6.

Electrospray (ES) technique consists in spraying the sample solution through a grounded needle, the so-called capillary, at atmospheric pressure. The use of a nebulizing gas, usually an inert gas such as N_2, further promotes the spraying process.

The difference between the velocity of the injected liquid and that of the nebulizer gas is usually so large that the strength, experienced by the liquid, breaks it apart into micrometer sized droplets [56], in which both positive and negative ions are solvated.

An adjacent induction electrode, at high potential relative to the nebulizing region, subsequently polarizes these droplets, so that all the entities (*i.e.*, the droplets and the ions they produced) have the same polarity, opposite to that of the electrode [57] but equal to that of the needle. This further enhances the spraying, since the droplets are repelled from the needle towards the counter electrode.

The additional presence of a dry gas, flowing at high temperatures and coaxial to the injected liquid, causes the evaporation of the solvent charged droplets (*i.e.*, desolvation).

The desolvation proceeds until the droplet becomes unstable upon reaching its Rayleigh limit, defined by

$$q^2 = 64\ \pi^2\ \varepsilon_0\ \alpha^3 \tag{3.22}$$

where ε_0 is the permittivity of free space and γ is the surface tension of the droplet; consequently, droplets deform since the Coulomb repulsion between like-charges overcomes the attractive surface tension, which holds the droplet together [58].

At this point the droplet undergoes a cascade of Coulomb explosions which result in the ejection of bare single ions to the gas-phase [56].

The ions, subjected to the so-called fragmentation voltage, are then driven to the skimmer, a region where they are accelerated up to excess kinetic energies which is converted into internal (vibrational/rotational) excitation during impact with N_2 gas molecules prior to undergoing collisionally induced dissociation [56].

Eventually, the gas-phase singly charged ions so-formed are directed towards the mass detector.

The ES-MS apparatus used is a HP 1100 LC/MSD, equipped with an Ion Trap mass spectrometer which allowed the detection of both cations and anions. Aldehydes, ketones and alcohols are usually detected in the positive mode, while the formation of carboxylic acids is detected by the negative-mode mass spectra.

In a typical homogeneous photochemical CO_2 reduction experiment (Section 3.3.4 and Chapter 5), the liquid withdrawn at the end of the kinetic runs was injected at controlled flow rate (50 μl/min) with a Harvard *PicoPlus* syringe pump, throughout a grounded stainless steel needle; the high-temperature (325°C) dry gas (N_2) was flown at 8 L min^{-1}, while the nebulizer (N_2) pressure was set at 45 psi (~ 3 bar). The high potential applied at the exit of the capillary was maintained at ± 2.5 kV and the fragmentation voltage fixed at 50V, for the detection of cations, and 10 V for the detection of anions [47].

In the Fenton-oxidation of gaseous isoprene experiments (Section 3.3.5 and Chapter 6) all the instrumental parameters were the same as those aforementioned, except for the fragmentation voltages kept at 20 V (for positive ions), and 40 V (for negative ions), adopted to optimize mass signals with minimal fragmentation of molecular ions [52].

REFERENCES

[1] M.A. Fox, M.T. Dulay, *Chem. Rev.* **1993**, *93*, 341.

[2] G. Oskam, *J. Sol-Gel Sci. Techn.* **2006**, *37*, 161.

[3] F. Riboni, G.L. Bettini, D.W. Bahnemann, E. Selli, *Catal. Today* **2013**, *209*, 28.

[4] M.V. Dozzi, S. Livraghi, E. Giamello, E. Selli, *Photochem. Photobiol. Sci.* **2011**, *10*, 343.

[5] A.A. Ismail, D.W. Bahnemann, *Green Chem.* **2011**, *13*, 428.

[6] X. Zhang, Q. Liu, Mater. Lett. 2008, 62, 2589.

[7] M. Bettinelli, V. Dallacasa, D. Falcomer, P. Fornasiero, V. Gombac, T. Montini, L. Romano, A. Speghini, *J. Hazard. Mater.* **2007**, *146*, 529.

[8] C. Liu, X. Tanga, C. Moa, Z. Qiang, *J. Sol. St. Chem.* **2008**, *181*, 913.

[9] S.K. Pradhan, P.J. Reucroft, F. Yang, A. Dozier, *J. Cryst. Growth* **2003**, *256*, 83.

[10] J.J. Wu, C.C. Yu, *J. Phys. Chem. B* **2004**, *108*, 3377.

[11] G.L. Chiarello, M.H. Aguirre, E. Selli, *J. Catal.* **2010**, *273*, 182.

[12] S.Y. Chae, M.K. Park, S.K. Lee, T.Y. Kim, S.K. Kim, W.I. Lee, *Chem. Mater.* **2003**, *15*, 3326.

[13] J. Yang, S. Mei, J.M.F. Ferreira, *Mater. Sci. Eng. C* **2001**, *C15*, 183.

[14] M. Li, S. Zhang, L. Lv, M. Wang, W. Zhang, B. Pan, *Chem. Eng. J.* **2013**, *229*, 118.

[15] D.P. Macwan, N.D. Pragnesh, S. Chaturvedi, *J. Mater. Sci*. **2011**, *46*, 3669.

[16] J.G. Li, H. Kamiyama, X.H. Wang, Y. Moriyoshi, T. Ishigaki, *J. Eur. Ceram. Soc.* **2006**, *26*, 423.

[17] M. Dahl, Y. Liu, Y. Yin, *Chem. Rev.* **2014**, *114*, 9853.

[18] M.V. Dozzi, A. Saccomanni, E. Selli, *J. Hazard. Mater.* **2012**, *211–212*, 188.

[19] M. Haruta, *Catal. Today* **1997**, *36*, 153.

[20] A. Naldoni, M. D'Arienzo, M. Altomare, M. Marelli, R. Scotti, F. Morazzoni, E. Selli, V. Dal Santo, *Appl. Catal. B Environm.* **2013**, *130–131*, 239.

[21] V.K. La Mer, R.H. Dinegar, *J. Am. Chem. Soc.* **1950**, *72*, 4847.

[22] X. Chen, S.S. Mao, *Chem. Rev.* **2007**, *107*, 2891.

[23] J.P. Jolivet, *Metal Oxide Chemistry and Synthesis – From Solution to Solid State*, John Wiley & Sons, **2003**.

[24] T. Sugimoto, *Adv. Colloid. Interf. Sci.* **1987**, *28*, 65.

[25] S. Melada, M. Signoretto, S. Ardizzone, C.L. Bianchi, *Catal. Lett.* **2001**, *75*, 199.

[26] S. Ardizzone, L. Binaghi, G. Cappelletti, P. Fermo, S. Gilardoni, *Phys. Chem. Chem. Phys.* **2002**, *4*, 5683.

[27] G. Cappelletti, C. Ricci, S. Ardizzone, C. Parola, A. Anedda, *J. Phys. Chem. B* **2005**, *109*, 4448.

[28] G. Oskam, A. Nellore, R.L. Penn, P.C. Searson, *J. Phys. Chem. B* **2003**, *107*, 1734.

[29] M.V. Dozzi, L. Prati, P. Canton, E. Selli, *Phys. Chem. Chem. Phys.* **2009**, *11*, 7171.

[30] A. Naldoni, M. Allieta, S. Santangelo, M. Marelli, F. Fabbri, S. Cappelli, C.L. Bianchi, R. Psaro, V. Dal Santo, *J. Am. Chem. Soc.* **2012**, *134*, 7600.

[31] S. Brunauer, P.H. Emmet, E. Teller, *J. Am. Chem. Soc.* **1938**, *60*, 309.

[32] B. Ohtani, *J. Photochem. Photobiol. C* **2010**, *11*, 157.

[33] X. Hou, B.T. Jones, *Encyclopedia of Analytical Chemistry,* R.A. Meyers (Ed.) John Wiley & Sons Ltd, **2000**, pages: 9468–9485.

[34] L.E. Smart, E.A. Moore, *Solid State Chemistry: an Introduction, 4th ed*, CRC Prress, **2012**

[35] M. Che, E. Giamello, *Catalyst Characterization: Physical Techniques for Solid State Materials*, **1994**, pages 131–179.

[36] D.H. Kim, M.A. Anderson, *Environm. Sci. Technol.* **1994**, *28*, 479.

[36] C. He, W. Xiong, X. Zhu, X. Li, *Appl. Catal. A Gener* **2004**, *275*, 55.

[37] G.L. Chiarello, L. Forni, E. Selli, *Catal. Today* **2009**, *144*, 69.

[38] G.L. Chiarello, D. Ferri, E. Selli, *J. Catal.* **2011**, *280*, 168.

[39] G.L. Chiarello, A. Di Paola, L. Palmisano, E. Selli, *Photochem. Photobiol. Sci.* **2011**, *10*, 355.

[40] M. Makosch, J. Sa, C. Kartusch, G. Richner, J.A. van Bokhoven, K. Hungerbühler, *Chem. Cat. Chem.* **2012**, *4*, 59.

[41] M. Makosch, L. Wan-Ing, V. Bumbálek, J. Sa, J.W. Medlin, K. Hungerbühler, J.A. van Bokhoven, *ACS Catal*. **2012**, *2*, 2079.

[42] M. Boronat, A. Corma, Langmuir **2010**, *26*, 16607.

[43] M. Boronat, P. Concepcion, A. Corma, S. Gonzalez, F. Illas, P. Serna, *J. Am. Chem. Soc.* **2007**, *129*, 16230.

[44] E. Barton Cole, P.S. Lakkaraju, D.M. Rampulla, A.J. Morris, E. Abelev, A.B. Bocarsly, *J. Am. Chem. Soc.* **2010**, *132*, 11539.

[45] D.J. Boston, C. Xu, D.W. Armstrong, F.M. MacDonnell, *J. Am. Chem. Soc.* **2013**, *135*, 16252.

[46] F. Riboni, E. Selli, M.R. Hoffmann, A.J. Colussi, *J. Phys. Chem. A* **2014**, just accepted.

[47] H. Krohn, R. Leuschner, J.K. Dohrmann, *Phys. Chem. Chem. Phys.* **1981**, *85*, 139.

[48] S. Terokubota, K. Akiyama, T. Ikoma, Y. Ikegami, *J. Phys. Chem.* **1991**, *95*, 766.

[49] M. Chachisvilis, A.H. Zewail, *J. Phys. Chem. A* **1999**, *103*, 7408.

[50] F.C. Bos, W.J. Buma, J. Schmidt, *Chem. Phys. Lett.* **1985**, *117*, 203.

[51] F.R. Kameel, F. Riboni, M.R. Hoffmann, S. Enami, A.J. Colussi, *J. Phys. Chem. C* **2014**, DOI: dx.doi.org/10.1021/jp505010e.

[52] S. Enami, A.J. Colussi, *J. Chem. Phys.* **2013**, *138*, 184706/1.

[53] S. Enami, H. Mishra, M.R. Hoffmann, A.J. Colussi, J. Chem. Phys. 2012, 136, 154707/1.

[54] S. Enami, Y. Sakamoto, A.J. Colussi, Proc. Natl. Acad. Sci. U.S.A. 2014, 111, 623.

[55] S. Enami, C.D. Vecitis, J. Cheng, M.R. Hoffmann, A.J. Colussi, *J. Phys. Chem. A* **2007**, *111*, 13032.

[56] J.B. Fenn, *J. Am. Soc. Mass Spectr.* **1993**, *4*, 524.

[57] D.C. Taflin, T.L. Ward, E. J. Davis, *Langmuir* **1989**, *5*, 376.

Chapter 4

Heterogeneous photocatalysis

4.1 Photocatalytic activity of TiO_2-WO_3 and Pt-modified TiO_2-WO_3 mixed oxides

ABSTRACT – Aiming at reducing the charge carriers recombination in titania-based photocatalytic materials, TiO_2-WO_3 mixed oxides were synthesized by the sol-gel method described in Section 3.1.1, starting from titanium(IV) isopropoxide (TTIP, $Ti(OCH(CH_3)_2)_4$) and tungsten(VI) hexa-ethoxide ($W(OC_2H_5)_6$), as titanium and tungsten precursors, respectively. The photocatalysts were prepared with different W/Ti molar ratios (0 – 5 mol%) and calcined at two different temperatures (*i.e.*, 500 or 700 °C). All samples were then surface-modified with photodeposition of Pt nanoparticles (for details about the preparation, see Section 3.1.2), with a fixed nominal amount of noble metal (0.5 wt.%). The so-obtained materials were characterized by XRD, BET, UV–vis reflectance, XPS and EPR analyses, while Scanning Transmission Electron Microscopy (STEM) provided atomic resolution images of the samples and ICP analysis revealed their actual Pt loading. The photoactivity was tested under UV-visible irradiation in both a down-hill reaction (*i.e.*, the photo-mineralization

of formic acid in aqueous suspension) and a up-hill reaction (*i.e.*, H_2 production by methanol photo-steam reforming).

For the samples calcined at lower temperature, the introduction of W led to a decrease in the photo-oxidation performances of TiO_2. On the other hand, the beneficial effect in formic acid photo-oxidation displayed by the TiO_2-WO_3 samples calcined at 700 °C, with respect to pristine TiO_2, was mainly ascribed to the persistence of pure anatase phase in W-containing photocatalysts, also after calcination at high temperature.

The Pt-modified photocatalysts, besides mirroring the photocatalytic activity trend displayed by the corresponding unmodified samples, exhibited also thermal catalysis, which may occur in the presence of Pt nanoparticles.

On the contrary, W addition played a beneficial role in H_2 production at both calcination temperatures, suggesting a more pronounced positive effect induced in the reduction ability of the mixed oxides photocatalysts. The optimum W content was fixed at W/Ti = 1 mol.%, with higher amounts possibly inducing the formation of charge carriers recombination centres. Further beneficial effect was also gained by Pt photodeposition on the synthesized photocatalysts surface, due to the e^--sink efficacy typical of noble metals.

The catalytic activity of Pt/TiO_2 and Pt/TiO_2-WO_3 samples calcined at 500 °C was also investigated in the hydrogenation of 4-nitrostyrene. In the presence of W, the selectivity switched from 4-ethylnitrobenzene to 4-aminostyrene with conversion levels close to 100% and with a remarkable increase of the reaction rate. The better performances may be tentatively attributed to the formation of a Brønsted acid sites on the catalysts surface, promoted by WO_3 modification.

Keywords – TiO_2-WO_3 photocatalysts, Pt-photodeposition, formic acid degradation, H_2 production, 4-nitrostyrene selective hydrogenation.

4.1.1 Crystal structure and physical properties

X-ray diffraction patterns reported in Figure 4.1(A) clearly evidenced the role of W addition in modifying the phase composition of the synthesized powders (see also Table 4.1).

Concerning the photocatalysts calcined at 500 °C (*i.e.*, TW*x*_500 series), all the samples were shown to consist of almost pure anatase phase, regardless of their W content, with the main reflections peaking at $2\vartheta \sim 25°$ and $\sim 38°$.

Conversely, pure TiO_2 calcined at higher temperature (TW0_700) mainly consisted of rutile phase, as revealed by the (1 1 0) reflection at $2\vartheta = 27.4°$ in Figure 4.1(A), also containing ca. 10 wt.% of anatase phase (signal at $2\vartheta = 25.5°$). However, as shown by the diffraction patterns, all the W-containing titania photocatalysts of the series calcined at 700 °C were composed of pure anatase (2ϑ

= 25.5°, 37.9°), suggesting that the presence of small amounts of W, in the 1-5 mol% range, completely inhibited the transformation of the anatase into the rutile phase, typically occurring around 600 °C in pure TiO_2 [1].

An increase of the TiO_2 anatase phase thermal stability induced by the addition of tungsten, hindering both the crystal growth and the anatase to rutile phase transition, has recently been reported [1-3].

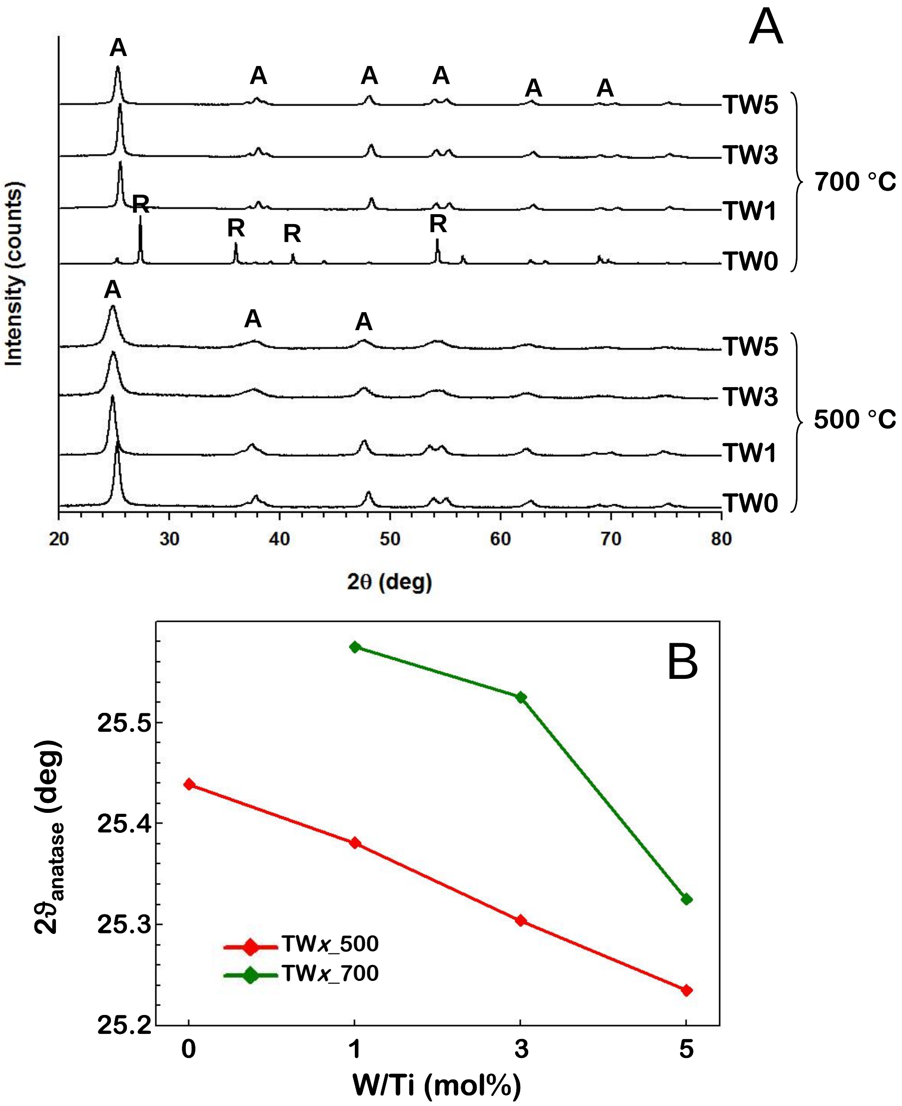

Figure 4.1 – A) XRD patterns of pristine TiO_2 and of all the W-containing samples, calcined at 500 (bottom) or 700 °C (top). A and R indicate the anatase and rutile phase reflections, respectively. B) Dependence of the 2ϑ anatase reflection on the W content in all prepared samples.

Finally, no reflections corresponding to the formation of new phases or pure WO_3 were detected by the XRD analysis. Tungsten oxide may either be amorphous or in concentration below the detection limit of the XRD technique.

As already suggested, W^{6+} can in principle be easily introduced in the titania lattice, substituting Ti^{4+}, due to the compatibility of their ionic radii (ionic radius of W^{6+} = 0.060 nm, that of Ti^{4+} = 0.0605 nm [4,5]).

Indeed, the absence of features attributable to WO_3, in the XRD pattern of mixed oxides, may also imply that tungsten ions could be incorporated into titania lattice substituting titanium ions to form W‒O‒Ti bonds or could be located at interstitial sites.

However, a more accurate analysis of the anatase phase main reflection (*i.e.*, 2ϑ = 25.5°) of the samples calcined at both temperature revealed a slight shift of the peak towards lower 2ϑ-values, with increasing the W amount, as evidenced in Figure 4.1(B) and Table 4.1 (for the TW0_700 sample, the contribution of the anatase phase was too small to confidently assign the 2ϑ-anatase reflection). This observation is in line with the anatase cell expansion occurring with increasing the W content, suggesting that a small fraction of WO_3 may also enter the TiO_2 lattice.

A detailed analysis of the anatase phase cell parameters already revealed that a non-monotonous dependence of the cell parameters on the W percent amount can also be envisaged, probably consequent to some anisotropic distortion of the anatase lattice induced by the different interactions among W cations and/or W cations and O vacancies [1,6].

Since evidence has already been provided that Pt post-synthesis photodeposition does not affect the crystal structure of the modified photocatalysts [7], all the above considerations on the effects induced by tungsten addition are valuable also for all Pt/TW*x_y* prepared samples.

	phase composition (wt.%)	d_A (nm)	$2\vartheta_A$ (deg)	SSA (m^2g^{-1})
TW0_500	100% A	13	25.4390	44.6
TW1_500	100% A	6	25.3809	205.8
TW3_500	100% A	5	25.30340	202.2
TW5_500	100% A	6	25.2352	198.2
TW0_700	10% A + 90% R	39	//	6.7
TW1_700	100% A	24	25.5750	14.8
TW3_700	100% A	20	25.5252	28.7
TW5_700	100% A	15	25.3248	52.9

Table 4.1 – Phase composition (A = anatase, R = rutile), anatase particle dimensions, d_A, obtained from XRD analysis, assuming the absence of amorphous material, anatase phase main reflection, $2\vartheta_A$, and specific surface area, SSA, from BET analysis of the synthesised TiO_2 and TiO_2-WO_3 materials.

The crystallite dimensions of pure TiO_2 and TiO_2-WO_3 samples were calculated from XRD data employing the Scherrer equation and are reported in Table 4.1.

The anatase crystallite dimensions of TiO_2-WO_3 mixed oxides calcined at the lower temperature (*i.e.*, TW*x*_500) were nearly independent of the fraction of WO_3 (d_A = *ca.* 6 nm), with that calculated for the pure TiO_2 sample (TW0_500) being slightly higher (Table 4.1). This phenomenon is in line with the ability attributed to tungsten of inhibiting the anatase crystallite growth [1,8].

On the contrary, the anatase particle size of the samples calcined at 700 °C slightly decreased with increasing the W amount, as reported also in recent literature [9].

Confirming the observation made on the crystallite sizes, BET analysis showed that all W-containing samples calcined at 500 °C exhibited similar specific surface areas (SSA, Table 4.1), only slightly lowering with increasing the W amount, in line with their comparable size. By contrast, pristine TiO_2 (TW0_500) is characterized by markedly smaller surface area, *ca.* 80% lower than TW*x*_500 samples.

The addition of tungsten in the photocatalysts calcined at 700 °C (*i.e.*, TW*x*_700) influenced also their specific surface areas: compared to pure TiO_2 (TW0_700), SSA of all W-containing samples was higher and increased with increasing W/Ti molar ratio, mainly by virtue of the W ability of enhancing the anatase thermal stability, along with the inhibition of the nanoparticles sintering process, typically induced by thermal treatments performed at high temperature.

This led to the conclusion that even a modest W content is beneficial in order to obtain samples with SSA values higher than that of pure TiO_2, regardless of the calcination temperature.

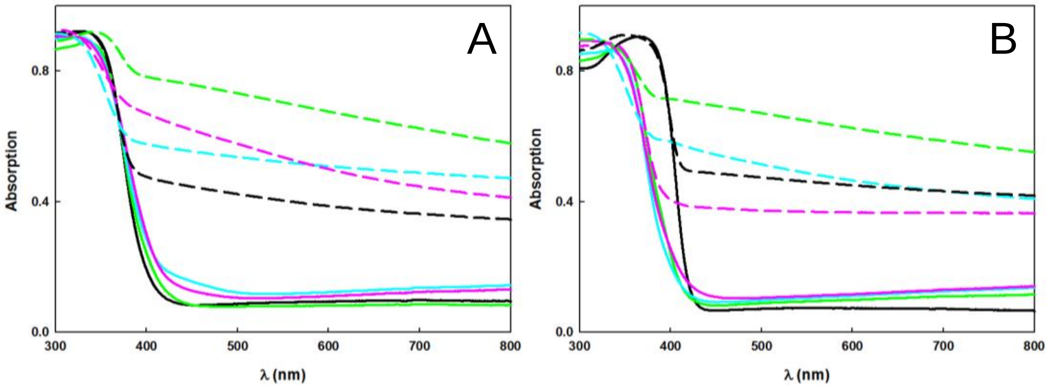

Figure 4.2 – UV-vis absorption spectra of naked (full lines) and Pt-modified (dashed lines) of TW0 (black trace), TW1 (green trace), TW3 (cyan trace) and TW5 (purple trace) calcined at 500 °C (panel A) and 700 °C (panel B).

The absorption spectra of all investigated photocatalysts are reported in Figure 4.2. All powders exhibited an optical absorption onset at ~ 400 nm, owing to TiO_2 band gap excitation, with no effect on the absorption threshold induced by Pt photodeposition. This confirmed that the presence of metal nanoparticles deposited on the photocatalysts surface did not affect their electronic properties [10].

Only TiO_2 calcined at 700 °C and the corresponding noble metal-modified sample (TW0_700 (full black line) and Pt/TW0_700 (dashed black line), respectively in Figure 4.2(B)) exhibited an absorption threshold red-shifted with respect to those of all the other samples, by virtue of their crystal composition being mainly rutile (Table 4.1) [1].

Interestingly, an absorption shoulder centred at *ca.* 450 nm characterized TW3_ and TW5_500 samples (Figure 4.2(A)), which might be attributed to WO_3 aggregates. In addition, all Pt-modified powders showed a broad, almost featureless, optical absorption extended over the entire visible range, *i.e.* $\lambda > 400$ nm, (Figures 4.2(A) and (B)) typical of semiconductor powders modified by noble metal NPs deposition [11].

Though all Pt/TW*x_y* samples were prepared by photodepositing the same amount of platinum (0.5 wt%), their different absorption properties at $\lambda > 400$ nm should be attributed to a non-homogeneous metal deposition (Table 4.2). This result suggested that several factors, such as the increase of surface area (and, consequently, of the number of available surface adsorption sites) with increasing the W amount (Table 4.1) possibly affected Pt deposition, leading to a noble metal loading different form the nominal one. This findings was confirmed by ICP-OES analysis, performed on all metal modified samples, which allowed the determination of the actual Pt contents (Table 4.2).

	Pt (wt%)	
	500 °C	700 °C
Pt/TW0	0.50	0.59
Pt/TW1	0.51	0.50
Pt/TW3	1.29	0.44
Pt/TW5	2.21	0.17

Table 4.2 –Pt amount (Pt (wt%)), reported as weight percentage, of all investigated photocatalysts, as determined by ICP-OES analysis.

Aside presumable experimental errors leading to Pt amounts extremely different from the expected loading (the effect was particularly marked in Pt/TW3_500, Pt/TW5_500 and Pt/TW5_700, Table 4.2), UV-vis absorption spectra revealed interesting features of the prepared samples.

Mainly focusing on Pt/TW0 and Pt/TW1, either calcined at 500 or at 700 °C (Figure 4.2 (A)and (B), respectively), it’s worth noting that the Ti-W mixed oxides exhibited a marked upward absorption shift in the visible range, though their Pt loadings were in line with those of pure titania samples (Table 4.2). This cannot be discussed only in terms of effect induced by surface Pt NPs.

Platinum photodeposition was achieved by pre-irradiating a 6 vol% methanol-water suspension containing the photocatalyst and subsequently adding the metal precursor, always keeping the system under irradiation in the absence of air (see Section 3.1.2). Methanol, and more generally, alcohols are widely used in photocatalysis as hole scavengers due to their e^--donor ability which fills up the holes photoproduced in the semiconductor valence band, making electrons more readily available for reduction processes [11-14].

As such, methanol may have induced the same effect on photoexcited Ti-W samples during the photodeposition procedure (most likely when irradiating in the absence of the metal precursor), thus generating an electron accumulation on W leading to the formation of reduced W^{5+} centres; conversely, when H_2PtCl_6 was introduced in the reaction suspension, a fraction of photopromoted electrons were directly involved in the Pt-photodeposition procedure by reducing the metal precursor, with the residual fraction trapped on W^{5+} sites generating the extended enhancement of visible light absorption.

Indeed, Abe *et al.* [15] reported an analogous upward shift in photoacustic spectra performed on WO_3 under UV irradiation, in the presence of isopropyl alcohol, and attributed this feature to the accumulation of pentavalent tungsten which broadly absorbed in the visible region due to the capture of photoexcited electrons at trapping sites in WO_3, while similarly holes were consumed by isopropanol. Moreover, a comparison between the absorption spectra of stoichiometric WO_3 and of reduced $WO_{2.96}$ highlighted the broad absorption of substoichiometric tungsten oxide due to the oxygen deficiency in the structure of the latter [16,17].

Accordingly, within the W-containing photocatalysts, the best performances in formic acid photodegradation (which implied that photogenerated holes oxidized formic acid, see below) were obtained with the TW1_500 and TW1_700 samples, suggesting the enhanced availability of h^+ in these samples.

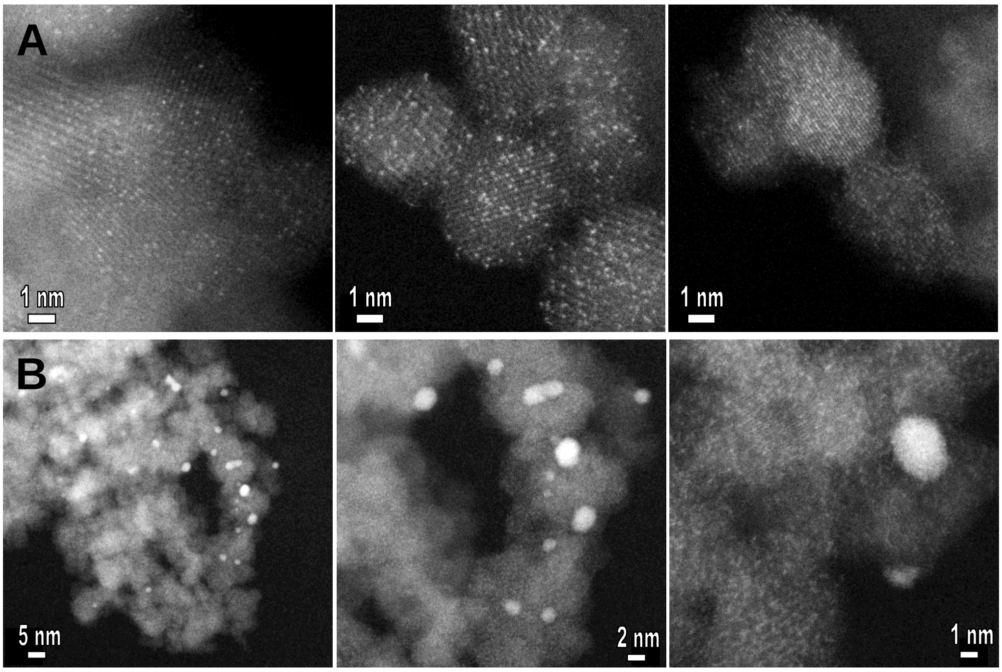

Figure 4.3 – HAADF-STEM images of A) TW1_500, TW3_500 and TW5_500, from left to right. All the images have the same magnification; B) Pt/TW5_500 with increasing magnification from left to right.

W addition and Pt deposition were corroborated by HAADF-STEM analysis (Figure 4.3) yielding direct information also on the size and distribution of the noble metal nanoparticles.

Images of the TW*x* samples (with *x* = 1 – 5 mol%) highlighted the presence of atomically dispersed W into the titania lattice (Figure 4.3(A), clearly visible due to Z-contrast that generated images with the brightest spots for the heaviest elements.

It's worth noting that both oxides were well oriented and it appeared reasonable, through the comparison with previous literature data, that W had diffused into titania nanoparticles [18].

Indeed, the tiny light dots in Figure 4.3(A) represent orderly aligned rows of W atoms, suggesting their incorporation into TiO_2 and, consequently, the successfulness of the adopted synthesis method for the preparation of intimately mixed Ti-W oxides.

Furthermore, the number of W centers raised with increasing the W/Ti nominal molar ratio, with the result of a less spread W dispersion in the TW5_*y* samples (see, as example, TW5_500 in Figure 4.3(A)).

The average diameter of TiO_2 crystallites, derived by STEM microscopy, confirms those independently calculated from XRD data by applying the Scherrer equation (Table 4.1).

Taking into considerations the effect induced by W on the TiO_2 anatase crystal cell (Figure 4.1B and Table 4.1) and the presence of W domains, as highlighted by HAADF-STEM microscopy, it can be suggested that W domains were introduced in the titania lattice, due to the already mentioned similarity of W^{6+} and Ti^{4+} ionic radii [1], though WO_3 aggregation on the TiO_2 surface could not be completely excluded.

Pt deposition effect is displayed in the HAADF-STEM images of Figure 4.3(B), which reports different magnification of the Pt/TW5_500 sample. Platinum clusters of 1.5 – 2 nm size were successfully deposited on the different TiO_2-WO_3 powders and the adopted photodeposition seems to ensure a good dispersion of Pt NPs on the oxide surface.

As clearly visible from the comparison between Figure 4.3(A) and (B) which highlights the poorly defined fringes of the metal modified TiO_2-WO_3 nanoparticles, the deposition of Pt resulted also in the accumulation of carbonaceous residues on the surface of the powders, most likely derived from the organics adopted in the deposition procedure.

Indeed, compared to naked TW*x*, all Pt-modified samples images were characterized by non-sharp profiles usually induced by C-containing species emitted during the analysis, when the electron beam hit the target sample.

With the aim of providing evidence of a potential interaction arising from Pt–W nanoparticles contact, EDX was also performed. The analysis was selectively carried out on the samples with the highest W content, also modified with Pt, *i.e.*, Pt/TW5_500 (Figure 4.4).

Aside from the peaks at ~ 1 and 8 kV assigned to the copper grid used as sample support in the microscope, both W and Pt were detected in same area, opening up to a possible interaction between them, which might affect the (photo)catalytic activity of the powders.

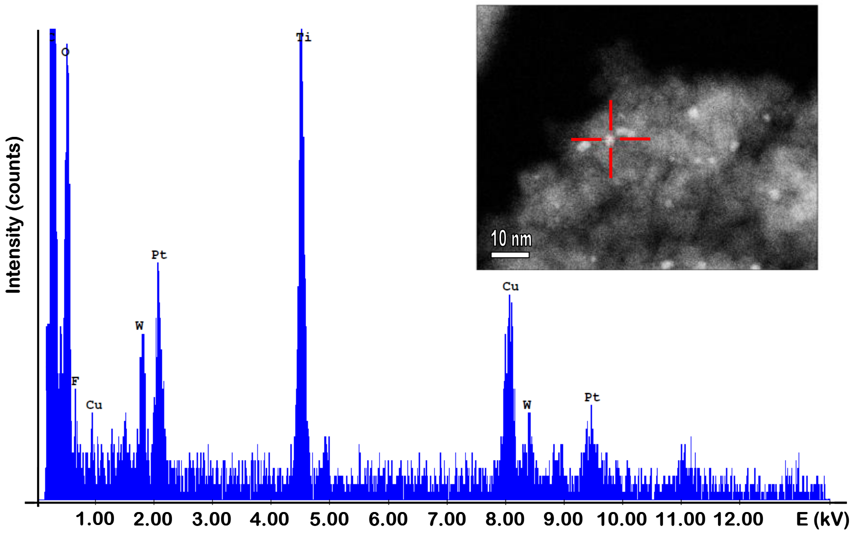

Figure 4.4 – EDX spectrum of Pt/TW5_500. The analysis was performed on the selected spot displayed in the STEM image reported in the inset.

X-ray Photoemission Spectroscopy was performed to elucidate any possible interaction between Ti and W in the samples calcined at 700 °C, due to the proved ability of tungsten of strongly influencing TiO_2 crystalline phase composition (see Figure 4.1(A)). The XPS survey spectra of the investigated samples exhibited the expected signals at binding energies corresponding to titanium, oxygen and tungsten photoemissions, together with a small carbon contribution arising from contaminants [1].

The W/Ti atomic ratios, 0.08, 0.14 and 0.18 for TW1, TW3 and TW5, respectively, though much higher than the nominal molar amounts, confirmed the progressive increase of tungsten amounts with increasing the nominal W/Ti molar ratio. The XPS spectra in the Ti 2*p*1/2 and Ti 2*p*3/2 binding energy region can be compared in Figure 4.5(A). The Ti 2*p* doublet signals showed very similar profiles, with the two components picking at 465.1 eV and 459.5 eV. This points to the formation of titanium dioxide with the correct TiO_2 stoichiometry [19], also in the case of the mixed oxides.

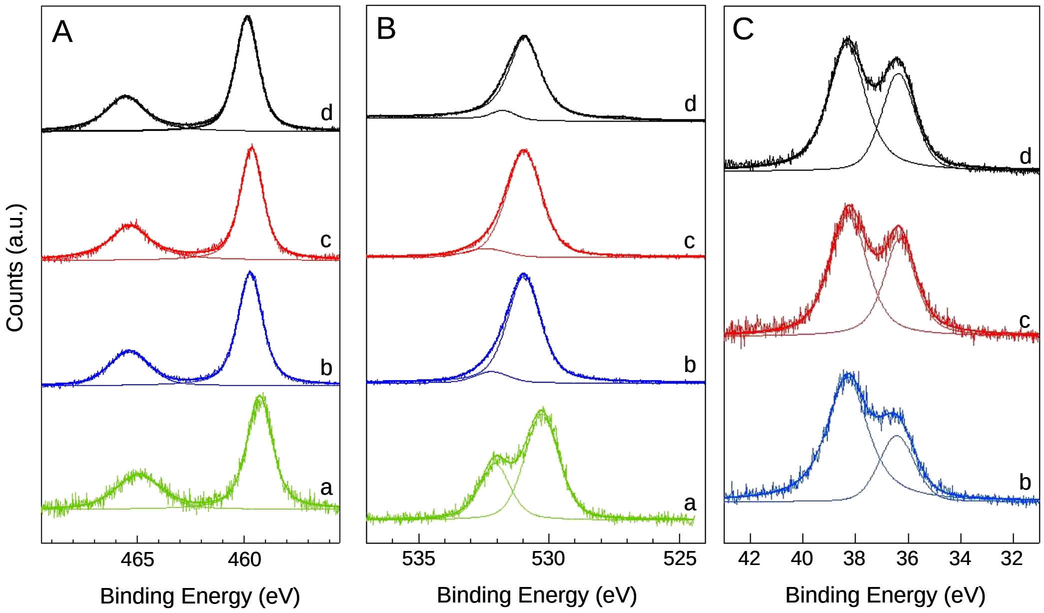

Figure 4.5 – XPS spectra recorded in the (A) Ti 2*p*, (B) O 1*s* and (C) W 4*f* binding energy ranges of the a) TW0_700, b) TW1_700, c) TW3_700 and d) TW5_700 photocatalysts.

The XPS signal of pure TiO_2 in the O 1*s* binding energy region (Figure 4.5(B), trace a) was composed of a main band peaking at 530.6 eV, typical of oxygen bound to Ti, and of a shoulder at higher binding energies, mainly originated from oxygen in surface hydroxyl groups [19]. On the contrary, in the XPS spectra of the Ti-W mixed oxides, the main O 1s band also peaked at 530.6 eV (Figure 4.5B(b-d)), while the contribution arising from hydroxyl groups was strongly reduced, as a consequence of the tungsten-induced reduction of surface hydration. Finally, Figure 4.5C shows the XPS signals collected in the binding energy range between 42 eV and 32 eV. A couple of bands located at 37.7 eV and 36.0 eV can be recognized in the spectra of Ti-W samples (Figure 4.5C(b-d)), corresponding to the W 4*f*5/2 and W 4*f*7/2 signals, respectively [20], while the XPS spectrum of pure TiO_2 calcined at 700 °C is perfectly flat in this region. This is compatible with the formation of small clusters of tungsten oxide in the mixed oxides.

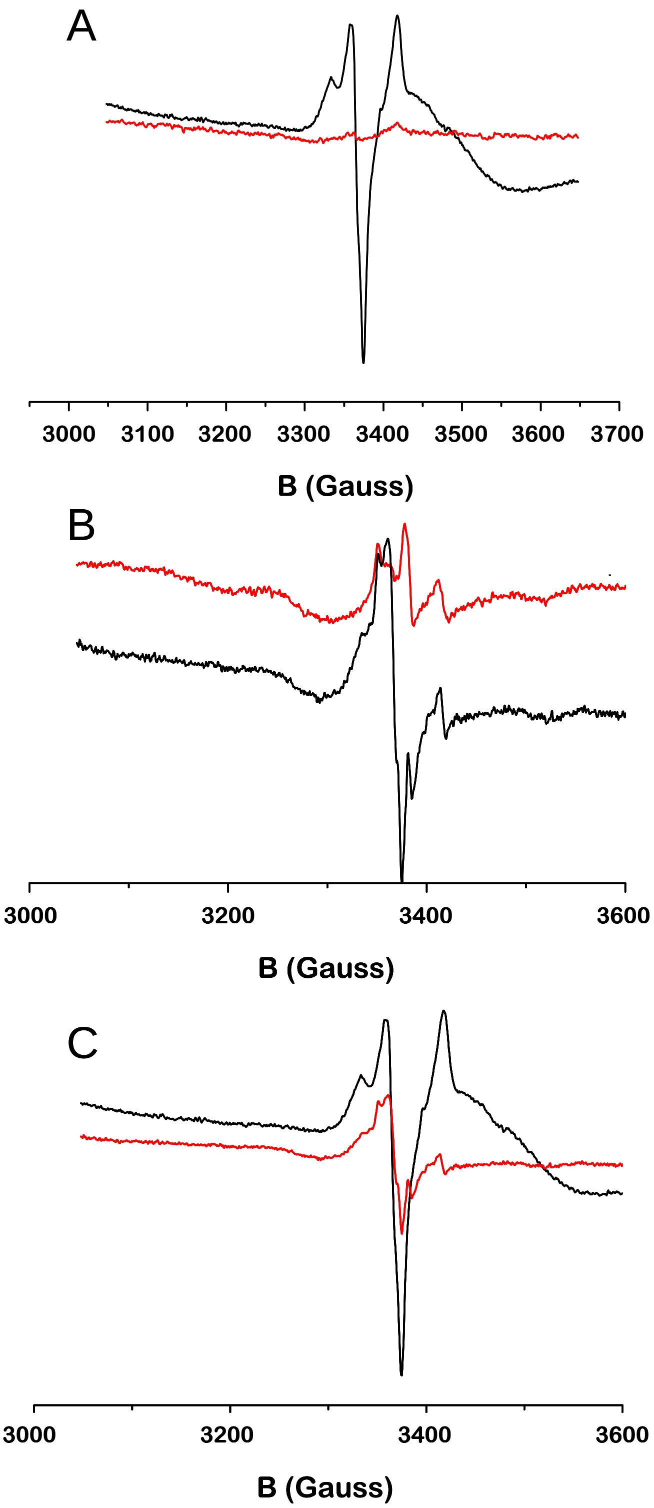

Figure 4.6 – EPR spectra of A) TW0_500, *as it is* (red trace) and under UV irradiation in O_2-atmosphere (black trace); B) TW1_500, *as it is* (red trace) and under UV irradiation in O_2-atmosphere (black trace); C) comparison between the EPR spectra of TW0_500 and TW1_500 (black and red traces, respectively), both under UV irradiation in O_2-atmosphere.

Being the most direct and effective technique for detecting systems bearing unpaired electrons, EPR was used to explore the status of photopromoted electrons, under UV irradiation and in the presence of O_2. The analysis was performed on pristine TiO_2 (TW0_500), while TW1_500 was selected as W-containing sample because of its good photoactivity performance.

Figure 4.6 shows the EPR signal detected with TiO_2 and TiO_2-WO_3 (panels (A) and (B), respectively) and their comparison (panel (C)). The EPR signal of pure TiO_2 corresponded to that of a nearly stoichiometric TiO_2 (Figure 4.6(A)).

Upon UV irradiation, the typical signal corresponding to Ti^{3+} (g = 1.972) was observed; the g-value, lower than 2.00, ensured that the paramagnetic species was not oxygen-based and was most likely associated with Ti^{3+} centres [21]. Furthermore, due to the presence of O_2, a fraction of the photogenerated electrons was captured by O_2 and the superoxide radical anion $O_2^{-\cdot}$ (g = 2.034, 2.003) and the O^- anion (g = 2.027, 2.017) signals appeared.

The background spectrum of TW1_500 (Figure 4.6(B), red trace) showed the presence of traces of nitric oxide (NO) likely trapped in closed cavities of the crystals. Also in the case of the TW1_500 sample (Figure 4.6(B), black trace), upon irradiation with UV light in the presence of O_2, the signals corresponding to the oxygen paramagnetic species (*i.e.*, $O_2^{-\cdot}$ with g = 2.034, 2.003 and O^- with g = 2.027, 2.017) were observed.

Nevertheless, the comparison between TW0_500 and TW1_500 resonance spectra, both recorded under UV irradiation and in O_2-atmosphere (Figure 4.6(C)), highlighted that superoxide and oxygen anion signals generated in the mixed oxide sample were much less intense than in pure titania, and this was paralleled by a less intense formation of Ti^{3+} in the W-containing sample.

Though W^{5+} paramagnetic species could not be detected in the applied experimental conditions and further experiments are needed (*e.g.*, EPR analysis in anaerobic conditions and under UV irradiation), the well-estblished photoelectron transfer mechanism in mixed oxides allows one to discuss present results in terms of photoproduced holes and electrons that can either recombine, be trapped in the bulk or react with species adsorbed on the surface of the semiconductor nanoparticles [22].

In pristine titania, photopromoted electrons can be trapped in TiO_2 in the absence of oxygen, as corroborated by Ti^{3+} paramagnetic signal formation [8,23,24]; however, the effective electron storage ability of the oxide is extensively quenched in the presence of O_2, indicating the essential role of molecular oxygen in scavenging electrons [8,24], as testified by the generation of oxygen reduced species (*e.g.*, O_2^-, H_2O_2, H_2O) with consequent decreased accumulation of electrons in the semiconductor nanoparticles.

In addition, literature reports about EPR experiments performed with irradiated TiO_2-WO_3 samples under anaerobic conditions suggest that the majority of photopromoted electrons are transferred to WO_3, as demonstrated by the largely

reduced intensity of Ti^{3+} signals with respect to those detected with pure titania and, most importantly, by the appearance of an intense feature accounting for W^{5+} centres formation [8].
Accordingly, experimental evidence for the formation of these W^{5+} domains was obtained during H_2 production through photo-steam reforming photocatalytic tests (see Section 3.3.2 for experimental details), performed under UV-vis irradiation and in the absence of O_2. In fact, all synthesized TW*x_y* nanopowders under such conditions assumed the blue colour characteristic of trapped electrons [25]. However, e^--trapping in the form of W^{5+} causes a decreased in reduction power, WO_3 conduction band being slightly lower than that of TiO_2 [1].
Considering that the one e^--reduction potential of O_2 to $O_2^{-\bullet}$

$$O_2 + 1e^- \rightarrow O_2^{-\bullet} \qquad \text{(R4.1)}$$

is $E^0 = -0.28$ V, that of the TiO_2 conduction band is CB(TiO_2) = -0.52 V (both referred to the Standard Hydrogen Electrode at pH = 7, [26]), while that of the conduction band of WO_3 is CB(WO_3) ~ 0 V [27] it seems reasonable to assume that photopromoted electrons trapped in the conduction band of WO_3, rather than reacting with oxygen yielding O-radicals, more favourably recombined with TiO_2 valence band holes accounting for the reduced Ti^{3+} and O-species signals in the performed EPR experiments.

4.1.2 Formic acid photocatalytic oxidation

Formic acid (FA) photocatalytic degradation occurred according to a zero order rate law, *i.e.* FA concentration decreased at constant rate during irradiation (see Figure 4.7), as in previous studies [1,7,28,29].

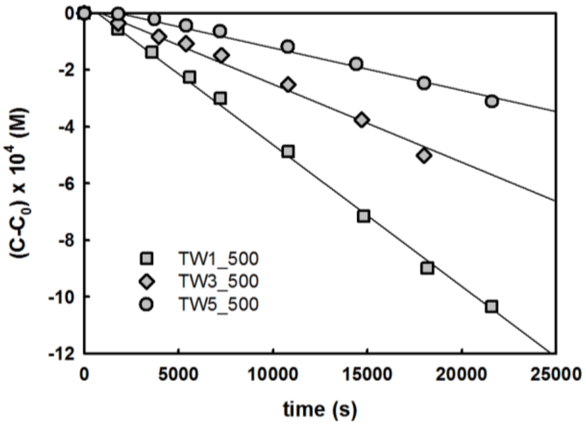

Figure 4.7 – Photocatalytic degradation of formic acid, performed in the presence of different photocatalysts, confirming the zero-order rate law.

Thus, the photocatalytic activity of both pure TiO_2 and TiO_2-WO_3 mixed oxides (either in the absence or in the presence of surface Pt NPs) were compared in terms of zero order rate constants k_{AV}, as in Figures 4.8 and 4.9.

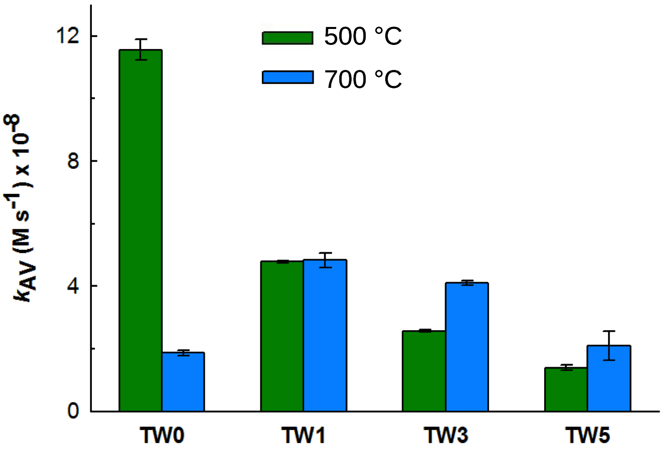

Figure 4.8 – Zero-order rate constants of formic acid degradation, k_{AV}, obtained with the TW*x*_500 (green) and TW*x*_700 (blue) photocatalysts.

Under dark conditions, formic acid was not degraded whereas, under UV-vis irradiation, two different photoactivity trends can be easily recognized for the samples calcined at 500 °C and those at 700 °C. For the TW*x*_500 powders (green series in Figure 4.8), k_{AV} was found to decrease with increasing the W amount and, hence, the best performance was attained with pristine TiO_2 sample (TW0_500). Quite unexpectedly, these photoactivity results couldn't be related to the physico-chemical characteristics of these powders, such as *i*) crystal structures, since XRD revealed the full anatase compositions of all TW*x*_500 samples (Figure 4.1(A) and Table 4.1); *ii*) UV-vis absorption, as all powders exhibited the same light absorption features (Figure 4.2(A)); *iii*) specific surface areas, considering that the addition of W *de facto* widely increased the Ti-W mixed oxides SSA (W-containing samples have SSAs nearly five times higher than that of TW0_500, Table 4.1).

Moreover, it is usually reported that WO_3, being around 15 times more acidic than TiO_2 [30], when mixed with titania ($pH_{PZC}(TiO_2) \sim 6$, [31]) greatly influences the resulting mixed oxide surface acidity, even when the W/Ti ratio is kept relatively low. This fact, of course, largely affects substrate surface adsorption [2,32,33]. For example, Kwon *et al.* reported a steep increase in surface Lewis acidity up to WO_3/TiO_2 = 3 mol% [30], amount of WO_3 that was previously demonstrated to completely cover TiO_2 surface [34].

Nonetheless, preliminary measurements of pH_{PZC}, performed with the TW0_ and TW1_500 samples, revealed pH_{PZC} = 6.4 (accordingly with literature data [2,31,35]) and 5.1 (also confirmed by previous reports [2]), respectively. Apart from the enhanced surface acidity of TW1_500 with respect to pure titania, this finding provided evidence that WO_3 domains partially nucleated on the surface of TiO_2, along with those penetrating its lattice, as evidenced by STEM images (Figure 4.3).

However, since formic acid photodegradation runs were always performed at pH ~ 3.3, part of HCOOH was present in the reaction aqueous suspension as formate anions, which could favourably adsorb on the photocatalyst surface, either on TiO_2 or on W-containing TiO_2, ruling out the possibility that substrate adsorption may somehow account for the reduced photoactivity of the Ti-W mixed oxides calcined at 500 °C.

Interestingly, EPR measurements highlighted that in Ti-W mixed oxide systems irradiated under aerobic conditions, the signals of both Ti^{3+} and O-species were notably decreased with respect to pure TiO_2 (Figure 4.6(C)) suggesting that photopromoted charge carriers in Ti-W mixed oxides are more prone to recombine, with a consequent decrease in formic acid photodegradation. Indeed, it has already been reported that, in parallel with the WO_3 ability of trapping electrons photogenerated on TiO_2 (*i.e.*, $W^{6+} + e^-_{CB(TiO2)} \rightarrow W^{5+}$) which enhances the charge carriers separation, W may act also as a recombination centre for e^-/h^+ pairs, according to $W^{5+} + h^+_{VB(TiO2)} \rightarrow W^{6+}$ [32].

Conversely, for the TW*x*_700 series (blue series of Figure 4.8), FA photodegradation appeared to be enhanced by W addition to TiO_2. The highest photoactivity was achieved with the TW1_700, in line with previous reports indicating an optimum W amount always much lower with respect to Ti [2,36].

Furthermore, the presence of W domains inhibited the anatase-to-rutile phase transition occurring at high calcination temperature [1], ensuring full anatase composition of samples calcined at 700 °C.

Thus, the persistence of the anatase phase, along with the increase in surface area of the Ti-W mixed oxides due to the inhibition of the sintering process (Table 4.1), may positively contribute to the observed photoactivity trend of the W containing samples calcined at 700 °C with respect to pure rutile TW0_700.

Furthermore, among all W containing samples (either calcined at 500 or 700 °C), TW1 always exhibited the best performance in FA oxidation, indicating W/Ti = 1 mol% as the optimum molar ratio for photocatalyst powders prepared under the here adopted conditions.

Larger W/Ti amounts may lead to a higher number of defects trapping sites responsible for increased charge carriers recombination, with consequent decrease of FA photodegradation rate.

Finally, considering samples containing the same nominal amount of W, those calcined at 700 °C always exhibited higher performances with respect to TW*x* calcined at 500 °C. This effect was particularly marked in the case of samples with W/Ti > 1 mol% and can be attributed to the higher crystallinity of the full anatase TW*x*_700 series, by virtue of the thermal treatment performed at higher temperature.

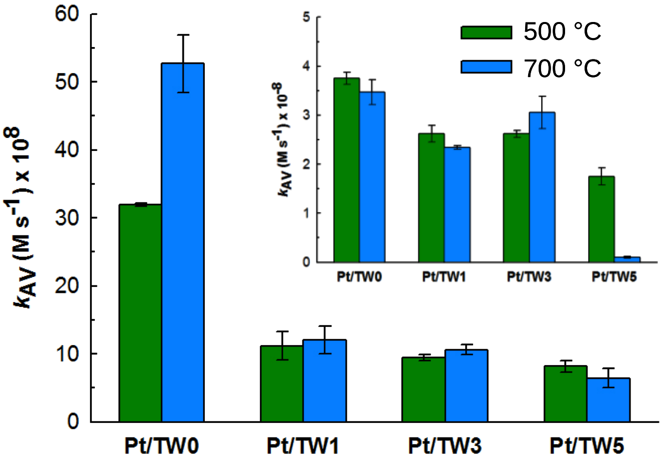

Figure 4.9 – Zero order rate constant of formic acid degradation, k_{AV}, obtained with the Pt/TW*x*_500 (green) and Pt/TW*x*_700 (blue) photocatalysts series containing different percent amounts of W. The inset reports the rate constants of FA degradation occurring under dark conditions in the presence of the same photocatalysts.

Noble metal NPs deposited on the surface of oxide semiconductors have been extensively studied as a route to reduce electron/hole recombination in photocatalysts, thus enhancing their photocatalytic efficiency [37].

TW*x* powders modified by Pt photodeposition confirmed the same photoactivity trend of the corresponding naked samples (Figure 4.9), the most relevant effect being that the rate constants k_{AV} of formic acid photo-oxidation almost doubled with respect to the values obtained with the corresponding naked samples.

In particular, the rate of formic acid photodegradation was confirmed to strictly depend on the W amount for samples calcined at 500 °C. As for the naked photocatalysts series (Figure 4.8), the highest performance was achieved with pure TiO_2 supporting the idea that, under aerobic conditions, W may favour the recombination of the photogenerated charge carriers.

Pt NPs deposited on the surface of the photocatalysts have been demonstrated to enhance the e^-/h^+ separation, by capturing the photopromoted electrons in the titania conduction band. Indeed, due to its high work function value (*i.e.*, the energy of the Fermi level related to the vacuum, see Scheme 4.1) Pt forms a Schottky junction at the interface with the semiconductor resulting in the movement of electrons from the semiconductor CB to the metal [38].

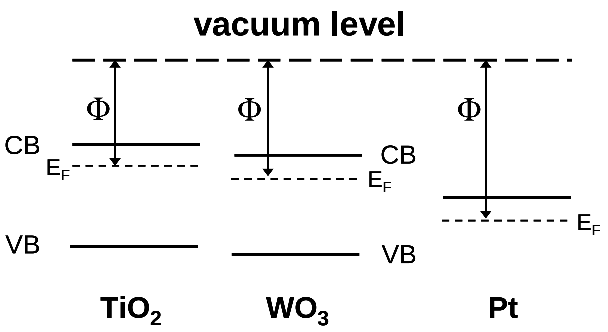

Scheme 4.1 – Work function (Φ) of TiO_2, WO_3 and Pt, relative to the vacuum level. According to literature [39]: Φ(TiO_2) ~ 4.3 eV, Φ(WO_3) ~ 4.6 eV and Φ(Pt) ~ 5.6 eV.

Also within the Pt-modified mixed oxides photocatalyst series calcined at 700 °C the best formic acid photoactivity was attained with pure titania (Pt/TW0_700). Thus, Pt NPs deposited on the TW0_700 surface overcame the low intrinsic photoactivity of the predominant rutile phase in this sample with respect to pure anatase phase TiO_2 (TW0_500 *vs* TW0_700 in Figure 4.9). The exceedingly higher photoactivity of Pt/TW0_700, compared to that of Pt/TW0_500, may also be ascribed to the larger Pt loading on the sample calcined at the highest temperature (Table 4.2).

The lower k_{AV} values obtained with the Pt-modified Ti-W mixed oxides calcined at 700 °C with respect to that obtained with Pt/TW0_700, can again be attributed to WO_3 acting as a recombination centre, under the here investigated conditions. Interestingly, all TiO_2-WO_3 mixed oxides modified with Pt NPs (regardless of their W content and calcination temperature) provided very similar photoactivity results, with the rate constant values comparable within the experimental error (Figure 4.9). The presence of Pt NPs levelled out the photoactivity of the different samples suggesting that this essentially results from the beneficial effect of noble metal NPs which cancels any intrinsic electronic effect due to the presence of W in the mixed oxides.

In the presence of the investigated Pt-modified powders, formic acid concentration decreased also under dark conditions (*i.e.*, in the absence of irradiation), though at much lower rate with respect to irradiation conditions (inset of Figure 4.9). Since comparable results were obtained regardless of the specific photocatalyst considered, any Pt-W interaction, possibly promoting secondary processes, can be excluded.

Previous extensive studies [37,40-42] evidenced that Pt/TiO_2 prepared by photodeposition of $PtCl_6^{2-}$, as well as in single step by flame spray pyrolysis, are able to mineralize organic compounds, such as formic acid, in aqueous suspensions in the absence of irradiation.

It has been suggested that Pt is responsible for formic acid oxidation in the dark, depending on its oxidation state. In particular, the rate of Pt-induced HCOOH degradation over Pt/TiO_2 was found to increase in the order: Pt(0) > Pt(II) > Pt(IV) [40].

He *et al.* [42] highlighted that, since the reduction potential of O_2, $E^0(O_2/H_2O)$, is 1.23 V (*vs* NHE) while that of formic acid, $E^0(CO_2/HCOOH)$, is 0.13 V (*vs* NHE) [43], HCOOH can be readily oxidized by O_2 in the presence of an appropriate catalyst, such as Pt. Indeed, by virtue of the suitable energy matching between its HOMO and the O_2 LUMO, Pt is characterized by high oxidation activity in thermal catalysis.

With the investigated Pt-modified TiO_2-WO_3 mixed oxides, the rate of formic acid dark degradation was ~ 30 – 40% that attained with the same photocatalysts under irradiation, while with Pt/TiO_2 samples the dark reaction occurred at a lower rate (*ca.* 10%) with respect to the photocatalytic oxidation promoted by irradiation on the same catalysts (Figure 4.9).

However, the dark catalytic activity, in terms of rate constants, was not subtracted from the rate constants obtained for the photo-promoted process to have an estimation of the "net" photocatalytic activity. In fact, under irradiation, any system behaves in a completely different manner with respect to dark conditions (*e.g.*, e^-/h^+ pairs are generated, $^\bullet OH$ radicals are produced). This makes a nonsense trying to evaluate how dark reactions, occurring in parallel to photoinduced reactions, affect the overall reaction rate.

4.1.3 H_2 production by methanol photo-steam reforming

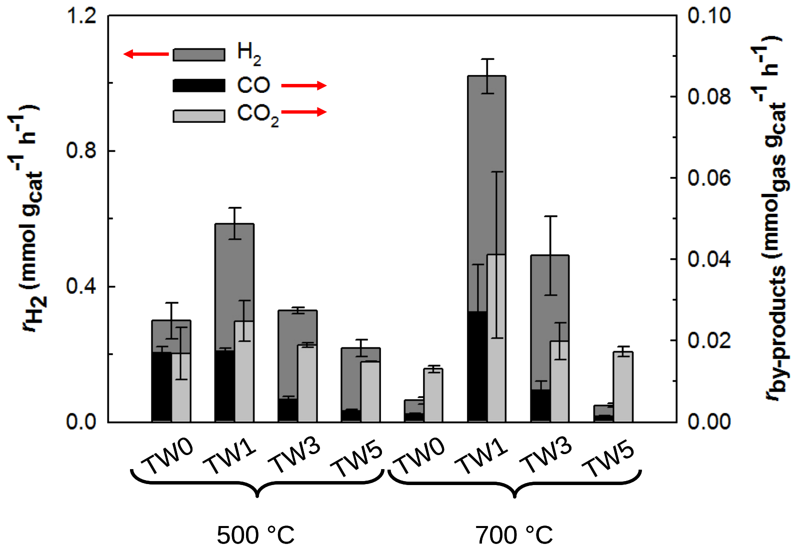

Figure 4.10 – Comparison of the rates of H_2 (r_{H2}, left axis), CO_2 and CO ($r_{by\text{-}products}$, right axis) production obtained with all the investigated TW*x* samples, calcined either at 500 or at 700 °C.

The results of H_2 production by photo-steam reforming obtained with all the TW*x* photocatalysts are reported in Figure 4.10. As in previous studies, the rates of H_2, CO_2, and CO production were evaluated as the slope of the straight lines of the produced amount (normalised per unit catalyst weight) as a function of the irradiation time [11-14].

Concerning the results obtained with samples calcined at 500 °C, H_2 production was found to increase upon TiO_2-WO_3 mixing, with the W-containing samples of the series exhibiting higher photoactivity or, at worst (considering TW5_500), comparable to that of anatase TW0_500 within the experimental error. In addition, similar CO and CO_2 production rates were achieved.

Mirroring the results obtained in FA photo-oxidation (Figure 4.8), the presence of W, also in the TW*x*_700 samples, resulted in enhanced H_2 production with respect to pure titania. The extensively higher surface areas characterizing all W-containing samples may play a remarkable influence, substrate adsorption being a crucial step in any gas-phase catalytic reaction. Furthermore, in the photocatalysts series calcined at 700 °C, the enhanced thermal stability of the anatase phase, induced by the presence of W within the TiO_2 lattice, which ensured its persistence even after calcination at temperatures above 600 °C [1], may be expected to positively affect photoactivity.

Nevertheless, these observations couldn't account, on their own, for the observed H_2 production trend. The reported initial step in the investigated photoreaction is

$$CH_3OH + h\upsilon + TiO_2 \rightarrow H_2CO + H_2 \qquad \text{(R4.2)}$$

with formaldehyde undergoing further oxidation yielding by-products such as HCOOH, CO_2 and CO [11].

Under conditions similar to those adopted here, Endoh *et al.* found that by irradiating WO_3, in the presence of formaldehyde acting as photogenerated holes scavenger, photopromoted electrons remained in the semiconductor lattice and resulted in a morphology change from WO_3 to tungsten bronze [16]:

$$WO_3 + yH^+ + ye^- \rightleftarrows H_yWO_3 \qquad \text{(R4.3)}$$

In the here investigated system, both CH_3OH and HCOH may act as hole scavenger, while protons may be provided by gaseous water recirculating in the set-up throughout the entire irradiation time. The proposed mechanism may be feasible due to the well-known electron storage capability of WO_3 [8,24]; indeed, electrons photopromoted in TiO_2 easily transfer to WO_3 domains embedded within the titania lattice, resulting in the formation of W^{5+} electron-rich sites. Available protons are then expected to intercalate into the Ti-W mixed oxide nanoparticles to balance the negative charge induced by accumulated electrons [8].

Thus, the readily available protons, in close vicinity of W^{5+} domains, could be easily reduced by photopromoted electrons accumulated on tungsten, thus promoting H_2 production under the investigated conditions.

However, not all W-trapped electrons took part to the reaction and, consequently, at the end of the irradiation time (*i.e.*, 6 hours) the TiO_2-WO_3 photocatalysts always assumed a blue colour characteristic of trapped electrons [25].

Moreover, electrons transferred to the CB of WO_3 were still energetically able to reduce H^+ to H_2, being CB(WO_3) ~ 0 V *vs* NHE and $E^0(H^+/H_2) = 0$ V *vs* NHE.

As in formic acid photodegradation (Figure 4.8), also in methanol photo-steam reforming W-containing samples calcined at 700 °C (*i.e.*, TW*x*_700) exhibited superior photoactivity over those calcined at 500 °C (Figure 4.10).

Either it was calcined at 500 or at 700 °C, TW1 proved to be the best photocatalyst (within the TW*x*_500 or the TW*x*_700 series, respectively), possibly on account of its similar anatase lattice cell with respect to that of TiO_2 (Figure 4.1(B)).

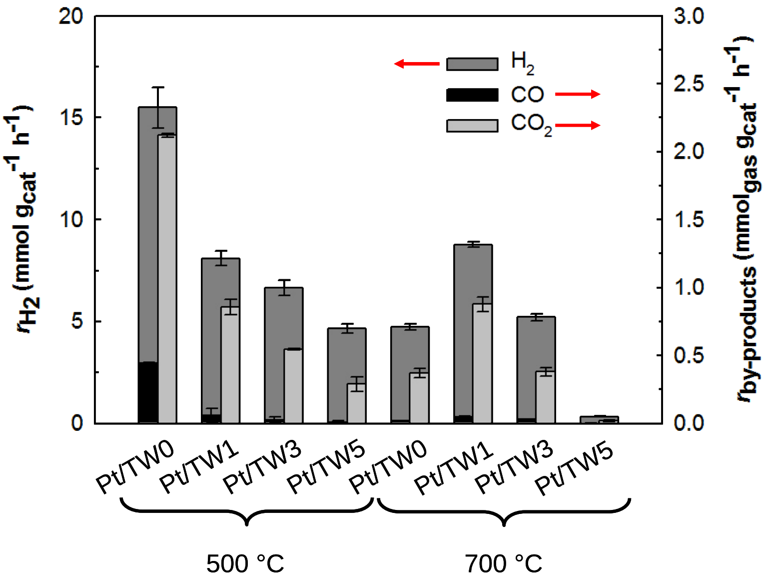

Figure 4.11 – Comparison of the rates of H_2 (r_{H2}, left axis), CO_2 and CO ($r_{by\text{-}products}$, right axis) production obtained with all investigated Pt/TW*x* samples, calcined either at 500 or at 700 °C.

Confirming the photoactivity results already discussed for FA photo-oxidation, Pt photodeposition on the surface of the TW*x* samples led to an at least ten-fold increased H_2 production rate by methanol photo-reforming (Figure 4.11).

The superior photoactivity of Pt/TW0_500 can be attributed to the large Pt work function (see Scheme 4.1) which, by trapping TiO_2 photopromoted electrons more efficiently, guarantees a better charge carriers separation than that achievable upon Ti-W mixing.

Thus, for the Pt-modified samples calcined at 500 °C, the typical mechanism of photocatalytic hydrogen production promoted on TiO_2 seems more likely to occur, with H^+ reduction to H_2 occurring on the noble metal nanoparticles, driven by photopromoted electrons trapped therein.

By contrast, Pt-modified TW*x*_700 samples exhibited a photoactivity trend in line with that obtained with the corresponding naked photocatalysts. Hence, it could be concluded that the enhanced charge carriers separation induced by the presence of W domains in TiO_2 increased in the presence of the noble metal acting as stronger electron acceptor, under the here investigated conditions. Finally, the remarkably low photoactivity of Pt/TW5_700 may be related to the low amount of Pt NPs effectively deposited (see Table 4.2).

4.1.4 Photocatalytic activity in Ti-W mixed oxides

XRD analysis and STEM images (Figures 4.1 and 4.3, respectively) provided evidence that W^{6+} cations were introduced within the lattice of hosting TiO_2. Thus, it seems reasonable that under UV irradiation electrons photopromoted on TiO_2 may be partially transferred into the embedded WO_3 clusters to form W^{5+} [8], also triggered by the lower WO_3 CB with respect to that of titania (*i.e.*, CB (TiO_2) = -0.52 V and CB(WO_3) ~ 0 V, both referred to NHE) [1,26,27].

Consistently with the UV-vis absorption spectra of the investigated photocatalysts, which exhibited comparable absorption onset owing to TiO_2 band gap excitation (Figure 4.2), electron storage at the W^{5+} sites was primarily attributed to TiO_2 absorption, followed by electrons transfer to WO_3 domains, though WO_3 direct excitation may also occur simultaneously under the adopted irradiation conditions [8].

Under irradiation in aerobic conditions, EPR analysis proved that less Ti^{3+} sites and $O_2^{-\bullet}$ paramagnetic species were produced in the Ti-W mixed oxides. This finding suggested that, when O_2 was present in the reaction environment (*e.g.*, during formic acid photo-oxidation reactions), electrons may be trapped at W^{5+} sites slightly losing their reduction power, so that, rather than reacting with O_2 (a well-known electron acceptor, $E^0(O_2/O_2^{-\bullet})$ = -0.28 V *vs* NHE), easily recombined with the photogenerated holes. Consequently, due to the reduced availability of h^+ in the VB of TiO_2, lower formic acid photo-oxidation was achieved with the Ti-W mixed oxides, with respect to pure TiO_2.

Conversely, under anaerobic conditions, the electrons accumulation at W^{5+} sites promoted e^-/h^+ separation, along with the improved contact of H^+ ions with the Ti-W lattice, to counterbalance the negative charge accumulation [8,16,24] and the favorable matching between the CB of WO_3 and the $E^0(H^+/H_2)$. The prompt availability of protons, also possibly located in the close vicinity of reduced W^{5+}, which can undergo reduction by the accumulated electrons, may account for the better performance of TiO_2-WO_3 mixed oxides in the photocatalytic hydrogen production (performed under anaerobic conditions).

Further evidence for the accumulation of photopromoted electrons at W^{5+} sites was provided by the blue color assumed by the tested Ti-W photocatalysts at the end of each photo-steam reforming run, indicative of electrons accumulated [25] and of their incomplete participation in hydrogen production.

When modified with Pt NPs, all TiO_2-WO_3 photocatalysts yielded comparable photoactivities in the degradation of formic acid, regardless of W content and calcination temperature. This finding highlighted that, at least in photo-oxidation reactions, mixing TiO_2 with WO_3 does not lead to improved catalytic performances.

Conversely, the photodeposition of Pt nanoparticles didn't largely modify the photoactivity trend (at least that of powders calcined at 700 °C, *i.e.*, Pt/TW*x*_700) for H_2 production by photo-steam reforming, suggesting that the beneficial effects on promoting the charge carriers separation induced by the presence of W domains within TiO_2 lattice was retained also after surface modification with a stronger electron acceptor (*i.e.*, Pt). More importantly, this further proved the proposed mechanism directly involving W^{5+} sites in the increased proton photoreduction to H_2, with respect to pure TiO_2.

Finally, the observation that, in naked TiO_2-WO_3 mixed oxides, TW1 (either calcined at 500 or 700 °C) was always the best performing photocatalyst, not only suggests that W/Ti = 1 mol.% should be considered the optimum tungsten content, but also implies that lattice cells as similar as possible to that of TiO_2 yielded the best photoactivity results (XRD analysis, indeed, revealed that TW1 samples were characterized by the lessistorted anatase cell, see Figure 4.1(B)).

4.1.5 Selective hydrogenation of 4-nitrostyrene to 4-aminostyrene

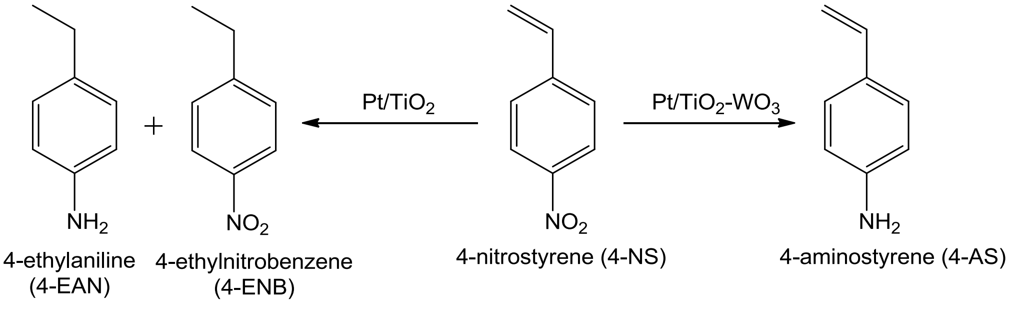

Scheme 4.2 – Products observed during the liquid phase hydrogenation of 4-nitrostyrene (4-NS) at 80 °C under 10 bar of H_2, over Pt/TiO_2 and Pt/TiO_2-WO_3 mixed oxides, all calcined at 500 °C.

Pt/TW*x*_500 samples were also tested in the selective catalytic hydrogenation of 4-nitrostyrene.

Over the Pt/TiO_2 sample (*i.e.*, Pt/TW0_500) the concentration of 4-nitrostyrene (4-NS) was found to exponentially decrease upon time (Figure 4.11), approaching zero within about 60 min. The main product obtained was 4-ethylnitrobenzene (4-ENB), even though after *ca.* 10 min also 4-ethylaniline (4-EAN) was detected, with the rate of the former being always higher than that of the latter.

After longer reaction time, all 4-ENB was completely converted into 4-EAN, the fully hydrogenated product. The carbon balance was always in the 90 – 100% range, thus ensuring that no side reactions occurred to a significant extent. Finally, only negligible quantities of 4-aminostyrene (4-AS) were detected.

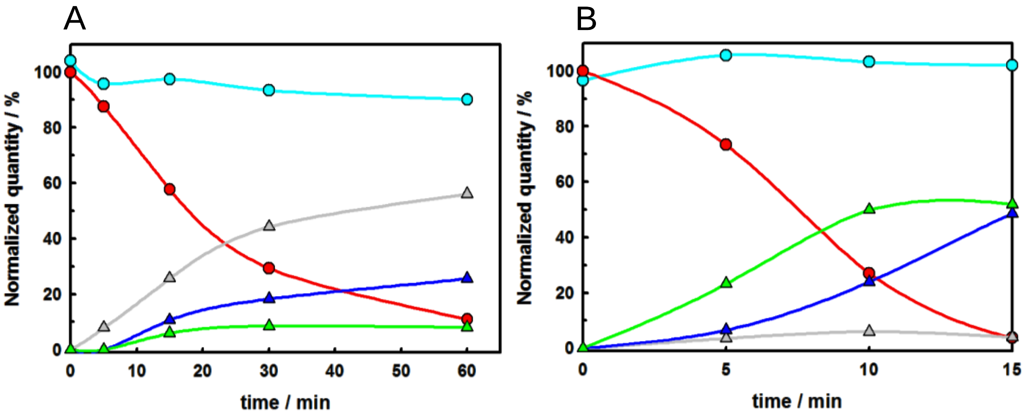

Figure 4.12 – Evolution of *i*) the substrate (4-nitrostyrene (4-NS), red trace); *ii*) the products: 4-ethylnitrobenzene (4-ENB, grey trace), 4-ethylanilina (4-EAN, blue trace) and 4-Aminostyrene (4-AS, green trace); *iii*) C-balance (cyan trace) over time, obtained with (A) Pt/TW0_500, (B) Pt/TW1_500.

By contrast, higher selectivity toward 4-aminostyrene was obtained with all Pt/TiO_2-WO_3 catalysts (Table 4.3), also exhibiting a significant production of 4-ethylaniline, which could compete with the main product formation thus affecting selectivity.

	Selectivity	d[4-AS]/dt [mmol/g s]	-d[4-NS]/dt [mmol/g s]
Pt/TW0_500	11%	0.0016	0.0167
Pt/TW1_500	66%	0.0570	0.0783
Pt/TW3_500	53%	0.0392	0.0697
Pt/TW5_500	45%	0.0272	0.0501

Table 4.3 – Results of 4-nitrostyrene hydrogenation, obtained at 80% conversion, in terms of: *i*) selectivity toward 4-aminostyrene, *ii*) 4-aminostyrene formation (d[4-AS]/dt) rate and *iii*) 4-nitrostyrene conversion rate (-d[4-NS]/dt).

The best performance was achieved with Pt/TW1_500, with a selectivity to 4-aminostyrene as high as ~ 70%, at 80 % of substrate conversion (Table 4.3). the obtained value was nearly six times higher than the selectivity achieved with Pt/TW0_500.

However, W contents higher than 1 mol.% resulted in a slightly suppressed selectivity to 4-aminostyrene. Indeed, 53% and 45% selectivities were attained with Pt/TW3_500 and Pt/TW5_500, respectively (Table 4.3).

Notably, the increased selectivity toward 4-aminostyrene obtained with the tungsten-containing catalysts was consistent not only with an increase in 4-aminostyrene formation rate (*i.e.*, d[4-AS]/dt in Table 4.3), but also with an enhanced overall substrate conversion rate (*i.e.*, -d[4-NS]/dt in Table 4.3).

In particular, by comparing the results obtained with Pt/TW0_500 and Pt/TW1_500, the following values were calculated:

$$\Delta_{(d[4\text{-}AS]/dt)}(\text{Pt/TW1\_500} - \text{Pt/TW0\_500}) = 0.06 \text{ mmol g}^{-1}\text{s}^{-1}$$

$$\Delta_{(-d[4\text{-}NS]/dt)}(\text{ Pt/TW1\_500} - \text{Pt/TW0\_500}) = 0.06 \text{ mmol g}^{-1}\text{s}^{-1}$$

This clearly evidenced that the enhanced rate of 4-aminostyrene production ($\Delta_{(d[4\text{-}AS]/dt)}$) and the increased overall substrate conversion rate ($\Delta_{(-d[4\text{-}NS]/dt)}$) had similar values.

Thus, not only the selectivity toward the $-NO_2$ group reduction was promoted in the presence of W, but also the observed increase in substrate conversion rate (-d[4-NS]/dt) could be mainly ascribed to the increased rate in 4-aminostyrene production (d[4-AS]/dt), as predictable from the large selectivity toward 4-AS.

After longer reaction times, in the presence of Pt-modified TiO_2-WO_3 mixed oxides, 4-aminostyrene was fully converted to the completely hydrogenated 4-ethylaniline, with no phenylhydroxylamine derivatives observed at any reaction time.

Finally, with all tungsten-containing samples, the formation rate of 4-ethylnitrobenzene (*i.e.*, the main product obtained with Pt/TW0_500) was shown to be always much lower than that achieved with Pt/TiO_2 sample and, more interestingly, the full conversion of the initial substrate was complete within the first 15 minutes, *i.e.* in one quarter of the time required when the reaction was carried out on Pt/TW0_500 (Figure 4.12).

The increased selectivity toward –NO_2 group reduction, at the expense of styrene ring reduction, was mainly ascribed to the WO_3 ability of introducing Brønsted acid sites on the surface of TiO_2, where NO_x moieties favorably adsorbed [44].

NO_x selective catalytic reduction (SCR) to NH_3 and N_2 at mild temperature has been extensively investigated, with the main purpose of controlling nitrogen oxides emissions from acid rain and photochemical smog [45].

Typically, V_2O_5-WO_3/TiO_2 based commercial catalysts are employed [46], along with CeO_2-WO_3 mixed oxides, also conveniently poisoned with alkali metal [45] and CeO_2-WO_3/TiO_2 powders surface-modified with SiO_2 [44], by virtue of their surface acidity characterized by the presence of Brønsted acid sites.

Akurati *et al.*, by means of ATR-IR spectroscopy, were able to identify both Lewis and Brønsted acidity on the surface of TiO_2-WO_3 powders synthesized by flame spray pyrolysis; by contrast, surface acidity of TiO_2 was proved to be of Lewis-type only [2]. These authors proposed that Brønsted acidity may rise from the coordinatevely unsaturated W terminal groups, directly in contact with TiO_2.

The here investigated Ti-W mixed oxides were characterized by more acid pH_{PZC} values with respect to that of pristine TiO_2. Though an evaluation of the nature and amount of the surface acid sites of the Pt/TiO_2-WO_3 mixed oxides employed in the catalytic hydrogenation of 4-nitrostyrene was not possible, on the basis of the aforementioned studies, it appeared feasible that the increased selectivity toward 4-aminostyrene obtained with W-containing samples may be a consequence of the presence of Brønsted-type acidity.

Furthermore, recent investigations performed with organic thiol modified Pt/TiO_2 catalysts, under the same conditions as those here reported, pointed to the superior performances of the S-modified samples [47] in the selective reduction of 4-nitrostyrene. Consistently, previous independent studies detected extensive Brønsted acidity on sulphated TiO_2 [48], corroborating the hypothesis of a strong substrate adsorption-surface acidity relation accounting for the observed activity results.

4.1.6 Conclusion

The sol–gel synthesis of mixed TiO_2-WO_3 photocatalysts led to materials with an intimate contact between the two oxides, regardless of the calcination temperature, with W domains embedded within the titania lattice.

Despite the negative effect induced by W addition in the TW*x*_500 series, the better performance in the photodegradation of formic acid of the TW*x*_700 oxides, with respect to the photoactivity of pure titania TW0_700, could be ascribed to the W-induced effect of enhancing TiO_2 anatase phase thermal stability, together with a decrease in anatase particles size, also paralleled by an increase in the specific surface area of the photocatalysts.

The Pt-modified photocatalysts (Pt/TW*x*_*y*), besides mirroring the photocatalytic activity trend displayed by the corresponding TW*x*_*y* samples, exhibited also thermal catalysis effects, which may occur in the presence of Pt NPs.

On the contrary, W addition proved to play a beneficial role in H_2 production through methanol photo-steam reforming, suggesting a more pronounced positive effect induced in the reduction ability of the mixed oxides photocatalysts, as a direct consequence of the increased charge carriers separation due to the accumulation of photopromoted electrons on W^{5+} sites. The optimum W content was fixed at W/Ti = 1 mol.%, with higher amounts inducing the formation of charge carriers recombination centres.

Further beneficial effect was gained by Pt NPs photodeposition on the synthesized photocatalysts surface, due to the e^--sink role displayed by noble metals.

Finally, the selective hydrogenation of 4-nitrostyrene to 4-aminostyrene achieved with Pt/TiO_2-WO_3 catalysts was ascribed to the formation of Brønsted acid sites on samples surface, induced by the modification with tungsten, where the $–NO_2$ moiety of the substrate could be favourably adsorbed.

4.2 Effect of the electronic structure of TiO_2 on the plasmon photoactivity of Au nanoparticles

ABSTRACT – Though plasmon-driven photocatalysis represents a promising route to promote photocatalytic reactions and harvest visible light energy, the actual mechanisms involved are still under debate, trying to distinguish between the so-called *Hot Electron Transfer* and *Plasmon Resonance Energy Transfer* mechanisms.

With the aim of elucidating the basic processes, also presuming a strong influence of the metal oxide used as support for gold nanoparticles (*i.e.*, with the hypothesis that Strong Metal-Support Interaction (SMSI) occurs) along with the amount of metal deposed on the semiconductors surface, Au NPs were deposited on three different TiO_2 samples, each characterized by its own electronic structure: *i*) stoichiometric TiO_2 (w-TiO_2), with a nearly non-defective band-structure; *ii*) nitrogen-doped TiO_2 (N-TiO_2), with intra band-gap states lying close to the semiconductor valence band (VB) and *iii*) reduced TiO_2 (b-TiO_2) with oxygen-vacancies (V_Os) states located close to the CB.

The synthesis of the selected metal oxides is reported in Sections 3.1.1 and 3.1.2; correspondingly, the Au nanoparticles surface deposition technique is described in Section 3.1.2.

The so-obtained materials were fully characterized by XRD, UV-vis optical absorption, HR-TEM, X-ray Absorption Spectroscopy and Resonant Photoemission Spectroscopy (RESPES), whereas the plasmon-induced photocatalytic activity was tested in the photodegradation of formic acid, achieved under monochromatic irradiation (λ = 532 nm) thus ensuring the selective excitation of Au nanoparticles surface plasmons.

At low metal loadings, the hot electron transfer mechanism accounted for the photodegradation activity and the best results were achieved with the stoichiometric w-TiO_2 support. Conversely, at higher metal loadings, Plasmon Resonance Energy Transfer promoted the photocatalytic activity, leading to the superior performance of the defective supports (namely, N-doped and oxygen vacancies-rich b-TiO_2). Photoactivity results pointed to both gold loadings and titania electronic properties strongly influencing the formic acid photo-oxidation performances.

Finite-Difference Time-Domain (FDTD) simulations were also performed, which confirmed the proposed relationship between photoactivity results and photocatalysts physical properties.

Keywords – Gold nanoparticles, TiO_2, visible light, localized surface plasmon resonance, formic acid photodegradation.

4.2.1 Crystal structure and physical properties

Figure 4.13 reports the X-ray diffractograms of all three different TiO_2 supports with particular attention devoted to N-TiO_2, since w-TiO_2 and b-TiO_2 crystal structures were already extensively discussed in [49].

TiO_2 produced in an oxygen-rich regime (*i.e.*, w-TiO_2) was confirmed to be composed of 100% anatase (A); indeed, under O-rich conditions, the temperature of the anatase thermal stability exceeds 700 °C, retarding the rutile (R) phase formation [50].

Conversely, upon the reduction conditions applied (for synthesis details, see Section 3.1.2 and ref [49]), the temperature for the anatase-to-rutile transition dropped to 500 °C, accounting for the formation of a mixed anatase/rutile titania (81 wt.% A and 19 wt.% R, Table 4.4).

It has already been pointed out that thermal treatments performed under reducing conditions create defects in the titania crystal structure, known as oxygen vacancies (V_Os), due to the interaction between TiO_2 (*i.e.*, the host matrix) and hot H_2 molecules [50].

Finally, doping with nitrogen resulted in the formation of only small amounts of rutile (2 wt.%), as clearly evidenced in the inset of Figure 4.13(b).

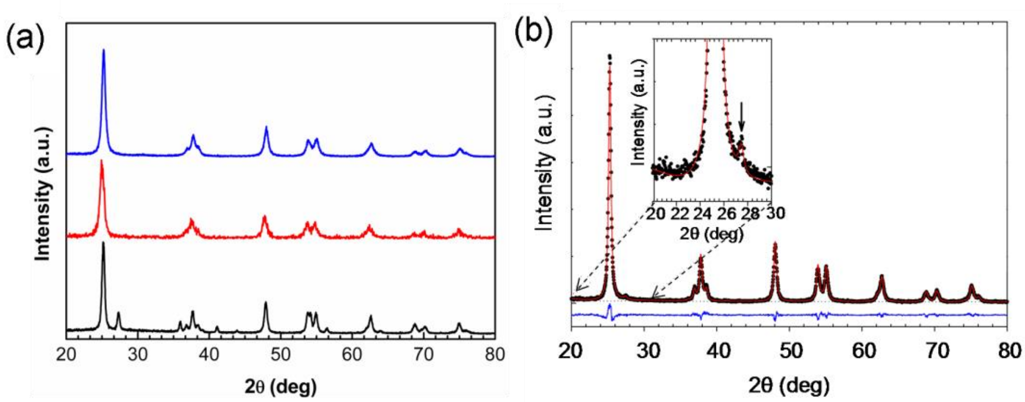

Figure 4.13 – (a) XRD patterns of w-TiO_2 (blue), N-TiO_2 (red) and b-TiO_2 (black). (b) N-TiO_2 XRD pattern acquired for longer time; the inset zooms on the 2θ region where the rutile contribution (highlighted by the black arrow) is clearly visible.

	phase composition (wt.%)	d_A (nm)
w-TiO_2	100 A	16
N-TiO_2	98 A + 2 R	22
b-TiO_2	81 A + 19 R	23

Table 4.4 – Phase composition (A = anatase, R = rutile) and anatase particles dimensions, d_A, obtained from XRD analysis, assuming the absence of amorphous material.

All TiO_2 samples were highly crystalline, with average particles size of 16 nm (w-TiO_2), 22 nm (N-TiO_2) and 23 nm (b-TiO_2) for the anatase phase (Table 4.4).

Concerning UV-vis absorption properties, Figure 4.14(a) evidences that w-TiO_2 perfectly mirrored the behaviour of pure anatase with the absorption onset at *ca.* 380 nm and no light absorption at longer wavelength; the enhanced absorption at $\lambda \sim 400$ nm of N-doped TiO_2 (curve (b)) confirms the formation of intra band-gap states related to titania bulk modification by nitrogen doping [51].

According to [49], a broad absorption starting at ~ 400 nm and extending to longer wavelengths characterized the b-TiO_2 support (curve (c)), due to the presence of oxygen vacancies and, hence, ensuring its black coloration.

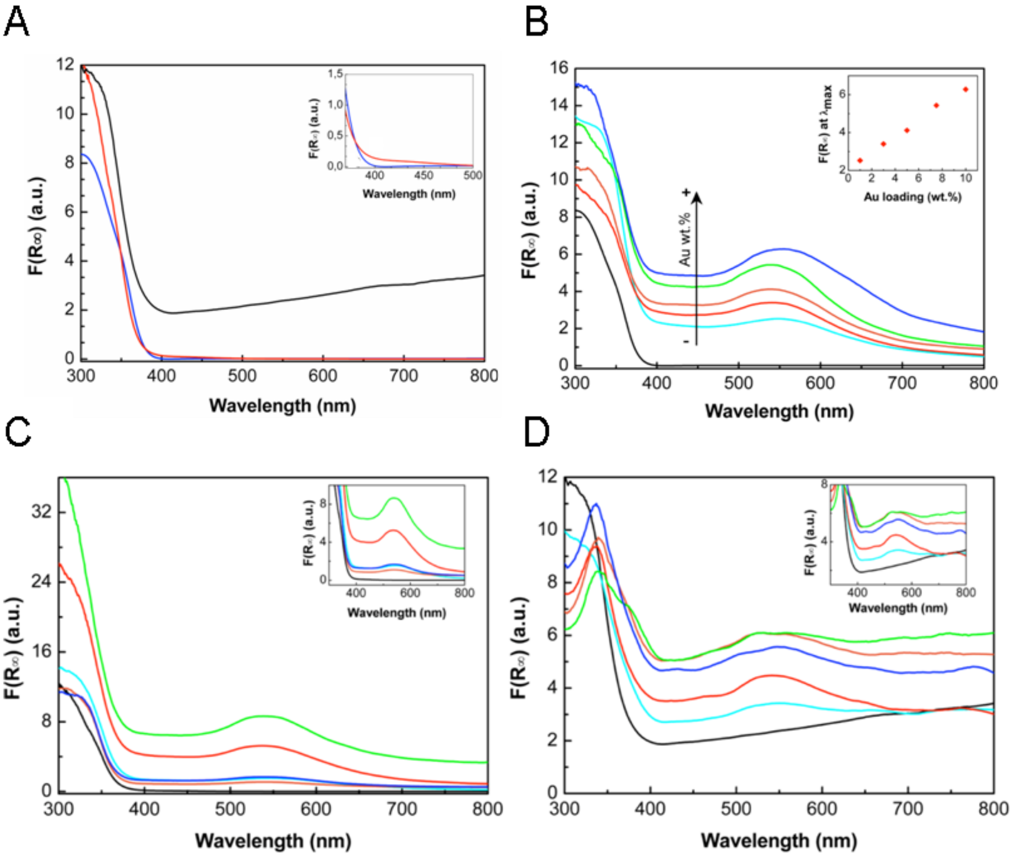

Figure 4.14 – UV-vis absorption spectra of (A) w-TiO_2 (blue trace), N-TiO_2 (red trace) and b-TiO_2 (black trace). The inset displays the spectral region of extended absorption due to nitrogen doping; (B) *x*%Au/w-TiO_2 samples. The inset of highlights the linear increase of the plasmon band absorption as a function of metal loading; (C) *x*%Au/N-TiO_2 samples; (D) *x*%Au/b-TiO_2 samples. The insets of (C) and (D) highlight the absorption peaks due to the plasmon resonance of Au NPs deposited on N-TiO_2 and b-TiO_2 supports, respectively. In b – d, 0%Au (black trace), 1%Au (cyan trace), 3%Au (red trace), 5%Au (orange trace), 7.5%Au (green trace) and 10%Au (blue trace).

In addition to the colour change of the powders, from white and yellowish to purple for w-TiO_2 and N-TiO_2, respectively, and from black to dark purple for b-TiO_2, also the extended absorption centred at *ca.* 530 nm (Figure 4.14(B-D)) confirmed the deposition of gold nanoparticles in Au^0 metallic form. Indeed, all Au-modified powders showed the typical absorption band due to the resonant excitation of localized surface plasmons (LSPR) [52], slightly red-shifted if compared to Au^0 NPs suspended in water, exhibiting λ_{LSPR} ~ 520 nm.

This shift is usually attributed to the interaction between gold and titanium dioxide [53]. Along with the peak broadening, such shift was particularly marked in b-TiO_2 samples, probably due to their relatively high rutile phase content.

Concerning the *x*%Au/w-TiO_2 series, the intensity of the LSPR band linearly increased with increasing the gold loading (inset of Figure 4.14(B)) and, as predicted by the trend of metal nanoparticles dimensions (see Table 4.5), the curve broadened with decreasing gold loading. Indeed, as reviewed in [53], plasmon band width is expected to increase with decreasing Au nanoparticles size in the intrinsic regime (*i.e.*, mean diameter smaller than 25 nm). The effect of the variation in nanoparticle dimensions was also reflected in the shift toward longer absorption wavelengths of the plasmon peak, with increasing d_{Au}.

Unlike the w-TiO_2 series, N- and b-TiO_2 samples didn't exhibit an increased absorption trend as a function of the Au loading (Figures 4.14(C) and (D)), though ICP analysis confirmed an effective increase in gold content with increasing nominal Au amount (Table 4.5).

	w-TiO_2		N-TiO_2		b-TiO_2	
Au (wt.%)	ICP (wt.%)	d_{Au} (nm)	ICP (wt.%)	d_{Au} (nm)	ICP (wt.%)	d_{Au} (nm)
1	0.70	3.6	0.76	3.2	0.83	4.6
3	2.31	4.3	2.69	5.2	2.89	4.9
5	4.00	4.4	4.44	4.8	4.48	4.2
7.5	6.24	5.3	6.92	5.7	8.66	5.3
10	8.90	5.9	8.69	4.7	9.32	4.9

Table 4.5 – Effective gold content, ICP(wt.%), with respect to the nominal amount, Au (wt.%), of all investigated photocatalysts, as determined through ICP-OES analysis; Au nanoparticles mean diameter, d_{Au}, obtained from high-resolution TEM analysis.

Synchrotron X-ray Absorption Spectroscopy data were collected at the BACH beamline of the Elettra synchrotron in Trieste (Italy), within a cooperation with Dr. M. Malvestuto. XAS experiments were carried out setting the monochromator resolution to 0.05 eV at the Ti $L_{2,3}$ edge photon energy, while RESPES data have been collected by scanning the photon energy from 456 to 470 eV with energy steps of 0.20 eV. These techniques were adopted to investigate the effect of both phase composition and introduction of defects (N and V_O doping) on the partial Density of States (DOS) of the conduction band in the three TiO_2 samples (Figure 4.15).

The line shape of the titanium $L_{2,3}$-edge was determined by the dipole $2p$-$3d$ transition. Spin-orbit splitting of the $2p$ orbitals into $2p_{3/2}$ (L_3) and $2p_{1/2}$ (L_2), along with crystal field splitting of the $3d$ orbitals into e_g and t_{2g}, exhibited four different absorption peaks for the Ti L-edge of TiO_2 (*i.e.*,L_3-t_{2g}, L_3-e_g, L_2-t_{2g} and

L_2-e_g). The L_3-e_g states were further split due to the tetragonal distortion from perfect octahedral symmetry, which is reported to occur for both anatase and rutile phases [54]; hence, accordingly, it was recorded for all the three investigated supports.

However, the intensity ratio of the split peaks was opposite for the two crystal structures; indeed, the TiO_2 spectra presented in Figure 4.15 were all characterized by the lower-energy e_g peak being more intense than the higher energy peak, consistently with previous reports of anatase L-edge spectra [55-56]. If this result was predictable for w-TiO_2 and N-TiO_2, due to their 100% and 98% anatase compositions, respectively (Figure 4.13 and Table 4.4), for b-TiO_2, unexpectedly, the 19% rutile present in the sample was found to have no influence on the XAS line shape, remarking the predominant anatase contribution also in this mixed phase sample.

The line shape and the position of e_g orbitals ($d_{x^2-y^2}$ and d_{z^2}) were strongly affected by the local symmetry of Ti cations since they formed σ-type bonds with O 2*p* orbitals and this translated into broadened signals. Conversely, the spectral features of the t_{2g} orbitals (d_{xy}, d_{xz}, and d_{yz}) were sharper due to the weaker interaction of π-type bonds with O 2*p* orbitals [19].

By comparing the results obtained with doped and stoichiometric TiO_2, Braun *et al.* [57] observed additional features in the Ti L-edge spectra, which increased with increasing N content in N-doped anatase nanopowders. This new feature was assigned to the contribution arising from the substantial quantity of V_Os introduced with N-doping during nanoparticle synthesis.

In the here investigated samples, Ti 2*p* XAS of w-TiO_2, N-TiO_2 and b-TiO_2 showed similar spectral features along the whole energy range. This suggested that both N atoms (in the N-TiO_2 sample) and V_Os (in the b-TiO_2 sample) have very small influence on the TiO_2 structure [19].

Interestingly, one small difference was recognized: the energy splitting for the Ti t_{2g}–e_g center at the L_2 edge was slightly larger in b-TiO_2 (2.0 eV) than in w-TiO_2 and N-TiO_2 (1.9 eV). This observation may be attributed to possible crystal field changes induced by the incorporation of *ca.* 5% of V_Os in b-TiO_2, as indicated in previous literature reports [58].

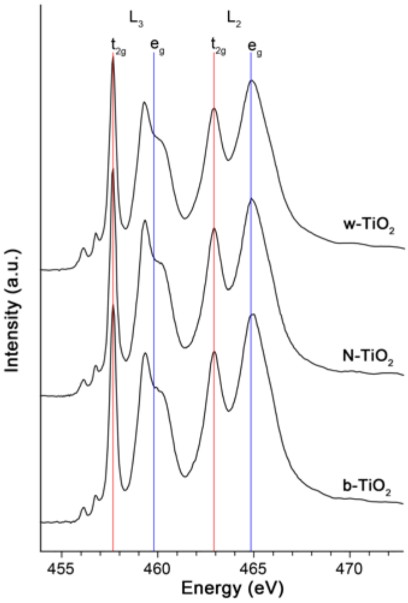

Figure 4.15 – Synchrotron X-ray absorption spectra at Ti $L_{2,3}$ edge of w-TiO_2, N-TiO_2 and b-TiO_2.

Resonant Photoemission Spectroscopy (RESPES) allowed a more detailed investigation of the effect induced by N-doping on the electronic structure of TiO_2.

The introduction of nitrogen in the titania lattice often induces the generation of V_Os, ensuring charge neutralization in the final N-TiO_{2-x} solid. Indeed, as recently reviewed, in the case of nitrogen substitutional doping, the presence of oxygen vacancies plays a beneficial role in the energy cost reduction to incorporate the dopant element in the titania lattice or, alternatively, lattice doping with non-metal elements reduces the energy required to form vacancies [59]. Since N-TiO_2 was characterized by a nitrogen content as low as 0.1 wt.% (as predicted from the weak light absorption shoulder at $\lambda \sim 400$ nm, Figure 4.14(A)), likewise a small concentration of V_Os was expected. Usually, for a very low concentration of V_Os, the spectroscopy feature of the electronic states are rather elusive; hence, ResPES techniques were applied to better highlight their existence and to determine the related electronic states binding energies.

In the performed experiments, the VB photoemission spectra were collected by changing the photon energy across the Ti $L_{2,3}$ absorption edge. In particular, 70 VB photoemission spectra were recorded in order to allow for a fine tracking of both energies and intensities of the resonating features and to emphasize titanium-related electronic states in the valence band, as well as in gap, that would be otherwise missed by an off-resonance tuning of the photon energy [55,56].

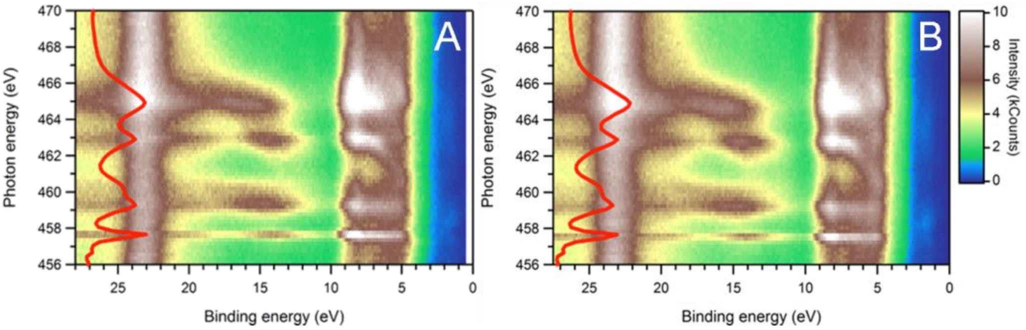

Figure 4.16 – Contour plot of the ResPES data, along with the Ti *2p–3d* X-ray absorption spectra (red traces referred to left axes) of: (A) w-TiO_2; (B) N-TiO_2.

Figures 4.16(A) and (B) report the contour plots of the ResPES data, along with the Ti *2p–3d* XAS spectra (left axes), of w-TiO_2 and N-TiO_2, respectively. In order to emphasize the difference between the VB electronic structure of N-doped and that of stoichiometric TiO_2, as well as intra gap states, that would be otherwise missed by an off-resonance tuning of the photon energy, spectra were collected under resonance conditions with photon energies across the Ti $L_{2,3}$-edge ($h\nu$ = 458.4 eV). For experimental details, please refer to references [55,56].

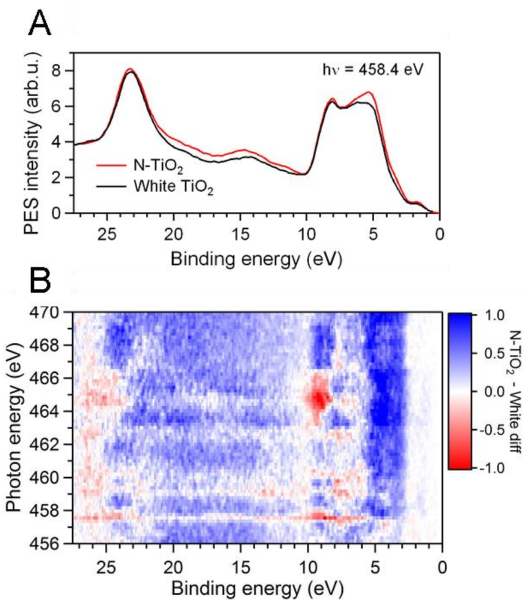

Figure 4.17 – (A) Photoemission spectra collected under resonance conditions (Ti $L_{2,3}$-edge, hν = 458.4 eV) of undoped w-TiO_2 (black trace) and N-doped (red trace) titania, in the valence band region. (B) Difference image between RESPES data of N-TiO_2 and w-TiO_2 highlighting the increased DOS in the valence band region due to N doping. The intensity of the enlargement relative to the 1-2 eV region was enhanced by a factor of 10 if compared to the total RESPES.

Band A, assigned to the O 2*s* shallow core level, peaked at BE = 23.3 eV for both N-TiO_2 and w-TiO_2. Peak B intensity appeared constant for low photon energies, but it shifted to higher values as the photon energy increased above 458 eV, as clearly highlighted in the contour plots of Figure 4.16, where the intensity related to peak B (BE = 15 eV) appeared increasingly more intense. Therefore peak B exhibited the so-called resonant Raman-Auger to normal Auger transition and, above $h\nu$ = 458 eV, peak C ended up as the normal LVV Auger [56].

Interestingly, peak B in N-TiO_2 spectrum presented an energy shift of 0.6 eV with respect to w-TiO_2 (Figure 4.17(A)), attributed to the presence of V_Os in the sample VB.

The BE range 0 – 10 eV represented the occupied DOS in the VB region (Figure 4.17(A)). Theoretical and experimental investigations have already shown that the TiO_2 VB is dominated by the oxygen 2*p* band, with a contribution given by Ti 3*d* projected DOS in the VB [56]. The TiO_2 VB showed the two typical features labelled C and C' (BE ~ 8.1 and 5.8 eV, respectively); the former was assigned to the Ti-O bonding part of the VB, while peak C', at lower BE, usually referred to the non-bonding part of the VB [55,60]. In particular, comparing the VB of w-TiO_2 (black trace, Figure 4.17(A)) and N-TiO_2 (red trace, Figure 4.17(A)) it was evidenced that the N-doped sample displayed a higher DOS with respect to the undoped sample for BE corresponding to peak C and, more markedly, to peak C'. In addition, N-doping produced a VB extension toward the Fermi energy (small shoulder contribution at ~ 3.5 eV in the red trace), which resulted in the typical band gap narrowing, usually observed in similar TiO_2 samples [56].

At low BE (*i.e.*, in 1 eV < BE < 2 eV range), peak D appeared only under resonance condition at $h\nu$ = 458.4 eV and was ascribed to oxygen states, yielding Ti^{3+} ions in the crystalline lattice.

In order to highlight the V_Os content, the difference image between RESPES data of N-TiO_2 and w-TiO_2 was calculated (Figure 4.17(B)). It remarked the increased DOS in the VB region due to N doping, while the enlargement relative to the 1–2 eV binding energy region showed that N-TiO_2 contained a higher concentration of V_Os.

TEM images of the Au modified N-doped TiO_2 samples are reported in Figure 4.18(a-e). The metal nanoparticles appeared uniformly deposited on the surface of the oxide and their density increased with increasing the Au nominal amount. This observation is in line with a nearly constant particle dimension confirmed by the determination of the NPs size distribution (Figure 4.19(c) and Table 4.5), which as previously discussed, also affected the optical properties of the materials (Figure 4.14(C)).

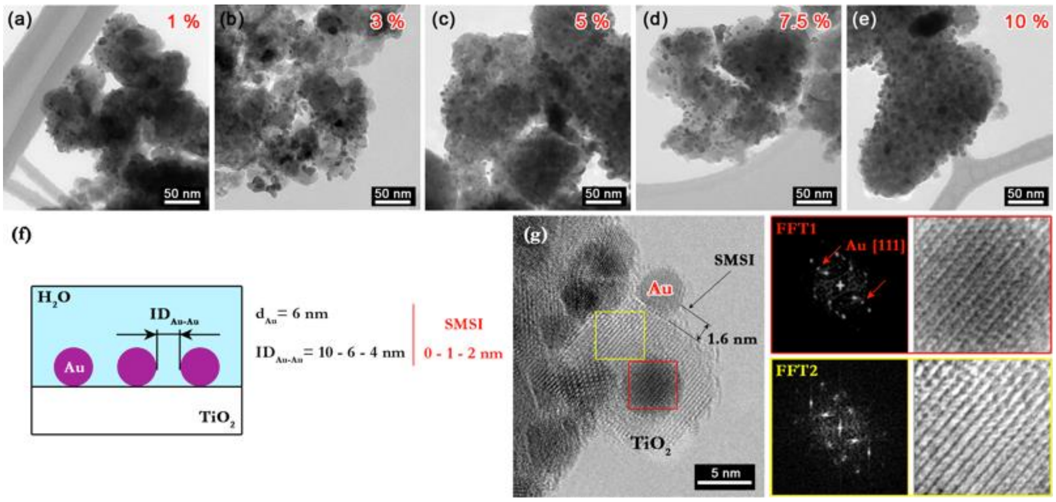

Figure 4.18 – (a-e) TEM images of Au/N-TiO_2 samples with Au loading in the 1 – 10 wt.% range. (f) Schematic models applied in the FDTD simulations for the determination of the electric field enhancement due to the selective excitation of Au plasmons. The panel reports also the parameters used in the simulation: fixed Au NPs dimension, d_{Au} = 6 nm, and different Au interparticles distance ($ID_{Au\text{-}Au}$ = 4, 6, 10 nm), along with different degrees of Au NPs embedding into the TiO_2 supports (SMSI = 0, 1, 2 nm). (g) HR-TEM of 10%Au/N-TiO_2 showing the SMSI effect. The coloured squares refer to the region where Fast Fourier Transform (FFT) and relative structural reconstruction were obtained.

In the w-TiO_2 series the NPs dimensions were found to be strictly related to the amount of Au deposited on the oxide surface, *i.e.* the mean diameter of metal nanoparticles increased with increasing the loaded amount (Figure 4.19(a) and Table 4.5), while, similarly to the N-doped samples, Au nanoparticles deposited on the b-TiO_2 series appeared to have a nearly uniform size distribution throughout the metal loading regime (Figure 4.19(b) and Table 4.5), as reflected by the increasing of the nanoparticles density.

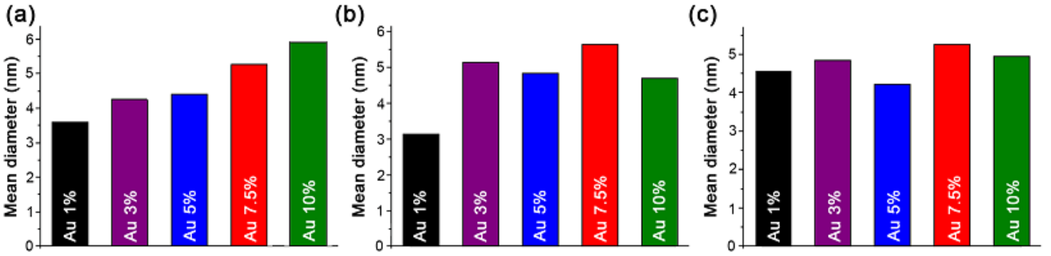

Figure 4.19 – Mean diameter obtained from TEM images analysis of gold nanoparticles deposited on (a) w-TiO_2, (b) b-TiO_2, (c) N-TiO_2 at different Au wt.% loading.

In addition, the size distribution of gold nanoparticles could be divided into two regimes: *i*) 1 – 12 nm region, where the metal NPs are narrowly distributed, at a certain extent, around their mean diameter (Figure 4.20(a,c,e)); *ii*) 12 – 18 nm regime, more likely suggesting the formation of gold nanoparticles clusters on the oxide surface (Figure 4.20(b,d,f)).

As clearly represented in Figure 4.18(g), a partial embedding of the metal nanoparticles by the oxide support also occurred (the detail of the 5wt.%Au/w-TiO_2 sample is here reported), accounting for the so-called Strong Metal-Semiconductor Interaction (SMSI), which influenced both the electric field formed at the Au-TiO_2 interface and promoted by the selective excitation of the metal plasmons (see below) and, hence, the plasmon-induced photoactivity (Figure 4.22(B)).

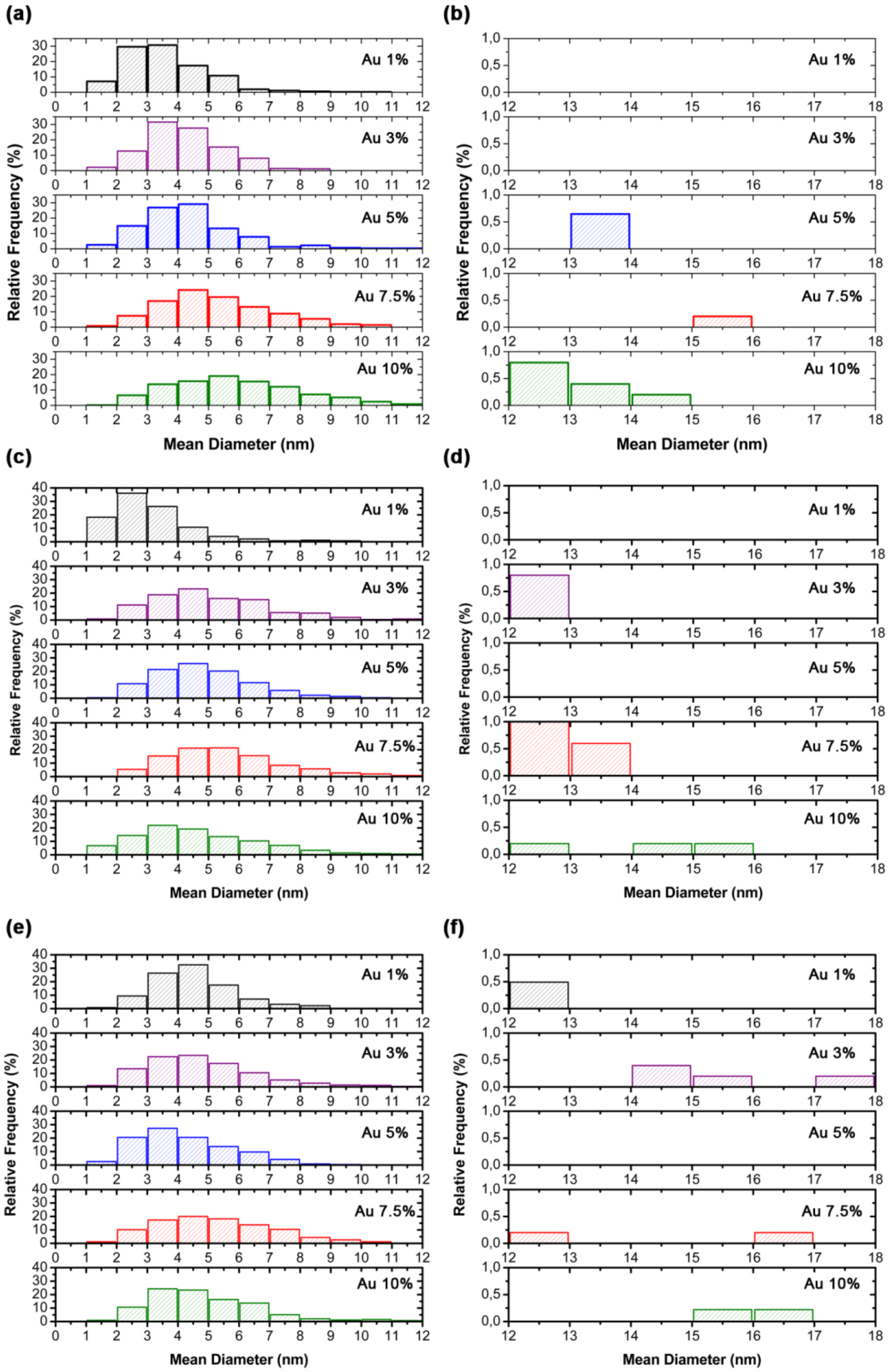

Figure 4.20 – Size distribution obtained from TEM images analysis of gold nanoparticles deposited on (a,b) w-TiO_2, (c,d) b-TiO_2, (e,f) N-TiO_2. The size distribution was divided into two size distribution regimes: (a,c,e) represent the 1-12 nm region, while (b,d,f) show the 12-18 nm region for all considered samples.

4.2.2 Plasmon-promoted photocatalytic activity

All naked titania samples exhibited no photoactivity toward formic acid oxidation, under LED irradiation at λ = 532 nm (Figure 4.21(A)).

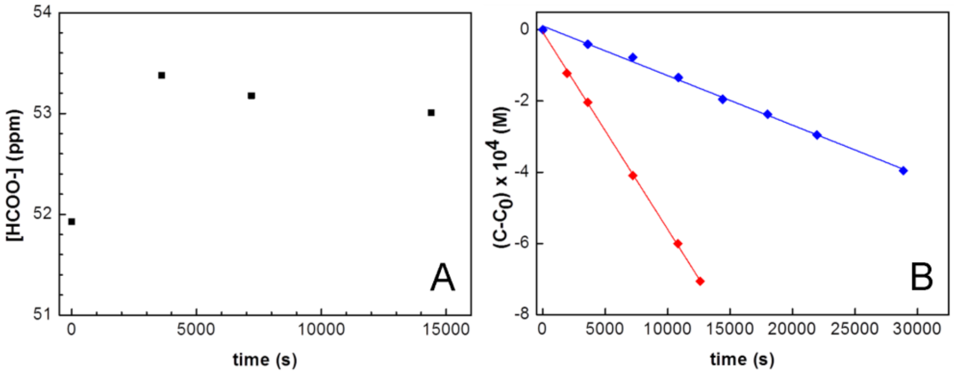

Figure 4.21 – Photocatalytic runs of FA degradation in the presence of: (A) naked N-TiO_2, indicating no activity in the absence of Au NPs; (B) 5%Au/w-TiO_2 either without (blue trace) or under LED irradiation (red trace).

With all the Au-modified titania supports, formic acid photocatalytic degradation occurred according to a zero order rate law, *i.e.* FA concentration linearly decreased during irradiation (Figure 4.22(A)) [1]. Thus, the photocatalytic activities of the tested samples were compared in terms of the zero order rate constants, *k* (Figure 4.22(B)).

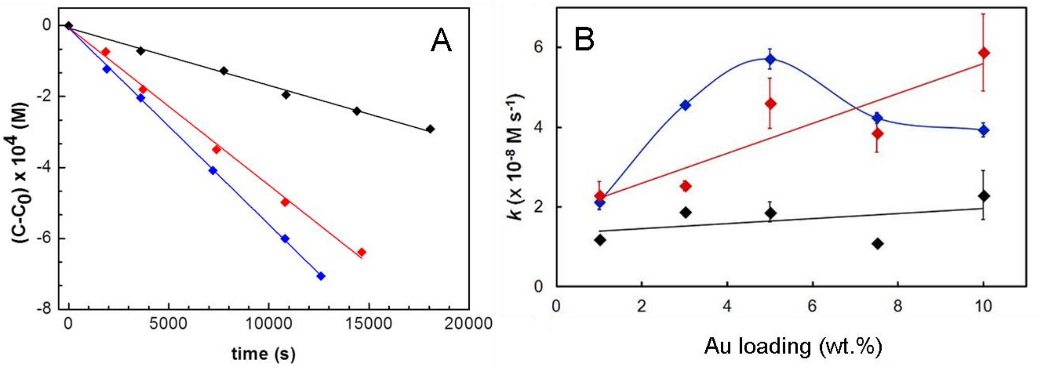

Figure 4.22 – (A) Photocatalytic kinetic run of FA degradation in the presence of the three investigated TiO_2 supports modified with 5 wt.% of Au NPs. (B) Zero order rate constants (*k*) for the photodegradation of formic acid obtained with the three TiO_2 samples (w-TiO_2 (blue diamond), N-TiO_2 (red diamond), b-TiO_2 (black diamond)), as a function of the nominal loading of Au NPs (Au/TiO_2 = 1 – 10 wt.%).

At a glance, depending on the gold loading amount, two different photoactivity trends could be identified: from 1 up to 5 wt.% Au and from 5 to 10 wt.% Au

(Figure 4.22(B)). In the former range, the photocatalytic activity increased in line with increasing the metal loading and the w-TiO_2 photocatalysts series was the most active. Differently, at higher gold content, *k* decreased for the w-TiO_2 metal-modified samples (blue trace), with the profile assuming the volcano-shaped trend typical of (photo)catalytic reactions with increasing the amount of noble metal NPs co-catalyst, while the photoactivity of the two defective TiO_2 structures (*i.e.*, N- and b-TiO_2, red and black traces, respectively) was found to slightly decrease (7.5 wt.% Au/N- and b-TiO_2) and then increased again reaching the highest value for the 10 wt.%Au/N-TiO_2 sample.

These results suggested a plasmon-promoted photoactivity, triggered by one of the possible mechanisms, *i.e.* heating effect, hot-e^- transfer or Plasmon Resonance Energy Transfer (PRET). However, also the concomitant occurrence of two of them cannot be excluded.

The contribution of any thermal effects could be excluded since, as recently reviewed, the temperature increase is typically small (~ 1–10 K) for plasmonic nanocrystals in suspension and irradiated with moderate light fluxes [61]. In fact, the temperature increase, due to plasmonic heat generation, occurring at the surface of a spherical nanoparticle (NP) at a constant rate is given by [61,62]:

$$\Delta T = q_{NP}/(4\pi k_0 R_{NP}) \qquad (4.1)$$

where q_{NP} is the heat generation rate, k_0 represents the thermal conductivity of the matrix surrounding the nanoparticle and R_{NP} is the nanoparticle radius. q_{NP} can be estimated from the absorption cross section of Au NPs (σ_{Abs}) multiplied by the power of the incident irradiation (I_0), assuming that the I_0 absorbed by the nanoparticles is fully converted into heat. Typically, σ_{Abs} for 5 nm Au NPs suspended in water are in the 10–10^2 nm^2 range [63].

Under the here investigated conditions, the incident irradiation intensity amounted at 6 W/cm^2, which gave a maximum absorbed power of *ca.* 10^{-12} W per Au NP. This value provided and, considering that $k_0(TiO_2)$ = 5–12 W/m^2, maximum ΔT of 6.4 μK can be estimated. This temperature increase is not sufficient to induce a relevant heating of TiO_2; therefore, the observed results couldn't be ascribed to samples heating.

This estimation is in agreement with the results proposed by Govorov *et al.* [61], who investigated 10 nm-Au NPs as potential heaters: sizeable temperature variations were obtained only when the incident I_0 exceeded 10^3 W/cm^2, at least three order of magnitude higher than that used in the here reported experiments.

Regardless of the plasmonic mechanism which promoted FA photodegradation, the excitation of Au NPs surface plasmon usually results in the accumulation of excited electrons on the TiO_2 conduction band, either through direct injection (*i.e.*, when hot electrons transfer from Au LSPR to TiO_2 CB), or through energy transfer, which resonates with the band-gap of the semiconductor. Conduction band electrons can then be consumed by O_2 reduction (electron acceptor), naturally dissolved in the reaction suspension, generating $O_2^{-\bullet}$, possibly able to oxidize formic acid [64].

In addition, it has also been proposed that hot e^- transfer implies the accumulation of positive charges on Au nanoparticles which, under aerobic conditions, might oxidize a substrate (electron donor), while e^- reduce O_2 on the semiconductor surface so that oxidation and reduction reactions take place simultaneously, as in conventional photocatalysts activated by UV light [65].

Participation of molecular oxygen as electron acceptor and of TiO_2 as electrons conductor had been verified by performing formic acid plasmonic photodegradation under anaerobic conditions *i.e.*, by bubbling N_2 (150 ml min^{-1}) during the 15-minute dark adsorption of the substrate on the catalyst surface and throughout the kinetic run. 5 wt.%Au/w-TiO_2 was selected as photocatalyst in these tests, due to its performance in the hot-e^- transfer regime (Figure 4.23).

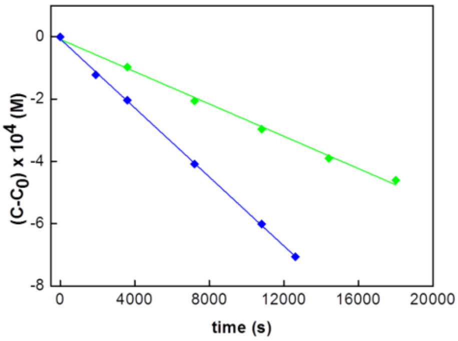

Figure 4.23 – Photodegradation of FA performed with 5%Au/w-TiO_2 under LED irradiation and under aerobic conditions (blue trace) or under LED irradiation in a suspension saturated with N_2 (green trace).

Under such conditions, formic acid photodegradation was retarded due to the lack of an electron acceptor species. Since the reaction was not performed in a sealed reactor, complete removal of O_2 from the reaction environment could not be achieved; thus, the residual activity was reasonably ascribed to the presence of molecular oxygen still dissolved in the suspension. This finding confidently confirmed the proposed mechanism for plasmon-promoted hot electrons transfer in w-TiO_2. Therefore, under aerobic conditions and in the 1 – 5 wt.% Au regime, the hot electrons transfer from excited Au NPs to the CB of TiO_2 mainly accounted for photoactivity, with w-TiO_2 samples being the most active due to the suitable conduction band potential position and the absence of defect states (see Figures 4.17).

It is generally accepted that the Schottky barrier formed at Au/TiO_2(anatase) interface is approximately 0.9 eV and that hot electrons generated through gold plasmon excitation may raise up to ~ 1 eV above the metal E_F, so that a significant fraction of them could be directly injected into the semiconductor CB [66,67] and thus initiating the photocatalytic reaction on the semiconductor surface.

On the contrary, with N- and b-TiO_2 samples this mechanism was less likely to be at work, so that lower photoactivity performances were obtained. Indeed, both supports were characterized by high concentration of electron-rich defect states (oxygen vacancies, V_Os), either introduced along with nitrogen-doping to keep the lattice charge balance (N-TiO_2 samples) [68] or by thermal reduction (b-TiO_2 samples) [49].

The presence of V_Os yielded intra-band gap donor states located *ca.* 0.8 – 1.2 eV below the CB, which could even overlap the conduction band in the case of highly defective structures and cause the shift of the Fermi level (E_F) of TiO_2 toward higher energy [69], paralleled by the simultaneous increase of the Schottky barrier formed at Au/defective TiO_2 interface, which suppressed the probability for hot electrons generated through Au LSPR to be injected into the semiconductor CB.

In addition, the amorphous and disordered shell of the b-TiO_2 support [49], retained also after Au NPs deposition, acted as a barrier for hot electrons transfer. Hence, charge carrier mobility was reduced accounting for the lowest efficiency of Au-modified b-TiO_2 samples in the considered metal regime.

Differently, at higher Au loadings (5-10 wt.%), the plasmon resonance energy transfer (PRET) process reasonably promoted the photoactivity in the presence of highly defective structures (*i.e.*, N- and b-TiO_2) [70-72].

Due to the reduced band gap energies, arisen from defect states formation, the energy provided by the relaxation of the localized surface plasmon dipole was sufficient to promote electrons from the VB to the defect states, then participating in substrate photo-oxidation [71,72].

Also the volcano-shaped trend displayed by the w-TiO_2 series, in contrast with a photoactivity increase of both N- and b-TiO_2 samples, suggested that two different plasmon-induced mechanisms were involved. However, the photoactivity trend of Au/w-TiO_2 samples could also be considered to better elucidate the contribution of the hot e^- transfer mechanisms in doped N- and b-TiO_2 supports. Indeed, the decrease of k, for Au amounts higher than 5 wt.% deposited on the stoichiometric support, suggested that metal overloading and the consequent increased light scattering were detrimental for plasmon resonance excitation and hot electrons injection, with PRET being excluded in w-TiO_2 due to the relatively high energy required to generate h^+/e^- couples in nearly non-defective TiO_2. Thus, it could be reasonably assumed that also in Au modified N- and b-TiO_2 the possible contribution to photoactivity due to hot e- injection decreased with increasing Au NPs loading.

On the contrary, the increased photoactivity in line with the increase of metal amount deposited on N- and b-TiO_2 samples validated the proposed PRET mechanism for Au loading > 5 wt.%; simultaneously, also Au NPs density increased on the two supports, by virtue of both their nearly homogeneous dimension, regardless of the metal loading, and of the consequent reduced NPs-NPs inter-distance at increasingly higher Au amounts (see Figure 4.18(a-e)).

This may create a feasible coupling of the plasmon-generated electromagnetic field, able to provide sufficient energy for charge carriers excitation on the supports.

Nevertheless, a contribution also from the Local Electromagnetic Field enhancement (LEMF) could not be completely excluded. This latter mainly consists in the increased rate of the semiconductor inter band transitions, rather than the direct carrier creation [72], and is particularly favourable at high metal loadings due to the resonance of multiple adjacent Au NPs.

To better estimate the dependence of the plasmon induced electromagnetic field on the NPs-NPs inter-distance, Finite-Difference Time-Domain simulations were performed by modelling Au NPs with fixed diameter ($d = 6$ nm) and progressively decreasing their distances.

4.2.3 Finite-Difference Time-Domain (FDTD) simulations

The Au-TiO_2 system, in powder form, cannot be envisaged as consisting of isolated titania nanoparticles, each modified by one single gold nanoparticle. It should be rather described as micrometer-sized clusters of TiO_2 ($d \sim 100 - 200$ nm), on which surface gold nanoparticles aggregates were deposited (as previously shown by TEM images; see Figure 4.18). On the basis of this picture, Finite-Difference Time-Domain (FDTD) simulations were performed, in order to study the effect of selective excitation of Au plasmons on the electric field generated at the interface of Au/TiO_2, along with that induced at the Au/H_2O interface. The simulations have been performed by Dr. G. Ulisse, within a cooperation with Prof. A Di Carlo research group (University of Rome, Tor Vergata).

Since, at the early stage, only the distribution of the electric field produced through plasmon excitation was the purpose of the performed simulations, the possible effects induced by the different titania supports were not taken into account. Hence, “TiO_2” below reported could be considered as a good model for any of the three TiO_2 supports so far mentioned.

The spatial distribution of the electric field, induced by the surface plasmon resonance in the simulated structures, is reported in Figure 4.24. By taking into account the results obtained from the TEM analysis (Figure 4.18(g)), two different models were considered: *i*) the case in which gold nanoparticles were deposited right above the TiO_2 surface, with the interface being a *single* point (*i.e.*, SMSI = 0 nm, first row of Figure 4.24); *ii*) that in which metal nanoparticles were partly embedded within the titania supports, for a depth ranging from 1 up to 2 nm (*i.e.*, SMSI = 1 nm and 2 nm, second and third rows of Figure 4.24, respectively).

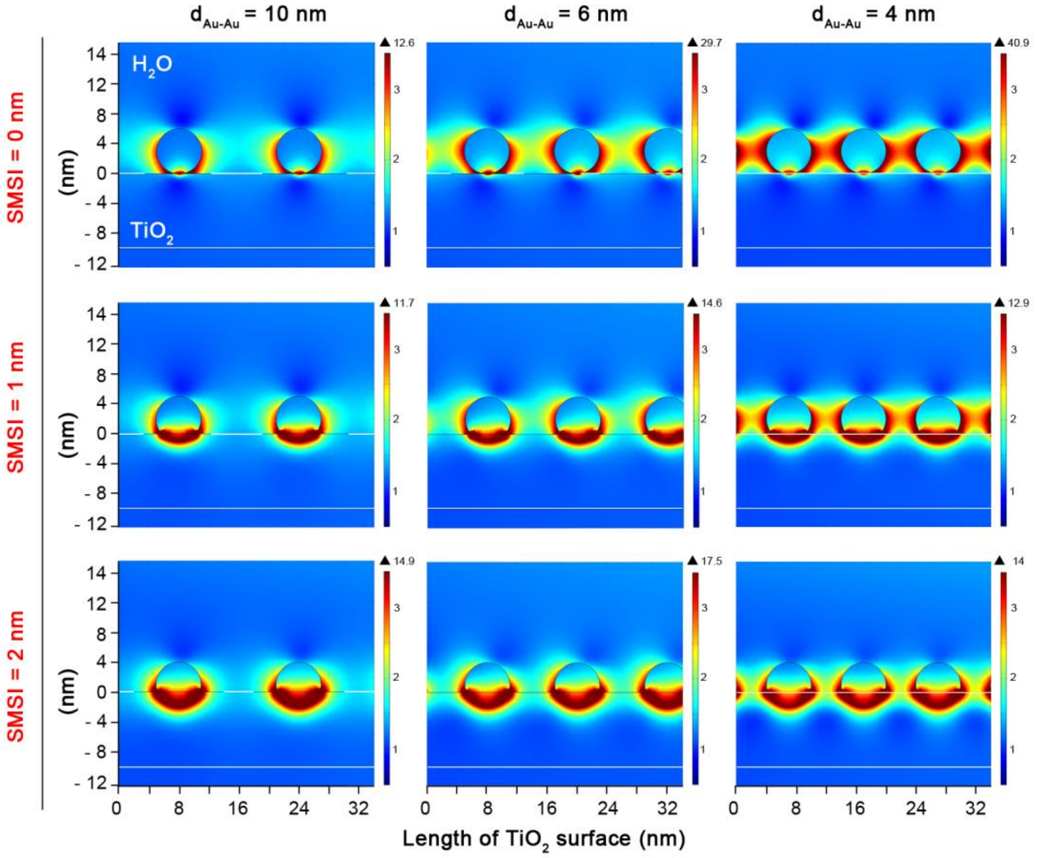

Figure 4.24 – Plasmon-promoted electric field intensity computed by FDTD simulations, as a function of the distance along the solid/liquid interface when Au/TiO_2 was immersed in H_2O. In the simulations the Au NPs diameter was kept fixed at 6 nm, while the interparticle distance was conveniently decreased (d_{Au-Au} = 10, 6, 4 nm). In addition, simulations for three different geometries were also carried out: Au NPs in direct contact with TiO_2 (SMSI = 0), Au NPs embedded in TiO_2 for 1 nm (SMSI = 1 nm) and for 2 nm (SMSI = 1 nm).

The Au NPs diameter was kept constant throughout the simulations and the size, for which the best photoactivity performances were achieved, was selected as that properly modelling the system (*i.e.*, d_{Au} = 6 nm).

Simultaneously, nanoparticle interdistances, calculated as the distance between two adjacent nanoparticles, were varied in the 4 up to 10 nm range (*i.e.*, d_{Au-Au} = 10, 6, 4 nm, from left to right in Figure 4.24, respectively).

Finally, TiO_2, Au and H_2O were modelled as dielectrics, each characterized by the refractive indexes and the extinction coefficients reported in Table 4.6 [73]. Incident λ = 532 nm, conveniently selected as irradiation wavelength in the simulations, guaranteed that also Au could be modelled as a dielectric material [74].

	n	*k*
TiO_2	2.558	4.04×10^{-4}
H_2O	1.334	1.32×10^{-9}
Au NPs	0.432	2.44

Table 4.6 – Refractive index (*n*) and extinction coefficients (*k*) of the materials (i.e., TiO_2, H_2O and Au nanoparticles) modelled by performing FDTD simulations.

The plasmon induced electric field, generated between two close NPs, was found to strongly increase with decreasing the gold nanoparticles interdistances presumably as a consequence of the positive interference between electric fields induced in adjacent NPs.

Moreover, *hot spots* characterized by intense electric field were found at the direct Au/TiO_2 and Au/TiO_2/H_2O contacts.

Since it was observed that the plasmon resonance effect on the electric field propagated also few nanometres below the direct Au/TiO_2 interface, progressively higher embedding of Au NPs into TiO_2 was also modelled.

The gradual inclusion of the nanoparticles into the titania support led to a pronounced enhancement of the electric field intensity in the metal nanoparticles portion embedded in the oxide, as well as of that generated at the Au-TiO_2 interface. Conversely, the electric field intensity generated at the Au/H_2O interface was found to progressively decrease with decreasing the Au interparticle distance and the simultaneously increase of the embedding degree. For example, for $d_{Au\text{-}Au}$ = 4 nm (right column of Figure 4.24), as the gold nanoparticles embedded portion gradually raised from 0 nm up to 2 nm, *hot regions*, characterized by highly intense electric field, formed inside metal nanoparticles, at the expense of the field generated at the Au/H_2O interface when SMSI = 0 nm was considered.

By means of the performed FDTD simulations, also the so-called Enhancement Factor (EF) was calculated, Figure 4.25. EF was introduced by Cronin *et al.* [70] and it was defined as the ratio between the volume influenced by the electric field generated through plasmon excitation (numerator of the formula in Figure 4.25) and the volume directly hit by the incident electric field (*i.e.*, incident irradiation), represented by the denominator of the formula in Figure 4.25.

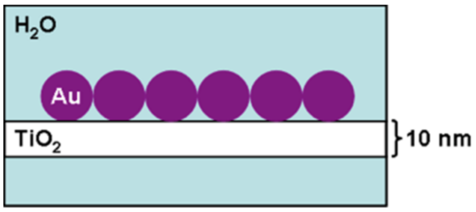

$$EF = \frac{\int_{-10\ \mathrm{nm}}^{0} dz \int dx\, dy\, |E|^2}{\int_{-10\ \mathrm{nm}}^{0} dz \int dx\, dy\, |E_0|^2}$$

Figure 4.25 – The panel on the left side reports the model applied for the simulation of the electric field enhancement (EF), by means of the FDTD method. A 10 nm-thick slide was considered, also modified with the deposition of gold nanoparticles; the system was modelled as completely suspended in H_2O, according to the photocatalytic activity tests performed. The formula applied for the determination of EF [70] is also reported.

In the present model, only the photons absorbed by the first 10 nm of the TiO_2 slide were considered as those effectively promoting Au plasmon resonance and, hence, contributing to photoactivity. From this assumption, –10 nm up to 0 nm was defined as the proper integration range along the *z*-axis.
The obtained results in terms of EF values are reported in Figure 4.26.

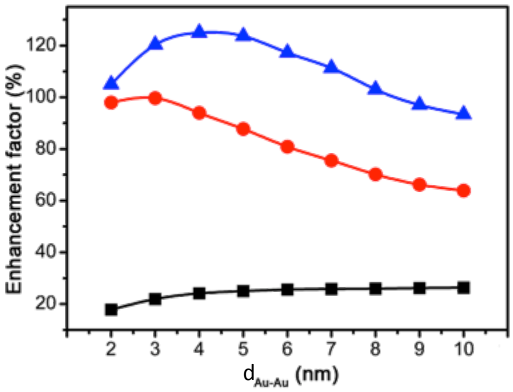

Figure 4.26 – Photocatalytic enhancement factor for Au NPs with 6 nm fixed diameters, as a function of the NPs interdistances (d_{Au-Au}) at progressively higher embedding degree: *i*) SMSI = 0 nm (black trace), *ii*) SMSI = 1 nm (red trace), *iii*) SMSI = 2 nm (blue trace).

Interestingly, when Au NPs were considered just deposited on the TiO_2 surface (*i.e.*, SMSI = 0 nm), EF only slightly increased with increasing the gold nanoparticles interdistance, nearly reaching a plateau value at d_{Au-Au} = 9 nm (black trace in Figure 4.26).
Conversely, at progressively higher Au NPs embedding degrees (*i.e.*, SMSI = 1 and 2 nm), EF increased until reaching a metal NP-NP distance optimum value (d_{Au-Au} = 3 nm for SMSI = 1 nm and d_{Au-Au} = *ca.* 5 nm for SMSI = 2 nm) and then dropped down to values even lower than that calculated for the closest gold nanoparticles (*i.e.*, d_{Au-Au} = 2 nm).

However, keeping d_{Au-Au} constant, the gradual embedding of Au nanoparticles resulted in a sizeable increase of EF, with the better situation represented by metal nanoparticles as close as *ca.* 5 nm, included for 2 nm inside titania.

4.2.4 Plasmon promoted photocatalytic activity

The parameters adopted in the simulations represented, with a good degree of approximation, the investigated gold modified doped titania supports (*i.e.*, N-TiO_2 and b-TiO_2) characterized by Au NPs with nearly constant dimensions throughout the entire 1–10 wt.% regime.

As previously discussed (see TEM analysis and Figures 4.18 and 4.19 and Table 4.5), at progressively higher metal loadings, uniform d_{Au} implied that Au NPs density on the surface of the supports gradually increased or, in other words, their interdistances (d_{Au-Au}) decreased.

FDTD simulations proved that, as metal nanoparticles approached each other, the plasmon promoted electric field became increasingly more intense either in the area within adjacent nanoparticles (when SMSI = 0 nm) or at the Au/TiO_2 interface (when SMSI > 0 nm).

As the plasmon generated electric field increased, also the calculated photoactivity enhancement factor increased (from the formula reported in Figure 4.26, $EF \div |E|^2$), reaching the highest value when d_{Au-Au} = *ca.* 5 nm.

In N- and b-TiO_2 samples the plasmon-promoted photoactivity was shown to be almost linearly dependent on the gold loading amount, with the best performances obtained with 10%Au/N-TiO_2.

Thus, considering the nearly homogeneous nanoparticles size distribution centered at ~ 5 nm characterizing Au NPs deposed on the surface of the doped supports, the trend obtained in formic acid plasmon-promoted photoactivity could be readily justified: by increasing Au loading, also the metal NPs density progressively increased, with the consequent decrease in the NP-NP interdistance (calculated as the distance between two adjacent nanoparticles), and the formation of a highly intense electric field induced by metal surface plasmon resonance. By assuming that this electric field is strictly correlated with the promotion of electron/hole pairs through the so-called PRET mechanism in the semiconductor support portion adjacent to a gold nanoparticle, it seems reasonable that plasmon-driven photoactivity in Au-modified doped titania increased with increasing the metal loading amount (Figure 4.22(B)).

Conversely, in w-TiO_2, higher metal loading regimes were characterized by progressively bigger metal nanoparticles. In this case, the increasingly more intense electric field generated by Au surface plasmon resonance may be detrimental for hot electron injection when the gold loading amount exceeded the optimum value (*i.e.*, 5 wt.%), accounting for the volcano-shaped trend of formic acid photodegradation rate observed with Au-modified w-TiO_2 (Figure 4.22(B)).

4.2.5 Conclusion

Formic acid photodegradation performed with Au-modified TiO_2 was achieved by selectively promoting Au NPs localized surface plasmon resonance (LSPR), through monochromatic irradiation ($\lambda = 532$ nm).

Metal loading was varied in the 1–10 wt.% range and three different titania samples (*i.e.*, stoichiometric TiO_2, N-doped TiO_2 and V_Os-rich TiO_2) were selected as supports. In line with the electronic properties of the investigated titania and depending on the amount of loaded metal, two different plasmon-promoted mechanisms may be invoked to accounted for the observed photoactivity: *i*) when Au/TiO_2 = 1–5 wt.%, hot electrons, generated through LSPR, readily transferred from excited Au nanoparticles to the conduction band of TiO_2; due to its CB suitable position, highest photoactivity performances were achieved with w-TiO_2; *ii*) at higher metal loadings, Plasmon Resonance Energy Transfer (PRET) occurred from the excited Au nanoparticles to the band gap of the investigated semiconductors, triggered by the highly intense electric field generated within adjacent Au NPs as well as at the Au/TiO_2 interface. In this regime, due to the presence of defect states in doped titania (*i.e.*, N- and b-TiO_2) detected through RESPES and XAS spectroscopies, the semiconductors band gap was reduced and, hence, could resonate with the energy provided by plasmon resonance. Accordingly, in N- and b-TiO_2 the photoactivity increased with metal loading, by virtue of the progressively increasing plasmon-generated electric field and the best performances were achieved with Au-modified N-TiO_2 samples.

Aside their dependence on the metal loading amount, photoactivity results were also strictly influenced by the titania supports considered, opening up to a likely Strong Metal-Support Interaction (SMSI), usually characterizing metal induced catalytic processes, also in light promoted reactions.

Finally, Finite-Difference Time-Domain simulations, performed on systems modeling the investigated ones, provided results perfectly compatible with the experimental results.

REFERENCES

[1] F. Riboni, L.G. Bettini, D.W. Bahnemann, E. Selli, *Catal. Today* **2013**, *209*, 28.

[2] K.K. Akurati, A. Vital, J.P. Dellemann, K. Michalowa, T. Graule, D. Ferri, A. Baiker, *Appl. Catal. B Environm*. **2008**, *79*, 53.

[3] N. Couselo, F.S. Garcia Einschlag, R.J. Candal, M. Jobbagy, *J. Phys. Chem. C* **2008**, *112*, 1094.

[4] R.D. Shannon, *Acta Crystall. Section A* **1976**, *32*, 751.

[5] A.M. Cant, F, Huang, X, Li Zhang, Y, Chen, Yi-Bing Cheng, R. Amal, *Nanoscale* **2014**, *6*, 3875.

[6] H. Kamisaka, T. Suenaga, H. Nakamura, K. Yamashita, *J. Phys. Chem. C* **2010**, *114*, 12777.

[7] M.V. Dozzi, L. Prati, P. Canton, E. Selli, *Phys. Chem. Chem. Phys.* **2009**, **11**, 7171.

[8] D. Zhao, C. Chen, C. Yu, W. Ma, J. Zhao, *J. Phys. Chem. C* **2009**, *113*, 13160.

[9] B. Tryba, M. Piszcz, A.W. Morawski, Intern. J. Photoen. 2009, 2009, 1.

[10] B. Tian, J. Zhang, T. Tong, F. Chen, *Appl. Catal. B Environm.* **2008**, *79*, 394.

[11] G.L. Chiarello, M.H. Aguirre, E. Selli, *J. Catal.* **2010**, *273*, 182.

[12] G.L. Chiarello, L. Forni, E. Selli, *Catal. Today* **2009**, *144,* 69.

[13] G.L. Chiarello, D. Ferri, E. Selli, *J. Catal.* **2011**, *280*, 168.

[14] G.L. Chiarello, A. Di Paola, L. Palmisano, E. Selli, *Photochem. Photobiol. Sci.* **2011**, *10*, 355.

[15] R. Abe, H. Takami, N. Murakami, B. Ohtani, *J. Am. Chem. Soc*. **2008**, *130*, 7780.

[16] E. Endoh, J.K. Leland, A.J. Bard, *J. Phys. Chem.* **1986**, *90*, 6223.

[17] K Tennakone, A Ileperumatz, J.M.S. Bandarat, W.C.B Kiridena, *Semicond. Sci. Technol*. **1992**, *7*, 423.

[18] A.C. Johnston-Peck, S.D. Senanayake, J.J. Plata, S. Kundu, W. Xu, L. Barrio, J. Graciani, J.F. Sanz, R.M. Navarro, J.L.G. Fierro, E.A. Stach, J.A. Rodriguez, *J. Phys. Chem. C* **2013**, *117*, 14463.

[19] T. Caruso, C. Lenardi, R.G. Agostino, M. Amati, G. Bongiorno, T. Mazza, A. Policicchio, V. Formoso, E. Maccallini, E. Colavita, G. Chiarello, P. Finetti, F. Sutara, T. Skala, P. Piseri, K.C. Prince, P. Milani, *J. Chem. Phys.* **2008**, *128*, 094704.

[20] H. Ishihara, G.K. Kannarpady, K.R. Khedir, J. Woo, S. Trigwellb, A.S. Biris, *Phys. Chem. Chem. Phys.* **2011**, *13*, 19553.

[21] S.K. Lee, P.K.J. Robertson, A. Mills, D. McStay, N. Elliott, D. McPhail, *Appl. Catal. B.* **2003**, *44*, 173.

[22] A.L. Linsebigler, G. Lu, J.T. Yates, *Chem. Rev.* **1995**, *95*, 735.

[23] M. Chiesa, M.C. Paganini, S. Livraghi, E. Giamello, *Phys. Chem. Chem. Phys.* **2013**, *15*, 9435.

[24] T. Tatsuma, S. Saitoh, P. Ngaotrakanwiwat, Y. Ohko, A. Fujishima, *Langmuir* **2002**, *18*, 7777.

[25] A. Yamakata, T. Ishibashi, H. Onishi, *J. Phys. Chem. B* **2001**, *105*, 7258.

[26] A. Fujishima, X. Zhang, D.A. Tryk, *Surf. Sci. Rep.* **2008**, *63*, 515.

[27] M. Grätzel, *Nature* **2001**, *414*, 338.

[28] M.V. Dozzi, S. Livraghi, E. Giamello, E. Selli, *Photochem. Photobiol. Sci.* **2011**, *10*, 343.

[29] M. Mrowetz, E. Selli, *J. Photochem. Photobiol. A* **2006**, *180*, 15.

[30] Y.T. Kwon, K.Y. Song, W.I. Lee, G.J. Choi, Y.R. Do, *J. Catal.* **2000**, **191**, 192.

[31] Y.G. Berubé, P.L. de Bruyn, *J. Colloid. Interf. Sci.* **1968**, *27*, 305.

[32] V. Keller, P. Bernhardt, F. Garin, *J. Catal.* **2003**, *215*, 129.

[33] K.Y. Song, M.K. Park, Y.T. Kwon, H.W. Lee, W.J. Chung, W.I. Lee, *Chem. Mater*. **2001**, *13*, 2349.

[34] F. Hilbrig, H.E. Göbel, H. Knözinger, H. Schmelz, B. Lengeler, *J. Phys. Chem.* **1991**, *95*, 6973.

[35] G.A. Parks, *Chem. Rev.* **1965**, *65*, 177.

[36] X.Z. Li, F.B. Li, C.L. Yang, W.K. Ge, *J. Photochem. Photobiol. A* **2001**, *141*, 209.

[37] F. Denny, J. Scott, K. Chiang, W.Y. Teoh, R. Amal, *J. Molec. Catal. A* **2007**, *263*, 93.

[38] H.M. Coleman, C.P. Marquis, J.A. Scott, S.S. Chin, R. Amal, *Chem. Eng. J.* **2005**, *113*, 55.

[39] *CRC Handbook of Chemistry and Physics*, *87th ed.*, Taylor & Francis, **2006**, 12.

[40] W.Y. Teoh, L. Mädler, R. Amal, *J. Catal*. **2007**, *251*, 271.

[41] J. Lee, W. Choi, *J. Phys. Chem. B* **2005**, *109*, 7399.

[42] C. He, Y. Xiong, X. Zhu, X. Li, *Appl. Catal. A Gener*. **2004**, *275*, 55.

[43] N. Chi, K.Y. Chan, D.L. Philips, *Catal. Lett.* **2001**, *71*, 21.

[44] Y. Peng, C. Liu, X. Zhang, J. Li, *Appl. Catal. B* **2013**, *140–141*, 276.

[45] Y. Peng, J. Li, L. Chen, J. Chen, J. Han, H. Zhang, W. Han, *Environm. Sci. Technol*. **2012**, *46*, 2864.

[46] J.A. Dumesic, N.Y. Topsoe, H. Topsoe, Y.Chen, T. Slabiak, *J. Catal.* **1996**, *163*, 409.

[47] M. Makosch, L. Wan-Ing, V. Bumbálek, J. Sa, J.W. Medlin, K. Hungerbühler, J.A. van Bokhoven, *ACS Catal*. **2012**, *2*, 2079.

[48] C. Morterra, G. Ghiotti, E. Garrone, E. Fisicaro, *J.C.S. Faraday Trans.* **1980**, *76*, 2102.

[49] A. Naldoni, M. Allieta, S. Santangelo, M. Marelli, F. Fabbri, S. Cappelli, C.L. Bianchi, R. Psaro, V. Dal Santo, *J. Am. Chem. Soc.* **2012**, *134*, 7600.

[50] M. Salari, K. Konstantinov, H.K. Liu, *J. Mater. Chem.* **2011**, *21*, 5128.

[51] F. Spadavecchia, S. Ardizzone, G. Cappelletti, C. Oliva, S. Cappelli, *J. Nanopart. Res.* **2012**, *14*,1301.

[52] P. Christopher, H. Xin, A. Marimuthu, S. Linic, *Nat. Mater.* **2012**, *11*, 1044.

[53] M.C. Daniel, D. Astruc, *Chem. Rev.* **2004**, *104*, 293.

[54] T.C. Kaspar, A. Ney, A.N. Mangham, S.M. Heald, Y. Joly, V. Ney, F. Wilhelm, A. Rogalev, F. Yakou, S.A. Chambers, *Phys. Rev. B* **2012**, *86*, 035322.

[55] G. Drera, M.C. Mozzati, P. Galinetto, Y. Diaz-Fernandez, L. Malavasi, F. Bondino, M. Malvestuto, L. Sangaletti, *Appl. Phys. Lett.* **2010**, *97*, 012506.

[56] G Drera, L Sangaletti, F Bondino, M Malvestuto, L Malavasi, Y Diaz-Fernandez, S Dash, M.C. Mozzati, P. Galinetto, *J. Phys. Condens. Matter* **2013**, *25*, 075502.

[57] A. Braun, K. Akurati, G. Fortunato, F.A. Reifler, A. Ritter, A.S. Harvey, A. Vital, T. Graule, *J. Phys. Chem. C* **2010**, *114*, 516.

[58] X. Chen, P.A. Glans, X. Qiu, S. Dayal, W.D. Jennings, K.E. Smith, C. Burda, J. Guo, *J. Electron. Spectr. Relat. Phenom.* **2008**, *162*, 67.

[59] C. Di Valentin, G. Pacchioni, *Catal Today* **2013**, *206*, 12.

[60] A.G. Thomas, W.R. Flavell, A.K. Mallick, A.R. Kumarasinghe, D. Tsoutsou, N. Khan, C. Chatwin, S. Rayner, G.C. Smith, R.L. Stockbauer, S. Warren, T.K. Johal, S. Patel, D. Holland, A. Taleb, F. Wiame, *Phys. Rev. B* **2007**, *75*, 035105.

[61] A.O. Govorov, H. Zhang, H.V. Demir, Y.K. Gun’ko, *Nano Today* **2014**, *9*, 85.

[62] A.O. Govorov, W. Zhang, T. Skeini, H.H. Richardson, J. Lee, N.A. Kotov, *Nanoscale Res. Lett.* **2006**, *1*, 84.

[63] M.A. van Dijk, A.L. Tchebotareva, M. Orrit, M. Lippitz, S. Berciaud, D. Lasne, L. Cognet, B. Lounis *Phys. Chem. Chem. Phys.* **2006**, *8*, 3486.

[64] E. Kowalska, O.O.P Mahaney, R. Abe, B. Ohtani, *Phys. Chem. Chem. Phys.* **2010**, *12*, 2344.

[65] D. Tsukamoto, Y. Shiraishi, Y. Sugano, S. Ichikawa, S Tanaka, T Hirai, *J. Am. Chem. Soc.* **2012**, *134*, 6309.

[66] E.W. McFarland, J. Tang, *Nature* **2003**, *421*, 616.

[67] A. Furube, L. Du, K. Hara, R. Katoh, M. Tachiya, *J. Am. Chem. Soc.* **2007**, *129*, 14852.

[68] C. Di Valentin, G. Pacchioni, A. Selloni, S. Livraghi, E. Giamello, *J. Phys. Chem. B* **2005**, *109*, 11414.

[69] X. Pan, M.Q. Yang, X. Fu, N. Zhang, Y.J. Xu, *Nanoscale* **2013**, *5*, 3601.

[70] Z. Liu, W. Hou, P. Pavaskar, M. Aykol, S.B. Cronin, *Nano Lett.* **2011**, *11*, 1111.

[71] D.B. Ingram, S. Linic, *J. Am. Chem. Soc.* **2011**, *133*, 5202.

[72] S.K. Cushing, J. Li, F. Me, T.R. Senty, S. Suri, M. Zhi, M. Li, A.D. Bristow, N. Wu, *J. Am. Chem. Soc.* **2012**, *134*, 15033.

[73] www.filmetrics.com

[74] P.B. Johnson, R.W. Christy, *Phys. Rev. B* **1972**, *6*, 4370.

Chapter 5

Homogeneous reduction of CO_2 by photogenerated pyridinyl radicals

ABSTRACT – 1-hydropyridinyl radicals (1-PyH$^\bullet$) photogenerated in isopropanol/water were reported to react with dissolved CO_2 towards its 2-e$^-$ reduction into carboxylic acids. Pyridine (Py), excited to its triplet state (^{3}Py*) in deaerated 2-PrOH/H_2O mixtures saturated with 1 atm CO_2, yielded a suite of products, among which $Na(HCOO)_2^-$ (m/z$^-$ = 113), $C_5H_6NCOO^-$ (m/z$^-$ = 124) and $C_5H_{10}O_2NCOO^-$ (m/z$^-$ = 160) were identified by electrospray ionization mass spectrometry. These products demonstrably contained carboxylate functionalities that split CO_2 neutrals via collisionally induced dissociation.

It is suggested that 1-PyH$^\bullet$, formed from ^{3}Py* + 2-PrOH → 1-PyH$^\bullet$ + $^\bullet$PrOH, adds to CO_2, in competition with radical-radical reactions, leading to intermediates that were in turn reduced by $^\bullet$PrOH into the observed species.

The formation of carboxylates in this system, which demonstrably required CO_2, Py, 2-PrOH and actinic radiation, amounted to the homogeneous 2e$^-$-reduction of CO_2 by 2-PrOH initiated by Py*. An estimation of the rate constant k(5.3) of the reaction 1-PyH$^\bullet$ + CO_2 → $^\bullet$Py-1-COOH ~ $O(10)$ M^{-1} s^{-1} was provided, which

allowed the determination of the reaction activation energy, $E_3 \geq 9$ kcal mol^{-1} that was compatible with thermochemical estimates for this reaction.

The experimental details dealing with photolysis experiments and set ups adopted are depicted in Sections 3.3.4 and 3.3.6, respectively. The possible reaction mechanism that leads to the detected products is provided in Scheme 5.1. Likewise, possible secondary radicals and radical disproportionation reactions are reported in Scheme 5.2.

Keywords – Carbon dioxide, CO_2 photoreduction, pyridine, photolysis.

5.1 Experimental results

Only Py/PyH$^+$ absorb at 254 nm in freshly prepared 2-PrOH/H_2O solutions [1-3], as proved by UV-vis absorption spectra, collected prior to photolysis (Figure 5.1(A)).

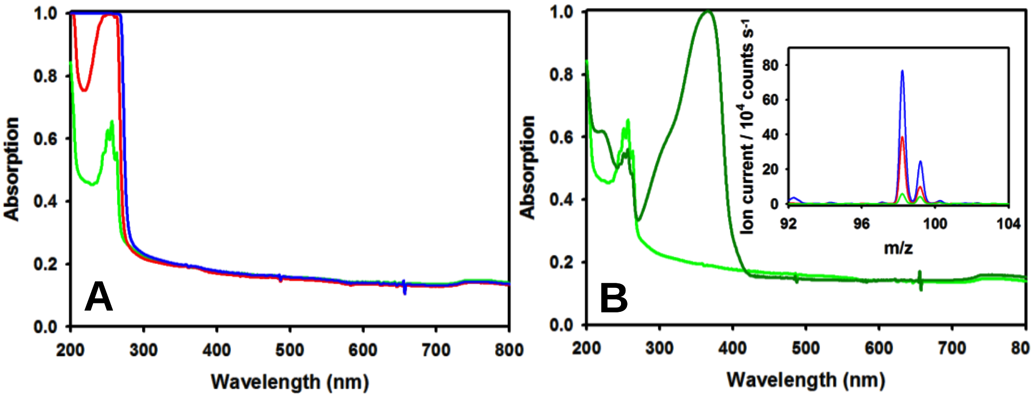

Figure 5.1 – A) UV-vis absorption spectra of Py solutions in 10% (v/v) 2-propanol/water mixtures at pH ~3. In details: [Py] = 1 mM (green trace); [Py] = 10 mM (red trace); [Py] = 100 mM (blue trace). B) Light green trace: UV-vis absorption spectra of 1mM Py in 10% (v/v) 2-propanol/water (pH~3); dark green trace: UV-vis absorption spectra of 1mM Py in 10% (v/v) 2-propanol/water (pH~3) irradiated at 254 nm for 1 h. The inset reports the ESI positive mass spectra of m/z$^+$ = 98 ion, obtained at different pyridine concentration (*i.e.*, [Py] = 1 mM (green trace); [Py] = 10 mM (red trace); [Py] = 100 mM (blue trace)).

The 254 nm-photolysis of pyridine has been previously investigated both in water [2,4] and in 2-PrOH [5-7], finding out that, in H_2O, Py is converted into a detectable (Dewar) valence isomer, which hydrolyzes thermally into 5-amino-2,4-pentadienal (C_5H_7NO, m = 97) and that was spectrophotometrically identified since it absorbs at $\lambda \sim 365$ nm (Figure 5.1(B)) and gives rise to a yellow deposit in the solution [5]. As evidenced in the inset of Figure 5.1(B), the yield of the photohydration reaction was pyridine-concentration dependent, with the highest amount of $m/z^+ = 98$ obtained for the most concentrated pyridine solution.

By adding the second water molecule, 5-amino-2,4-pentadienal converts into its gem-diol ($C_5H_9NO_2$, m = 115). It is reasonable to assume that C_5H_7NO retained the original ring-structure since only pyridine-like molecules readily react with water [2]. The overall quantum yield for the photohydration reaction is ~ 0.06 [1]. It has already been reported that photohydration products are short-lived species, since Py is completely recovered after ~ 1 minute under no irradiation. Nevertheless, the thermal and photochemical properties of Py allow accumulation of moderate quantities of hydrated products, also at low temperatures [2], ensuring their availability for further reactions under the investigated conditions.

The photolysis of pyridine in isopropanol has revealed that excited triplet states ($^3Py^*$) can abstract a H atom from 2-PrOH leading to 1-hydropyridinyl (1-$PyH^\bullet$) and to ketyl radicals ($^\bullet C(OH)(CH_3)_2$), respectively, according to reaction R5.1:

$$^3Py^* + 2\text{-}PrOH \rightarrow 1\text{-}PyH^\bullet + {}^\bullet PrOH \qquad (R5.1)$$

Since also the ketyl radical $^\bullet$PrOH readily transfers a H atom to pyridine [5], the overall stoichiometry of R5.1 is actually

$$Py + h\upsilon + 2\text{-}PrOH \rightarrow 2\ 1\text{-}PyH^\bullet + (CH_3)_2CO \qquad (R5.2)$$

In accordance with these considerations, positive ion ESI mass spectra of the products of Py photolysis in 2-PrOH/H_2O solutions displayed intense $m/z^+ = 98$ and 116 signals that correspond to protonated species with mass 97 and 115 Da, respectively, along with the $m/z^+ = 80$ signal belonging to pyridinium ion (PyH^+), largely present in the mixtures (Figure 5.2 and Scheme 5.1).

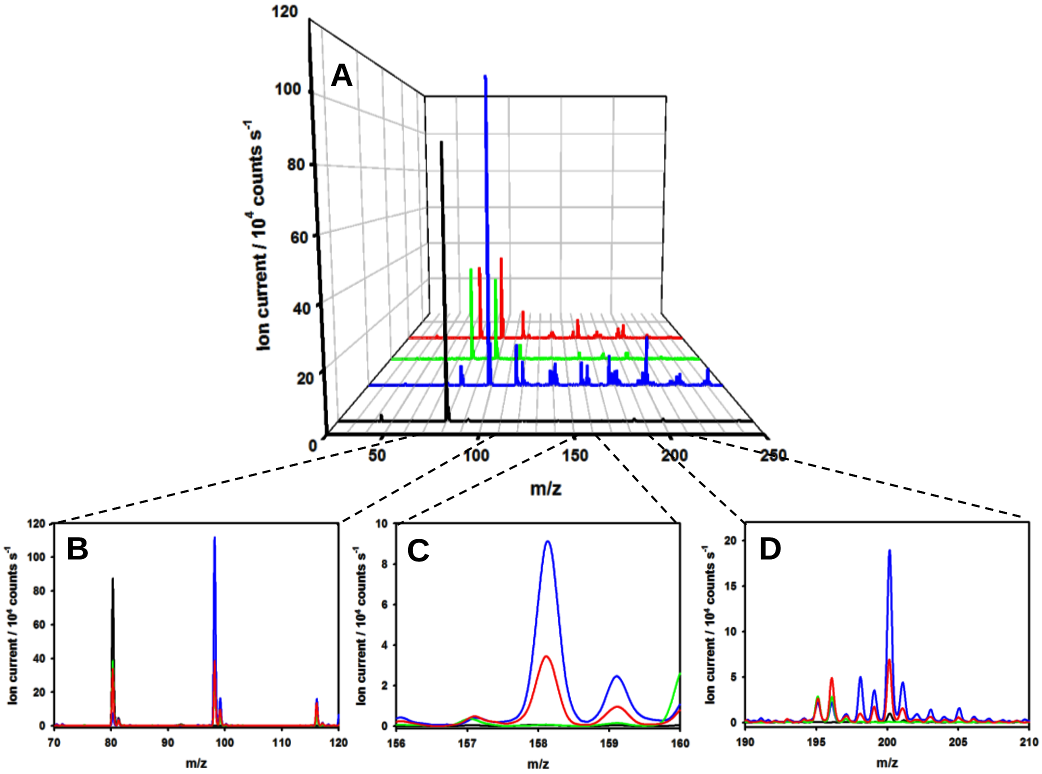

Figure 5.2 – A) Positive ESI mass spectra of 10 mM Py solution in H_2O or in 10%(v/v) 2-PrOH/H_2O under various conditions. Black trace: initial solutions. ESI mass spectra of solutions, irradiated at 254 nm for 1 h, follow. Blue trace: in 10%(v/v) 2-PrOH/H_2O. Green trace: in neat H_2O, saturated with CO_2. Red trace: in 10%(v/v) 2-PrOH/H_2O saturated with 1 atm CO_2. B), C) and D) zoom into the mass ranges where the $m/z^+ = 80$, 98 and 116, 158, 200 signals appear, respectively.

As predicted from the UV-vis absorption spectrum of the solution photolyzed in the absence of CO_2 (Figure 5.1(B)), Py/PyH^+ were mainly converted into C_5H_7NO, yielding the highest intensity for the peak at $m/z^+ = 98$; the reaction appeared somehow quenched in the absence of isopropanol (H-donor species) or for the CO_2-saturated solution (green and red traces in Figure 5.2, respectively). These observations provided strong evidence that 2-PrOH is strictly required and, more relevantly to the issue of the work, that in the presence of CO_2 side-reactions involving Py/PyH^+ occur.

Concerning $C_5H_9NO_2$ ($m/z^+ = 116$), in Py solution in neat water (green trace) the species was not formed at all (again highlighting the essential role of 2-PrOH), whereas both in the presence and in the absence of CO_2 (red and blue traces) the gem-diol was formed at nearly the same extent. It’s important to note that all even mass ions carried a N-atom, *i.e.*, they derived from pyridine.

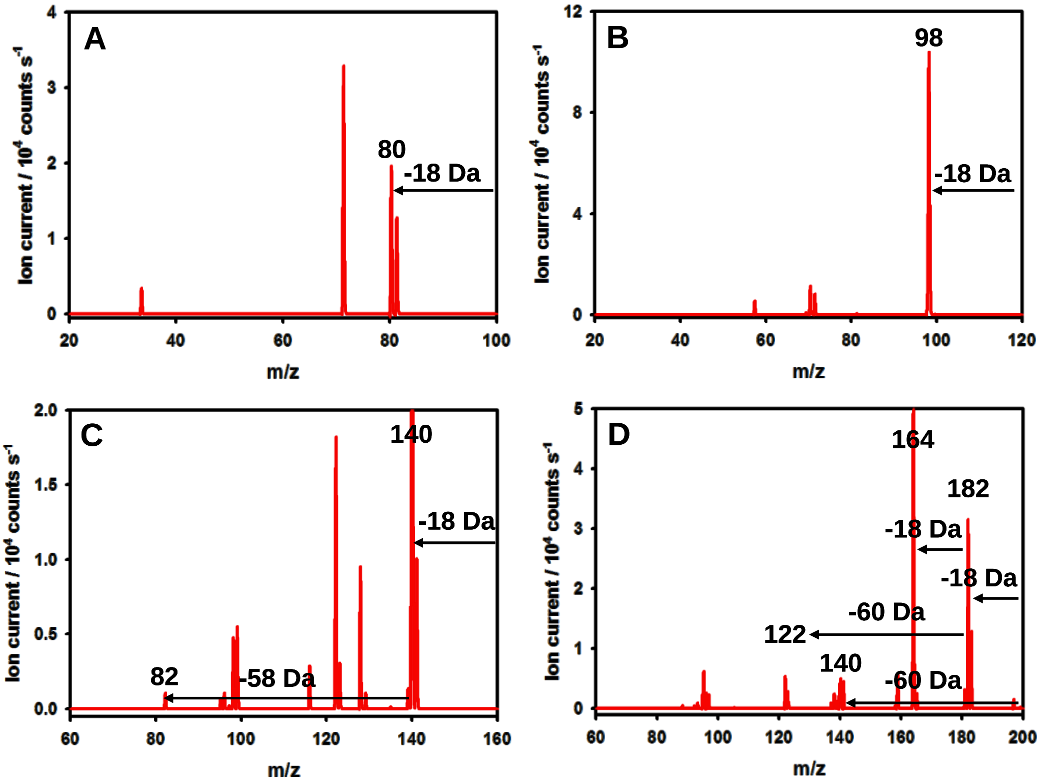

Figure 5.3 – A) MS^2 of $m/z^+ = 98$; B) MS^2 of $m/z^+ = 116$; C) MS^2 of $m/z^+ = 158$; D) MS^2 of $m/z^+ = 200$. Note the neutral 18 Da (H_2O), 58 Da ($CO(CH_3)_2$) and 60 Da (2-PrOH) losses.

To give further evidence of the elemental composition of $m/z^+ = 98$ and 116 ions, MS^2 spectra of both were collected (Figure 5.3(A-B)). They revealed -17 (OH) and -18 (H_2O) Da neutral losses, as expected.

The photolysis of pyridine in 10% (v/v) 2-PrOH/H_2O mixtures generated additional peaks at $m/z^+ = 140$ (Figure 5.4(A)) and 158 (Figure 5.2(C)). The former ensued from the reaction of 1-PyH$^\bullet$ and $^\bullet$PrOH radicals (139 ($C_8H_{13}NO$) = 80 (1-PyH$^\bullet$) + 59 ($^\bullet$PrOH), see Scheme 5.1) thus, as a matter of fact, its formation was totally quenched when photolysis was performed in neat H_2O solution (green trace in Figure 5.4(A)) and partially inhibited in the presence of CO_2 (red trace).

Conversely, in competition with its complete photohydration, the 97 Da mass species yielded $m/z^+ = 158$ (see Scheme 1) that corresponded to the protonated form of 157 ($C_8H_{18}NO_2$) = 97 (C_5H_7NO) + 59 ($^\bullet$PrOH), again displaying the same trend towards 2-POH and CO_2, as the $m/z^+ = 140$ peak (see Figure 5.2(B)).

More generally, most of the myriad products observed in the mass spectra could be accounted for radicals addition and disproportionation reactions among [1-PyH$^\bullet$, $^\bullet$PrOH] primary and secondary radicals.

For example, positive $m/z^+ = 200$ (Figure 5.2(C)) is due to the protonated form of the neutrals 199 Da resulting from the addition of $^\bullet$PrOH to the above described mass 139 Da (see Scheme 5.1), followed by a radical disproportionation that incorporates an additional H atom: 199 ($C_{11}H_{21}NO_2$) = 139 ($C_9H_{13}NO$) + 59 ($^{\bullet}$PrOH) + 1 (H-atom).

As expected, the essential role played by 2-PrOH was evidenced by the complete inhibition of positive m/z$^+$ = 200 formation during the photolysis experiment run in Py neat H_2O solution along with the lower species amount produced in the presence of CO_2 (green and red traces of Figure 5.2(C), respectively).

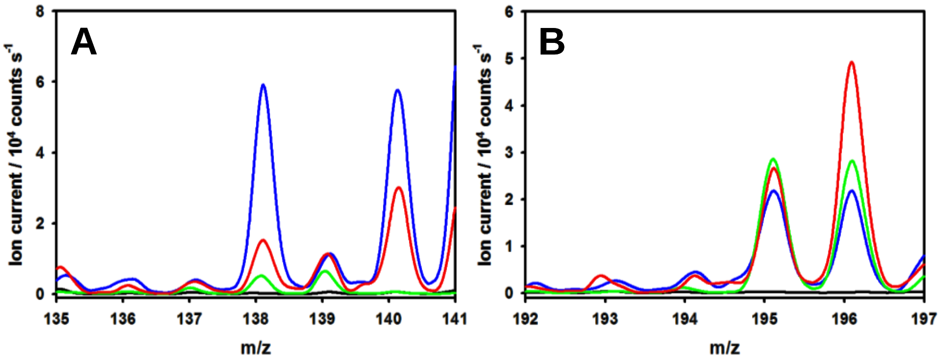

Figure 5.4 – Positive ESI mass spectra of 10 mM Py solution in H_2O or in 10%(v/v) 2-PrOH/H_2O under various conditions. Black trace: initial solutions. ESI mass spectra of solutions, irradiated at 254 nm for 1 h, follow. Blue trace: in 10%(v/v) 2-PrOH/H_2O. Green trace: in neat H_2O, saturated with CO_2. Red trace: in 10%(v/v) 2-PrOH/H_2O saturated with 1 atm CO_2. A) and B) zoom into the mass ranges where the radical disproportionation products m/z$^+$ = 138 and 196 appear, respectively.

MS^2 spectra recorded for the m/z$^+$ = 158 and 200 ions (Figure 5.3(C-D) respectively) pointed out 18 (H_2O), 58 ($(CH_3)_2CO$), and 60 ($HC(OH)(CH_3)_2$) Da neutral losses, by virtue of the cations composition.

Similarly, several other species were formed through radicals disproportionation reactions (Scheme 5.2): *i)* m/z$^+$ = 138 is the protonated form of 137 Da and resulted from the successive addition of $^{\bullet}$PrOH to 1-PyH$^{\bullet}$, followed by H-atom losses via disproportionation. In details: 137 ($C_8H_{11}NO$) = Py + $^{\bullet}$PrOH – H-atom = 79 + 59 – 1 (Figure 5.4(A)); *ii*) m/z$^+$ = 196 is the protonated form of 195 Da (*i.e.*, 195 ($C_{11}H_{17}NO_2$) = Py + 2 $^{\bullet}$PrOH – 2 H-atom = 79 + 118 – 2, Figure 5.4(B)). In addition, α-hydroxyalkyl radicals produced from 2-PrOH photolysis, releasing their unpaired electron to Py, lead to acetone (R5.2) [8], which in turn could then be photolyzed yielding the acetyl radical ($^{\bullet}COCH_3$) [9], promptly reacting with Py and other species dissolved in the solution, with the consequent formation of products from secondary radical reactions (Scheme 5.2): *i*) m/z$^+$ = 180 is the protonated 179 Da species and was formed through acetyl radical ($^{\bullet}COCH_3$, m = 43 Da) addition to the above mentioned 137 Da species, followed by H-atom release. In details: 179 ($C_{10}H_{13}NO_2$) = $C_8H_{11}NO$ + $^{\bullet}COCH_3$ – H-atom = 137 + 43 – 1 (Figure 5.5(A)); *ii*) m/z$^+$ = 222 corresponds to the protonated form of 221 Da (*i.e.*, 221 ($C_{12}H_{16}NO_3$) = $C_{10}H_{13}NO_2$ + $^{\bullet}COCH_3$ – H-atom = 179 + 43 – 1, Figure

5.5(B)); *iii*) m/z$^+$ = 124 (*i.e.*, 123 (C_7H_9NO) = 1-PyH$^•$ + $^•COCH_3$ = 80 + 43, Figure 5.5(C)); *iv*) m/z$^+$ = 166 (*i.e.*, 165 ($C_9H_{11}NO_2$) = C_7H_9NO + $^•COCH_3$ – H-atom = 123 + 43 – 1), along with all the products, up to m/z$^+$ = 250, formed by successive addition of acetyl radical and H-atom losses.

Though all mentioned radicals disproportionation products were not formed in the absence of 2-PrOH and their ESI mass spectra signals appeared largely quenched in the CO_2-saturated solutions, m/z$^+$ = 124 – 250 species were formed in much lower amount (I ~ 0.5 – 1 × 10^4 counts s^{-1}) with respect to all the other ions detected, by virtue of the dependence on secondary acetyl radical formation rate.

Notwithstanding recently published quantum mechanical calculations, no evidence for putative dihydropyridine PyH_2 [10] or a hydrogen-bonded pyridine dimer PyH^+---Py [11], which should have appeared as m/z$^+$ = 82 and 159, respectively, were found in positive ES spectra under any experimental conditions.

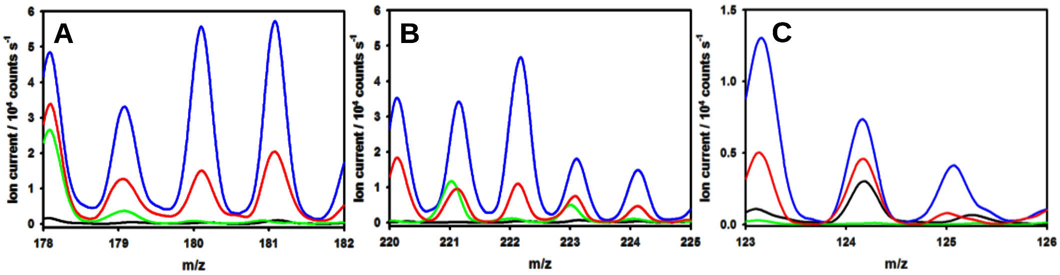

Figure 5.5 – Positive ESI mass spectra of 10 mM Py solution in H_2O or in 10%(v/v) 2-PrOH/H_2O under various conditions. Black trace: initial solutions. ESI mass spectra of solutions, irradiated at 254 nm for 1 h, follow. Blue trace: in 10%(v/v) 2-PrOH/H_2O. Green trace: in neat H_2O, saturated with CO_2. Red trace: in 10%(v/v) 2-PrOH/H_2O saturated with 1 atm CO_2. A), B) and C) zoom into the mass ranges where the radical disproportionation products m/z$^+$ = 180 and 222 and the secondary radicals product m/z$^+$ = 124 appear, respectively.

More relevantly, even mass negative ions appeared as products of the photolysis of Py in 2-PrOH/H_2O, directly involving CO_2 (Figure 5.6(A)). The addition of 1-PyH$^•$ to CO_2 gave rise to a 124 Da radical preserving the O-C-O moiety (Scheme 5.1) and which ended up as a 125 Da = 1-PyH$^•$ + CO_2 + H-atom = 80 + 44 + 1 carbamic acid that, due to its carboxylic group, appeared as m/z$^-$ = 124 anion (Figure 5.6(C)).

Following this criterion, other even mass negative ion peaks were identified, such as 161 Da = (C_5H_6NCOOH) + $2H_2O$ = 125 + 36, detected as m/z$^-$ = 160 anion (Figure 5.6(D)).

As outlined in Figures 5.6 and 5.7(A), the formation of carboxylates demonstrably required the presence of CO_2, Py, 2-PrOH and actinic radiation;

indeed, all these peaks intensities increased significantly in the presence of CO_2 (red traces throughout) and, not less importantly, $m/z^- = 124$ carbamic acid formation was totally inhibited in 2-propanol/water mixtures, clearly highlighting that the carboxylate retained both CO_2 and pyridine structures.

Furthermore, photolysis experiments performed with solutions containing different pyridine concentrations (*i.e.*, [Py] = 1 – 100 mM) allowed the determination of an optimal pyridine content, identified in 10 mM, with lower and higher concentrations leading to nearly identical amount of $m/z^- = 124$ and 160 anion evolved. This finding is in perfect agreement with what previously determined by Bocarsly et *al.* [12-17], though CO_2 reduction was achieved (photo)electrochemically and pyridine was used as co-catalyst.

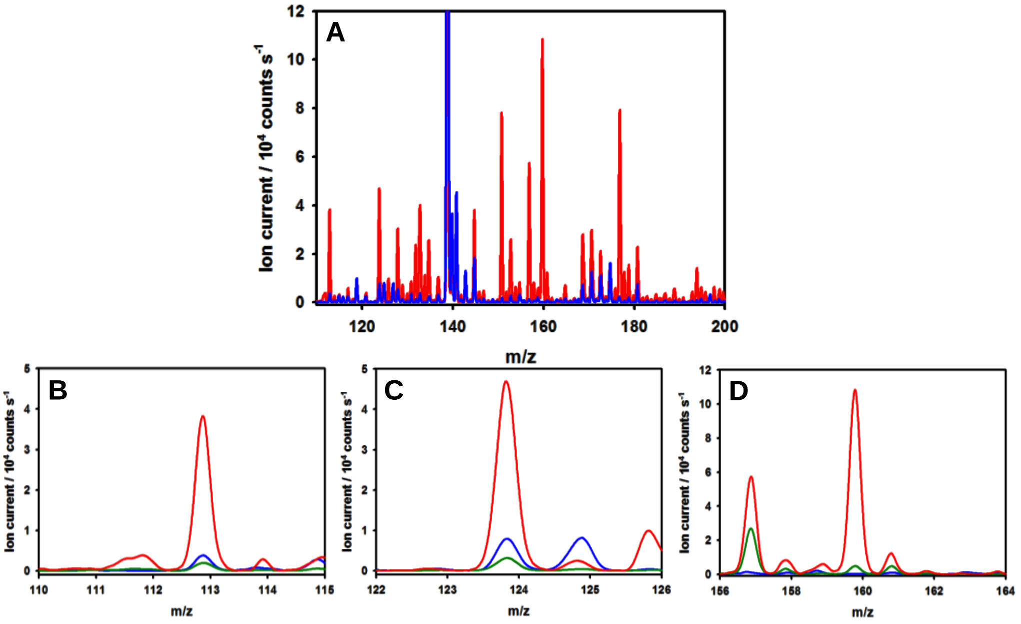

Figure 5.6 – Negative ion ESI mass spectra of *i*) blue trace: 10 mM Py in 10% (v/v) 2-PrOH/H_2O initial solution; *ii*) red trace: 10 mM Py in 10% (v/v) 2-PrOH/H_2O saturated with CO_2 and irradiated at 254 nm for 1 h. B), C) and D) zoom into the mass ranges where the $m/z^- = 113$, 124 and 160 products appear, respectively and, in addition, report also the photolysis experiment performed with 10 mM Py in 10% (v/v) 2-PrOH/H_2O irradiated at 254 nm for 1 h, in the absence of CO_2 (dark green trace).

Interestingly, also odd $m/z^- = 113$ was identified as a CO_2-containing product and was tentatively ascribed to $(HCOO)_2Na^-$, as generally accepted in mass-spectrometry [18]. Aside displaying the same behavior of carboxylates species, thus strictly requiring both carbon dioxide and 254 nm-irradiation (Figure 5.6(B)), the adduct formation provided strong evidence for the occurrence of the $2e^-$-reduction of CO_2 to $HCOO^-$ (see below).

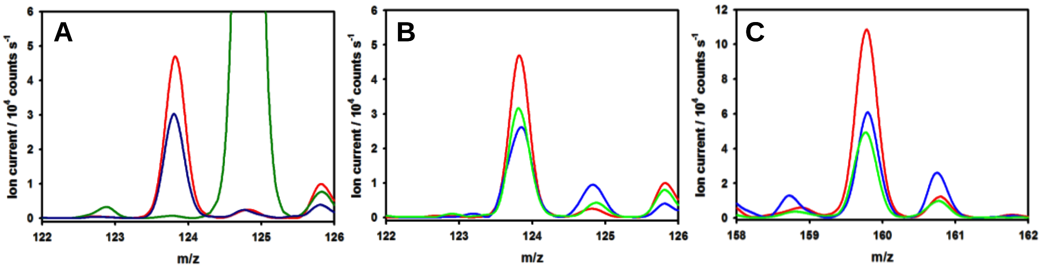

Figure 5.7 – A) Negative ion ESI mass spectra of *i*) red trace: 10 mM Py in 10% (v/v) 2-PrOH/H_2O saturated with CO_2 and irradiated at 254 nm for 1 h; *ii*) dark blue trace: 10 mM Py in neat H_2O saturated with CO_2 and irradiated at 254 nm for 1 h; *iii*) dark green trace: 10% (v/v) 2-PrOH/H_2O saturated with CO_2 and irradiated at 254 nm for 1 h, in the absence of Py. B) and C) Negative ion ESI mass spectra of Py solutions in 10% (v/v) 2-propanol/water mixtures, saturated with CO_2 and irradiated at 254 nm for 1 h. In details: [Py] = 1 mM (green trace); [Py] = 10 mM (red trace); [Py] = 100 mM (blue trace).

In addition, the photolysis of pyridine in 2-PrOH/H_2O saturated with CO_2 was also performed by irradiating the solution for longer time (*i.e.*, 2 hours) and, interestingly, m/z^- = 124 carbamic anion peak intensity dropped down to zero (Figure 5.8(B)), maybe due to competing reactions involving pyridine-like species and radicals in solution (for reaction kinetic and thermodynamic see Section 5.2). Conversely, the m/z^- = 113 anion peak intensity was much higher than that produced under 1 hour irradiation (Figure 5.8(A)) suggesting that, by increasing the irradiation time, CO_2 had been reduced to a higher extent.

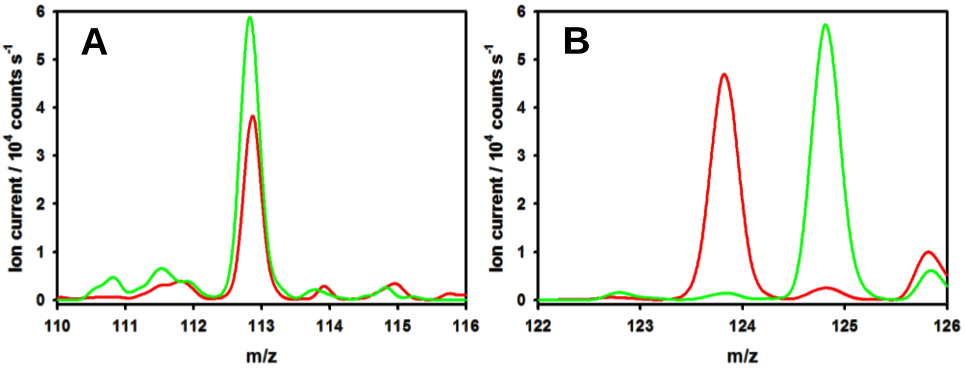

Figure 5.8 – Negative ion ESI mass spectra of *i*) red trace: 10 mM Py in 10% (v/v) 2-PrOH/H_2O saturated with CO_2 and irradiated at 254 nm for 1 h; *ii*) green trace: 10 mM Py in 10% (v/v) 2-PrOH/H_2O saturated with CO_2 and irradiated at 254 nm for 2 h. A) and B) zoom into the mass ranges where the m/z^- = 113 and 124 products appear, respectively.

As a confirmation to the anions structural assignments, these three species were found to split 44 Da CO_2 neutrals *via* collisionally induced dissociation, as reported in the MS^2 spectra of Figure 5.9.

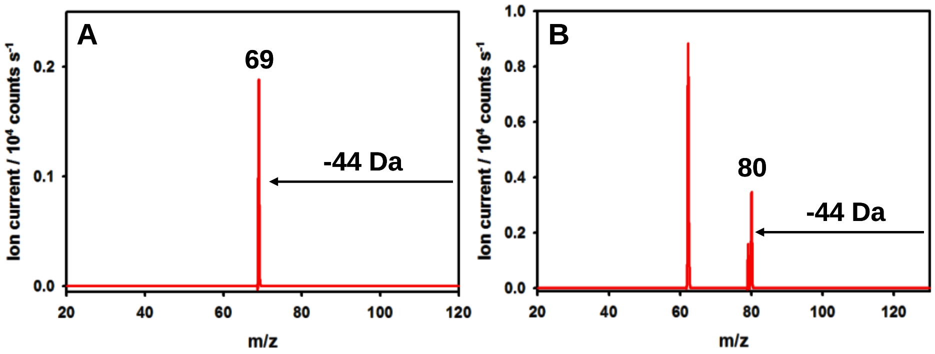

Figure 5.9 – A) MS^2 of $m/z^- = 113$; B) MS^2 of $m/z^- = 124$.

All negative species represented evidence of a process induced by the photoexcitation of Py in *iso*-propyl alcohol (see reaction R5.1 above), followed by reaction R5.3:

$$\text{1-PyH}^{\bullet} + CO_2 \rightarrow {}^{\bullet}\text{Py-1-COOH} \qquad \text{(R5.3)}$$

and subsequent reactions of $^{\bullet}$Py-1-COOH toward the observed products (see Scheme 5.1).

The reasons why 1-PyH$^{\bullet}$ is notably able to add CO_2 through a relatively accessible reaction pathway at room temperature have already been presented (see Section 2.2). The net process here discussed, which can be envisaged as a net H-atom transfer from 1-PyH$^{\bullet}$ to linear O=C=O, accounted for the so-called Proton-Coupled Electron Transfer (PCET) mechanism initiated by the nucleophilic attack by the pyridine N lone pair at the expense of the electrophilic CO_2 carbon atom, followed by proton-transfer [19].

Previously reported ESR studies provided evidence that most of the unpaired spin in 1-PyH$^{\bullet}$ is effectively localized on the N-atom, identified as the electron-richest atom of the pyridine ring [20,8,21,22].

Proton transfer, which appeared to be largely mediated by surrounding water molecules, has a dramatic effect in stabilizing the product and lowering the activation barrier for $^{\bullet}$Py-1-COOH formation (R5.3). Once the product is stabilized into the carbamic form 1-PyCOO$^-$, pyridine regains its original aromaticity whereas CO_2 is halfway reduced to formate through a mechanism triggered by pyridine (see Scheme 5.1).

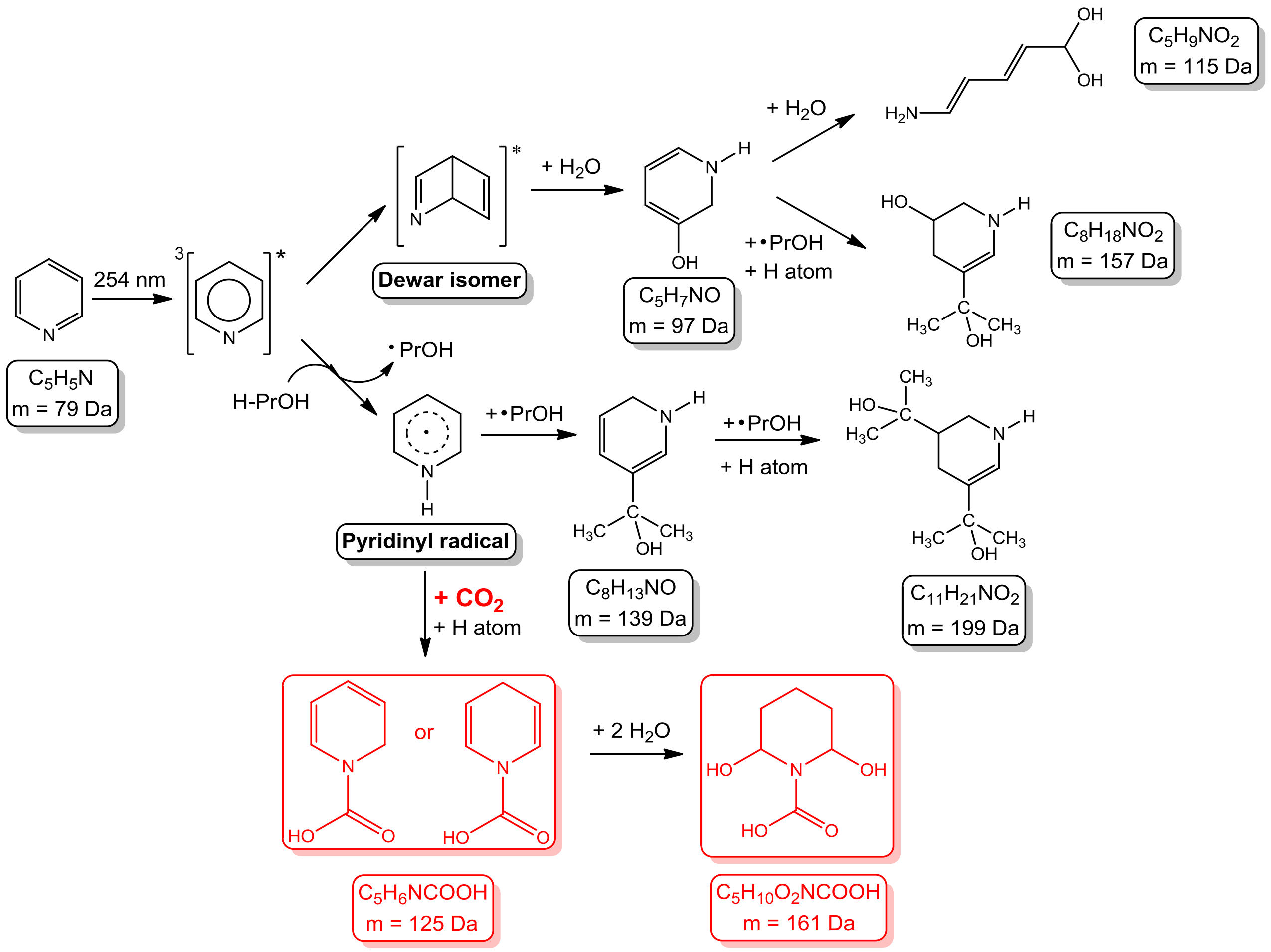

Scheme 5.1 – Possible reaction mechanism explaining the pathways leading to the observed products in the 254 nm photolysis of pyridine in 2-PrOH/H_2O mixtures containing dissolved carbon dioxide. The main products involving CO_2 reduction (*i.e.*, carbamic species detected as anions) are highlighted in red.

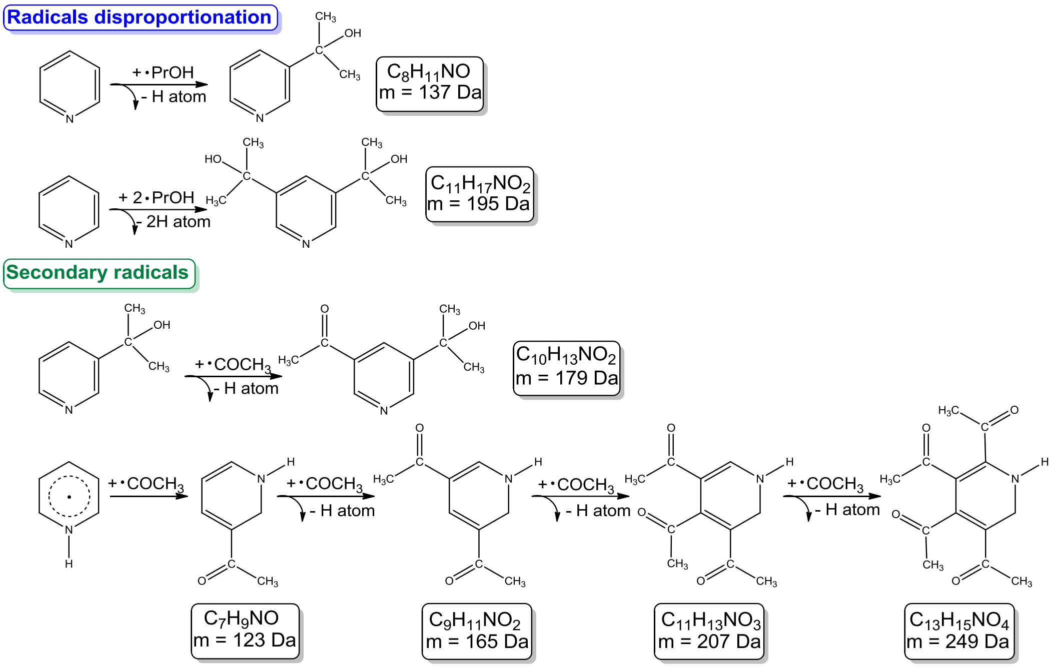

Scheme 5.2 – Possible reaction mechanism explaining the radical disproportionation pathways (top section) and the reactions involving secondary radicals (*i.e.*, acetyl radical) (bottom section).

5.2 Kinetic and thermodynamic implications

An estimation of the order of magnitude of the rate constant *k*(5.3) at which 1-PyH$^\bullet$ adds CO_2 (R5.3) can be obtained by assuming that R5.3 competes with the faster radicals termination reactions in the system, occurring within pyridinyl radicals and a general radical formed in the system, X$^\bullet$:

$$\text{1-PyH}^\bullet + \text{X}^\bullet \rightarrow \text{1-PyH-X} \qquad \text{(R5.4)}$$

From the reported photon output of the adopted lamp: $F = 3 \times 10^{15}$ photons s^{-1} = 5×10^{-9} moles s^{-1} [23], which can be fully absorbed by a pyridine solution with concentration higher than 1 mM (thus, in line with the [Py] used in photolysis experiments), the upper limit to the free radicals initiation rate in the system was determined, *i.e.*, $R_i = 5 \times 10^{-7}$ M s^{-1}.

Furthermore, by assuming a typical value of diffusionally controlled radical recombination rate constant, $k(5.4) \sim 1 \times 10^9$ M s^{-1} (predicted according to the Debye's equation for a diffusion controlled process in a water(90%)/isopropanol(10%) system [24]), an upper limit for steady state radical concentration could be calculated, *i.e.*, $[\text{1- PyH}^\bullet]_{SS} \leq 1 \times 10^{-8}$ M [1].

By making the reasonable assumption that the overall quantum yield of the products resulting from the addition of 1-PyH$^\bullet$ + CO_2 is small, *i.e.*, $\Phi_{CO2} \sim 0.01 - 0.1$ (in accordance with the values for pyridine photolysis in *iso*-propyl alcohol proposed by Livingston *et al.* [5,6]), reaction R5.3 may be neglected as a first approximation into the overall radical mass balance.

However, taking into account that [CO_2] dissolved in solution, under saturation conditions, is ~ 3.5×10^{-2} M [25], *i.e.*, several order of magnitude higher than the concentration of photoproduced 1-PyH$^\bullet$, the bi-molecular collision probability between pyridinyl radicals and CO_2 is sufficiently higher and equation 5.1 was derived:

$$\Phi\ 2\ k(5.4)\ [1\text{- PyH}^\bullet]_{SS} \sim k(5.3)\ [1\text{- PyH}^\bullet]_{SS}\ [CO_2] \qquad (5.1)$$

Thus, $k(5.3)/\Phi \leq 570$ M s^{-1}. This rough estimation led to the more general statement that the order of magnitude of this reaction is $k_3 \sim O(10)$ M s^{-1}, under the investigated conditions.

Hence, by applying the Arrhenius equation also assuming a typical value of the A-factor for the polyatomic radical addition (*i.e.*, pyridinyl addition to linear CO_2), $A_3 \sim 10^8$ M s^{-1} [26], R5.33 activation energy was calculated:

$$\text{from } k(5.3) = A_3 \exp(-E_3/RT) \qquad (5.2)$$

$$E_3 \geq 9 \text{ kcal mol}^{-1}$$

This value is only a few kcal mol^{-1} smaller, but certainly comparable, than the 13.5 – 13.6 kcal mol^{-1} energy barrier calculated by Musgrave *et al.* for the addition of 1- PyH$^\bullet$ to CO_2 in neat water [15,19].

Finally, the compatibility of the estimated kinetic parameters with the thermochemical parameters for R5.3 was checked. Table 5.1 reports the estimated values for enthalpies of formation and dissociation energies of relevant gas-phase species at 298 K. By making the assumption that the enthalpy of hydration of these neutral species is small, so that they will nearly compensate each other, the semi-quantitative arguments presented appear reasonable also in aqueous solution.

species	ΔH_f, D (kcal mol^{-1})
CO_2	-94 [27]
Py	33
D[•$C(CH_3)_2O$–H]	25 [28]
1-PyH•	< 60[a], 56 [29]
HPy-1-COOH	-61[b]
•Py-1-COOH	-36[c]

Table 5.1 – Thermodynamic data for gas-phase species at 298 K. ([a]), from D[1-Py-H•] > D[•$C(CH_3)_2O$–H], as from [5,30]; ([b]) from group additivity [31]; ([c]) the reported value takes into account that the dissociation of the C-H bond in HPy-1-COOH yields a di-allylic •Py-1-COOH radical (i.e., D[HPy-1-COOH] ~ 77 kcal mol^{-1} [32,33]).

Since •PrOH can reduce Py by transferring an H-atom [30], the dissociation energy of the N–H bond in 1-PyH• (*i.e.*, D[1-PyH•]) can be assumed higher than the O–H bond in 2-propanol radical (*i.e.*, D[•$C(CH_3)_2O$–H]); thus the following relation can be hypothesised:

$$D[1\text{-PyH}^\bullet] > (D[^\bullet C(CH_3)_2O\text{–H}] = 25 \text{ kcal mol}^{-1}) \qquad (5.3)$$

This lower limit is in agreement with the dissociation energy D[1-PyH•] ~ 30 kcal mol^{-1} value, recently obtained from quantum mechanical calculations [29]. These D[1-PyH•] values led to an estimation for the enthalpy of formation of the pyridinyl radicals: ΔH_f = 56 – 60 kcal mol^{-1}.

Hence, the required enthalpy of formation of •Py-1-COOH (R5.3) can be evaluated from that of the parent di-hydropyridine carboxylic acid (ΔH_f [HPy-1-COOH] = 61 kcal mol^{-1}), as obtained from group additivity [31], by assuming that the dissociation of the C–H bond in HPy-1-COOH generates a di-allyl 3-pentadienyl radical, *i.e.*, D[HPy-1-COOH] ~ 77 kcal mol^{-1} [32,33].

Thus, from the data reported in Table 5.1:

$$\Delta H(R5.3) = [-36 - (-94) - 58] = +2 \text{ kcal mol}^{-1} \qquad (5.4)$$

within a few kcal mol^{-1} and reasonably smaller than both that experimentally estimated ($E_3 \geq 9$ kcal mol^{-1}, as determined from 5.3) and the lower bound reported by Musgrave et *al.* for the reaction occurring in water clusters (E ~ 14 kcal mol^{-1}, [19]), since the parameters adopted for their calculations were estimated for gas-phase species (see Table 5.1).

Therefore, •Py-1-COOH, the neutral product of R5.3, can be considered as a marginally stable radical species that could readily revert to the reactants (*i.e.*, 1-PyH• and CO_2) but could be easily stabilized as •Py-1-COO^- by releasing a proton, or as closed-shell *via* H-atom abstraction by disproportionation with •PrOH.

5.3 Conclusion

It was experimentally proved that photopromoted 1-pyridinyl radicals (1-PyH$^{\bullet}$) do react, in homogeneous conditions, with CO_2 in isopropanol/water yielding products that accounted for a 2e$^-$-reduction process.

Along with those involving carbon dioxide, a detailed characterization was provided of all the species obtained form pyridine photolysis which include photohydration products, as well as those obtained from radicals disproportionation and secondary radicals reactions.

The homogeneous photoreduction of CO_2 was proved to proceed through a carbamic species formation (HPy-1-COOH), triggered by a stepwise mechanism where electron transfer (ET) from 1-PyH$^{\bullet}$ to CO_2 preceded proton transfer (PT).

The collected results showed that α-hydroxyalkyl radicals, produced from 2-PrOH photolysis, along with 254 nm-actinic radiation, were strictly required for the overall reaction. Only formate ($HCOO^-$) was obtained providing evidence that, at least for the 2-electron reduction step, metal surfaces are not a requirement for pyridine-catalyzed CO_2 reduction. Formate concentration was also proved to increase with increasing the irradiation time and the optimal pyridine concentration, that accounted for the highest yield in HPy-1-COOH formation, was fixed at 10 mM, confirming previous findings of Bocarsly *et al.* for the analogous photoelectrochemical process.

REFERENCES

[1] F. Riboni, E. Selli, M.R. Hoffmann, A.J. Colussi, *J. Phys. Chem. A* **2014**, just accepted.

[2] K.E. Wilzbach, D.J. Rausch, *J. Am. Chem. Soc.* **1970,** *92,* 2178.

[3] L. Kaplan, K.E. Wilzbach, J.W. Pavlik, *J. Am. Chem. Soc.* **1972,** *94*, 3283.

[4] J.C. Andre, M. Niclause, *J. Chem. Educ*. **1977**, *54*, 387.

[5] H. Zeldes, R. Livingston, *J. Phys. Chem.* **1972,** *76*, 3348.

[6] H. Zeldes, R. Livingston, *J. Magn. Reson.* **1977,** *26*, 103.

[7] S. Terokubota, K. Akiyama, T. Ikoma, Y. Ikegami, *J. Phys. Chem.* **1991,** *95*, 766.

[8] P. Neta, L.K. Patterson, *J. Phys. Chem.* **1974,** *78*, 2211.

[9] P.W. Seakins, M.A. Blitz, *Annu. Rev. Phys. Chem*. **2011**, *62,* 351.

[10] J.A. Keith, E.A. Carter, *J. Phys. Chem. Lett.* **2013,** *4*, 4058.

[11] Y. Yan, J. Gu, A.B. Bocarsly, *Aerosol and Air Qual. Res.* **2014,** *14*, 515.

[12] G. Seshadri, C. Lin, A.B. Bocarsly, *J. Electroanal. Chem.* **1994,** *372,* 145.

[13] E.E. Barton, D.M. Rampulla, A.B. Bocarsly, *J. Am. Chem. Soc.* **2008,** *130*, 6342.

[14] E. Barton Cole, P.S. Lakkaraju, D.M. Rampulla, A.J. Morris, E. Abelev, A.B. Bocarsly, *J. Am. Chem. Soc.* **2010,** *132*, 11539.

[15] A.J.Morris, R.T. McGibbon, A.B. Bocarsly, *Chemsuschem* **2011,** *4*, 191.

[16] A.B. Bocarsly, Q.D. Gibson, A.J. Morris, R.P. L'Esperance, Z.M. Detweiler, P.S. Lakkaraju, E.L. Zeitler, T.W. Shaw, *ACS Catal.* **2012**, *2*, 1684.

[17] A.M. Appel, J.E. Bercaw, A.B. Bocarsly, H. Dobbek, D.L. DuBois, M. Dupuis, J.G. Ferry, E. Fujita, R. Hille, P.J.A. Kenis, C.A. Kerfeld, R.H. Morris, C.H.F. Peden, A.R. Portis, S.W. Ragsdale, T.B. Rauchfuss, J.N.H. Reek, L.C. Seefeldt, R.K. Thauer, G.L. Waldrop, *Chem. Rev.* **2013**, *113*, 6621.

[18] http://www.sepscience.com/Information/Archive/MS-Solutions/233-/MS-Solutions-3-Dealing-with-Metal-Adduct-Ions-in-Electrospray-Part-1.

[19] C.H. Lim, A.M. Holder, C.B. Musgrave, *J. Am. Chem. Soc.* **2013,** *135*, 142.

[20] J.K. Dohrmann, W. Kieslich, *J. Magn. Reson.* **1978,** *31*, 69.

[21] H.J. Bower, J.A. McRae, M.C.R. Symons, *J. Chem. Soc A* **1968**, 1918.

[22] C.J. Rhodes, H. Morris, I.D. Reid, *Magn. Res. Chem.* **2001,** *39*, 438.

[23] P.V. Johnson, R. Hodyss, V.F. Chernow, D.M. Lipscomb, J.D. Goguen, *Icarus* **2012,** *221*, 800.

[24] P. Debye, *Trans. Electrochem. Soc.* **1942**, *82*, 265.

[25] J. Tokunaga, *J. Chem. Eng. Data*, **1975**, *20*, 41.

[26] B. Abel, J. Assmann, M. Buback, C. Grimm, M. Kling, S. Schmatz, J. Schroeder, T. Witte, *J. Phys. Chem. A* **2003,** *107*, 9499.

[27] NIST Standard Reference Database Number 69. U.S. Department of Commerce, 2011.

[28] S.W. Benson, *Thermochemical Kinetics*. 2nd Ed. Wiley: New York, NY, 1976.

[29] B. Golec, P. Das, M. Bahou, Y.P. Lee, *J. Phys. Chem. A* **2013,** *117*, 13680.

[30] P. Neta, *Radiation Research* **1972,** *52*, 471.

[31] K.G. Joback, R.C. Reid, *Chem. Eng. Comm.* **1987,** *57*, 233.

[32] F. Agapito, P.M. Nunes, B.J.C. Cabral, R.M.B. dos Santos, J.A. Simooes, *J. Org. Chem.* **2007,** *72*, 8770.

[33] K.B. Clark, P.N. Culshaw, D. Griller, F.P. Lossing, J.A.M. Simoes, J.C. Walton, *J. Org. Chem.* **1991,** *56*, 5535.

Chapter 6

Fenton oxidation of gaseous isoprene on aqueous surfaces

ABSTRACT – Experimental evidence was provided that gaseous isoprene, ISO(g), is oxidized into soluble species on the surface of aqueous acidic $FeCl_2$ solutions simultaneously exposed to H_2O_2(g). In the performed experiments, ISO(g) and/or H_2O_2(g) streams intersected with aqueous $FeCl_2$ microjets at acidic pH ~ 2, for *ca.* 10μs. The products formed in the reactive encounters were identified *in situ via* online electrospray ionization mass spectrometry. $(ISO)_nH^+$ oligomers were generated from ISO(g) on the surface of pH < 4 water drops and were subsequently oxidized into myriad of products, whose yields totally exceeded 5%. MS^2 analysis revealed that the positive ions, derived from the protonation of neutral products, split H_2O and O neutrals, whereas the less abundant negative carboxylate ion products underwent CO, H_2O and CO_2 losses.

Noteworthy, all the products were fully quenched in the presence of *tert*-butyl alcohol, an efficient $^{\bullet}OH$ radicals scavenger.

The results appeared consistent with an oxidation process triggered by the addition of $^{\bullet}OH$, produced *in situ via* Fenton reaction (Fe^{2+}(aq) + H_2O(g)), to isoprene oligomers, $(ISO)_nH^+$, followed by fast reactions involving dissolved

H_2O_2, $HO_2^{\bullet}$ and O_2, that led to polyols, carbonyls and, to a lower extent, carboxylic acids.

Performed experiments demonstrated that gas-phase olefins can be oxidized upon colliding on the surface of Fe-containing acidic aqueous drops, mimicking typical tropospheric conditions.

All details concerning the performed experiments and the adopted set up are thoroughly described in Sections 3.3.5 and 3.3.6, respectively.

Keywords – Secondary Organic Aerosol; Heterogeneous Atmospheric Chemistry; Interfacial Atmospheric Chemistry; Surface Protonation; Atmospheric Iron; Air-Water Interface.

6.1 Results and Discussion

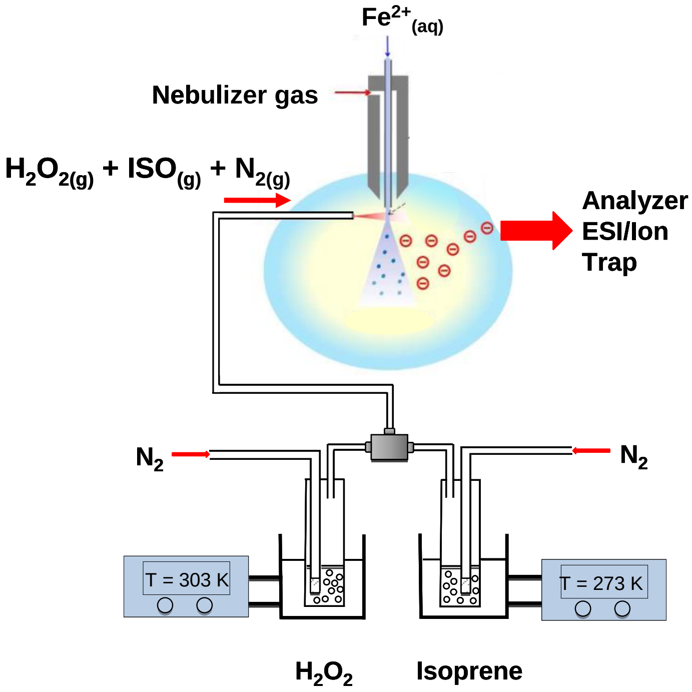

Scheme 6.1 – Experimental set up. Microjets of 1 µM aqueous $FeCl_2$ at pH ~ 2 were continuously injected at 25 µL min^{-1} into the spraying chamber of an electrospray ionization mass spectrometer, where they were alternatively exposed to gas streams consisting of *a*) ISO(g)/N_2(g); *b*) H_2O_2(g)/N_2(g); or *a*) + *b*).

Fenton reaction may produce $^{\bullet}OH$ radicals *via* a one-electron transfer (*i.e.*, according to the Haber–Weiss mechanism, R6.1) and $Fe^{IV}O^{2+}$ ferryl species *via* a two-electron process through O atom transfer (*i.e.*, Bray–Goring mechanism, R6.2):

$$Fe^{2+} + H_2O_2 \rightarrow Fe^{3+} + OH^- + \bullet OH \qquad (R6.1)$$

$$Fe^{2+} + H_2O_2 \rightarrow Fe^{IV}O^{2+} + H_2O \qquad (R6.2)$$

As represented in Scheme 6.2, initial step is followed by further reactions that, recycling Fe(II), concurrently generates $HOO^\bullet$ radicals and $O_2(g)$ as additional products [1-3].

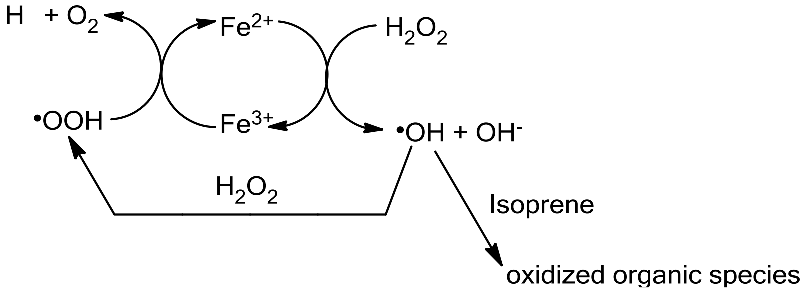

Scheme 6.2 – Fe^{2+}/Fe^{3+} catalytic Fenton reactions, involving H_2O_2, and faith of the produced $^\bullet OH$ in the presence of organic species (*i.e.*, isoprene).

Recent publications reported that R6.2 is the dominant channel at the air-water interface, yielding mono- and poly-iron species containing the ferryl $Fe^{IV}O^{2+}$ moiety, which may disproportionate with Fe^{2+} into Fe^{3+} or react with suitable O atom acceptors [4]. Moreover, Fe(II)-catalyzed decomposition of gaseous H_2O_2 at the air-water interface had been shown to occur ~ 10^3 times faster than in bulk water [4]. Negative ES mass spectra are reported in Figure 6.1.

As previously reported, mass spectral multiplets at $m/z^- = 161$, 163 and 165 corresponded to $Fe^{II}Cl_3^-$. The characteristic multiplet patterns arose from natural abundance $^{35}Cl(75\%)$ and $^{37}Cl(25\%)$ chlorine isotopes which unequivocally led to the determination of the number of chlorine ions contained in each detected species and, for that reason, to the molecular composition of these negatively charged ions [4,5].

Additional main clusters were also detected at *i*) $m/z^- = 196$, 198, 200 and 202, which was readily assigned to $Fe^{II}Cl_4^-$, in accordance to [4] and *ii*) $m/z^- = 303$, 305 and 307 corresponding to the mixed valence dinuclear ferryl $O{=}Fe^{IV}{\cdot}Cl{\cdot}Fe^{II}Cl_4^-$, attributed on the basis of the peak masses and the characteristic Cl_5-multiplet pattern.

These products formation was extensively inhibited when switching from $H_2O_2(g)/N_2(g)$, green trace, to $ISO(g)/N_2(g)$ mixtures, blue trace, as expected due to the lack of oxidants available at the surface of aqueous Fe^{II} droplets.

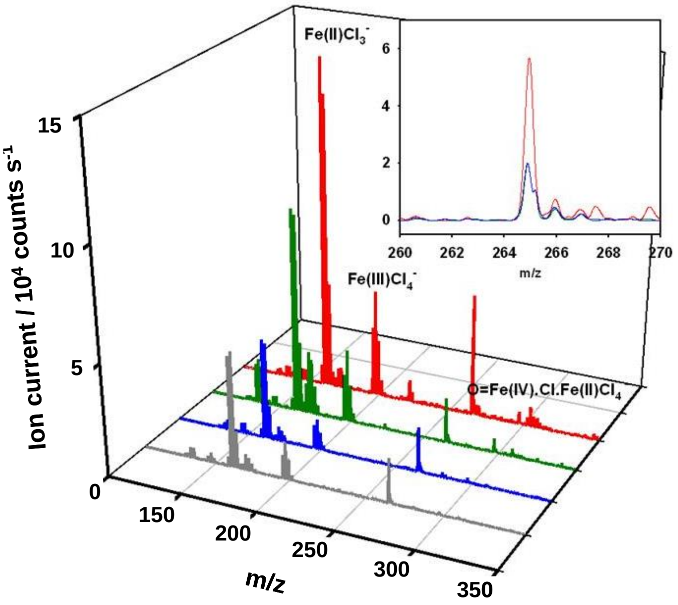

Figure 6.1 – Negative ion ESI mass spectra of $FeCl_2$ microjets exposed to: N_2(g) (grey trace); ISO(g)/N_2(g) (blue trace); H_2O_2(g)/N_2(g) (green trace); ISO(g)/H_2O_2(g)/N_2(g) (red trace) streams. The inset zooms into the mass range where the m/z$^-$ = 265 product appeared. Note that the intensity of the m/z$^-$ = 265 species significantly increased upon the simultaneous presence of ISO(g) and H_2O_2 (g). [ISO(g)] ~ 5 × 10^{15} molecules cm^{-3}; [H_2O_2 (g)] ~ 4 × 10^{14} molecules cm^{-3}.

When exposing Fe^{II} aqueous surfaces to ISO(g)/H_2O_2(g)/N_2(g) mixtures, a multitude of minor peaks was formed but, noteworthy, is the appearance of a new significant peak at m/z$^-$ = 265 (inset of Figure 6.1), which was tentatively ascribed to the anion of a carboxylic acid product and whose intensity appeared particularly marked only when ISO(g) and H_2O_2(g) were simultaneously sparged toward the liquid microjet (red trace).

The MS^2 of the m/z$^-$ = 265 anion, shown in Figure 6.2, confirmed the proposed species composition. Indeed, the 44 and 28 Da neutral losses were consistent with the presence of carboxylic and a carbonyl functionalities, respectively, splitting CO_2 and CO [6].

The detection of an intense peak at m/z$^+$ = 267 (see below, Figure 6.3(B)), which corresponded to the doubly protonated counterpart of the m/z$^-$ = 265 anion, implied the formation of a 266 Da neutral acid, derived from the oxidation of the most abundant $(ISO)_3H^+$, m/z$^+$ = 205, oligomer at the air-water interface under present conditions (see below).

The *algebra* linking $(ISO)_3$ oligomer with neutral 266 Da product is $(ISO)_3$ + 4 O-atom – 2 H-atom (*i.e.*, 204 + 64 – 2) and led to the assignment of $C_{15}H_{22}O_4$ molecular formula to the acid peaking at m/z$^-$ = 265.

Possible structures for the 204 Da $(ISO)_3$ sesquiterpenes and associated 266 Da $C_{15}H_{22}O_4$ products are depicted in Scheme 6.3.

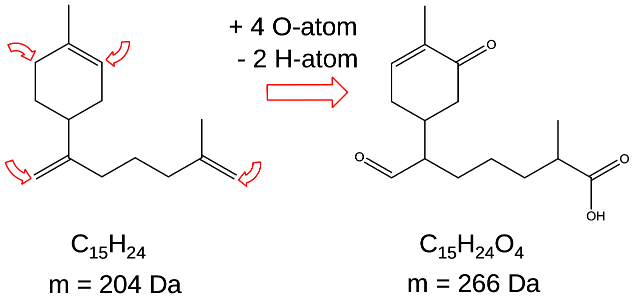

Scheme 6.3 – Possible structures for the $(ISO)_3$ oligomer ($C_{15}H_{24}$, m = 204 Da) and associated oxidized carboxylic acid ($C_{15}H_{22}O_4$, m = 266 Da)

The remarkable finding that protonated isoprene $(ISO)_3H^+$ added 4 O-atoms and lost 2 H-atom to produce $C_{15}H_{22}O_4$ species suggested that ~ 5 O-atom per $(ISO)_3$ unit should be available at the air-water interface within ~ 10 µs which, being the gas-liquid contact time, corresponded to the accessible time for the reaction to occur.

As a consequence, $H_2O_2(g)$ is expected to generate oxidant species (*i.e.*, $^{\bullet}OH$, $HOO^{\bullet}$, O_2 and $Fe^{IV}O^{2+}$) in excess with respect to $(ISO)_nH^+$ in the outermost interfacial layers, where, under the experimental conditions, they were rapidly consumed by reacting with isoprene polymers, before they could diffuse into deeper layers.

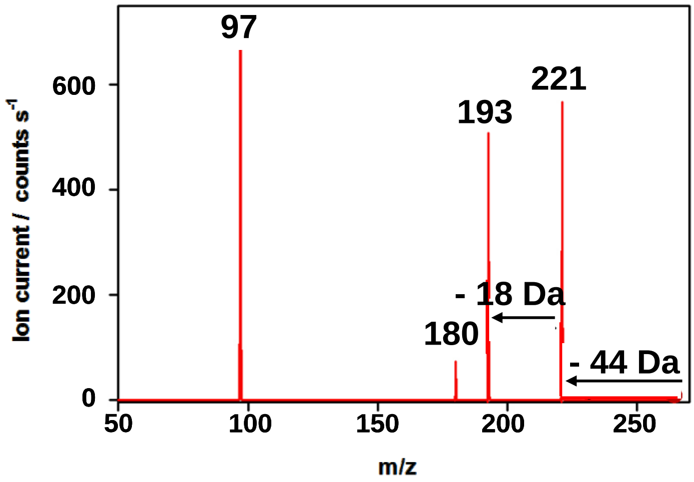

Figure 6.2 – MS^2 of $m/z^- = 265$.

Positive ES mass spectra appeared more complex. Figures 3(A) and (B) show positive ESI mass spectra of the surface of 1 µM $FeCl_2$ aqueous microjets exposed to $ISO(g)/N_2(g)$, $H_2O_2(g)/N_2(g)$ and $ISO(g)/H_2O_2(g)/N_2(g)$ mixtures.

Gaseous isoprene gave rise to a series of protonated oligomer homologues, *via* cationic polymerization at the air-water interface (Figure 6.3(A)):

$$(ISO)_nH^+,\ n = 1 - 8$$

$$m/z^+ = 137\ (n = 2),\ 205\ (n = 3),\ 273\ (n = 4)$$

All these species were conspicuously absent from the mass spectra of ISO previously dissolved in pH ~ 2 water, proving that the protonation of isoprene and, hence, the cationic polymerization to $(ISO)_nH^+$ took place only at the air-water interface, rather than in bulk solution, triggered by the acidity of interfacial H_3O^+, which is enhanced by the surface limited hydration [7]. Indeed, previous studies reported that strongly acidic hydronium species, H_3O^+(if), emerged to the surface of water even in mildly acidic bulk conditions (pH ~ 4) [8-10].

H_3O^+(if) are partially hydrated species and, like H_3O^+(g), can protonate gases provided that their proton affinities (PA) are larger than that of gaseous water [11].

The majority of nonalkane gases (*e.g.*, gaseous isoprene) fulfil the latter requirement and, hence, can be protonated on the surface of mildly acidic water.

For example, the proton affinity of isoprene has been estimated to be 197 kcal mol^{-1} [12], PA(H_2O) being 165 kcal mol^{-1} [11].

From saturation curves determined by measuring the variation of gaseous isoprene oligomers concentration as a function of the aqueous media pH, Enami *et al.* provided an estimation of the rate constants for the following reactions:

$$H_3O^+(if) + ISO(g) \rightarrow (ISO)H^+ \qquad (R6.1)$$

$$(ISO)H^+(if) + ISO(g) \rightarrow (ISO)_2H^+ \qquad (R6.2)$$

$$(ISO)_2H^+ + ISO(g) \rightarrow (ISO)_3H^+ \qquad (R6.3)$$

where $k(6.1) < k(6.2) \sim k(6.3)$.

In this context, $(ISO)H^+$ should be considered as an intermediate and its formation assumed as the rate-determining step in the protonation reaction at the gas-water interface [7]. Once formed, it is readily converted to $(ISO)_2H^+$ ($C_{10}H_{17}^+$, $m/z^+ = 137$) which represents the first oligomer appearing in the positive ESI mass spectra with relatively sizeable intensity.

Under the adopted experimental conditions, the extent of oligomerization clearly increased with respect to previous publications [7], yielding up to $(ISO)_8H^+$ oligomers (See Figure 6.3(A)), due to the larger [ISO(g)] adopted.

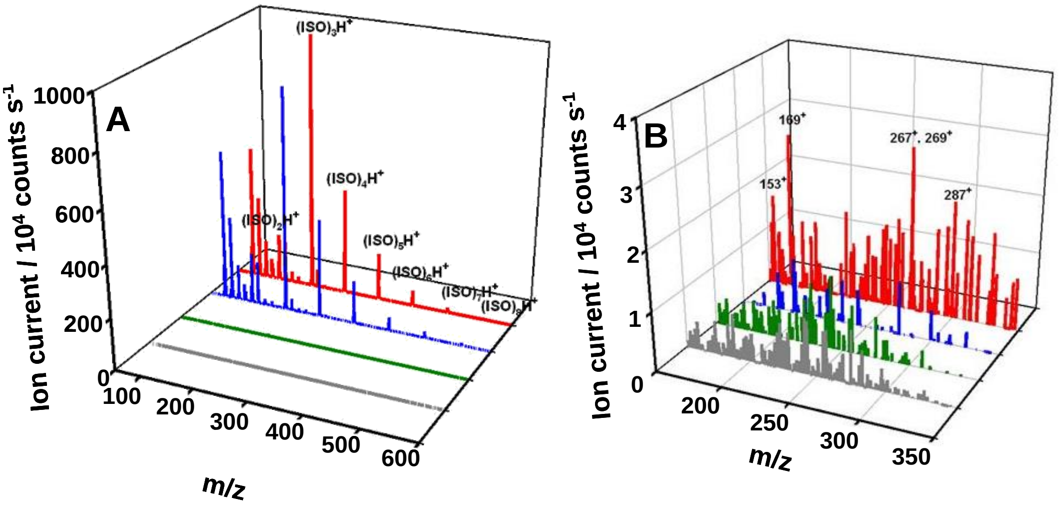

Figure 6.3 – Positive ion ESI mass spectra of 1 µM $FeCl_2$ at pH ~ 2 microjets exposed to: N_2(g) (grey traces); ISO(g)/N_2(g) (blue traces); H_2O_2(g)/N_2(g) (green traces); ISO(g)/H_2O_2(g)/N_2(g) (red traces). A: spectra in the $m/z^+ = 50 – 600$ Da range. B: spectra of the less abundant product species in the $m/z^+ = 150 – 350$ Da range. Note the 250:1 Y-axis scale expansion in B relative to A. The largest $(ISO)_{1\text{-}8}H^+$ signals of A were subtracted from the blue and red trace spectra of B for clarity. [ISO(g)] ~ 5×10^{15} molecules cm^{-3}; [H_2O_2(g)] ~ 4×10^{14} molecules cm^{-3}.

The most abundant of such species was the $m/z^+ = 205$ $(ISO)_3H^+$ oligomer (blue and red traces in Figure 6.3(A))

The MS^2 fragmentation patterns of isoprene oligomers revealed 28 (CH_2=CH_2) and 42 (CH_3–CH=CH_2) Da neutral losses (see Figure 6.4(A) which, by way of example, reports the MS^2 of $m/z^+ = 137$ $(ISO)_2H^+$ oligomer), as expected from polyolefins characterized by terminal –CH=CH_2 and –C(CH_3)=CH_2 groups [5].

Predictably, the exposure of $FeCl_2$ microjets to H_2O_2(g)/N_2(g) stream did not lead to any detectable positive ion products (green trace of Figure 6.3(A)), whereas the simultaneous sparging of ISO(g) along with H_2O_2(g), red traces, gave rise to the formation of a large number of species (Figure 6.3(B)).

The signals were associated with products of fast oxidation of $(ISO)_nH^+$, initiated by $^{\bullet}$OH radical addition to the isoprene double bonds, followed by the combined action of $^{\bullet}$OOH and O_2 species on the resulting free radicals (as suggested in Scheme 6.2). As mentioned above, also oxidation products were assumed to be the result of extremely fast reactions (*i.e.*, within ~ 10 µs) involving multiple oxidation steps at the interfacial layers where the oxidants, generated from Fe^{II} and H_2O_2(g) contact, reached high concentrations.

The detection of several relatively small signals was consistently attributed to the multiple ways in which the three main oxidants ($^{\bullet}$OH, HOO$^{\bullet}$ and O_2) can react with all the possible structural isomers of $(ISO)_{1\text{-}8}H^+$ oligomers.

Though the reduced intensity of these m/z$^+$ oxidation products signals, experiments performed under different gas compositions (Figure 6.5) revealed their validity as actually evolved species (for deeper discussion, see below).

Figure 6.4(C) reports the MS^2 collisionally induced fragmentation spectra of some of these oxidation products which, beside the 42 Da neutral losses typical of the molecular framework of parental $(ISO)_nH^+$ (and already discussed for m/z$^+$ = 137 $(ISO)_2H^+$), displayed 16 (O-atom), 18 (H_2O) and 28 (CO) Da losses, typical fragmentation of species containing epoxide, alcohol and carbonyl functionalities, respectively [6].

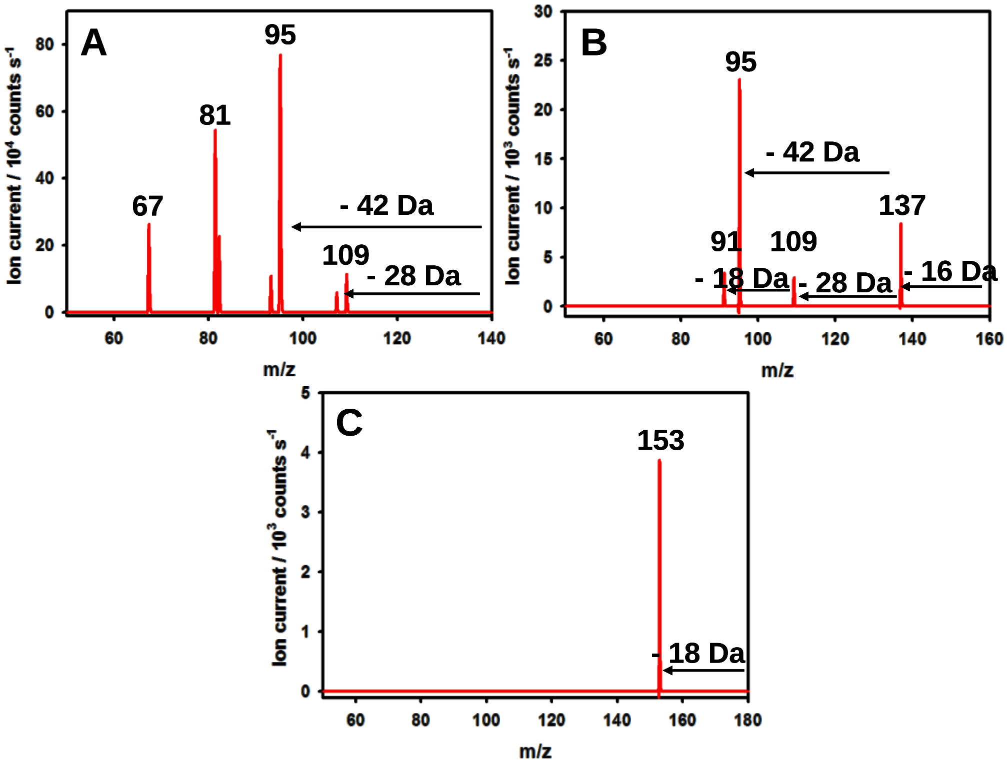

Figure 6.4 – A) MS^2 of $(ISO)_2H^+$, m/z$^+$ = 137; B) MS^2 of m/z$^+$ = 153 and C) MS^2 of m/z$^+$ = 171.

The progeny of the most abundant species was traced from their molecular formulas and typical fragmentation patterns.

Thus, from the addition of 2 $^{\bullet}OH$ radicals to $(ISO)_2H^+$ ($C_{10}H_{17}^+$, m/z$^+$ = 137):

a.1) $C_{10}H_{17}^+ + 2^{\bullet}OH \rightarrow C_{10}H_{19}O_2^+$, m/z$^+$ = 171 (Figures 6.4(C) and 6.5(D))

a.2) $C_{10}H_{19}O_2^+ - H_2O \rightarrow C_{10}H_{17}O^+$, m/z$^+$ = 153 (Figure 6.4(B))

Alternately,

b.1) $C_{10}H_{17}^+ + {}^{\bullet}OH + {}^{\bullet}OOH \rightarrow C_{10}H_{19}O_3^+$, m/z$^+$ = 187 b.2) $C_{10}H_{19}O_3^+ - H_2O \rightarrow C_{10}H_{17}O_2^+$, $m/z^+ = 169$ (Figure 6.5(B))

b.3) $C_{10}H_{19}O_3^+ - O_2 \rightarrow C_{10}H_{19}O^+$, $m/z^+ = 155$ (Figure 6.5(A))

Similarly, $(ISO)_3H^+$ ($C_{15}H_{25}^+$, $m/z^+ = 205$) the most abundant oligomer gave rise to:

c.1) $C_{15}H_{25}^+ + 2^{\bullet}OH \rightarrow C_{15}H_{27}O_2^+$, $m/z^+ = 239$

c.2) $C_{15}H_{25}^+ + {}^{\bullet}OH + {}^{\bullet}OOH \rightarrow C_{15}H_{27}O_3^+$, $m/z^+ = 255$

c.3) $C_{15}H_{27}O_3^+ - H_2O \rightarrow C_{15}H_{25}O_2^+$, $m/z^+ = 237$

Possible structures for these species are shown is Scheme 6.4 and 6.5, along with ring-closure reactions that can stabilize some of the radicals species proposed.

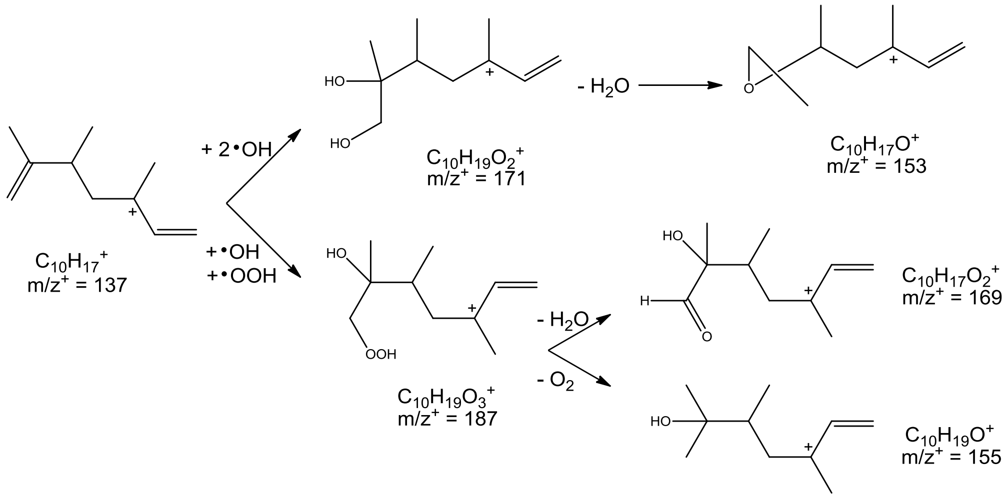

Scheme 6.4 – Possible structures of some of the oxidized species observed in Figure 6.5.

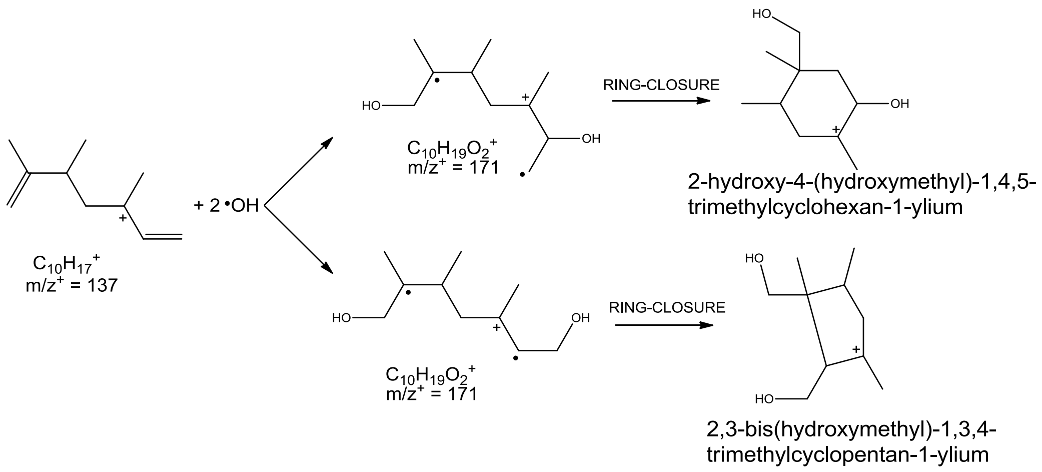

Scheme 6.5 – Alternative structures of the oxidized species obtained form the addition of 2 $^{\bullet}$OH radicals to the double bonds of (ISO)$_2$H$^+$. The so-formed radicals can undergo ring-closure and form a stable cyclohexane ring (upper part) or a cyclopentane ring (bottom part).

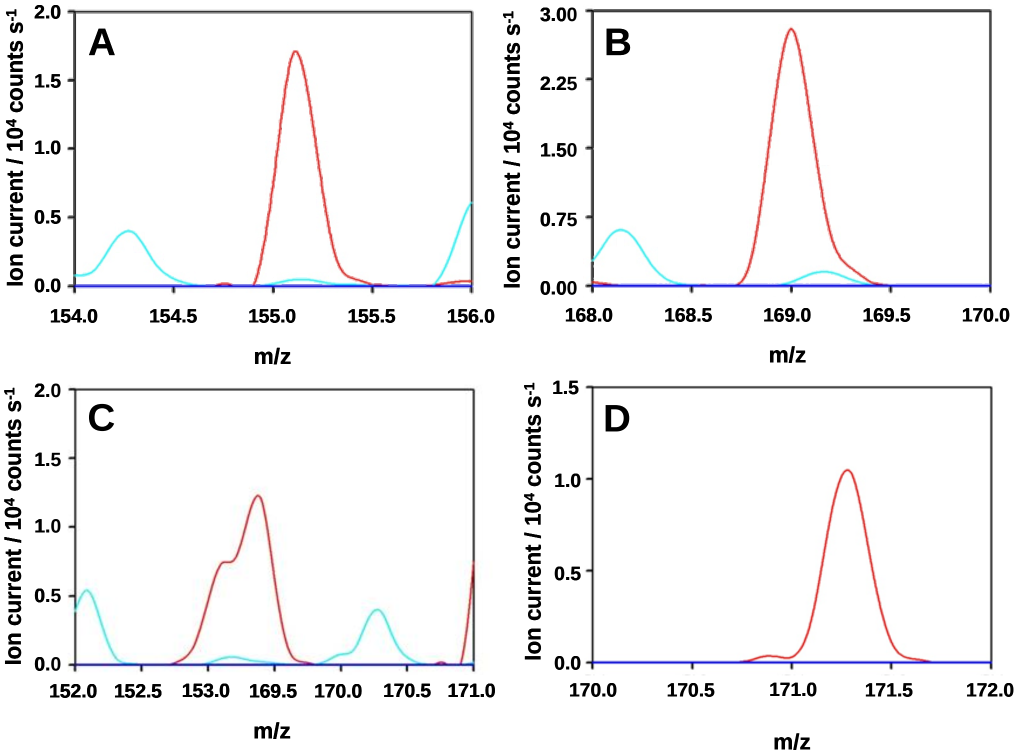

Figure 6.5 – Zooming on the evolution of specific mass spectral peaks as functions of gas composition, and the presence of *tert*-BuOH as $^{\bullet}$OH radicals scavenger. ISO(g): blue trace; ISO(g)/H$_2$O$_2$(g)/N$_2$(g): red trace; ISO(g)/H$_2$O$_2$(g) in the presence of excess dissolved *tert*-BuOH (see text): light blue trace. A: m/z$^+$ = 155. B: m/z$^+$=169. C: m/z$^+$= 153. D: m/z$^+$ = 171. [ISO(g)] ~ 5 × 10^{15} molecules cm^{-3}; [H$_2$O$_2$(g)] ~ 4 × 10^{14} molecules cm^{-3}.

A lower limit to the overall yield of the oxidation products was calculated by summing the intensities of all positive ion signals detected in the 50 to 600 Da mass range in the presence of ISO(g), before and after adding H_2O_2(g). The estimated yields (~ 5%) should be considered the lower limit because oxidation reaction can also turn the positively charged $(ISO)_nH^+$ into neutral or negatively charged species.

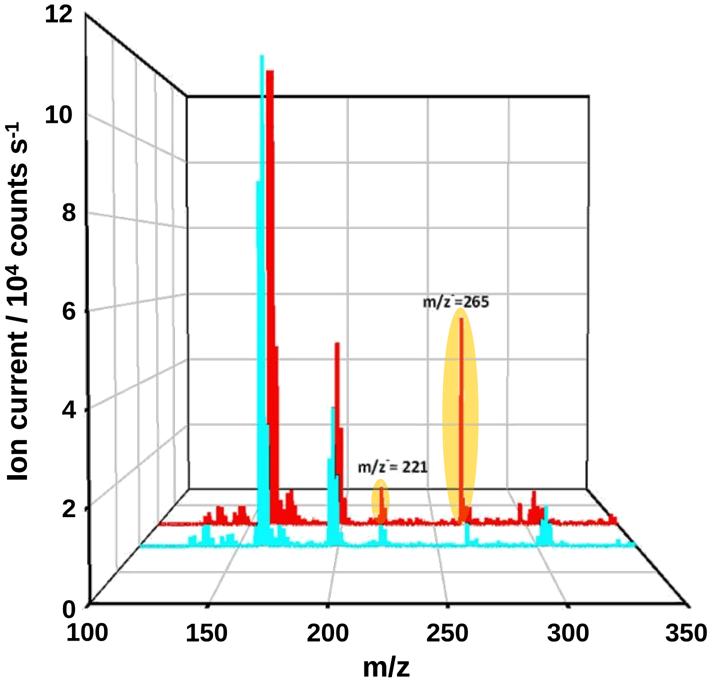

Figure 6.6 – Negative ion ESI mass spectra of 1 µM Fe^{2+} at pH ~ 2, exposed to ISO(g)/ H_2O_2(g)/N_2(g) (red line), ISO(g)/H_2O_2(g)/N_2(g) in the presence of excess dissolved *tert*-BuOH (~ 100 × [$FeCl_2$]) (light blue line) in the m/z^- = 100 – 350 Da range. [ISO(g)] ~ 5 × 10^{15} molecules cm^{-3}; [H_2O_2(g)] ~ 4 × 10^{14} molecules cm^{-3}.

Aiming at clarifying the oxidation mechanism of gaseous isoprene, also distinguishing whether the oxidized products were produced through •OH- or O-driven reactions, 100 µM of *tert*-BuOH (an efficient and largely adopted •OH radicals scavenger) was added to the Fe(II) initial solution, prior to injection, keeping all the other parameters unmodified.

Indeed, in addition to •OH radicals, interfacial Fenton reaction produced also ferryl (Fe(IV)=O) species that were proved to efficiently transfer an O-atom to the S(VI) center of the dimethyl sulfoxide [4,13]; hence, the presence of an •OH scavenger was expected to reveal the products possibly arising from the addition of an O-atom to the isoprene double bond.

Figure 6.6 shows that *tert*-BuOH completely inhibited the formation of carboxylates (the effect was particularly marked for the m/z^- = 265 peak) and,

Figure 6.7 further reveals that it had also similar effect on the formation of protonable products (*i.e.*, m/z$^+$ = 153, 155, 169 and 171 as also clearly visible in Figures 6.5).

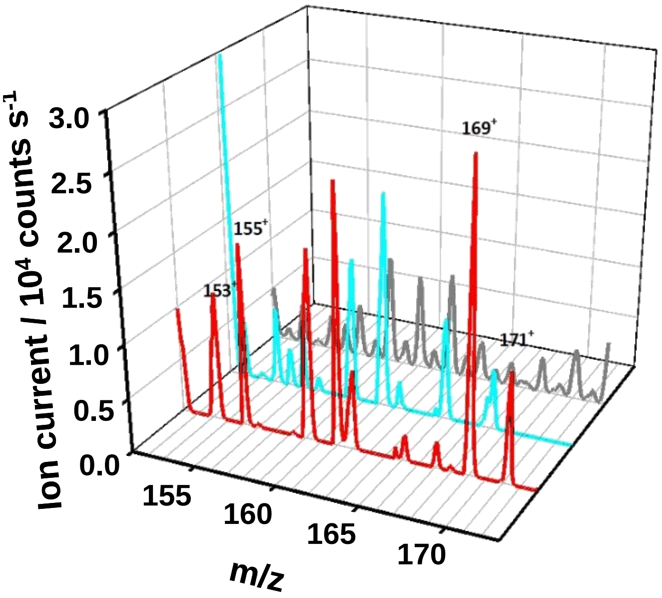

Figure 6.7 – Positive ion ESI mass spectra of 1 µM Fe^{2+} at pH ~ 2 in the presence of excess dissolved tert-BuOH (~ 100 × [$FeCl_2$]) (grey trace), exposed to ISO(g)/H_2O_2(g)/N_2(g) (light blue line) in the range of m/z$^+$ = 151 – 173 Da range of the less abundant product species. The red trace represents the ISO(g)/H_2O_2(g)/N_2(g) beams in the absence of *tert*-BuOH. The large $(ISO)_{1-8}H^+$ large signals were subtracted from the light blue and red trace spectra for clarity. [ISO(g)] ~ 5 × 10^{15} molecules cm^{-3}; [H_2O_2(g)] ~ 4 × 10^{14} molecules cm^{-3}.

These findings indicated that the oxidation of ISO(g) on the surface of water is mainly driven by $^{\bullet}OH$ radical addition to the double bonds of interfacial $(ISO)_nH^+$ oligomers. Moreover, it was highlighted that *tert*-BuOH behaved, in a wider sense, as a chemical scavenger since it quenched ISO oxidation products by generating new products of its own (light blue trace in Figure 6.7).

Thus, the observed products resulted from $^{\bullet}OH$-initiated chemistry and were consistent with the smaller yield of $^{\bullet}OH$ radicals (from R6.1) versus Fe(IV)=O ferryls (from R6.2) at the air-water interface [4,5,13].

6.2 Atmospheric implications

Due the generally accepted belief that global chemistry substantially influences climate, a biochemical model providing reliable estimation of isoprene emissions would represent a useful tool in the investigation of the Earth's response to the environmental changes occurred over the past century [14].

Indeed, isoprene emissions depend both on vegetation cover and on climate and, as such, are highly sensitive to global change. Moreover, they are positively influenced by temperature increase and vegetation productivity, whereas they are negatively affected by atmospheric CO_2 concentration increase [15]. ISO is produced in leaves chloroplasts from precursors formed during photosynthetic processes [16]. After being released, it can be converted by atmospheric free radicals (*e.g.*, $^{\bullet}OH$ and $^{\bullet}OOH$ radicals) and, only marginally, by ozone O_3 into a variety of chemical compounds (such as aldehydes, hydroperoxides, epoxides) which, mixed into water droplets, contribute to the raise of atmospheric aerosol and haze. The contribution of these secondary organic particles (*i.e.*, those formed from the oxidation of natural plants emissions) is complex to be evaluated and highly uncertain [17]. It has been estimated that ~ 0.6 petagrams (10^{15} g) of gaseous isoprene are annually emitted by the biosphere, accounting for half of the volatile organic compound (VOC) emissions and for up to 10% of carbon fixed *via* photosynthetic processes [18].

Though the urgent need of providing a reliable estimation, it is not yet entirely clear why some plants emit ISO or at what extent isoprene is converted to aerosol; moreover, at present, isoprene emissions atop tropical forests are systematically overestimated [7]. Recent studies reported that unsaturated (hydrophobic) VOCs such as isoprene and most biogenic terpenes, are always physisorbed but can also be protonated on the surface of mildly acidic water upon inelastic collision [7,9,10,19]. The probabilities that these colliding molecules are adsorbed on the acidic surface for finite times (*i.e.*, surface accommodation coefficient α_S) or, in other words, the fraction of colliding molecules which are inelastically reflected on the surface without entering the bulk, are larger than the conventional mass accommodation coefficient (α_M), corresponding to the probabilities that these impinging molecules enter the bulk before they are desorbed form the surfaces [19].

Within the environmental modeling framework, this findings implies that a significant fraction of gaseous terpenes can be readsorbed on the surface of mildly acidic leaves (pH ~ 4), where they are protonated and remain as such [9,19]. The frequency of sticking collisions of ISO molecules, ω_{ISO}, with acidic aerosol/cloud/fog droplets is given by the kinetic theory of gases (6.1):

$$\omega_{ISO} = (1/4)\,\gamma\, c_{ISO}\,(S/V) \qquad (6.1)$$

where γ is the uptake coefficient (~ 10^{-3} – 10^{-4} depending on the pH), c_{ISO} represents the average speed of isoprene molecules (c_{ISO} ~ 3×10^4 cm s^{-1}) and S/V is the typical fog specific surface area (S/V ~ 3×10^{-5} cm^{-1}) [19]. For a detailed definition of the uptake coefficient, see Section 2.3.2.

On this basis, $\omega_{ISO} \sim 4 \times 10^{-5}$ s^{-1} which is commensurate with the first-order rate constant $\omega_g \sim 2.5$ h^{-1} = 1×10^{-4} s^{-1} for the removal of ISO(g) by diurnal $^\bullet$OH(g) [5]. Thus, once ISO molecules stick to fog, they can react irreversibly with $^\bullet$OH radicals, generated *in situ*, boosting secondary organic aerosol (SOA) emissions.

Actual rates will clearly depend on atmospheric conditions, such as actinic irradiance, relative humidity and Fe(II) content of the aerosol phase [5].

H_2O_2(g), with a Henry's law constant H = 10^5 M atm^{-1}, is extremely soluble in water; typically, ~ 1 ppbv gas-phase H_2O_2 concentration leads to 0.1 mM H_2O_2 dissolved in aqueous fog and aerosol droplets, which generate $^\bullet$OH(aq) *via* Fenton chemistry [7,9,10] or *via* photolysis under $\lambda < 350$ nm sunlight [19-28]. Thus, airborne dispersed water represents a significant pool of oxidizing power in the troposphere [19,24-26]. Since air masses transported from the polluted sources, such as megacities and industrial conglomerates, contain remarkable H_2O_2 concentrations at nighttime [20], interfacial Fenton chemistry can drive oxidations in the aerosol phase throughout the day [29]. Accordingly, VOCs can be oxidized day and night on acidic aerosol *via* Fenton chemistry and this process represents an additional, hitherto unknown, mechanism for the conversion of organic gases into SOA matter.

6.3 Conclusion

Gaseous isoprene oligomers, ISO$_n$(g), were successfully oxidized into soluble species on the surface of acidic Fe(II) solutions where, due to the simultaneous presence of H_2O_2(g), powerful oxidizing radicals (*e.g.*, $^\bullet$OH, $^\bullet$OOH) were produced *via* Fenton reactions.

A myriad products, with total estimated yield of ~ 5%, were produced, among which, carboxylic acids (*i.e*, m/z$^-$ = 265 species), alcohols and epoxides (such as m/z$^+$ = 153, 155, 167, 171, 187, 237, 239 and 255 species) were identified. MS^2 spectroscopy and neutral losses patterns were useful to provide possible structures of the main detected products.

Significantly, all the oxidation products were quenched in the presence of *tert*-BuOH, a standard $^\bullet$OH radicals scavenger, consistently with an oxidation process initiated by the addition of $^\bullet$OH (formed *via* Fe(II) + H_2O_2(g) interfacial reactions) to ISO$_n$(g)H$^+$ and then followed by fast reactions with dissolved H_2O_2, $^\bullet$OOH and O_2.

The obtained results may account for the conversion of organic gases into secondary organic aerosol, occurring under tropospheric conditions, and may be incorporated into atmospheric chemistry models, providing extra feasible mechanisms.

REFERENCES

[1] M.S. Stark, *J. Am. Chem. Soc.* **2000,** *122*, 4162.

[2] S.M. Villano, H.H. Carstensen, A.M. Dean, *J. Phys. Chem. A* **2013,** *117*, 6458.

[3] J. Zador, S.J. Klippenstein, J.A. Miller, *J. Phys. Chem. A* **2011,** *115*, 10218.

[4] S. Enami, Y. Sakamoto, A.J. Colussi, *Proc. Natl. Acad. Sci. U. S. A.* **2014,** *111*, 623.

[5] F.R. Kameel, F. Riboni, M.R. Hoffmann, S. Enami, A.J. Colussi, *J. Phys. Chem. C* **2014**, DOI: dx.doi.org/10.1021/jp505010e.

[6] A. Kahnt, Y. Iinuma, A. Mutzel, O. Boge, M. Claeys, H. Herrmann, *Atmos. Chem. Phys.* **2014,** *14*, 719.

[7] S. Enami, H. Mishra, M.R. Hoffmann, A.J. Colussi, *J. Phys. Chem. A* **2012,** *116*, 6027.

[8] S. Enami, M.R. Hoffmann, A.J. Colussi, *J. Phys. Chem. Lett.* **2010,** *1*, 1599.

[9] S. Enami, M.R. Hoffmann, A.J. Colussi, *J. Phys. Chem. Lett.* **2012,** *3*, 3102.

[10] S. Enami, L.A. Stewart, M.R. Hoffmann, A.J. Colussi, *J. Phys. Chem. Lett.* **2010,** *1*, 3488.

[11] E.P.L. Hunter, S.G. Lias, *J. Phys. Chem. Ref. Data* **1998**, *27*, 413.

[12] S.D. Maleknia, T.L. Bell, M.A. Adams, *Int. J. Mass Spectrom.* **2007**, *262*, 203.

[13] H. Bataineh, O. Pestovsky, A. Bakac, *Chem. Sci.* **2012,** *3*, 1594.

[14] N. Unger, *J. Geoph. Res. Atm.* **2013**, *118*, 13606.

[15] R.K. Monson, N. Trahan, T.N. Rosenstiel, P. Veres, D. Moore, M. Wilkinson, R.J. Norby, A. Volder, M.G. Tjoelker, D.D. Briske, D.F. Karnosky, R. Fall, *Philos. Trans. R. Soc. A* **2007**, *365*, 1677.

[16] N. Unger, K. Harper, Y. Zheng, N.Y. Kiang, I. Aleinov, A. Arneth, G. Schurgers, C. Amelynck, A. Goldstein, A. Guenther, B. Heinesch, C.N. Hewitt, T. Karl, Q. Laffineur, B. Langford, K.A. McKinney, P. Miszta, M. Potosnak, J. Rinne, S. Pressley, N. Schoon, D. Serça, *Atmos. Chem. Phys.* **2013**, *13*, 10243.

[17] G. McFiggans, *Nature* **2014**, *506*, 442.

[18] Y. Pan, R.A. Birdsey, J. Fang, R. Houghton, P.E. Kauppi, W.A. Kurz, O.L. Phillips, A. Shvidenko, S.L. Lewis, J.G. Canadell, P. Ciais, R.B. Jackson, S.W. Pacala, A.D. McGuire, S. Piao, A. Rautiainen, S. Sitch, D. Hayes, *Science* **2011**, *333*, 988.

[19] F.R. Kameel, M.R. Hoffmann, A.J. Colussi, *J. Phys. Chem. A* **2013**, *117*, 5117.

[20] A. Marinoni, M. Parazols, M. Brigante, L. Deguillaume, P. Amato, A.M. Delort, P. Laj, G. Mailhot, *Atmos. Res.* **2011**, *101*, 256.

[21] C. Minero, M. Lucchiari, V. Maurino, D. Vione, *Rsc Advances* **2013**, *3*, 26443.

[22] A. Tilgner, P. Brauer, R. Wolke, H. Herrmann, *J. Atmos. Chem.* **2013**, *70*, 221.

[23] M. Vaitilingom, T. Charbouillot, L. Deguillaume, R. Maisonobe, M. Parazols, P. Amato, M. Sancelme, A.M. Delort, *Atmos. Chem. Phys.* **2011**, *11*, 8721.

[24] D.J. Jacob, *Atmos. Environ.* **2000**, *34*, 2131.

[25] J. Mao, S. Fan, D.J. Jacob, K.R. Travis, *Atmos. Chem. Phys.* **2013**, *13*, 509.

[26] S.L. Wu, L.J. Mickley, D.J. Jacob, J.A. Logan, R.M. Yantosca, D. Rind, *J. Geophys. Res. Atmos.* **2007**, *112*, D05302/1.

[27] R.L. Siefert, A.M. Johansen, M.R. Hoffmann, S.O. Pehkonen, *J. Air & Waste Manag. Assoc.* **1998**, *48*, 128.

[28] R.L. Siefert, S.M. Webb, M.R. Hoffmann, *J. Geophys. Res. Atmos.* **1996,** *101*, 14441.

[29] J. Guo, A. Tilgner, C. Yeung, Z. Wang, P.K.K. Louie, C.W.Y. Luk, Z. Xu, C. Yuan, Y. Gao, S. Poon, H. Herrmann, S. Lee, K.S. Lam, T. Wang, *Environ. Sci. Technol.* **2014**, *48*, 1443.

THESIS SUMMARY

General upward trends in fossil fuel consumption and CO_2 emissions require that scientific research provides efficient remedies and/or alternatives to the present scenario. Photocatalysis can be envisaged as one of the most promising technique to achieve these purposes. Photocatalytic reactions notoriously proceed through the photogeneration of electron/hole (e^-/h^+) pairs, by the absorption of photons with energy suitable for semiconductor band gap (E_g) excitation.

The most widely adopted photocatalyst, *i.e.* TiO_2, has well-known limitations due to the relatively high e^-/h^+ recombination rate, negatively affecting the photoactivity performances, together with the requirement of UV light to efficiently excite its E_g.

Furthermore, the abatement of CO_2 through (photo/electro)chemical reduction toward fuels is still a very challenging process, mainly due to its unfavourable thermodynamics ($E^0(CO_2/CO_2^{-\bullet} = -2.14$ V *vs* SCE)).

Finally, due to the general belief that global chemistry heavily influences climate, a chemical model providing reliable estimation of isoprene emissions (the most abundant greenhouse gas) would represent a useful tool in the investigation of the Earth's response to the environmental changes.

This PhD work has been focused on the study of different strategies to *i*) limit the drawbacks related to TiO_2 photocatalysis, *ii*) provide an alternative method for CO_2 photoreduction and *iii*) investigate the Fenton oxidation reaction under atmospheric conditions, involving isoprene as a model compound.

1. Photocatalytic activity of TiO_2-WO_3 and Pt-modified TiO_2-WO_3 mixed oxides

Among the strategies limiting the recombination of photoproduced e^-/h^+ pairs, coupling TiO_2 with another metal oxide may be suggested. In fact, the intimate contact with a semiconductor, such as WO_3, characterized by a conduction band (CB) slightly lower than the CB of TiO_2 and a valence band (VB) closed to that of titania, ensures enhanced separation between photopromoted electrons (which migrate into the CB of the coupled semiconductor) and photogenerated holes (which preferentially remain trapped within TiO_2 VB) [1].

Furthermore, post-synthesis surface modification with Pt nanoparticles (NPs) promotes e^-/h^+ separation to a higher extent, by virtue of the noble metal high work function (Φ) and consequent e^- sink capability, further enhancing the photocatalytic activity.

1.1 Photocatalysts synthesis and physico-chemical characterization

Titanium(IV) isopropoxide ($Ti(OC_3H_7)_4$), dissolved in anhydrous ethanol, and tungsten(VI) hexa-ethoxide ($W(OC_2H_5)_6$) were used as TiO_2 and WO_3 precursors, respectively, in the sol-gel synthesis of TiO_2-WO_3 mixed oxide photocatalysts [1]. The samples were labelled as TW*x*_*y*, with *x* referring to W/Ti molar ratio (0–5 mol.%) and *y* to the calcination temperature (500 or 700 ˚C).

After the annealing treatment, the powders were also modified by Pt NPs photodeposition (0.5 wt.%), employing hydrated H_2PtCl_6 as noble metal precursor. Pt(IV) to Pt^0 reduction and the consequent deposition on the photocatalyst surface was achieved by irradiating the suspension with a 300-400 nm emitting lamp [2]. Recalling the aforementioned labels, samples were identified as Pt/TW*x*_*y*.

Table 1.1 summarizes the main physico-chemical characteristics of the photocatalysts. XRD analysis revealed that all TW*x*_500 photocatalysts were composed of full anatase (A), with nanoparticle dimensions nearly halved upon W addition, this being in line with a large increase in surface area, as proved by BET analysis.

Furthermore, though TW0_700 was of mixed anatase-rutile phase, the full anatase composition of the mixed oxides calcined at 700 ˚C suggested that even modest amounts of W were able to inhibit the well known anatase-to-rutile phase transition, also preventing nanoparticles sintering and ensuring highly crystalline powders with SSA higher than that of the pure titania sample TW0_700 [1].

	phase composition (wt.%)	d_A (nm)	$2\vartheta_A$ (deg)	SSA (m^2g^{-1})
TW0_500	100% A	13	25.4390	44.6
TW1_500	100% A	6	25.3809	205.8
TW3_500	100% A	5	25.30340	202.2
TW5_500	100% A	6	25.2352	198.2
TW0_700	10% A + 90% R	39	//	6.7
TW1_700	100% A	24	25.5750	14.8
TW3_700	100% A	20	25.5252	28.7
TW5_700	100% A	15	25.3248	52.9

Table 1.1 – Phase composition (A = anatase, R = rutile) and anatase particle dimensions, d_A, obtained from XRD analysis, assuming the absence of amorphous material; anatase phase main reflection, $2\vartheta_A$; specific surface area, SSA, from BET analysis.

A more accurate analysis of XRD data also revealed a slight shift of the main anatase peak toward lower diffraction angles, progressively decreasing with increasing the W content, in both naked and platinated series. This result provided evidence for the insertion of W domains within the titania lattice, resulting in the distortion of its cell.

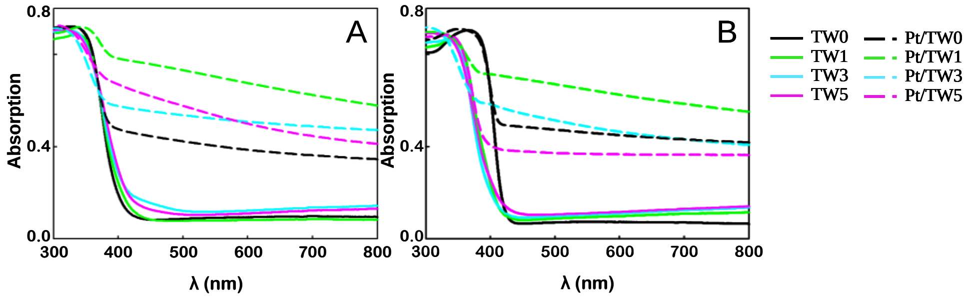

Figure 1.1 – UV-vis absorption spectra of: (A) TW*x*_500 and Pt/TW*x*_500 samples; (B) TW*x*_700 and Pt/TW*x*_700 samples.

UV-vis absorption spectra in Figure 1.1 A and B showed that all samples were characterized by an absorption onset at λ ~ 380 nm, owing to anatase TiO_2 band gap excitation, except for TW0_700 (and the corresponding Pt-modified) material, which exhibited a red-shift in the absorption onset due to its prevalent rutile phase composition [1]. Furthermore, the extended absorption at λ > 400 nm of all Pt-modified samples further confirmed the deposition of noble metal NPs on the photocatalysts surface, with the different absorption properties to be possibly ascribed to a non-homogeneous Pt deposition.

1.2 Photocatalytic activity tests

The results of FA photocatalytic oxidation pointed to a superior performance of anatase TW0_500 in the series calcined at the lower temperature (Figure 1.2A), suggesting that WO_3 may favour photogenerated e^-/h^+ recombination.

The enhanced photoactivity obtained with the Ti-W mixed oxides calcined at 700 °C was attributed to their full anatase composition, with respect to the 90% rutile phase content of TW0_700.

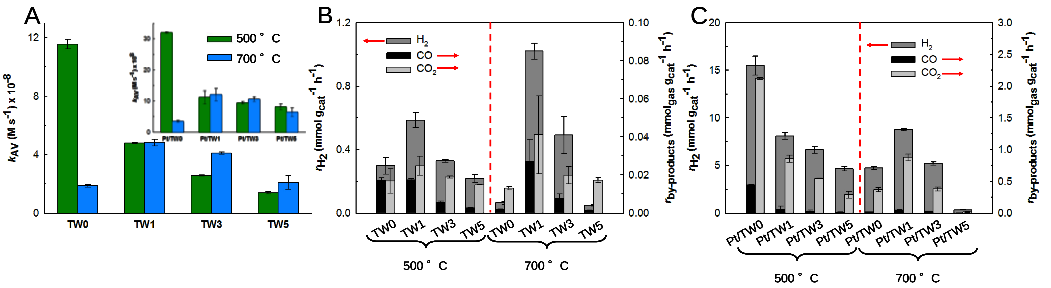

Figure 1.2 – (A) Zero order rate constants, k_{AV}, of formic acid photodegradation obtained with sol-gel synthesized TW*x*_*y* samples. The results obtained with the Pt-

modified TW*x_y* samples are reported in the inset. (B, C) H_2, CO and CO_2 production rates obtained with the TW*x_y* and Pt/TW*x_y* samples, respectively.

Either it was calcined at 500 or at 700 °C, the most active Ti-W mixed oxide was TW1 proving that enhanced charge carriers recombination promoted by WO_3, along with extensive distortion of the anatase cell, were detrimental for the photocatalytic activity of TiO_2 in oxidation reactions.

Pt NPs deposition, besides mirroring the photoactivity trend displayed by the corresponding TW*x_y* samples (inset of Figure 1.2A), levelled out the results obtained with all Ti-W mixed oxides, suggesting that the observed photoactivity should be ascribed to TiO_2 charge carriers which did not undergo W-promoted recombination and, hence, were efficiently separated by Pt NPs resulting in photoactivities higher than the corresponding naked samples.

H_2 production by methanol photo-steam reforming was performed using a laboratory scale apparatus [3]. The results are summarized in Figure 1.2B. Unlike in FA photo-oxidation, the presence of W in the TW*x_y* samples resulted in enhanced H_2 production with respect to pure TiO_2. In addition to the effect induced by W in increasing the SSA of the mixed oxides, guaranteeing a more extensive substrate adsorption, it should be considered that electrons photopromoted in the titania CB can be easily transferred to WO_3. Under anaerobic conditions and in the presence of a hole scavenger (*i.e.*, CH_3OH), the enhanced separation between the charge carriers led to the more efficient reduction of H^+ to H_2 than in pristine TiO_2, with h^+, trapped in TiO_2 VB, oxidizing CH_3OH to CO and CO_2.

By contrast, Pt photodeposition resulted in a better performance of pure TiO_2, Pt/TW0_500 (Figure 1.2C), due to the high work function of this noble metal (Φ = 5.6 eV). By trapping photopromoted electrons more favourably, Pt NPs guaranteed a better charge carriers separation than that achievable upon Ti-W mixing. Conversely, in the Pt/TW*x*_700 series, the inhibition of the anatase-to-rutile phase transition induced by W pointed to a better performance of Ti-W mixed oxides with respect to the Pt-modified titania sample (Pt/TW0_700).

1.3 Conclusion

Mixing TiO_2 with WO_3 resulted in the transfer of e^- from the CB of TiO_2 to that of WO_3, with h^+ remaining trapped in TiO_2 VB. Along with the enhanced charge carriers separation, transferred e^- had a slightly lowered reduction potential (CB(WO_3) ~ 0 V *vs* NHE). Thus, the investigated systems behaved differently, depending on the considered reactions. In FA photodegradation, the reduced performances of the mixed oxides suggested that e- didn't readily react with O_2 ($E^0(O_2/O_2^{-\bullet})$ = -0.28 V *vs* NHE) thus maintaining h^+ available to oxidize the substrate; hence, the charge carriers more favourably recombined. Conversely, e^- trapped by WO_3 CB were able to reduce H^+ to H_2 ($E^0(H^+/H_2)$ = 0 V *vs* NHE), while h^+ oxidized CH_3OH, leading to the superior performances of Ti-W mixed oxides. The optimum W content was fixed at W/Ti = 1 mol.%, with higher amounts inducing extensive distortion of the hosting TiO_2 lattice and promoting e^-/h^+ recombination to higher extents.

2. Effect of the electronic structure of TiO_2 on the plasmon photoactivity of Au nanoparticles

Surface modification of TiO_2 with metal nanostructures (*e.g.*, Au, Ag or Cu) possessing a Localized Surface Plasmon Resonance (LSPR) can be an efficient way to promote TiO_2 photoactivity under visible light irradiation.

For Au NPs (whose plasmon band peaks at $\lambda = 530$ nm) supported on metal oxides, LSPR can either promote hot electrons transfer from plasmonic metals to the semiconductor CB or result in the energy transfer (PRET) from the electromagnetic field generated on the surface of metal NPs to the band-gap of the material, promoting the formation of e^-/h^+ pairs in TiO_2.

Since the discriminating factors for one of the two phenomena to occur may be the band alignment at the semiconductor/metal junction and the presence of intra-band gap defect states in the semiconductor, respectively, three different TiO_2 supports have been selected: *i*) w-TiO_2, a nearly stoichiometric titania; *ii*) N-TiO_2, characterized by VB defect states, formed upon N-doping; *iii*) b-TiO_2, a substoichiometric TiO_2, rich in oxygen vacancies (V_Os), introducing defect states close to the CB.

2.1 Photocatalysts synthesis and physico-chemical characterization

w- and b-TiO_2 supports were prepared by annealing a titania commercial powder for 1 h at 500 ˚C, under O_2 or H_2 streams, respectively, according to [4].

N-TiO_2 was prepared by conveniently modifying the sol-gel procedure described in [1], with titanium(IV) isopropoxide and aqueous ammonia used as precursors. N/Ti was fixed at a 25% nominal molar ratio and the sample was calcined at 500 ˚C in air flow.

Au NPs (1–10 wt.%) were deposited on the surface of each support. $HAuCl_4$ was added to the photocatalyst aqueous suspension and the reduction of the metal precursor to Au^0 was chemically achieved by means of $NaBH_4$.

XRD data confirmed that w-TiO_2 was composed of full anatase phase, while b-TiO_2 had a A:R = 80:20 mixed composition. Similarly, also N-TiO_2 was of mixed anatase and rutile phase (A:R = 98:2).

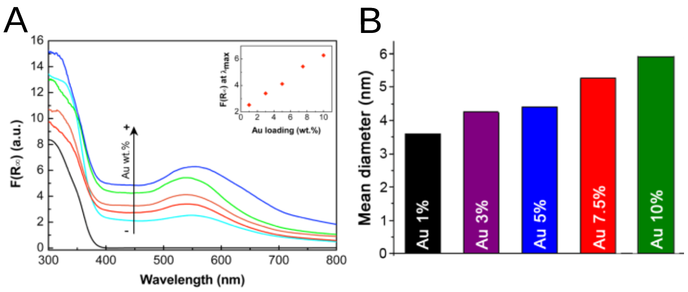

Figure 2.1 – (A) UV-vis abs spectra of 0%Au (black), 1%Au (cyan), 3%Au (red), 5%Au (orange), 7.5%Au (green), 10%Au (blue), supported on w-TiO_2. The inset highlights the linear increase of the LSPR absorption as a function of the metal loading. (B) Mean diameter of Au NPs deposited on w-TiO_2, determined from TEM images.

All three substrates exhibited the expected UV-vis absorption features: in line with their anatase composition, w-TiO_2 and N-TiO_2 were characterized by the typical absorption edge at $\lambda \sim 380$ nm, with the enhanced absorption of the latter at ~ 400 nm due to N-doping. Likewise, a broad absorption starting at ~ 400 nm and extending at longer λ characterized b-TiO_2, giving it a black coloration. The deposition of Au NPs led to the appearance of metal LSPR, peaking at $\lambda \sim 530$ nm, whose intensity was found to linearly increase with Au loading, in the w-TiO_2 modified series (Figure 2.1A).

TEM images provided evidence for the homogeneous distribution of metal NPs over each substrate surface and the obtained size distribution of Au NPs revealed *i*) bigger gold nanoparticles, progressively increasing Au loading, in w-TiO_2 samples (Figure 2.1B); *ii*) conversely, metal NPs deposed either on N- or b-TiO_2, exhibited uniform dimensions ($d_{Au} \sim 5$ nm, on average) regardless of the metal loading amount; thus, necessarily, higher metal loadings implied higher Au NPs density.

2.2. Plasmon-promoted photocatalytic activity

FA photo-oxidation was performed according to [1], under irradiation by means of a LED emitting at $\lambda = 532$ nm, to selectively excite Au plasmon band (see Fig. 2.1A).

As shown in Figure 2.2A, two photoactivity regimes could be distinguished, reflecting different SPR-semiconductor interactions: in the 1–5 wt.% Au loading range, the reaction proceeded mainly through a hot electron transfer from Au NPs to the TiO_2 CB (Figure 2.2B), thus reflecting the defects concentration in TiO_2 samples, with the less defective one (*i.e.*, w-TiO_2) being the most active.

Indeed, it is generally accepted that the Schottky barrier formed at Au/TiO_2 (anatase) interface is ~ 0.9 eV and that hot electrons generated through gold plasmon excitation may raise up to ~ 1 eV above metal Fermi level (E_F), so that a significant fraction can be injected into the semiconductor CB and initiate the photocatalytic reaction [5]. Nevertheless, this mechanism was inhibited in N- and b-TiO_2, consistently with the presence of V_Os (introduced either to balance N-doping or along with reducing thermal treatment, respectively), with the consequent shift of titania E_F to higher energies and a larger Schottky barrier formed.

Conversely, at higher Au loadings (5–10 wt.%) the resonance between multiple adjacent Au NPs induced a strong electromagnetic field amplification [6], which provided sufficient energy to promote electrons from the VB to the defect states, then participating in substrate photo-oxidation; hence, the photoactivity in the presence of highly defective structures (*i.e.*, N- and b-TiO_2) was facilitated.

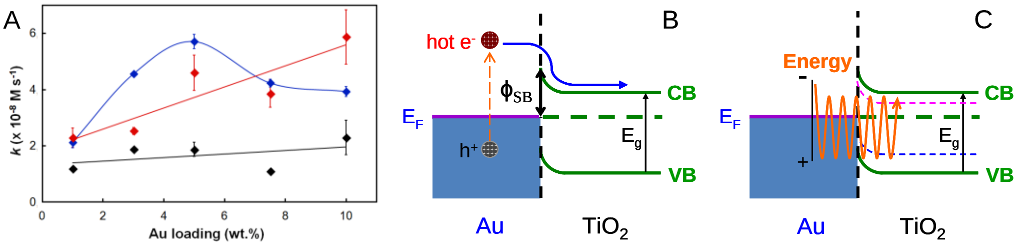

Figure 2.2 – (A) Zero order rate constant, *k*, for the degradation of formic acid obtained with 1–10% Au-modified w-TiO_2 (blue), N-TiO_2 (red) and b-TiO_2 (black). (B) Mechanism of hot electron generation due to Au LSPR and consequent injection into TiO_2 CB. (C) Mechanism of Energy Transfer from resonating Au plasmon to TiO_2 band gap.

Also the volcano-shaped trend displayed by the w-TiO_2 series, in contrast with a photoactivity increase of both N- and b-TiO_2 samples, suggested that two different plasmon-induced mechanisms were involved. In particular, metal loading higher than 5 wt.% in w-TiO_2 appeared detrimental due to metal overloading and consequent increased light scattering; on the contrary, the increased photoactivity in the presence of progressively higher metal amounts on N- and b-TiO_2 samples, validated the PRET mechanism. As further confirmation, Finite-Difference Time-Domain (FDTD) simulations performed by modelling the investigated systems, proved that the plasmon resonance of suitably excited adjacent Au NPs generates intense electric field, increasingly stronger as the NPs approach (situation that most likely represents Au NPs deposed on N- and b-supports).

2.3 Conclusion

The Au plasmon-promoted mechanism of FA photodegradation strictly depends both on metal loading and on the electronic properties of the semiconductor. Evidence was provided of hot e^- transfer from Au to TiO_2 when its CB was suitably located (*i.e.*, in a non-defective support); conversely, PRET mechanism, triggered by the highly intense electric field generated within adjacent Au NPs, was more favourable with reduced band gap TiO_2 (*i.e.*, for defective supports).

3. Homogeneous reduction of CO_2 by photogenerated pyridinyl radicals

The endoergonic reduction of CO_2 into organic matter is still very challenging, mainly because of its negative electron affinity in the gas-phase, which makes its conversion into $CO_2^{-\bullet}$ thermodynamically unfavourable [7].
The chemical stabilization of $CO_2^{-\bullet}$ has recently been achieved with the formation of a carbamate intermediate from the homogeneous reaction between 1-hydropyridinyl radicals (1-$PyH^{\bullet}$), formed through the electrochemical reduction of pyridinium (PyH^{+}), with dissolved CO_2 [8]. However, the mechanism has not yet been fully clarified.
With the aim of assessing the reaction feasibility and ascertaining the mechanism, CO_2 reduction was performed under monochromatic irradiation (λ = 254 nm), in homogeneous aqueous solutions containing pyridine (Py) and an H-atom donor (2-PrOH). The 1-hydropyridinyl radical (1-$PyH^{\bullet}$), produced by 254 nm-excitation of pyridine (Py) [from $^3Py^* + 2\text{-}PrOH \rightarrow 1\text{-}PyH^{\bullet} + {}^{\bullet}PrOH$] reacted with CO_2, yielding, among all products identified through Electrospray Ionization Mass Spectrometry (ESI), species containing both pyridine moiety and carboxylate functionalities, thus providing evidence for the carbon dioxide reduction promoted by photogenerated pyridinyl radicals [9].
The experiments here reported were carried out at the Linde Center for Global Environmental Science at the *California Institute of Technology*.

3.1 Experimental results and discussion

The homogeneous reduction of CO_2 in Py/2-PrOH aqueous solution was performed as described in [9]: Py/2-PrOH/H_2O solutions were degassed *in situ* by freeze-and-thaw cycles, to evacuate oxygen; CO_2 was then bubbled for 1 h, guaranteeing the saturation of both the solution and the reactor dead volume. Finally, the lamp was introduced into the reactor and the photolysis was run by irradiating for 1 h. The pH was always adjusted to pH ~ 3 with HCl, ensuring that Py (pK_a = 5.3 [8]) was largely present as PyH^{+}.
Aside all the species formed through disproportionation of photogenerated radicals and secondary radicals reactions (*e.g.*, pyridine photohydration and 1-$PyH^{\bullet}$ addition to ${}^{\bullet}PrOH$), more relevant to the aim of the work was the formation of the three main species recorded in the ESI negative mode. m/z^- = 113 species was tentatively ascribed to the adduct composed of a sodium cation and two formate anions, $(HCOO)_2Na^-$, as generally accepted in mass-spectrometry [9]. The two peaks at m/z^- = 124 and 160 were identified as $C_5H_6NCOO^-$ and

$C_5H_{10}O_2NCOO^-$, respectively, with the second being the di-hydrated form of the former (160 = 124 +36), both containing Py (C_5H_5N) and CO_2 (Scheme 3.1).

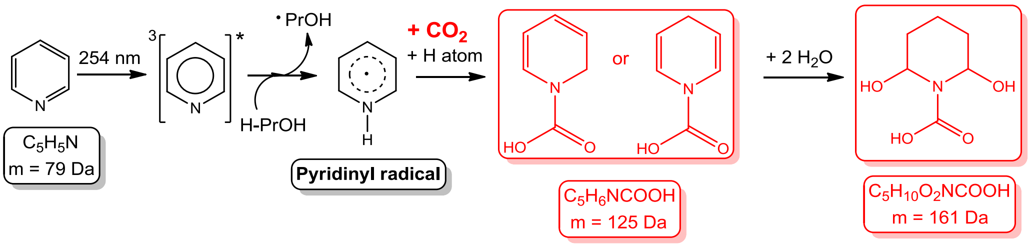

Scheme 3.1 – Photolysis reaction mechanism leading to the observed carbamic species.

MS/MS spectroscopy performed on these three selected species, confirmed CO_2 neutral losses and additional experiments run in the absence of one of the reagents, demonstrated that the formation of carboxylates (and formate) required CO_2, Py, α-hydroxyalkyl radicals, produced from 2-PrOH photolysis, and 254 nm-irradiation.

Furthermore, the yields in carboxylate species (*i.e.*, $C_5H_6NCOO^-$ and $C_5H_{10}O_2NCOO^-$) was found to be concentration-dependent, with an optimum [Py] = 10 mM, as for the electrochemically activated process [8].

Finally, the evaluated rate constant k (~ $O(10)$ M^{-1} s^{-1}) and activation energy ($E \geq$ 9 kcal mol^{-1}) for $1\text{-PyH}^{\bullet}$ addition to CO_2 were found to be compatible with thermochemical estimates for this reaction [9].

3.2 Conclusion

The homogeneous photoreduction of CO_2, in Py/2-PrOH/H_2O mixtures, was proved to proceed through the formation of a carbamic species (HPy-1-COOH, C_5H_6NCOOH), triggered by a stepwise mechanism where electron transfer (ET) from $1\text{-PyH}^{\bullet}$ to CO_2 precedes proton transfer (PT).

Furthermore, formate ($HCOO^-$) was obtained, demonstrating that photoexcited pyridine does catalyze the 2 e^--reduction of CO_2.

4. Fenton oxidation of gaseous isoprene on aqueous surfaces

Isoprene (ISO) emissions depend both on vegetation cover and on climate and, as such, are highly sensitive to global changes. Moreover, they are largely influenced by temperature increase and vegetation productivity, whereas they are negatively affected by the increase of atmospheric CO_2 concentration. Isoprene is usually produced in leaves from precursors formed during photosynthetic processes. Though the strict dependence on global environment and, hence, the urgent need of providing a reliable estimation of isoprene emissions, it is not yet completely understood at what extent it is converted to aerosol becoming one of the most abundant greenhouse gases.

Experimental evidence was provided that gaseous isoprene, under atmospheric conditions, is oxidized into soluble species on the surface of aqueous $FeCl_2$ solutions simultaneously exposed to H_2O_2(g) yielding, among all products identified *in situ* via Electrospray Ionization Mass Spectrometry, $(ISO)_nH^+$ oligomers and, more importantly, carboxylic acids, alcohols, epoxides, aldehydes and ketons whose identification was further supported by MS/MS spectroscopy generating neutral losses patterns useful to provide possible structures for the detected products [10].

The experiments here reported were carried out at the Linde Center for Global Environmental Science at the *California Institute of Technology*.

4.1 Experimental results and discussion

In the performed experiments, ISO(g) and/or H_2O_2(g) streams intersected with aqueous $FeCl_2$ microjets at acidic pH (~ 2), for *ca.* 10μs. The products formed in the reactive encounters confirmed the formation of $(ISO)_nH$+ oligomers generated form ISO(g) on the surface of pH < 4 water drops [11], along with $Fe(IV)O^{2+}$ ferryl species and powerful oxidizing radicals (*e.g.*, $^{\bullet}OH$, $^{\bullet}OOH$) generated as primary products of Fenton reaction occurring when intersecting H_2O_2(g) streams and Fe^{2+} aqueous droplets [12].

According to Scheme 4.1, isoprene oligomers were subsequently oxidized into myriad of products, whose yields totally exceeded ~ 5%.

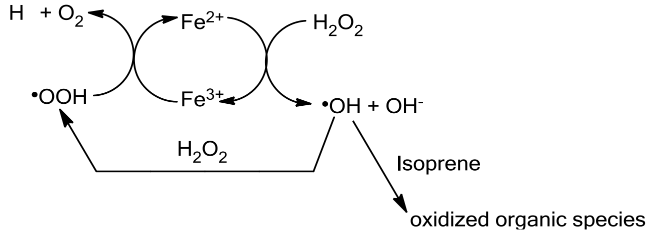

Scheme 4.1 – Fe^{2+}/Fe^{3+} catalytic Fenton reactions, involving H_2O_2, and faith of the produced $^{\bullet}OH$ in the presence of organic species (*i.e.*, isoprene).

Carbonyls, alcohols and epoxides were identified as positive ions (*e.g.*, m/z^+ = 153, 155, 167, 171, etc.) and MS/MS analysis of selected species split H_2O and O neutrals. In addition, the less abundant carboxylic acids (*e.g.*, m/z^- = 265) appeared as negative ions, undergoing CO, H_2O and CO_2 losses via collisionally induced dissociation.

Significantly, all the oxidation products were quenched in the presence of *tert*-BuOH, a standard $^{\bullet}OH$ scavenger, consistently with an oxidation process initiated by the addition of hydroxyl radicals, formed via interfacial Fenton reaction, to gaseous isoprene.

4.2 Conclusion

Gaseous isoprene oxidation was performed on the aqueous surface of $FeCl_2$ droplets. The results appeared consistent with an oxidation process triggered by the addition of $^{\bullet}OH$ radicals, produced *in situ* via interfacial Fenton reaction ($Fe^{2+}(aq) + H_2O_2(g)$), to isoprene oligomers, $(ISO)_nH^+$, followed by fast reactions involving dissoved H_2O_2, $HO_2^{\bullet}$ and O_2, that led to polyols, carbonyls and, to a lower extent, carboxylic acids. Performed experiments demonstrated tha gas-phase olefins can be oxidized upon colliding on the surface of Fe-containing acidic aqueous drops, mimicking typical tropospheric conditions and accounting for alternative feasible mechanism of secondary organic aerosol generation.

REFERENCES

[1] F. Riboni, L.G. Bettini, D.W. Bahnemann, E. Selli, *Catal. Today* **2013**, *209*, 28.

[2] M.V. Dozzi, A. Saccomanni, M. Altomare, E. Selli, *Photochem. Photobiol. Sci.* **2013**, *12*, 595.

[3] G.L. Chiarello, M.H. Aguirre, E. Selli, *J. Catal.* **2010**, *273*, 182.

[4] A. Naldoni, M. Allieta, S. Santangelo, M. Marelli, F. Fabbri, S. Cappelli, C.L. Bianchi, R. Psaro, V. Dal Santo, *J. Am. Chem. Soc.* **2012**, *134*, 7600.

[5] E.W. McFarland, J. Tang, *Nature* **2003**, *421*, 616.

[6] D.B. Ingram, S. Linic, *J. Am. Chem. Soc.* **2011**, *133*, 5202.

[7] C.H. Lim, A.M. Holder, C.B. Musgrave *J. Am. Chem. Soc.* **2013**, *135*, 142.

[8] G. Seshadri, C. Lin, A.B. Bocarsly *J. Electroanal. Chem.* **1994**, *372*, 145.

[9] F. Riboni, E. Selli, M.R. Hoffmann, A.J. Colussi, *J. Phys. Chem. A* **2014**, just accepted.

[10] F.R. Kameel, F. Riboni, M.R. Hoffmann, S. Enami, A.J. Colussi, *J. Phys. Chem. C* **2014**, DOI: dx.doi.org/10.1021/jp505010e.

[11] F.R. Kameel, M.R. Hoffmann, A.J. Colussi, *J. Phys. Chem. A* **2013**, *117*, 5117.

[12] S. Enami, Y. Sakamoto, A.J. Colussi, *Proc. Natl. Acad. Sci. U.S.A.* **2014**, *111*, 623.

List of scientific contributions and activities

Status of November 2014

Peer-Reviewed Articles

F. Riboni, E. Selli, “*Photocatalytic activity of TiO_2-WO_3 and Pt-modified TiO_2-WO_3 mixed oxides*”. In preparation.

A. Naldoni, F. Riboni, M. Marelli, M. Malvestuto, F. Bossola, R. Psaro, V. Dal Santo, E. Selli, “*Effect of the electronic structure of TiO_2 on the plasmon photocatalytic activity of Au nanoparticles*”. In preparation.

F. Riboni, E. Selli, M.R. Hoffmann, A.J. Colussi, *J. Phys. Chem. A* **2014**, just accepted.

F.R. Kameel, F. Riboni, M.R. Hoffmann, S. Enami, A.J. Colussi, *J. Phys. Chem. C* **2014** accepted. DOI: dx.doi.org/10.1021/jp505010e.

F. Riboni, L.G. Bettini, D.W. Bahnemann, E. Selli, *Catal. Today* **2013**, *209*, 28–34.

Oral Communications

F. Riboni, M.R. Hoffmann, A.J. Colussi, E. Selli, “*Homogeneous Reduction of CO_2 by Photogenerated Pyridinyl Radicals*”, Italian Photochemistry Meeting 2014, November 27 – 29, 2014, Abbiategrasso, Italy.

F.Riboni, A. Naldoni, M. Marelli, M. Malvestuto, F. Bossola, R. Psaro, V. Dal Santo, E. Selli, “*Plasmonic interaction in defective Au/TiO_2 heterostructures: effects on the photocatalytic activity*”, 20th International Conference on Photochemical Conversion and Storage of Solar Energy – IPS-20, July 27 – August 1, 2014, Berlin, Germany.

F. Riboni, E. Selli, “*Effect of the W precursor and amount on the photocatalytic activity of WO_3-TiO_2 mixed oxides*”, Italian Photochemistry Meeting 201, October 11 – 12, 2012, Bologna, Italy.

Poster Communications

F. Riboni, E. Selli, “*WO_3-TiO_2 Mixed Oxides: Effect of the W Amount and Pt Deposition on the Photocatalytic Activity*”, 2013 MRS Spring Meeting, April 1 – 5, 2013 San Francisco, CA, USA.

F. Riboni, E. Selli, "*WO_3-TiO_2: effect of W precursor on the photocatalytic activity of mixed oxides*", 7th European Meeting on Solar Chemistry and Photocatalysis: Environmental Applications - SPEA7, June 17 – 20, 2012, Oporto, Portugal.

Other Scientific Contributions

G. Sinibaldi, F. Riboni, G.L. Chiarello, E. Selli, "*F-doped TiO_2 prepared by flame spray pyrolysis: effect on the photoelectrochemical performance*", (POSTER) Italian Photochemistry Meeting 2014, November 27 – 29, 2014, Abbiategrasso, Italy.

F.R. Kameel, F. Riboni, S. Enami, M.R. Hoffmann, A.J. Colussi, "*Fenton Oxidation of Gaseous Isoprene on Aqueous Surfaces*", (POSTER) 248th Annual American Chemical Society Meeting, August 10 – 14, 2014, San Francisco, CA, USA.

E. Selli, M.V. Dozzi, F. Riboni, S. Marzorati, M. Longhi, "*Photocatalytic Activity of TiO_2-WO_3 mixed oxides in oxidation and reduction reactions*", (POSTER) 8th European Meeting on Solar Chemistry and Photocatalysis: Environmental Applications – SPEA8, June 25 – 28, 2014, Thessaloniki , Greece.

Experience Abroad

March 2013 – March 2014. Linde Center for Global Environmental Science at the *California Institute of Technology*, Pasadena – CA, USA under the supervision of Prof. Michael R. Hoffmann and Dr. Augustin J. Colussi.